

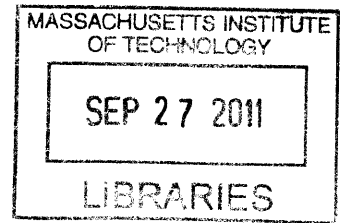
# Integrated Photonic Analog-To-Digital Converters

by

Anatol Khilo

B.S., Belarus State University (1999)

S.M., Massachusetts Institute of Technology (2008)



Submitted to the Department of Electrical Engineering and Computer Science  
in partial fulfillment of the requirements for the degree of

Doctor of Philosophy

**ARCHIVES**

at the

MASSACHUSETTS INSTITUTE OF TECHNOLOGY

September 2011

© Massachusetts Institute of Technology 2011. All rights reserved.

Author .....

Department of Electrical Engineering and Computer Science

September 2, 2011

Certified by .....

Franz X. Kärtner

Adjunct Professor of Electrical Engineering

Thesis Supervisor

Accepted by .....

Leslie A. Kolodziejski

Professor of Electrical Engineering

Chairman, Department Committee on Graduate Students



# Integrated Photonic Analog-To-Digital Converters

by

Anatol Khilo

Submitted to the Department of Electrical Engineering and Computer Science  
on September 2, 2011, in partial fulfillment of the requirements for the degree of  
Doctor of Philosophy

## Abstract

Accurate conversion of wideband multi-GHz analog signals into the digital domain has long been a target of analog-to-digital converter (ADC) developers, driven by applications in radar systems, software radio, medical imaging, and communication systems. Aperture jitter has been a major bottleneck on the way towards higher speeds and better accuracy. Photonic ADCs, which perform sampling using ultra-stable optical pulse trains generated by mode-locked lasers, have been investigated as a promising approach to overcome the jitter problem and bring ADC performance to new levels. This work demonstrates that the photonic approach can deliver on its promise by digitizing a 41 GHz signal with 7.0 effective bits and 52 dBc spur-free dynamic range (SFDR) using a discrete-component photonic ADC. This corresponds to 15 fs jitter, a 4-5 times improvement over the jitter of the best electronic ADCs, and an order of magnitude improvement over the jitter of electronic ADCs operating above 10 GHz. The feasibility of a practical photonic ADC is demonstrated by creating an integrated ADC with a modulator, filters, and photodetectors fabricated on a single silicon chip and using it to sample a 10 GHz signal with 3.5 effective bits and 39 dBc SFDR. In both experiments, a sample rate of 2.1 GSa/s was obtained by interleaving two 1.05 GSa/s channels; higher sample rates can be achieved by increasing the channel count. A key component of a multi-channel ADC – a dual multi-channel high-performance filter bank – is successfully implemented. A concept for broadband linearization of the silicon modulator, which is another critical component of the photonic ADC, is proposed. Nonlinear phenomena in silicon microring filters and their impact on ADC performance are analyzed, and methods to reduce this impact are proposed. The results presented in the thesis suggest that a practical integrated photonic ADC, which successfully overcomes the electronic jitter bottleneck, is possible today.

Thesis Supervisor: Franz X. Kärtner

Title: Adjunct Professor of Electrical Engineering





# Contents

<b>I.</b>	<b>INTRODUCTION TO PHOTONIC ANALOG-TO-DIGITAL CONVERTERS.....</b>	<b>9</b>
1.	ANALOG-TO-DIGITAL CONVERTERS .....	9
2.	STATE-OF-THE-ART ADCs; WALDEN CHART .....	14
3.	TIMING JITTER OF RF AND PHOTONIC SOURCES.....	17
4.	PHOTONIC ANALOG-TO-DIGITAL CONVERTERS .....	19
5.	POWER BUDGET AND SHOT NOISE.....	27
<b>II.</b>	<b>DEMONSTRATION OF PHOTONIC ADCS .....</b>	<b>32</b>
6.	DISCRETE-COMPONENT PHOTONIC ADC .....	32
7.	PERFORMANCE OF THE DISCRETE-COMPONENT PHOTONIC ADC.....	35
8.	INTEGRATED PHOTONIC ADC .....	43
9.	PERFORMANCE OF THE INTEGRATED PHOTONIC ADC .....	49
10.	DATA ANALYSIS FOR ADC EXPERIMENTS .....	51
11.	SUMMARY AND DISCUSSION.....	59
<b>III.</b>	<b>LINEARIZED SILICON MODULATOR.....</b>	<b>62</b>
12.	INTRODUCTION TO SILICON MODULATORS AND MODULATOR LINEARIZATION .....	62
13.	CONCEPT OF LINEARIZATION OF A MODULATOR WITH NONLINEAR PHASE SHIFTERS .....	65
14.	LINEARIZATION OF A REVERSE-BIASED SILICON MODULATOR.....	69
15.	OPTICAL BANDWIDTH OF THE LINEARIZED SILICON MODULATOR.....	78
16.	SUMMARY AND DISCUSSION.....	81
<b>IV.</b>	<b>SILICON NONLINEARITIES IN PHOTONIC ADCS.....</b>	<b>84</b>
17.	TWO-PHOTON AND FREE-CARRIER EFFECTS IN STRONGLY CONFINING WAVEGUIDES .....	84
18.	NONLINEARITY OF MICRORING FILTERS IN PHOTONIC ADCS .....	93
19.	IMPACT OF SILICON NONLINEARITIES ON PHOTONIC ADC PERFORMANCE.....	104
20.	MITIGATION OF SILICON NONLINEARITIES IN A PHOTONIC ADC .....	111
21.	SUMMARY AND DISCUSSION.....	117
<b>V.</b>	<b>MICRORING RESONATOR FILTER BANKS .....</b>	<b>121</b>
22.	INTRODUCTION TO MICRORING RESONATOR FILTERS .....	121
23.	ELEVEN-CHANNEL FILTER BANK .....	123
24.	DUAL TWENTY-CHANNEL FILTER BANK .....	129
25.	SUMMARY AND DISCUSSION.....	131

<b>VI. TWO-STAGE FIBER-TO-CHIP COUPLERS.....</b>	<b>133</b>
26. INTRODUCTION TO FIBER-TO-CHIP COUPLERS.....	133
27. CONCEPT OF THE TWO-STAGE COUPLER .....	139
28. OPTIMIZATION OF TWO-STAGE COUPLERS .....	141
29. PERFORMANCE OF OPTIMIZED TWO-STAGE COUPLERS .....	146
30. CHOICE OF REFRACTIVE INDEX OF THE LOW-INDEX WAVEGUIDE .....	153
31. POLARIZATION DEPENDENCE IN TWO-STAGE COUPLERS.....	156
32. SUMMARY AND DISCUSSION.....	157
<b>APPENDIX A. LIST OF ACRONYMS.....</b>	<b>160</b>
<b>BIBLIOGRAPHY.....</b>	<b>161</b>

## Acknowledgments

The results described in this thesis would not have been possible without my colleagues, family, and friends.

First of all, I would like to thank my research advisor, Prof. *Franz Kaertner*. I feel very privileged to have him as my advisor for the 6 years of my PhD studies. Franz is a great source of help, advice, and kind encouragement. Perhaps equally important is his unlimited and contagious positive energy and enthusiasm, which energizes people around him, drives things forward, and makes things happen.

It is difficult to select one single best thing about MIT, but if I am to so, it would be how smart the professors and students here, how much they know, and how hard they work. I learned from them a lot during my studies and without them, this thesis would be impossible. The professors with whom I had privilege to work together are (apart from Franz), *Prof. Vladimir Stojanovic*, *Prof. Erich Ippen*, and *Prof. Hank Smith*.

From the beginning and almost until the end of my PhD studies, I have been working with *Milos Popovic*, then a senior member of the group. His sharp mind, amazing talent, and persistent work made him a world's top expert in the field of silicon photonics. He is now successfully running his own research group, and it would be very surprising if it were otherwise. A large percent of the things which I know I learned from him. I also used the simulation tools he developed to obtain many results from this thesis. I would like to thank *Cheri Sorace-Agaskar* for our joint work on silicon modulators and for her patience during discussion of the details of this work. I'm very grateful to her for the great work she did presenting our results at the conferences. Cheri did design, simulations, and analysis for the silicon diode phase shifters used to study linearized silicon modulators. I am happy that I got to know *Ali Motamedi* during our joint work. I enjoyed his superb humor and his wise observations about life, as well as his coffee machine, open 24/7. I am grateful to him for his help when the help was needed. His insights into modeling nonlinear phenomena in silicon waveguides contributed significantly to the analysis presented in this thesis. I had a chance to work with *Amir Nejadmalayeri* for the last year of my PhD program, and I wish I started working with him earlier, so that I could borrow even more from his deep understanding of experimental optics and RF electronics. I also admire his passion for making things work and expanding the state-of-the-art. Amir has made significant contribution to ADC demonstration experiments. I was happy to work with *Marcus Dahlem*, who performed many experiments which enabled this work, such as the 11-channel filter bank experiments. Only a small fraction of his work is mentioned here. His impressive energy, optimism, initiative, and courage are routinely making impossible possible. I am glad I had a chance to work with *Jason Orcutt* on the exciting project of electronic-photonic integration. His area of expertise and first-hand knowledge seems to include everything. I am thankful to *Michael Peng* for many useful discussions we had on photonic ADCs. Michael did the 20-channel filter bank experiments and significantly contributed to ADC demonstrations. *Charles Holzwarth* (Trey) was the man beyond many important steps towards photonic ADC results reported in this thesis. He fabricated top-quality microring filters (such as 11-channel filter bank reported in this work) as well as fiber-to-chip couplers. *Jie Sun* did microfabrication at the latest stages of ADC development. This work would not have been possible without the people who built mode-locked lasers with extremely low jitter, *Michelle Sander*, *Hyunil Byun*, and *Jeff Chen*. Although germanium photodetectors were not mentioned in this thesis, these photodetectors have great

potential for photonic ADC; germanium photodetectors have been developed by *Nicole DiLello*, *Prof. Judy Hoyt*, and *Jung Yoon*.

I would like to separately mention the Lincoln Lab team, with which I had a chance to work in the course of the project. *Steven Spector* has been steadily running the fabrication of the ADC chip with a huge number of fabrication steps, starting from chip layout, and ending in characterization of fabricated devices. His expertise and persistence made possible a large fraction of results reported in this work. I was glad to work with *Mathew Grein*, the man in command of ADC experiments. His bitter fight for that one extra bit yielded an order-of-magnitude improvement over the state of the art, as reported in this thesis. *Mike Geis* created silicon photodetectors which made demonstration of an integrated photonic ADC possible. *Jade Wang* contributed to development of the experimental setup for ADC demonstrations.

I would like to separately mention my friends *Vasileios-Marios Gkortsas* and *Siddharth Bhardwaj*. I was happy to have them as my officemates for many years. We had many intriguing conversations about research as well as things way beyond it. I learned many amazing things from both of them. I would also like to thank my former officemates, *Aleem Siddiqui* and *Jonathan Cox*, who seriously helped me in the beginning of my studies, when I first came to the US and had to adopt to a very different society.

My family was very supportive and patient in the course of my PhD program. It is hard to express in words my gratitude to my wife *Marina*, who, at times, believed in me more than I did myself. My dear son *Andrey* was always so happy to see me when I came home after a long day at work. My parents *Nikolay* and *Zoya Khilo* are the ultimate people behind the successful completion of this work. They invested in me so much that I can only hope that one day I can be as good parent of my children as they are.

The sponsor of this work has been the Defense Advanced Research Projects Agency (DARPA).

# **I. Introduction to photonic analog-to-digital converters**

This thesis describes the progress made towards implementation of an integrated photonic analog-to-digital converter (ADC), which uses low-jitter pulse trains generated by mode-locked lasers to sample high-frequency electrical signals. After an introduction to photonic ADCs in the first part of the thesis, the results of implementation of photonic ADCs are presented in the second part. The following parts of the thesis are studying steps towards further progress in integrated photonic ADCs.

The first part of the thesis gives an introduction to electronic and photonic analog-to-digital converters. Chapter 1 gives a basic introduction to ADCs and defines their main performance metrics. Next chapter describes the current state-of-the art in electronic ADCs and defines the main factors limiting their performance – the aperture jitter and the comparator ambiguity. Chapter 3 gives a basic explanation of the fact that the timing jitter of optical sources can be 3-4 orders of magnitude lower than that of electronic sources typically used in ADCs. Chapter 4 describes the principles of operation of the photonic ADC considered in this thesis and explains how the photonic approach solves the problems of the aperture jitter and comparator ambiguity. An overview of the previous work on photonic ADCs is given in this chapter as well. The remaining chapter discusses the importance of power budget and determines power requirements due to shot noise limitations.

## **1. Analog-to-Digital Converters**

Analog-to-digital converters are the circuits which convert real-world continuous signals into the discrete-time digital representation, suitable for digital signal processing in digital circuits or computers. Analog-to-digital conversion has two steps. The first step is sampling, which means that the values of the signals are taken at certain discrete time moments, which are usually equally spaced in time. The time moment  $t_n$  can be expressed as  $t_n = n \cdot T$ , where  $T$  is the time interval between samples and  $n$  is an integer. The sample rate is defined as the number of samples recorded per second,  $f_s = 1/T$ . For example, in an ADC sampling at  $f_s = 1$  MSa/s, the

samples are taken at 1  $\mu\text{s}$  intervals, and in an ADC sampling at  $f_s = 1 \text{ GSa/s}$ , the samples are taken at 1 ns intervals. The second step is quantization, when the continuous amplitude of the samples is replaced with its discrete representation. In an ADC with  $N$  bits, the discrete signal has  $2^N$  distinct equally-spaced levels.

The number of bits  $N$  is called the nominal number of bits. The nominal number of bits defines the number of quantization levels used (which is  $2^N$ ), but does not carry information about how the ADC accuracy, i.e. about how precisely the obtained discrete-time, discrete-amplitude signal represents the actual analog input signal. The accuracy of ADCs is described by the effective number of bits (ENOB). Roughly speaking, the ENOB defines how many of the nominal bits are accurate. For example, an ADC with 8 nominal bits might have only 5 effective bits, which means that the last 3 of the nominal 8 bits are just noise. It is important to keep in mind this difference between the effective and nominal number of bits, as it can be significant.

To understand the exact meaning of the effective number of bits, it is useful to understand how exactly the ENOB formula is introduced [1-3]. To this purpose, consider an ADC with  $N$  nominal bits, which is assumed to be ideal, which means that it introduces no errors except the inevitable error due to quantization of a continuous signal to  $2^N$  discrete levels. The error introduced by quantization changes within  $[-0.5 \dots 0.5] \Delta V$ , where  $\Delta V$  is the least significant of the ADC, i.e. the size of one “step” of the quantized signal. The least significant bit is  $\Delta V = V_{pp}/2^N$ , where  $V_{pp}$  is the full-scale peak-to-peak voltage of the ADC, which is the maximum voltage the ADC can accept without truncation. In general, the probability density function of quantization error depends on the signal applied to the ADC. It is now assumed that the distribution of the quantization error in the  $[-0.5 \dots 0.5] \Delta V$  interval is uniform; this is a reasonable approximation especially for quickly-varying signals. The quantization error can be considered as a noise source, with noise power found as

$$\text{Noise Power} \sim \int_{-\Delta V/2}^{\Delta V/2} V^2 f(V) dV = \frac{1}{\Delta V} \int_{-\Delta V/2}^{\Delta V/2} V^2 dV = \frac{\Delta V^2}{12},$$

where  $f(V)$  is the probability density function of the noise signal,  $f(V) = 1/\Delta V$ .

The next step is to assume that the ADC is digitizing a sinusoidal signal which occupies the full-scale voltage of the ADC. The power of this signal can be found as

$$\text{Signal Power} = \int_0^{2\pi} \left[ \frac{V_{pp}}{2} \sin(t) \right]^2 dt = \frac{V_{pp}^2}{8}.$$

The signal-to-noise ratio (SNR), in dB units, is

$$SNR_{quant} = 10 \log_{10} \left( \frac{\text{Signal Power}}{\text{Noise Power}} \right) = 10 \log_{10} \left( \frac{V_{pp}^2}{8} \bigg/ \frac{\Delta V^2}{12} \right) = 10 \log_{10} \left( \frac{6}{4} 2^{2N} \right),$$

$$SNR_{quant} = 1.76 + 6.02 \cdot N.$$

The number of bits  $N$  can be expressed from the quantization noise-limited  $SNR$  as

$$N = \frac{SNR_{quant} - 1.76}{6.02}. \quad (1.1)$$

The derivation above was assuming an ideal ADC, where quantization is the only source of errors. In a non-ideal ADC, errors are also caused by non-deterministic noise sources and deterministic distortions, resulting in some limited signal-to-noise-and distortion ratio (SINAD; more about SINAD definition below). Effective number of bits (ENOB) of a non-ideal ADC with given SINAD is defined as the number of quantization bits of an ideal ADC which has quantization-limited SNR equal to SINAD of the non-ideal ADC,

$$ENOB = \frac{SINAD - 1.76}{6.02}. \quad (1.2)$$

This is a well-known formula defining ENOB of a non-ideal ADC. Note that, unlike the nominal number of bits, ENOB is usually a non-integer number.

Apart from ENOB, ADC performance is characterized by several other parameters, such as signal-to-noise ratio (SNR), spur-free dynamic range (SFDR) and total harmonic distortion (THD). To define these values, assume that a single-frequency sinusoidal signal is applied to the ADC input. The signal recorded by the ADC might have the spectrum shown in Fig. 1. In general, the spectrum has not only the fundamental frequency which was applied to the ADC, but also some noise floor, as well as some additional frequency components not present in the input signals, in this case these are the 2nd, 3rd, and 4th harmonic distortions. The spur-free dynamic range (SFDR) is defined as the ratio of the power of the fundamental to the power of the largest distortion. In the example of Fig. 1, the largest distortion is the second harmonic distortion. The corresponding SFDR is 30 dB. Note that y-axis in Fig. 1 shows the powers

normalized to the power of the fundamental. The units of y-axis are dBc, dB below carrier. In these units, the power of the fundamental tone is always 0 dBc. The SFDR is an important characteristic because it defines the dynamic range of the ADC, i.e. in situation when a strong and a weak signal are applied to the ADC, the weak signal can be resolved if it is below the strong signal by no more than SFDR.

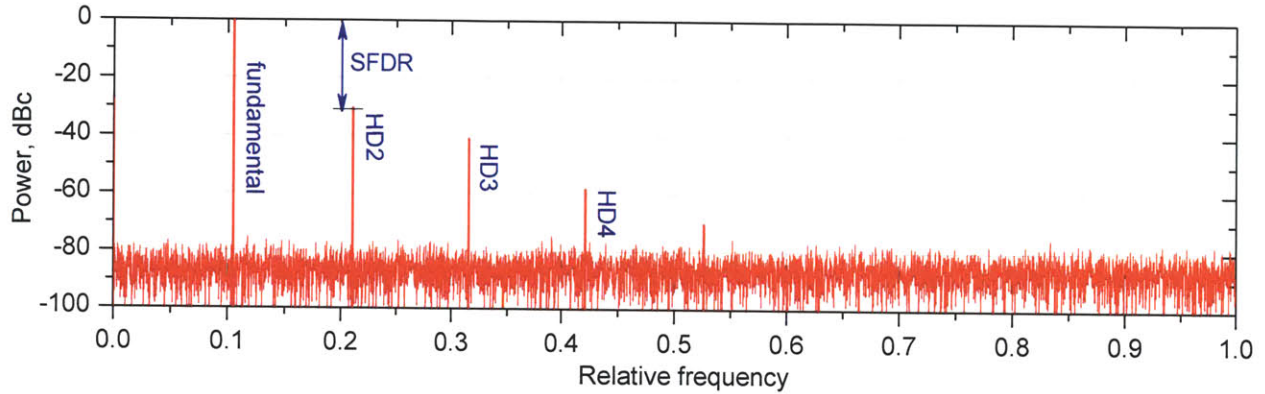


Figure 1. An example of spectrum of the signal recorded by the ADC when a single-tone sinusoidal signal is applied to its input. The tone corresponding to the input signal is labeled as "fundamental", and its 2nd, 3rd, and 4th harmonics are labeled as "HD2", "HD3", and "HD4". The y-axis shows the spectral power, normalized to the power of the fundamental (carrier) frequency; the units of the y-axis are dBc, i.e. dB below carrier.

The total harmonic distortion (THD) is the ratio of the power of the fundamental to the sum of the powers of all distortions; in Fig. 1, this is the sum of 2nd, 3rd, and 4th harmonic distortions.

The signal-to-noise ratio (SNR) is the ratio of the signal power to the noise power within the full bandwidth of the ADC. In Fig. 1, all the noise components need to be integrated to find the total noise power. The noise power can be roughly estimated from the spectrum of Fig. 1. The noise floor in this figure is located at roughly -83 dBc level. However, this number by itself is meaningless, because it depends on frequency resolution, i.e. on the number of points used to create the spectral plot. In Fig. 1, this number of points was  $5 \cdot 10^3$ , so the total noise within full bandwidth is  $-83 + 10 \cdot \log_{10}(5 \cdot 10^3) \approx -46$  dB, i.e.  $\text{SNR} \approx 46$  dB. Rigorous summation of all noise components gives  $\text{SNR} = 48$  dB, which is close to the rough estimate of 46 dB.

The signal-to-noise and distortion ratio (SINAD) is the ratio of the power of the fundamental to the sum of all the distortions and full noise power. SINAD is the most rigorous



characteristic in the sense that it includes all sources of errors. The same is true for ENOB, which is defined through SINAD according to Eq. (1.2).

The SFDR and SNR are sometimes measured in bits instead of dB. The number of SFDR bits and SNR bits are defined as:

$$SNR_{bits} = \frac{SNR - 1.76}{6.02},$$

$$SFDR_{bits} = \frac{SFDR}{6.02}.$$

Note that in view of these definitions, ENOB can be thought of as the number of "SINAD bits" (although this terminology is not used).

SNR and SFDR are important ADC metrics which are normally quoted separately from ENOB. In general, all these metrics depend on the frequency of the test signal. For this reason, specifications of commercial ADCs often provide these metrics as a function of signal frequency.

Apart from the metrics which define the accuracy with which an ADC digitizes the input signal, important characteristics of the ADC are its analog bandwidth and sample rate. In general, the two are not constrained by Nyquist theorem and are independent of each other. The analog bandwidth comes from the frequency response of the ADC, which rolls off at high frequencies. As frequency increases, the ADC response goes down, which reduces the signal with respect to the noise level (SNR). At some point, the response is so low that the signal cannot be distinguished from the noise. The sample rate is different - it just determines how many samples per second the ADC records. For Nyquist sampling, the sample rate must be half the analog bandwidth. However, the sample rate can be larger higher or lower than half the analog bandwidth, in which case the signal is oversampled or undersampled, respectively. In case of undersampling (like in experiments described in Part II), input frequencies are aliased because of insufficient sample rate, but these frequencies are nevertheless recorded. In case of oversampling, high sample rate does not mean that high frequencies are recorded; for example, an ADC might have the sample rate of 80 GSa/s, but it can only work for frequencies up to 10 GHz.

## 2. State-of-the-art ADCs; Walden chart

This paragraph describes the best performance results achieved in electronic ADC technologies, and describes limitations which determine the rate of the progress towards higher accuracy and rates.

The field of electronic data conversion has witnessed significant progress over the last decade. With the unity gain frequency of CMOS technology reaching hundreds of gigahertz and matured SiGe technology, data converters based on the silicon platform operating at sampling rates of tens of GSa/s now exist. For instance, Fujitsu Inc. recently introduced a 65 GSa/s ADC in CMOS [4]. Prior to that, Nortel Inc. had demonstrated a 40 GSa/s CMOS ADC [5], and Rensselaer Polytechnic Institute had introduced its 40 GSa/s SiGe ADC [6]. Fig. 2 shows the "Walden chart", the chart which represents ADCs as points according to their ENOB and analog frequency at which this ENOB has been achieved. This chart is based on the definitive survey of ADC field by R. Walden [1]. The light blue circles in Fig. 2 represent ADCs from the latest version of the survey, dated late 2007 [1]. A number of new ADCs has appeared since Walden's survey (some of which are already mentioned); Fig. 2 contains an updated version of the Walden chart, with the new ADCs represented with dark circles. The full list of new ADCs<sup>1</sup> added to Walden chart is given in Table 1.

---

<sup>1</sup> The ADC list was compiled by Amir H. Nejadmalayeri of Optics and Quantum Electronics group at MIT.

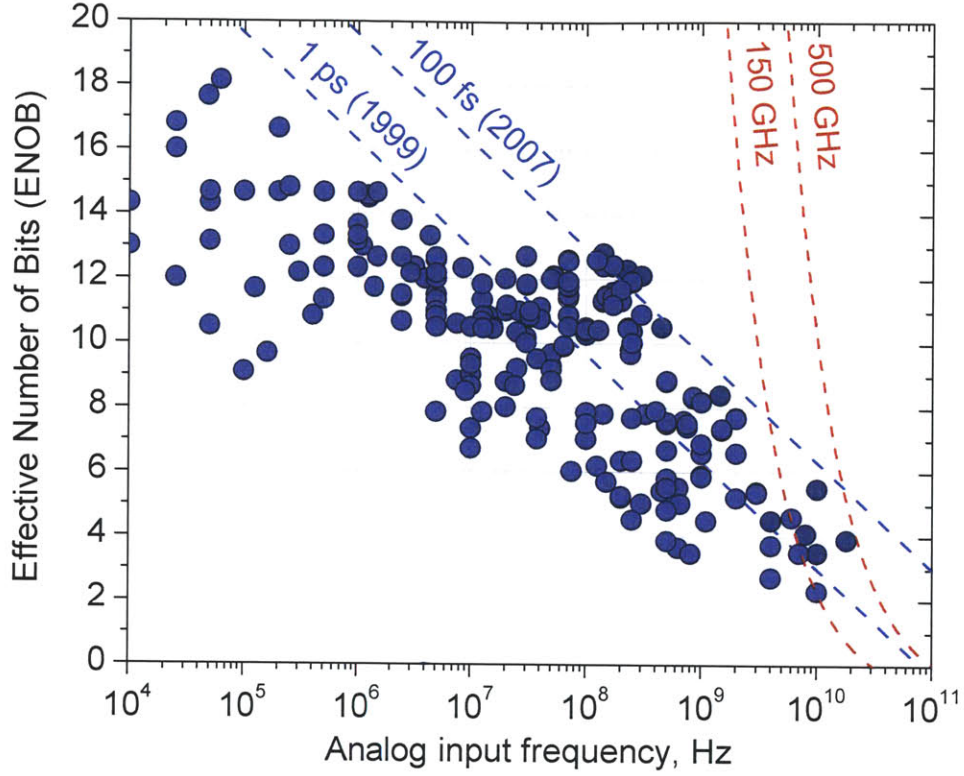


Figure 2. "Walden chart" showing ENOB of existing ADCs as a function of analog input frequency. Each point represents an ADC: blue circles correspond to the ADCs from Walden's survey of ADCs as of late 2007 [1], and dark blue circles correspond to some high-performance ADCs that have been demonstrated since 2007 (Table 1). The dashed blue lines are loci of constant values of rms aperture jitter  $\tau_a$ , as described by Eq. (2.1); the jitter values are indicated next to the lines together with the year when this jitter value was achieved. The dashed red lines represent limitations due to comparator ambiguity, as described by Eq. (2.2); the values shown next to the lines are the transistor transit-time frequencies  $f_T$ . According to [1], the state-of-the-art as of 2007 is  $f_T = 150\text{GHz}$ , and the projection for 2015 is  $f_T = 500\text{GHz}$ .

Table 1. List of high-performance electronic ADCs<sup>1</sup> which appeared since the 2007 version of ADC survey by Walden [1]. The effective number of bits given in column 2 is reported for analog frequencies of input signals shown in column 3. The ADCs of this table are represented by dark blue circles in the updated Walden chart of Fig. 2.

ADC name	ENOB	Analog frequency
Nortel, ISSCC 2009 paper	4.1 bits	8 GHz
Nortel, ISSCC 2010 paper [5]	3.9 bits	18 GHz
Rensselaer Polytechnic, JSSC 2010 paper [6]	3.5 bits	10 GHz
Rockwell RAD006	5.5 bits	10 GHz
Teledyne RAD004	4.5 bits	4 GHz
National Semiconductor ADC12D1800	8.4 bits	1.45 GHz
Analog Devices AD9446	11.6 bits	0.17 GHz
Analog Devices AD9460	12.3 bits	0.225 GHz
Texas Instruments ADS5474	10.5 bits	0.45 GHz
Analog Devices AD9467-250	12.1 bits	0.3 GHz
Linear Technologies LTC2217	12.8 bits	0.14 GHz
Linear Technologies LTC2208-14	11.9 bits	0.25 GHz
Linear Technologies LTC2216	12.8 bits	0.14 GHz

The main factors which limit the accuracy of analog-to-digital conversion are the aperture jitter and the comparator ambiguity. The aperture jitter (or "aperture ambiguity", or "timing jitter") is the random variation of the position of the temporal sampling interval. The result is that the sampling interval is not constant, but is varying randomly, leading to accuracy degradation. The comparator ambiguity, a major limiting factor at high signal frequencies, comes from the finite speed with which the ADC comparator responds to small variations in the input signal to produce the correct quantization decision relative to the comparator reference [3, 1]. It can be shown that the limits on ENOB due to aperture jitter and comparator ambiguity are given by [1]

$$ENOB_{jitter} = \log_2 \left( \frac{1}{2\pi f_{sig} \Delta t} \right) - 1, \quad (2.1)$$

$$ENOB_{ambiguity} = \frac{\pi f_T}{13.9 f_{sig}} - 1.1. \quad (2.2)$$

---

<sup>1</sup> The ADC list was compiled by Amir H. Nejadmalayeri.

In these formulas,  $f_{sig}$  is the analog frequency of the signal being digitized,  $\Delta t$  is the rms value of the aperture jitter, and  $f_T$  is the transit-time frequency of the transistor.

The limitations due to aperture jitter and comparator ambiguity are represented with dashed lines in Fig. 2. The dashed blue lines correspond to jitter values of 1 ps and 100 fs, which were approximately the state-of-the-art in 1999 and 2007. The best ADCs available now surpass this jitter level, with 60-80 fs of jitter in 100-400 MHz frequency range. The dashed red lines correspond to comparator ambiguities for the transit frequency of  $f_T = 150$  GHz, which was the state-of-the-art in 2007, and of  $f_T = 500$  GHz, the projection for the year 2015 [1]. From Fig. 2 one can see that the performance trends in electronic ADCs indeed follow timing jitter lines for frequencies below several gigahertz. The comparator ambiguity becomes the limiting factor at high frequencies (around 10 GHz), reducing the ADC accuracy extremely rapidly as frequencies increase further.

Photonic ADCs base their operation on ultra-stable mode-locked laser sources which can have jitter levels many orders of magnitude lower than the electronic state-of-the-art [7, 8], as explained in the next paragraph. Such lasers can eliminate the limitations of electronic jitter described above, which is one of the major reasons for pursuing the photonic approach to analog-to-digital conversion.

### 3. Timing jitter of RF and photonic sources<sup>1</sup>

Today's electronic data converters derive their sampling clock from RF oscillators. The timing jitter or phase noise of these oscillators is governed by the laws of thermodynamics and therefore is fundamentally limited by the thermal noise of the resonator and active elements of the oscillator, which sets stringent limits at room temperature operation. Whatever the noise source is, the addition of random noise to a sinusoidal signal of given amplitude leads to an uncertainty of the zero crossing proportional to the signal period, as illustrated in Fig. 3. Higher frequency oscillators will therefore show lower timing jitter than a lower frequency oscillator with otherwise identical components and noise [7]. Specifically, for ultra-short laser pulses whose microwave phase undergoes a random walk in the laser cavity due to spontaneous

---

<sup>1</sup> Most of this paragraph was contributed by Amir H. Nejadmalayeri and Franz X. Kärtner.

emission noise, the standard deviation  $\Delta t$  of the center of gravity of pulses from their nominal positions grows in time according to a diffusion law [9] and scales with the measurement time  $T_M$  as

$$\Delta t \sim \tau \sqrt{\frac{h\nu T_M}{E_p \tau_c}}, \quad (3.1)$$

where  $\tau$  is the pulse duration,  $E_p$  is the intracavity pulse energy,  $\tau_c$  is the cavity decay time and  $h\nu$  the photon energy. Thus mode-locked lasers producing 10-100 fs optical pulses can serve as sampling clocks that can be  $10^3$  to  $10^4$  times lower in jitter compared to their microwave driven counterparts with a typical period of 100 ps and otherwise similar parameters. Note that ultra high Q microwave oscillators, such as sapphire loaded cavity resonators (eventually even cryogenically cooled) or opto-electronic delay line oscillators, can deliver very low jitter, but at a significantly higher cost and size.

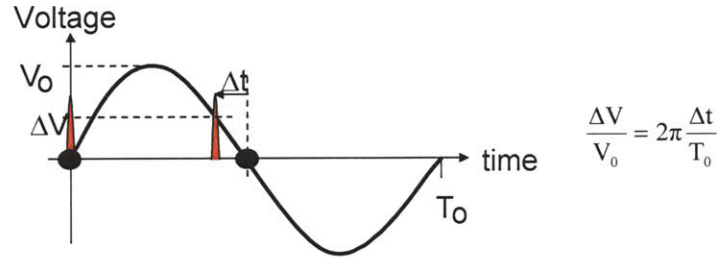


Figure 3. A simple illustration of the fundamental law that the given amount of noise, shown as  $\Delta V$ , correspond to timing error of  $\Delta t$ , which is directly proportional to the period of the signal.

Experimental verification of the low timing jitter of mode-locked lasers started as early as 1986 [10-13]. Optical techniques for timing jitter measurements, such as the recently introduced balanced optical cross-correlation technique [7], confirmed that passively mode-locked lasers show jitter levels of less than 3 fs for standard fiber lasers [14, 15] and about 10 as for solid-state lasers due to their shorter pulses, higher intracavity pulse energy and lower intracavity loss [8]. In fact, this latter value is the lowest jitter or phase noise level ever observed in any oscillator. Some of these sources can even be integrated on a chip [16]. The microwave phase noise at low frequencies or slow drift of the repetition rate, although present in free-running mode-locked



lasers, can be suppressed using standard long-term stable frequency references or ultra-stable high Q cavities [17-19]. Note that the low timing jitter or microwave phase noise has also been explored in the past in different mode-locked laser platforms [20, 21].

## 4. Photonic Analog-to-Digital Converters

This chapter describes principles of operation and review of previous work on photonic analog-to-digital converters, with the emphasis on converters which perform sampling optically and quantization electronically.

To overcome the aperture jitter in the sampling process, photonic ADCs perform sampling in the optical domain using low-jitter optical pulse trains. Sampling occurs when such pulse trains pass through an electro-optic modulator while the voltage signal to be sampled is applied [22]; the output pulse energies represent the RF signal values at the temporal positions of the pulses. The optical pulses can then be converted into electrical domain with photodetectors and digitized by electronic ADCs. The operation of this basic photonic ADC is illustrated in Fig. 4.

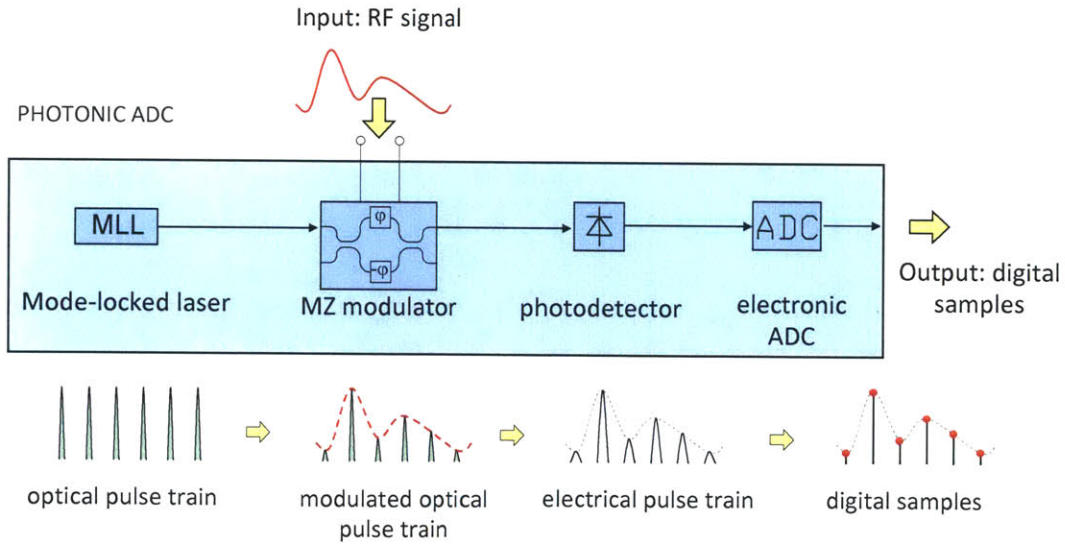


Figure 4. Operation of a single-channel photonic ADC. Optical sampling occurs in an electrooptic modulator, which modulates a train of short optical pulses with the RF signal to be sampled. The energies of the output pulses are proportional to the values of RF signal being sampled at the corresponding time moments.

A major benefit of optical sampling approach is that the jitter of the optical sampling process is determined by the jitter of the optical pulse train, which, as explained above, can be extremely low. The jitter scaling from microwave to optical sources described in the previous chapter, together with rapid progress in electronic-photonic integration via the silicon photonics technology platform, gives confidence that the 3-4 orders of magnitude in jitter reduction, possible with mode-locked lasers, can be exploited to increase the sampling speed resolution product beyond the 100-as boundary as indicated in Fig. 5. This has potential to revolutionize processing of signals potentially up to THz bandwidths with more than 10 ENOB (provided that modulators working at such high frequencies are available). Another benefit of the optical sampling approach is that electro-optical interactions are very fast, which means that the aperture over which the RF signal is sampled, as defined by the duration of optical pulses, can be very short.

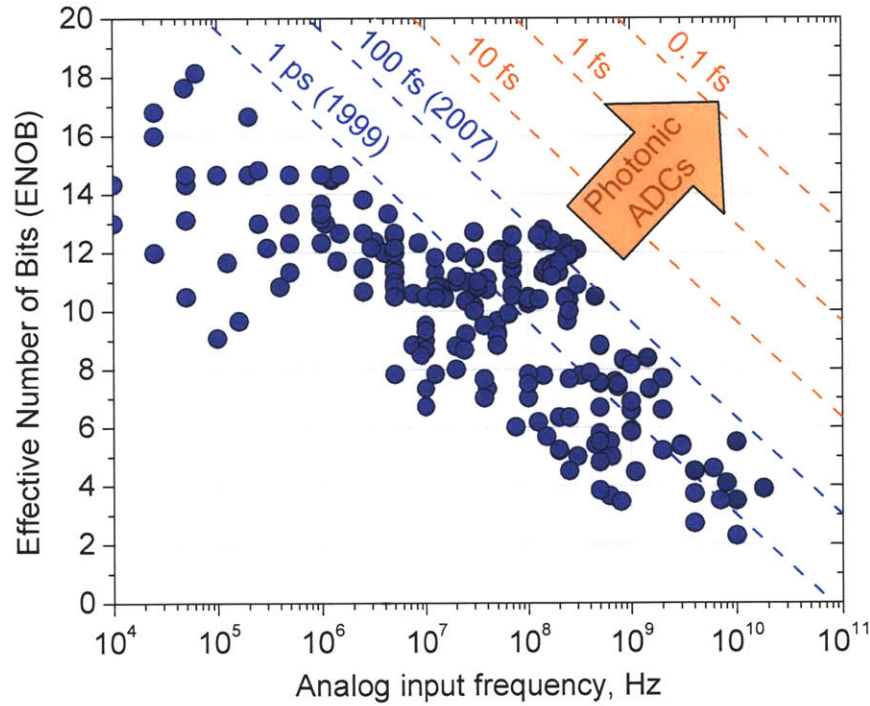


Figure 5. "Walden chart" which, similar to Fig. 2, shows the ENOB of existing ADCs as a function of analog input frequency. Photonic ADCs, operating with very low timing jitter, are envisaged to bring ADC performance to completely new levels, as indicated by the arrow labeled "Photonic ADCs", by reducing the aperture jitter to values as low as 0.1 fs.



The simple scheme shown in Fig. 4 ensures low-jitter sampling, but the sample rate is limited by the sample rate of the electronic ADC. This makes accurate sampling at high sample rates difficult to achieve. To increase the sample rate, the scheme with multiple interleaved channels can be used. Two variants of channel interleaving have been proposed: time-interleaving [23, 24] and wavelength interleaving [25, 26]. In time-interleaving approach illustrated in Fig. 6(a), a fast switch sends consecutive pulses into different paths, effectively reducing the repetition rate of the pulse train. The switch can be implemented as a series of Mach-Zehnder interferometers [26]. The pulse trains in each channel are then processed independently. Another approach is to use wavelength demultiplexing, as illustrated in Fig. 6(b). In this approach, the center wavelengths of the pulses at the input of the modulator change periodically in time; for a system with  $N$  channel,  $N$  distinct wavelengths must be used. This wavelength-interleaved pulse train is modulated and split into  $N$  trains with a wavelength demultiplexer. This approach, which was selected for this work, requires only passive optical filters and does not need active switching of optical pulses.

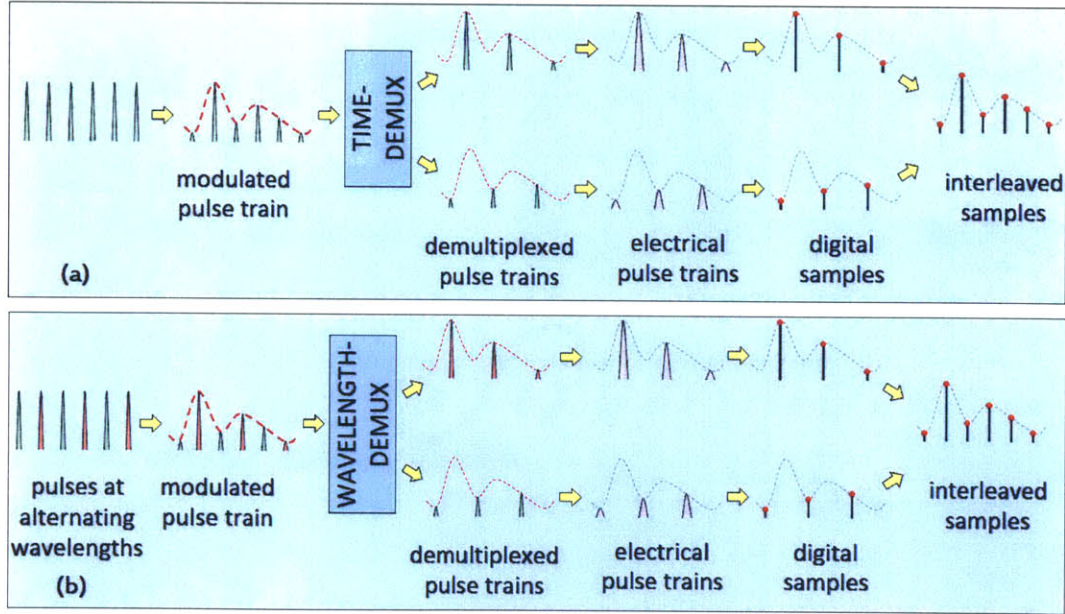


Figure 6. Schematic illustration of operation of photonic ADC with (a) time interleaving and (b) wavelength interleaving. The work presented in this thesis uses the wavelength interleaving approach.

As mentioned above, the wavelength-interleaving approach requires a pulse train where center wavelength changes periodically from pulse to pulse. One way to create such a pulse is

illustrated in Fig. 7(a). A demultiplexer is used to split optical pulses into sub-pulses centered at different wavelengths; for an  $N$ -channel ADC, 1-to- $N$  demultiplexer needs to be used. The obtained pulse trains are then delayed with respect to each other with differential delay lines. The delayed pulses are then combined into a single path with an  $N$ -to-1 multiplexer. The result is a pulse train with repetition rate increased by  $N$ , with discrete time-to-wavelength mapping introduced in the train, i.e. the pulses separated in time are also separated in wavelength [27, 28]. A continuous version of time-to-wavelength mapping can also be implemented, see Fig. 7(b) [25, 26]. This approach uses a dispersive element, such as an optical fiber, where the group delay is proportional to wavelength. This element introduces linear chirp to the optical pulses, which means that the wavelength of the chirped pulse is continuously changing in time. The pulses are chirped to completely fill the interval between the pulses, as illustrated in Fig. 7(b). When the train of chirped pulses is modulated with the RF signal in a modulator, the RF waveform is effectively imprinted onto the spectrum of the pulses. This work uses the first approach with discrete time-to-wavelength mapping.

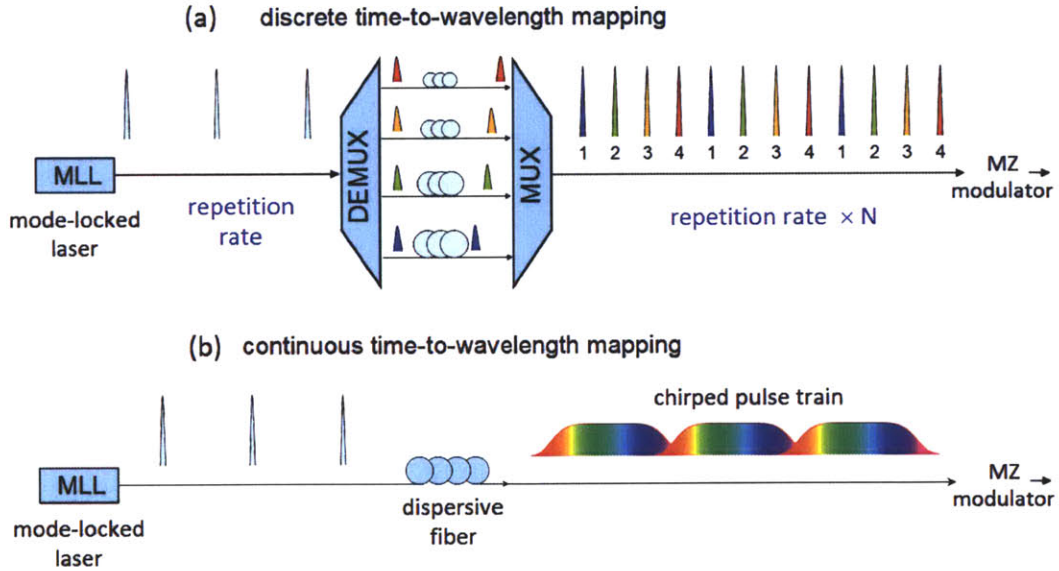


Figure 7. Two ways to implement wavelength-interleaving in a photonic ADC. (a) The approach with discrete time-to-wavelength mapping, which uses wavelength demultiplexer to split pulses into sub-pulses at different wavelengths, delay them by different amounts in differential delay lines, and combine them back into a single train with a multiplexer. (b) The approach with continuous time-to-wavelength mapping, where a dispersive fiber (or some other element with group delay linearly proportional to frequency) is used to chirp the pulses, spreading wavelengths continuously over the pulse repetition period.



The ADC architecture used in this work, based on discrete wavelength-demultiplexing approach with  $N$  wavelength channels, is illustrated in Fig. 8. The optical pulse train with repetition period  $T$  is split into  $N$  trains, each centered at a different wavelength, with a 1-to- $N$  wavelength demultiplexer. These trains pass through optical delay lines, which introduce incremental delays of  $T/N$  between them. The trains are then recombined with a multiplexer to produce a pulse train with repetition period  $T/N$ , where pulse wavelengths repeat periodically every  $N$  pulses, thus establishing the discrete time-to-wavelength mapping within the pulse train. The next step is the optical sampling, i.e. modulation of the optical pulse train with the RF signal to be sampled [22]. The modulated pulse train is then taken apart into  $N$  channels using a wavelength demultiplexer matched to the one used earlier to establish the time-to-wavelength mapping. The pulse trains in all channels are converted to the electrical domain with photodetectors, boosted in amplitude with RF amplifiers, and digitized with electronic ADCs. These ADCs are synchronized with the mode-locked laser and take one sample per pulse, exactly at the pulse peak. Alternatively, the pulses can be integrated in time with an integrator prior to sampling. During post-processing, the samples captured in different channels are compensated for distortions and interleaved to obtain the final digital representation of the RF signal.

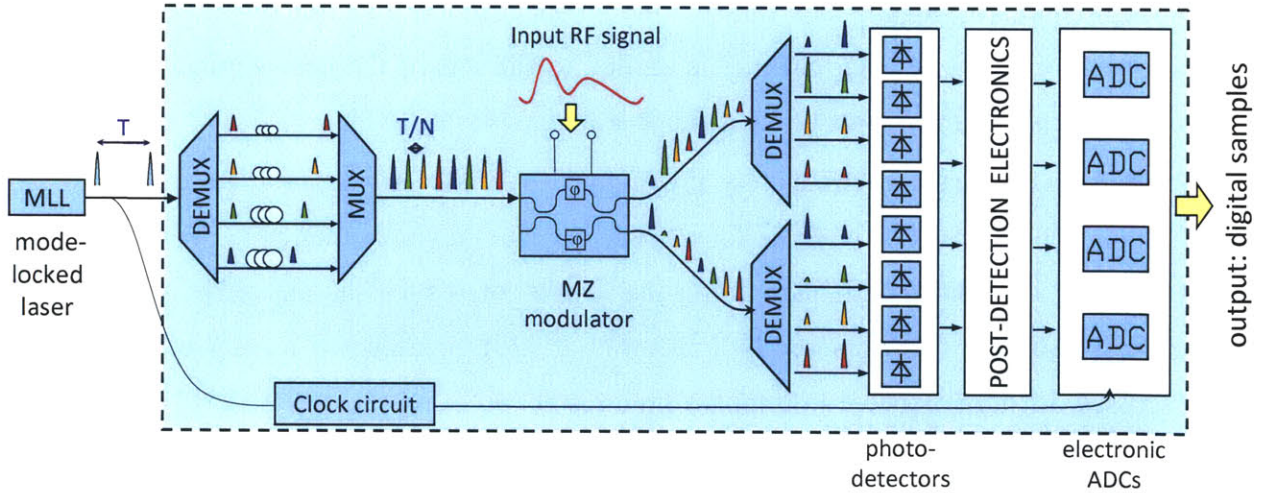


Figure 8. Layout of the photonic ADC studied in this work. The components of the ADC inside the dashed box can ultimately be integrated on a single electronic-photonic chip.

As mentioned above, the timing jitter of the photonic ADC is defined by the timing jitter of the optical pulse train, which is one of the major reasons for interest to photonic ADCs. Note that

the electronic ADCs used to digitize the pulse of electrical trains have some inherent aperture jitter. However, the accuracy of the photonic ADC is insensitive to the timing jitter of electronic ADCs because the electronic ADCs sample the relatively flat-top regions of the pulses.

Note that the scheme with  $N$  channels not only increases the sample rate by a factor of  $N$ , but also reduces the required analog bandwidth of photodetectors and electronic ADCs by the same factor [26], which needs to be only as high as several times the original laser repetition rate to avoid inter-symbol interference between subsequent pulses. This makes it possible to create photonic ADCs with large sample rates and analog bandwidths using relatively slow components. This is a very important advantage of the multi-channel approach, and is another major reason why photonic ADCs attract continuous interest.

Another important advantage of the multi-channel photonic approach is that because of reduced analog bandwidth at the input of electronic ADCs, the impact of comparator ambiguity – the major factor limiting accuracy at frequencies around 10 GHz and above [1] – is completely eliminated. Indeed, the impact of comparator ambiguity on ENOB depends on signal frequency in an extreme way: according to (2.2), the ENOB is inversely proportional to signal frequency, resulting in almost vertical lines in Fig. 2. As mentioned above, the multi-channel approach significantly reduces the analog bandwidth of individual channels; in terms of Fig. 2, this means that the operation point of each channel is shifted to the left of the near-vertical comparator ambiguity lines, where the impact of comparator ambiguity is negligible.

Photonic ADCs have been actively investigated over the last decades; an overview and classification of photonic ADCs can be found in an excellent review paper by G. Valley [2]. The idea of optical sampling originates from the works of Taylor et al. [22]. Wavelength-demultiplexing scheme was proposed by Frankel et al. [26], preceded by a work of Valdmanis, who discussed a similar concept to improve time resolution of oscilloscopes [25]. Wavelength-demultiplexing based on discrete time-to-wavelength mapping – the approach adopted in this work – was proposed by Yariv [27] and Kang [28]. A time-demultiplexing approach [23] was adopted by Juodawlkis et al. [24], who analyzed the performance of optically-demultiplexed ADCs and developed calibration techniques which helped to demonstrate 9.8 ENOB for a 733 MHz signal sampled at 505 MSa/s in an 8-channel system in a work by Williamson et al. [29]. A prominent way to increase ADC speed is the photonic time-stretch approach pioneered by the group of Jalali [30]. In this approach, one fiber introduces continuous time-to-

wavelength mapping at the input of the modulator, and another fiber further stretches the modulated signals to slow them down and enable high-speed sampling [30, 31]. A short-pulse digitizer operating at astonishing 10 TSa/s with 4.5 ENOB has been demonstrated with this approach [32]. On the way to achieving continuous time operation, 6-7 effective bits were recently reported over a 10 GHz bandwidth by the group of Valley [33], 6.7-7.2 effective bits were obtained over a 10 GHz bandwidth by the group of Jalali [34], and 2.5 bits were reported for a 35 GHz input sampled at 150 GSa/s [35]. Sophisticated calibration of time-stretch ADCs was applied to achieve these results [33-35]. Other impressive results include 8.0 ENOB at 10 GHz [36] and 7.0 ENOB at 40 GHz [37], achieved in narrowband optically-sampled ADCs. The systems described above use electronic quantization. Another class of ADCs performs quantization optically [2, 22, 38-40]; many promising schemes have been demonstrated, and efforts are in progress to improve their accuracy beyond a few bits.

The high-performance photonic ADCs mentioned above has been put onto the Walden chart shown in Fig. 9. The full list can be found in Table 2. Note that the emphasis of this work is on wideband ADCs. Therefore, although some optically-sampled ADCs intended for narrowband operation demonstrated impressive results [36, 37], they were not included into Fig. 9 and Table 2 because they cannot be easily scaled to wideband operation. It can be seen that while the photonic ADCs has been able to demonstrate very good results, they are only slightly exceed the performance of electronic ADCs. We can speculate that the reason might have been that the timing jitter of the laser sources used in previous works was not low enough. Using a low-jitter laser source, this work has been able to achieve 7.0 effective bit for 41 GHz input frequency, represented by a large orange star in Fig. 9. Detailed explanation of this result can be found in Part II of the thesis.

As a final remark, note that while the ADC studied in this work is referred to as a "photonic ADC", this terminology is not exact because an important part of signal digitization is carried out by purely electronic means. A more precise term would be an "electronic-photonic ADC", or, an "optically sampled electronically quantized ADC" in classification of G. Valley [2]. In this work, the term "photonic ADC" is used for brevity, and it is necessary to keep in mind that both photonic and electronic parts of the ADC play very important role.

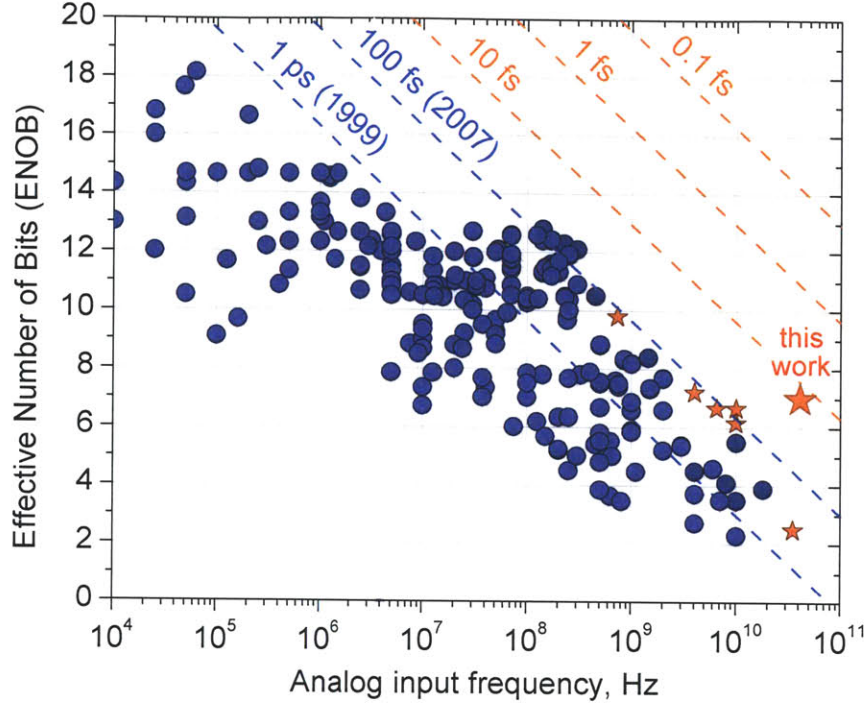


Figure 9. "Walden chart" which, similar to Figs. 2 and 5, shows the ENOB of existing ADCs as a function of analog input frequency. The chart was updated with some high-performance wideband photonic ADC results, shown with orange stars (see Table 2 for photonic ADC list). The large orange star is the result achieved this work, which will be described in detail in Chapter 7.

Table 2. List of high-performance wideband photonic ADC results. The ADCs of this table are represented by small orange stars in Fig. 9.

ADC reference	ENOB	Analog frequency
Williamson et al., LEOS 2003 [29]	9.8	0.733 GHz
Chou et al., Journal of Lightwave Tech. 2009 [35]	2.5	35 GHz
Gupta et al., Optics Letters 2008 [34]	7.2	4 GHz
	6.65	10 GHz
Sefler et al., Journal of Lightwave Tech. 2010 [33]	6.15	10 GHz
	6.65	6.5 GHz

## 5. Power budget and shot noise

A fundamental limit on performance of a photonic ADC is set by the shot noise. Achieving certain shot noise-limited performance requires certain optical power, which sets the power requirements for the mode-locked laser and determines the level of nonlinearities in ADC components. This chapter derives an expression for shot-noise limited SNR and provides an example of the power budget of an integrated photonic ADC.

### Shot noise impact

The shot noise limit originates from the fundamental law that the number of photons in an optical pulse cannot be precisely defined but follows Poisson statistics [41]. According to this statistics, for an optical pulse with the average number of photons  $N$ , the actual measured number of photons fluctuates with standard deviation of  $N^{1/2}$ . This limits the SNR of a photonic ADC as described below.

Consider train of optical pulses with  $N_0$  photons in each pulse at the input of the modulator. For a sinusoidal RF signal is applied to the modulator, the number of photons in the pulses at the complimentary outputs of the modulator can be written as

$$N_A \approx N_0 \left( \frac{1}{2} + \frac{1}{2} m \sin(\omega t) \right), \quad (5.1)$$

$$N_B \approx N_0 \left( \frac{1}{2} - \frac{1}{2} m \sin(\omega t) \right). \quad (5.2)$$

where  $m$  is the modulation index. By definition, SNR is

$$SNR = \frac{\langle P_{sig} \rangle}{\langle P_n \rangle}.$$

The average signal power  $\langle P_{sig} \rangle$  and the average noise power  $\langle P_n \rangle$  are

$$\langle P_{sig} \rangle = \left\langle \left( \frac{N_0}{2} m \sin(\omega t) \right)^2 \right\rangle = \left( \frac{N_0}{2} m \right)^2 \cdot \frac{1}{2} = \frac{N_0^2}{8} m^2, \quad (5.3)$$

$$\langle P_n \rangle = \left\langle N_0 \left( \frac{1}{2} + \frac{\pi}{4} m \sin(\omega t) \right) \right\rangle = \frac{N_0}{2}. \quad (5.4)$$

Finally, the SNR in one of the complimentary modulator outputs, expressed in linear units, is

$$SNR = \frac{N_0}{4} m^2. \quad (5.5)$$

According to this equation, to improve the shot noise-limited SNR by 1 bit, it is necessary to increase either the number of photons by a factor of 4, or the modulation depth by a factor of 2. Note that modulation depth has large impact on shot noise performance. The strong dependence of SNR on modulation index comes from the fact that the signal power is proportional to  $m^2$  (see Eq. (5.3)) and does not depend on the DC component of pulse energies (5.1), (5.2). However, the noise power does not depend on the modulation depth and is defined solely by the DC part of pulse energies (see Eq. (5.4)). Therefore, if the modulation index is decreased, the signal decreases while noise stays the same. For low modulation depths, the shot noise coming from the DC component can completely obscure the signal.

Formula (5.5) describes SNR in one of the two complimentary channels. If both channels are used in differential detection scheme, the signal amplitude is increased by a factor of 2, which gives a factor of 4 improvement in signal power. The noise power is increased by 2 because of incoherent addition. Therefore, the SNR defined by (5.5) needs to be multiplied by 2 in case of differential detection.

Note that the above derivations imply an approach when the electrical pulses are integrated, because only in this case all photons in the pulse are taken into account. If peak sampling of current pulses is used, the photons outside the peak region of the pulse are not included into consideration. Evaluation of shot noise-limited SNR for this case requires further analysis.

### Power budget example

To get a feeling of how much optical power is needed to achieve given performance level, let us consider an example of an integrated photonic ADC system with some realistic parameters.

Consider a photonic ADC with target performance level of 9 ENOB at 40 GSa/s sample rate. Such an ADC would exceed the current electronic state-of-the-art by more than an order of



magnitude. This ADC can be realized using 40 channels with a laser with 1 GHz repetition rate, and can be implemented on a silicon chip, as described in Part II of the thesis.

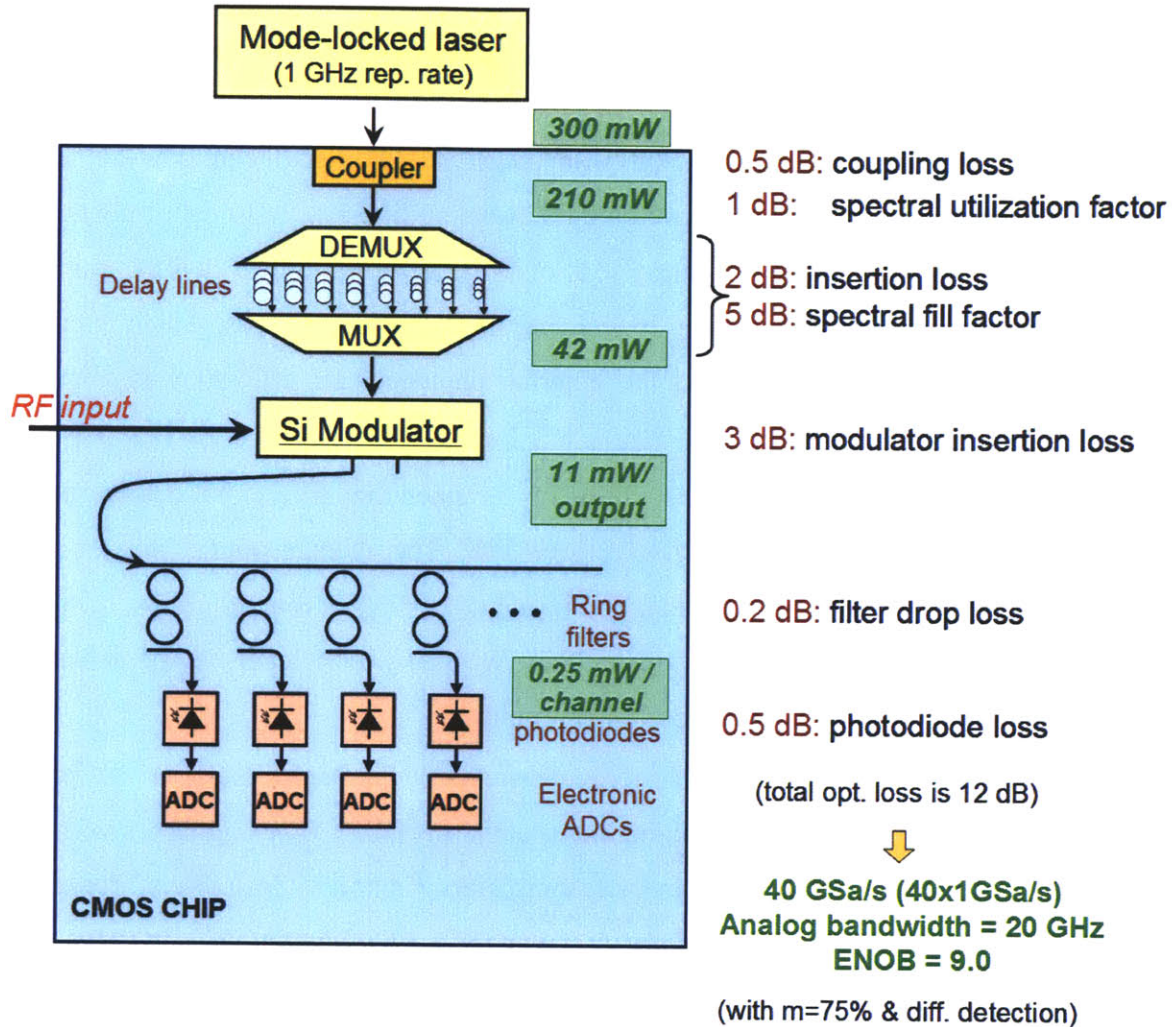


Figure 10. Example of the power budget of an integrated photonic ADC. The powers shown are the average optical powers. The power at the modulator output corresponds to one of the two complimentary outputs. The power at the output of ring filters corresponds to one wavelength channel in one of the two complimentary outputs. Modulation depth of 75% and differential detection are assumed.

An ADC with the desired performance level is schematically shown in Fig. 10, together with realistically good loss values in each of the ADC components. The coupling loss from the laser to the chip is assumed to be 0.5 dB, which is the state-of-the art in fiber-to-chip couplers (see Part VI of the thesis). The "spectral utilization factor" arises from the fact that the spectrum of the laser is not flat, and the wavelength channels of the ADC can only be located in the

relatively flat region of the laser spectrum. The associated loss is assumed to be 1 dB, which corresponds to a good matching between channel wavelength range and the spectrum of the laser. The insertion loss in the demultiplexer, delay lines, and the multiplexer is assumed to be 2 dB, which is a realistic number of delay lines are implemented as SiN waveguides (see the discussion at the end of Chapter 11). A major contributor to optical loss is the spectral fill factor, which comes from the fact the spectral regions in-between the wavelength channels are not used. The associated loss of 5 dB is a realistic estimate for two-ring filters with 30 dB of next-channel suppression. The silicon modulator insertion loss of 3 dB is an optimistic number for today's state-of-the-art. Finally, it is assumed that optical ring filters has 0.2 dB loss, which is currently achievable with silicon waveguides, and the external photodetector efficiency is about 90% (0.5 dB loss).

To arrive at the power numbers, it is additionally assumed that differential detection is used and the modulation depth is a somewhat aggressive 75%. The average optical powers at each stage of the photonic ADC are shown in Fig. 10. To achieve 9.0 ENOB at 40 GSa/s, the average optical power at the input of the chip must be 300 mW. This power level can be achieved by amplifying the laser output with an Er-doped fiber amplifier.

The following steps can be envisaged to decrease the power requirements of the photonic ADC. First, there is a lot to gain by optimizing the spectral fill factor, by using filters with higher spectral efficiency, i.e. the bandwidth/channel spacing ratio. Next, it is desirable to decrease the insertion loss of silicon modulator, which was assumed to lose half the optical power because of contact of the optical field with doped regions and scattering losses in the coupling regions. The insertion loss of the wavelength interleaver can potentially be reduced as well by decreasing the losses in the delay lines (or, if the application permits it, using dispersive fiber instead of delay lines).

The power budget presented above makes multiple assumptions about system parameters. What is then the value of this analysis? First, the assumptions made are realistic, so analysis gives a rough idea about the required powers. Second, the analysis lists the loss mechanisms in a photonic ADC and pinpoints the most important of these mechanisms. Finally, the presented numbers can be scaled to different system parameters using the following simple rules:

- the optical power must be increased by 4 per each additional effective bit (see Eq. (5.5));

- for given ENOB, the optical power must be increased by 4 if modulation index is decreased by 2 (see Eq. (5.5));
- for given ENOB, the optical power must be changed in proportion to the number of wavelength channels;
- for given ENOB, the power must be change in proportion to the repetition rate;
- for given ENOB, the optical power must be increased by 2 if a single-output modulator is used instead of differential detection scheme.
- for given ENOB, any change in loss of the optical components must be compensated for by adjusting the optical power.

## II. Demonstration of Photonic ADCs

This part of the thesis describes experimental demonstrations of two photonic ADC systems. The first demonstration used discrete commercially available components to build a photonic ADC prototype. The performance achieved with this system is multiple times better than the performance of the best electronic ADCs which exist today. The second demonstration featured a silicon photonic chip with the core photonic components of the ADC integrated on this chip. High level of performance achieved with this chip supports the feasibility of a fully integrated electronic-photonic ADC.

### 6. Discrete-component photonic ADC

To demonstrate highly accurate low-jitter sampling of high-frequency signals, a photonic ADC was built using discrete commercially available off-the-shelf components (COTS)<sup>1</sup> [42]. The goal of this demonstration is to verify the validity of the photonic approach and to find out which problems need to be overcome to achieve high performance. This section describes the details of implementation of this system.

The diagram of the implemented discrete-component ADC is shown in Fig. 11. The ADC had two interleaved channels, each running at 1.05 GSa/s, providing 2.1 GSa/s aggregate sampling rate. To form the wavelength-interleaved pulse train, the DEMUX-delay-MUX approach was used. The demultiplexers were standard fiber-coupled 1:8 thin-film wavelength demultiplexers from JDSU, model DWM-2F8DS, with 200 GHz channel spacing and 150 GHz channel bandwidth. Variable delay lines from Santec, model ODL-330, were used to introduce proper amount of delay between the channels. The wavelength-interleaved pulse train was then amplified by an EDFA from MPB, model R35/130, which provided 40 dB of gain. The pulse trains were modulated with a high-performance dual-output LiNbO<sub>3</sub> modulator from EOSpace, model AZ-1x2-AV5-40-PFU-SFU, with 3 dB bandwidth of about 40 GHz. The analog

---

<sup>1</sup> The system was built by Mathew E. Grein with contributions from Jade P. Wang and Steven J. Spector of MIT Lincoln Laboratory, as well as Michael Y. Peng and Amir H. Nejadmalayeri of Optics and Quantum Electronics group at MIT.

bandwidth of the whole photonic ADC was therefore about 40 GHz. To demultiplex the pulse trains at the two outputs of the modulator, thin-film wavelength demultiplexers of the same model were used (JDSU, DWM-2F8DS).

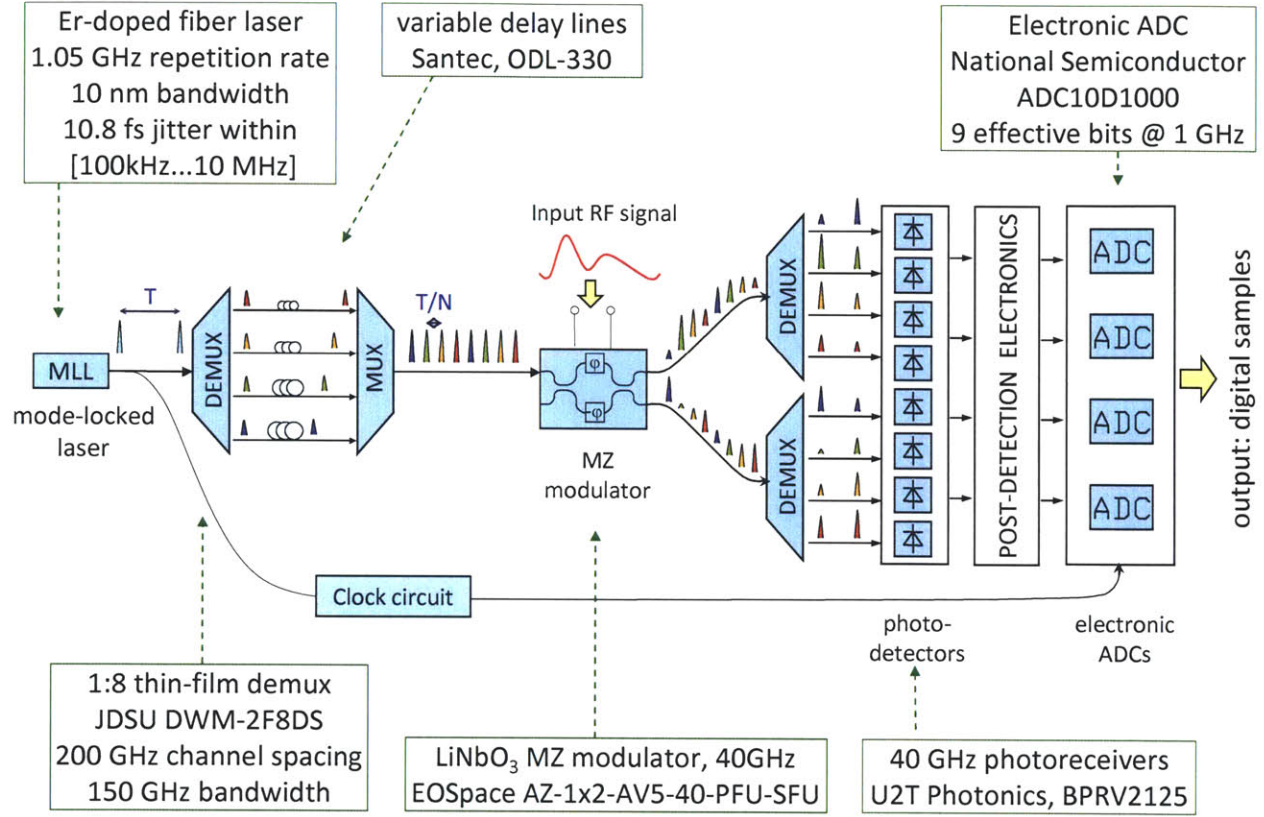


Figure 11. The layout of the implemented discrete-component photonic ADC system with description of its the most important components.

The complementary outputs of the modulator were detected with 40 GHz balanced photoreceivers from U2T Photonics, model BPRV2125). The balanced photoreceivers produced signal equal to the difference of the signals in the two complimentary channels, which yielded several important benefits [42]:

- with differential detection, signal power is increased by 6 dB, while noise power is increased by 3 dB, yielding SNR improvement of 3 dB;
- differential detection rejects common mode noise, i.e. the additive noise which might be present in both complimentary channels;

- differential detection cancels quadratic and other even-order nonlinearities, such as nonlinearities of silicon modulator transfer function (Chapter 13) and microring resonator filters (Chapter 19);

- differential detection creates a signal which spans both positive and negative voltage values, and therefore can match the input voltage range of electronic ADCs. Electronic ADCs typically have input voltage range spanning both positive and negative values (from -0.5 V to +0.5 V in the present experiment). If only one of the two complimentary outputs were detected, this would produce a signal which is only positive (as the optical power is positive). Such a signal can cover only half of the voltage range of electronic ADC, leading to ENOB degradation. Differential detection generates signal which spans both positive and negative values, and therefore can be matched to the electronic ADC voltage range. An alternative solution can be to introduce a proper (negative) DC offset with a bias-tee.

To boost the detected differential signal to the 1.0 V peak-to-peak input voltage of electronic ADCs, a post-detection electronic link was used, consisting of a 3 GHz Gaussian low-pass filter, a DC block, a preamplifier (H2 Com 24471, 19-dB gain), another DC block, an amplifier (Hittite 641, 13-dB gain), and a balun. The electronic ADCs from National Semiconductor, model ADC10D1000), had two 1 GSa/s differential input channels and were preconfigured on an evaluation board with a Virtex 5 FPGA. The accuracy of these ADCs was about 9.2 effective bits at input frequencies below 500 MHz, and was reduced to about 8.7 effective bits for 1.0 GHz inputs. The electronic ADCs were synchronously clocked with an RF signal regenerated from the unmodulated optical pulse train using an amplified photodiode, RF filter, and clock distribution circuit from National Semiconductor, model LMK01000. Variable optical and RF delay lines were used to precisely align the modulated pulse train with the ADC sampling clock to ensure that pulses are sampled at their peaks.

A test RF signal was generated with an RF synthesizer from Anritsu, model 69077B, and amplified with an RF amplifier (SHF 803). An important step was to pass the obtained RF signal through a bandpass filter, which rejected undesired frequencies from the input signal. For 40 GHz test signal, the filter was Wiltron W-band BPF, with 33-50 GHz passband.

A mode-locked erbium-doped fiber laser was the only custom-built component, generating a 1.05 GHz optical pulse train with at most 11 fs timing jitter in the [100 kHz...10 MHz] frequency range. The laser used in experiments was a soliton mode-locked Er-doped fiber laser,



self-starting with a semiconductor saturable Bragg reflector [43]. The linear laser cavity consisted of a 93-mm long erbium-doped gain fiber (Liekki Er80-8/125) that was spliced to a 7-mm long piece of standard single mode fiber (SMF-28e) to prevent thermal damage of the butt-coupled saturable Bragg reflector. With 10% output coupling, 10 mW of output power was obtained for an optical spectrum centered at 1560 nm with a 10 nm 3-dB bandwidth at a fundamental repetition rate of 1.048 GHz. The integrated timing jitter for the free-running laser, extracted from a single-side band phase noise measurement with a signal source analyzer, was determined to be about 13.8 fs within [10 kHz...10 MHz] frequency interval and 10.8 fs within [100 kHz...10 MHz] interval [43]. These values are the upper limits for the timing jitter of the laser since the noise floor of the signal source analyzer contributes to the measurements; the real jitter of the laser can be lower.

## **7. Performance of the discrete-component photonic ADC**

The discrete-component photonic ADC system was characterized using standard single-tone and two-tone tests. This chapter presents results of a single-tone and a two-tone test for input frequencies around 10 GHz, and a single-tone test for input frequency around 40 GHz, and discusses their significance.

All tests described in this chapter were performed using two wavelength channels. The data points taken in these channels were interleaved with compensation for timing skew and gain errors at post-processing step. An inverse sine was also applied to compensate for the sinusoidal transfer function of the MZ modulator [44, 45] in order to improve the spurious-free dynamic range (SFDR). Despite careful adjustment of the delay values, some amount of timing skew between the channels was observed; the timing skew was digitally compensated by finding numerically the amount of timing offset which would minimize spurious frequency components in the interleaved data. Gain and offset mismatch between the two channels were digitally compensated as well. The details of the data processing applied to the recorded data are described in detail in Chapter 10.

## Single-tone test, 10 GHz

In this experiment, a 10 GHz single-frequency test signal has been applied to the discrete-component photonic ADC. Fourier spectra of the data points captured in two wavelength channels are shown in Fig. 12(a). These spectra correspond to the raw unprocessed data; the only processing used was the application of the Blackman windowing function in order to improve the dynamic range. Without windowing, the dynamic range was insufficient because only 4096 points per channel could be captured due to test board limitations. Blackman windowing function has also been used to obtain all other ADC spectra shown in this part of the thesis.

The spectrum of the linearized and interleaved signal is shown in Fig. 12(b). Linearization reduced the third harmonic distortion by about 17 dB, which improved SFDR from 37 to 54 dBc (Fig. 12). The achieved ENOB is 7.2 bits, limited almost exclusively by the noise floor. The total harmonic distortion is 52 dBc, corresponding to 8.7 bits of accuracy (which is close to the accuracy limit of the electronic ADCs used in the experiment).

The sample rate achieved in this two-channel ADC demonstration was about 2.1 GSa/s, which is much lower than the required Nyquist rate for the 10 GHz test signal. The signal frequency was therefore aliased to the frequency band of the ADC, in this case to 455 MHz. To understand why the aliased frequency is equal to this specific value, it is necessary to use a more accurate value of the repetition rate of the laser, which was 1.048 GSa/s, and a more accurate value of the applied frequency, which was 10.025 GHz. With these values, the aliased frequency is found as  $|10 \cdot 1.048 - 10.025|$  GHz, which is indeed 455 MHz.

The ENOB values reported above were found directly from the ENOB definition through the signal-to-noise and distortion ratio (SINAD), which was determined by dividing the power at the fundamental frequency by the sum of powers of all distortions plus the total power of noise within the full bandwidth of the ADC. This approach was used to find ENOB throughout this work. The numbers of SNR bits, SFDR bits, and THD bits mentioned in Fig. 12(b) correspond to the numbers of bits found as if the only source of ADC errors were the noise, the harmonic distortion of the largest power, or combinations of all harmonic distortion, respectively. These numbers of bits are given as supplementary information, as it is often done by ADC developers; ENOB values cited in this work always include the combination of all error sources.



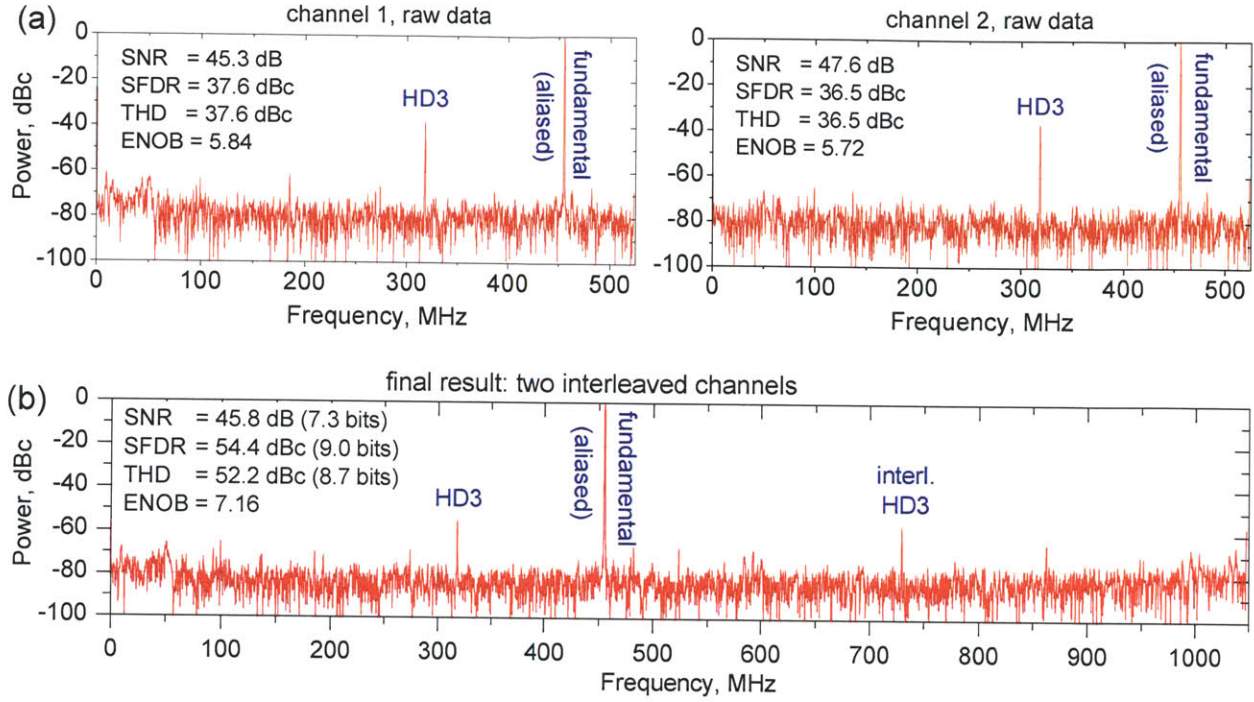


Figure 12. Digitization of a single 10.025 GHz RF tone with the discrete-component photonic ADC with two 1.048 GSa/s channels. Fourier transforms of the data points recorded in individual channels are shown in (a), and Fourier transform of interleaved and linearized data is shown in (b). The spectra are normalized to the power of the fundamental frequency, i.e. dBc (dB below carrier) units are used along the Y-axes. The signal at fundamental frequency is labeled as "fundamental", the third harmonic distortions is labeled as "HD3", and the corresponding spurs which arise from imperfect interleaving are labeled with "interl." 4096 data points were captured in each channel; Blackman window was applied to improve the dynamic range.

### Dual-tone test, 10 GHz

A test with two input tones at frequencies close to 10 GHz (10.025 GHz and 10.033 GHz) has also been performed. The spectra of the points recorded in two photonic ADC channels are shown in Fig. 13(a), and the spectrum of interleaved and linearized signal is shown in Fig. 13(b). The linearization reduced the total harmonic distortion by about 14 dBc, bringing down both the third harmonic and third-order inter-modulation products. The final result is ENOB of 6.9, which is less than ENOB for a single-tone test by only 0.3 bits.

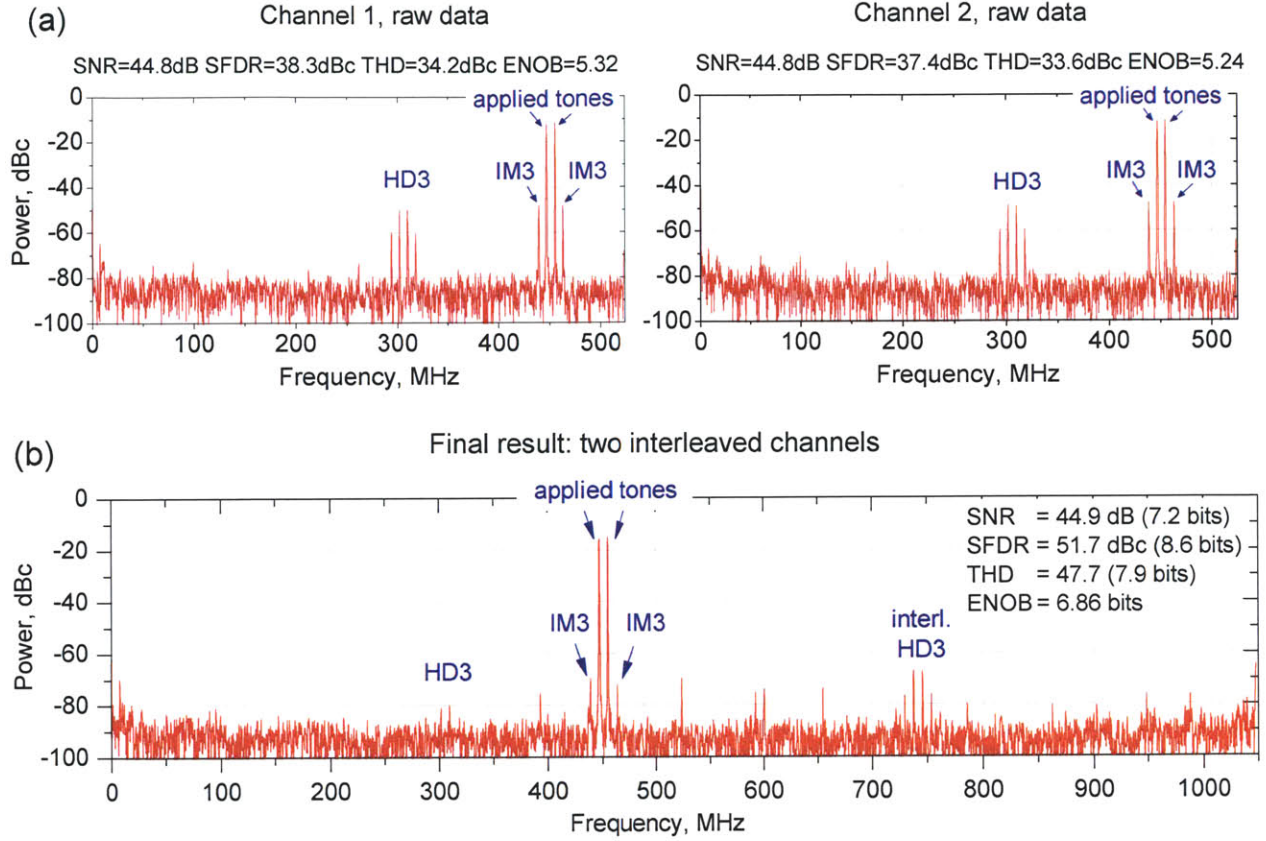


Figure 13. Digitization of a signal with two RF tones, 10.025 GHz and 10.033 GHz, using the discrete-component photonic ADC with two 1.048 GSa/s channels. Fourier transforms of the data points recorded in individual channels are shown in (a), and Fourier transform of interleaved and linearized data is shown in (b). The signal at fundamental frequency is labeled as "fundamental", the third harmonic distortions is labeled as "HD3", the third-order inter-modulation products are labeled as "IM3", and interleaving spurs are labeled as "interl." 4096 data points were captured in each channel; Blackman window was applied to improve the dynamic range.

### Single-tone test, 41 GHz

To push the performance constructed discrete-component photonic ADC to its limit, an experiment with a 41 GHz test signal has been performed. This frequency is close to the 40 GHz bandwidth of the LiNbO<sub>3</sub> modulator used in this experiment and therefore is close to the analog bandwidth of the present photonic ADC. This test is intended to demonstrate the full advantage of the photonic approach as hardly any electronic ADC can boast such high analog bandwidth.

The spectra of the data points recorded in the two channels are shown in Fig. 14(a), and the spectrum of the interleaved and linearized data is shown in Fig. 14(b). Similar to the other



experiments described above, ENOB is limited mostly by the noise floor. A new thing in comparison to the previous cases is the presence of the second harmonic. Additionally, the linearization is now less successful, with SFDR improvement of only 5 dB, compared to the 17 dB improvement for the 10 GHz test case. It was not clearly established why linearization was less successful for the 41 GHz signal and what causes the 2nd harmonic to appear. Still, the harmonic distortions in the interleaved signals are low (SFDR = 52 dBc) and the accuracy is limited almost exclusively by noise; the final result corresponds to 7.0 ENOB, which is significantly better than what is possible with today's ADC technology.

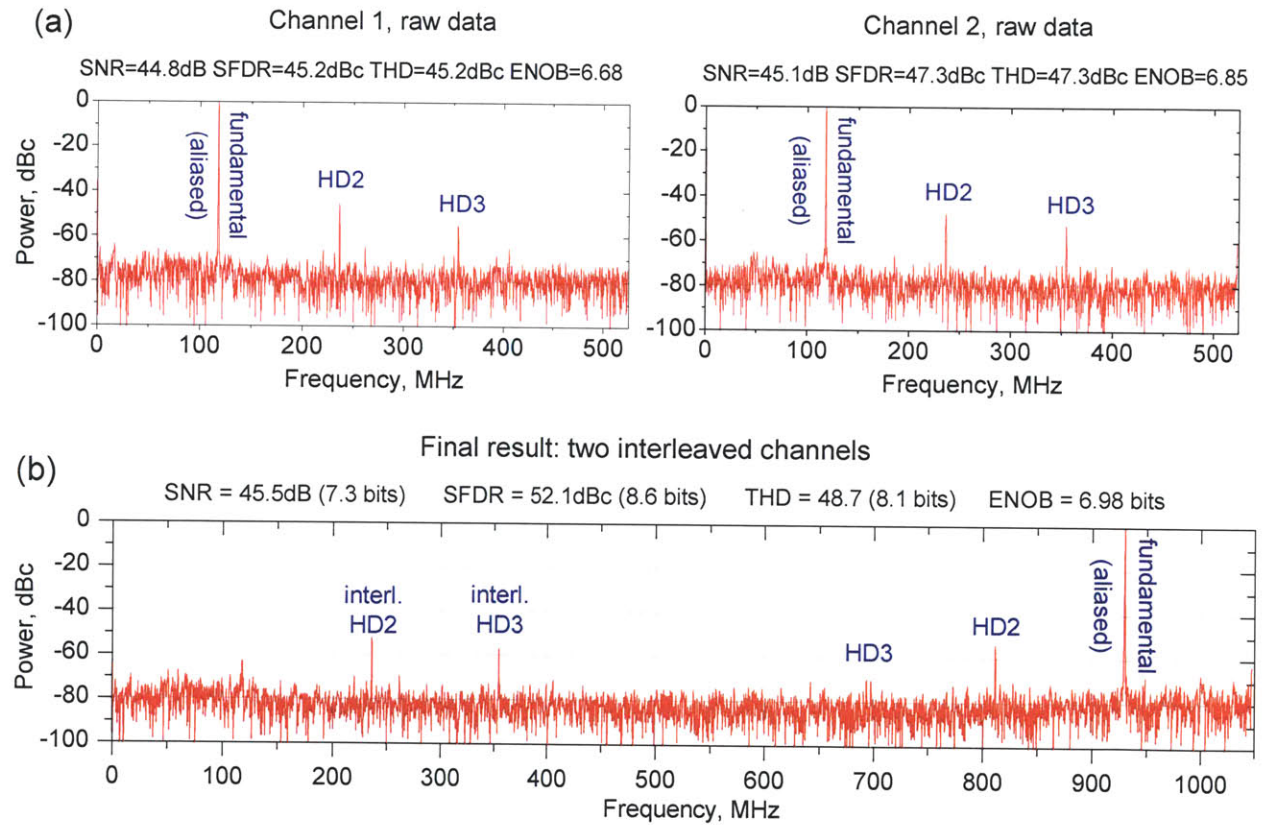


Figure 14. Digitization of a single 40.025 GHz RF tone with the discrete-component photonic ADC with two 1.048 GSa/s channels. Fourier transforms of the data points recorded in individual channels are shown in (a), and Fourier transform of interleaved and linearized data is shown in (b). The signal at fundamental frequency is labeled as "fundamental", second and third harmonic distortions are labeled as "HD2" and "HD3", and interleaving spurs are labeled as "interl. HD2" and "interl. HD3". The 40.99 GHz input signal was aliased to  $|40.99 - 1.048 \cdot 39|$  GHz = 118 MHz in (a) and  $|40.99 - 1.048 \cdot 40|$  GHz = 930 MHz in (b). 4096 data points were captured in each channel; a Blackman window was applied to improve the dynamic range.

## Conclusions

The experiments with discrete-component ADC demonstrated that the photonic approach can significantly improve ADC performance relative to today's state-of-the-art. The best result achieved in the demonstrations described above is 7.0 effective bits for a 41 GHz input tone (Fig. 14(b)). This result, represented with a large orange star in the Walden plot shown in Fig. 15, significantly exceeds any result achieved with electronic ADCs at such high frequencies. Such performance corresponds to the aperture jitter of 15 fs or smaller, which is a 4-5 times improvement over the jitter of the best electronic ADCs and about an order of magnitude improvement over electronic ADCs operating at frequencies above 10 GHz. Note that this result is definitely not the limit of what photonic ADCs can achieve. The jitter of the mode-locked laser, already low in this experiment, can be orders of magnitude lower, opening the door to completely new ADC performance levels.

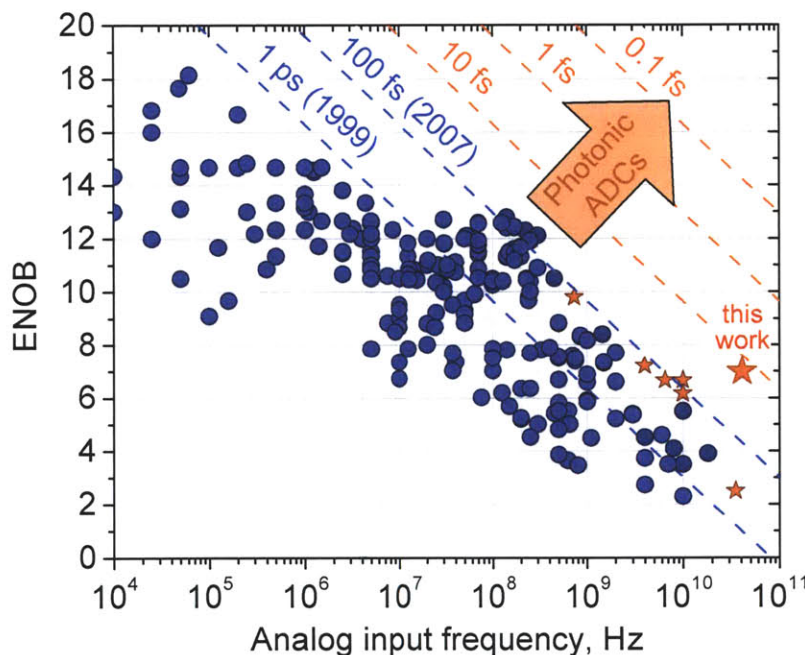


Figure 15. "Walden" plot showing ENOB of existing electronic ADCs versus input signal frequency, similar to Figs. 2 and 9. Electronic ADCs are represented with blue circles, and other photonic ADCs are represented with small orange stars. The large orange star indicates the result achieved in this work.

The results reported in this work were obtained in the undersampling mode, i.e. the sample rate used ( $2 \times 1.05 \text{ GSa/s} = 2.1 \text{ GSa/s}$ ) was much smaller than the sample needed to sample 10 GHz and 40 GHz signals according to the Nyquist theorem. Despite this fact, the results reported in this work are important for the following reasons.

*First*, the sampling rate of the photonic ADC can be raised by simply adding more wavelength channels. It is important that these additional channels are similar to the ones demonstrated in this work and increasing the channel count does not require modification of the photonic ADC architecture. What is required is that the optical bandwidth of the laser is sufficient to accommodate all the channels. For example, if the number of channels of the present ADC is increased from 2 to 20, the required optical bandwidth is 10-15 nm (assuming 60-90 GHz channel spacing), which is easily within the bandwidth of mode-locked lasers at 1550 nm. The total optical power needs to be increased commensurately with the number of channels; this can be achieved with an erbium-doped fiber amplifier.

*Second*, a key component of a multi-channel photonic ADC is a filter bank, and it has been shown that this component can be implemented with the technology which exists today by fabricating and demonstrating several high-performance multi-channel filter banks, as described in Part V of this work.

*Third*, the ENOB values reported in this work are limited almost exclusively by the noise floor of the system. There are no reasons to expect the noise floor to change when more identical channels are added. Therefore, the noise-limited ENOB is expected to stay unchanged, and it is reasonable to argue that the 7.0 ENOB achieved for 41 GHz signal sampled at 2.1 GSa/s can be extrapolated to the Nyquist-rate photonic ADC.

*Fourth*, one of the main conclusions of this work is that the problem of electronic jitter can be eliminated with the photonic ADC approach. The effect of jitter manifests itself as the noise floor, and does not depend on the number of channels. Therefore, this conclusion holds regardless of the number of implemented channels. In fact, demonstrating just one channel would have been sufficient to show low-jitter performance.

Having said the above, it is necessary to add that increasing the channel count to a large number is of course a formidable task. First, it increases the complexity of the system to the point that building a discrete-component ADC becomes unreasonable and manual adjustment and matching of multiple channels becomes very problematic. Second, calibration and error

compensation in an ADC system with large channel count is a challenge. These problems can be significantly simplified if photonic ADC can be integrated on a chip, which is an important motivation to pursue the integrated approach described in this thesis.

The linearization and interleaving approaches used in this work were not rigorous, as mentioned above and discussed in detail in Chapter 10. Namely, several unknown calibration coefficients were fitted to obtain the highest possible ENOB. The rigorous way to perform error compensation and interleaving would be to extract the unknown coefficients from independent measurements, possibly in real time while the ADC is capturing data. However, despite the fact that this was not done, the reported ENOB values are important for several reasons. First, the data processing algorithm was not arbitrary, but was derived from the physics of the problem, and the fact that this algorithm succeeded means that the system behavior is consistent with what is expected from the physics of the problem, and a rigorous compensation algorithm has a good chance to be successful as well. Second, the ENOB was limited by the noise, which was unaffected by the data processing used. Therefore, the conclusion that the photonic approach can overcome the jitter problem and bring ADC technology to new performance levels holds regardless of the data processing which has been applied.

Finally, it is necessary to mention steps which can further improve the accuracy achieved in the present discrete-component ADC demonstration. The ENOB reported above was limited by the noise floor of the electronics following the photoreceivers, therefore perfecting the electronic link is the first step which needs to be taken. For demonstrations with high input frequencies, such as 41 GHz used above, it is necessary to make sure the timing jitter of the mode-locked laser used in the experiments is not the limitation. For example, if 9.0 effective bits are to be achieved, the timing jitter of the laser must be below 4 fs. This low jitter is definitely achievable with the available technology, it is just necessary to be sure that the particular laser used in experiments has this low jitter. Next, if more than 9.0 effective bits are desired, the accuracy of electronic ADCs starts to become the bottleneck. This accuracy is improving quite slowly with years, so if more than 9 effective bits are desired, the only feasible solution might be to decrease the per-channel sample rate (from 1 GHz in present experiments to 500 MSa/s or even 250 MSa/s) and increase the number of channels to preserve the overall sample rate.

## 8. Integrated photonic ADC

The photonic ADC presented above was made with discrete components in a laboratory setting, similarly to most other photonic ADCs demonstrated to date. However, to be a viable alternative to electronic ADCs, a photonic ADC must be integrated on a chip. Integration enables robustness, miniaturization, potential low-cost mass production, possibility to implement large number of channels, and promises to improve power efficiency and signal integrity by eliminating interconnects between separate chips. A major benefit of the photonic ADC approach pursued in this work is that it allows integration, and a full photonic ADC can potentially be implemented on a single chip using silicon photonics technology, as envisaged in Fig. 16. Such an ADC would use microring-resonator filters, a silicon carrier-depletion modulator [46-48], and germanium [49] or silicon defect-based [50] photodetectors. Post-detection electronics, electronic ADCs, and digital error correction circuits would be integrated on the same CMOS chip. The demultiplexer, differential time delays, and multiplexer necessary to create a wavelength-interleaved pulse train can also be on the same chip. The pulse train can be generated with a separate chip, for example with an integrated erbium-doped mode-locked planar waveguide laser [16]. This ADC would be an example of a device operating on completely new principles enabled by silicon photonics and electronic-photonic integration.

In a move towards a fully-integrated photonic ADC, a silicon chip with core components of the above ADC has been fabricated [51]. The chip included a modulator, two matched three-channel filter banks, and photodetectors. The packaged chip is shown in Fig. 17(a), and a photograph of the chip is shown in Fig. 17(b). The details of this chip are described below.



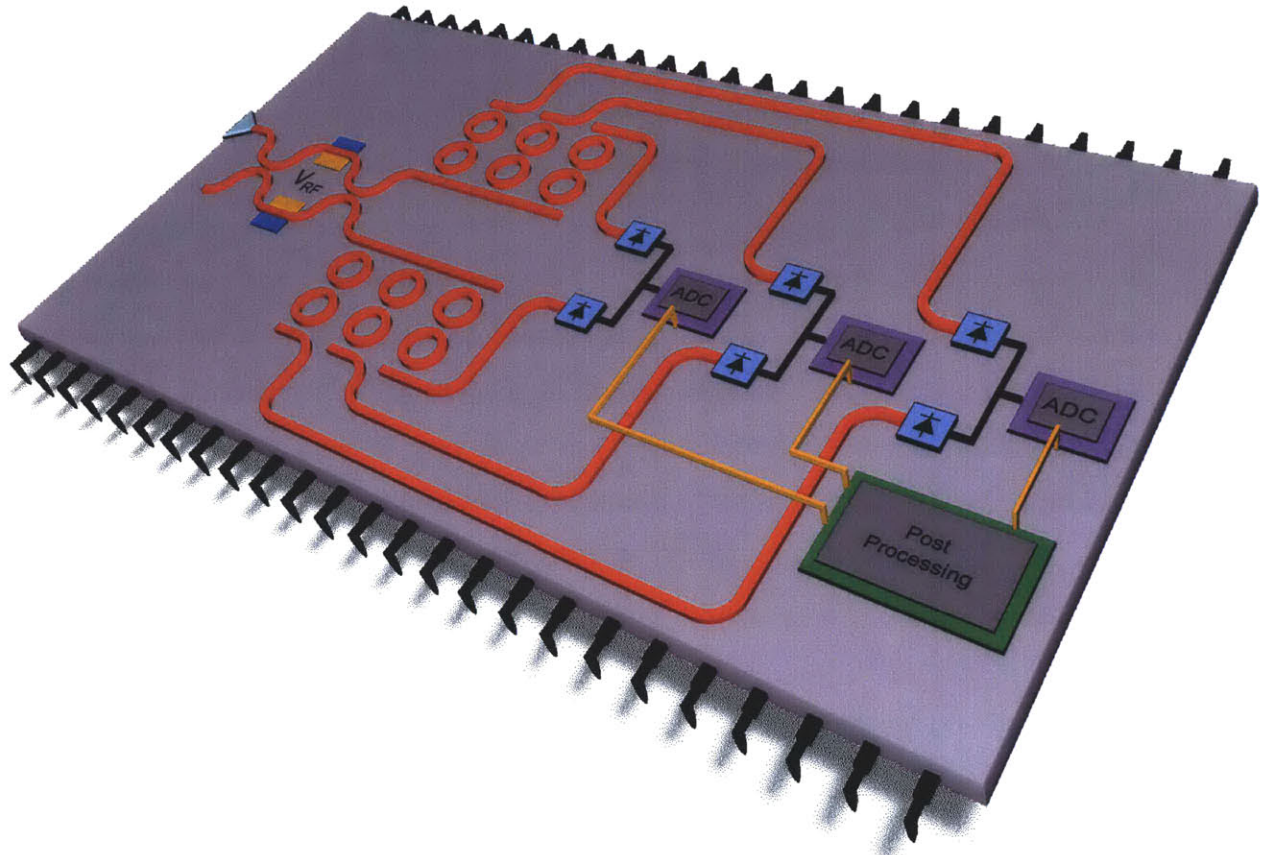


Figure 16: A vision of a fully integrated electronic-photonic ADC. The chip would include both photonic and electronic components, i.e. a dual-output silicon modulator, two matched banks of microring-resonator filters, balanced photoreceivers, electronic ADCs, and digital post-processing circuits. The generation of the wavelength-interleaved pulse train (not shown in the figure) can also be integrated on the same chip. For simplicity, only 3 wavelength channels are shown; channel count can be significantly higher. The chip presented in this work is a first step toward full integration and includes photonic components of the ADC.



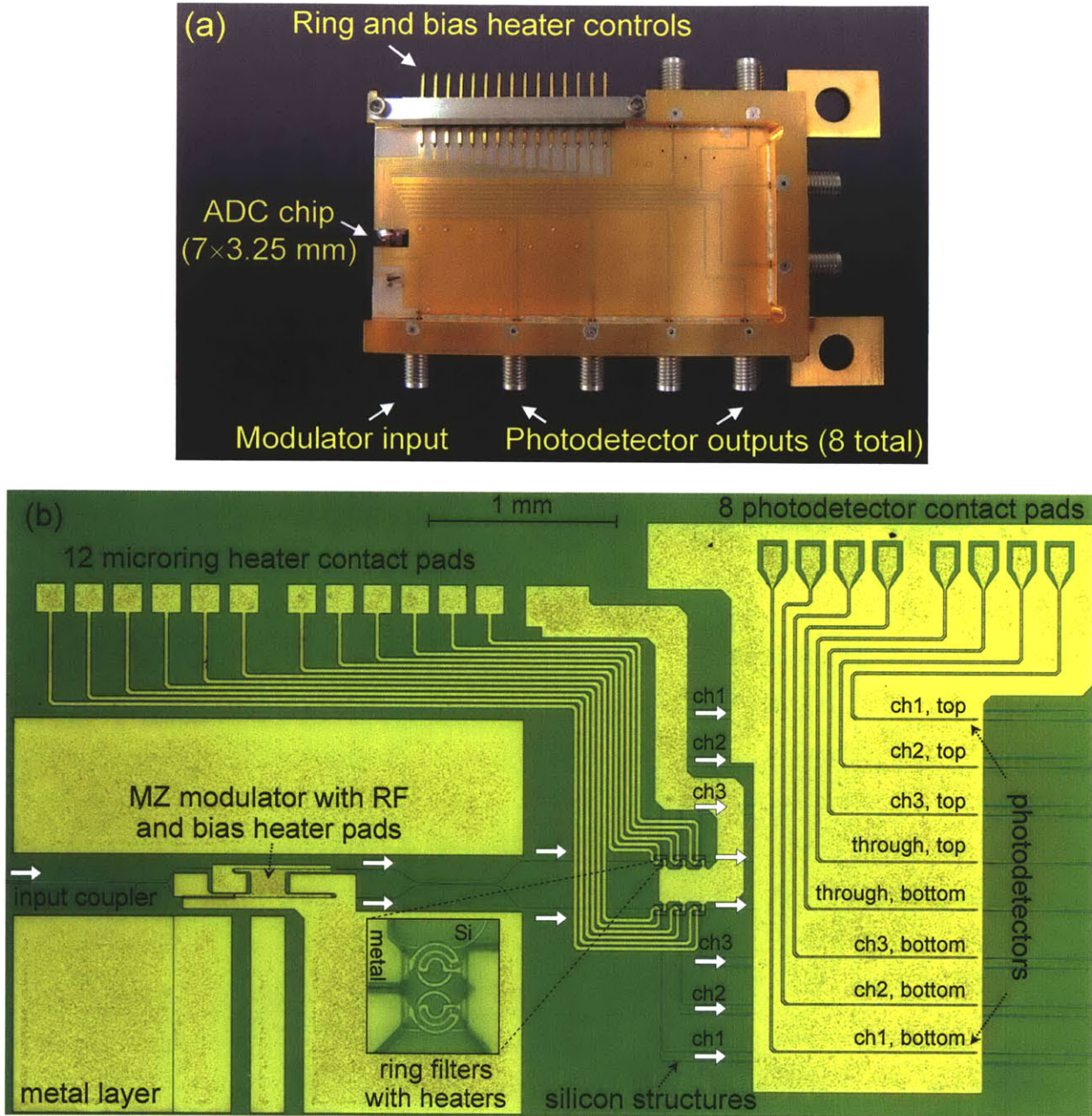


Figure 17. (a) Photograph of the packaged photonic ADC chip with three wavelength channels. The chip includes a Mach-Zehnder silicon modulator, two matched three-channel microring-resonator filter banks, silicon photodetectors, and fiber-to-chip couplers. The packaging provides access to 8 RF photodiode outputs (each of the two filter banks has 4 outputs: 3 outputs for 3 wavelength channels and 1 output for off-resonance light, which passes through unaffected by the filters and is used for testing purposes). The package also has DC contacts for microheaters for the filters and MZ modulator. The wavelength-interleaved pulse train generator and all electronic components of the ADC system are implemented off-chip. (b) Photograph of the photonic ADC chip with metal heaters, wiring, and contact pads fabricated on top of the overcladding on the silicon layer. The zoom-in shows the photograph of one of the microring filters taken at higher magnification.

## Silicon chip

The integrated photonic ADC chip (Fig. 17(b)) was fabricated on a Unibond silicon wafer with 3  $\mu\text{m}$  buried oxide layer using conventional 248 nm optical lithography<sup>1</sup>. The chip was overlapped with a 1.0  $\mu\text{m}$ -thick PECVD deposited oxynitride layer (refractive index 1.57).

To create smoother sidewalls, and thereby lower the scattering in the waveguides, the resist can be reflowed prior to the etching of the waveguides. After exposure and development, the photoresist (Rohm and Haus, UV5) was baked at 160°C for 5 minutes. This step was applied for the photonic ADC chip which had 240nm-thick silicon waveguides; resist reflow step was found to be unnecessary for thin (110nm) silicon waveguides.

## Fiber-to-chip coupler

Optical pulses were coupled from a lensed fiber into the coupler fabricated on top of the chip (note that the coupler design was different from the one proposed in part VI of the thesis). The optical radiation from the fiber was focused onto an oxynitride rib waveguide fabricated on the chip. The rib was made directly on top of the 1.0  $\mu\text{m}$ -thick oxynitride overlatching and was 3.0  $\mu\text{m}$  wide and 2.0  $\mu\text{m}$  tall. The mode of the rib waveguide was matched in size to the field size at the focal spot of the fiber. The matching was not perfect because the mode of the rib waveguide could not be made symmetric (the mode extends more into the base than into the rib of the waveguide), which resulted in theoretical mode mismatch loss of at no less than 1 dB. The benefit of the rib waveguide approach was that this waveguide was single mode. If a more common rectangular waveguide were fabricated instead of the rib waveguide, the mode matching to the fiber would be improved, but the rectangular waveguide would have to be multi-mode because of its high refractive index (1.57). It was not clear whether the fact that the rectangular waveguide was multi-mode would cause multi-mode effects, therefore, the single-mode rib waveguide design was selected over the multi-mode rectangular waveguide design. Additional advantage of the rib waveguide approach is that it is easier to fabricate than the rectangular waveguide. Specifically, to fabricate a rib waveguide, a thick layer of oxynitride was deposited over all area of the chip, and the rib was formed by a single etch step. This left a

---

<sup>1</sup> The chip was fabricated by Steven J. Spector of MIT Lincoln Laboratory.

1.0  $\mu\text{m}$  layer of oxinitride everywhere except the rib region, which was a useful layer because the microheaters could be fabricated on top of it. For comparison, if a rectangular waveguide were to be fabricated, this would require to completely remove the oxinitride at the sides of the rectangular coupler. Besides, this would create discontinuity at the end of the coupler, possibly causing back-reflections.

The light coupled into the oxinitride rib was transferred into the silicon waveguide by means of an adiabatic inverse silicon taper [52], described in detail in Part VI, fabricated inside the rib waveguide. The taper length was 200  $\mu\text{m}$ .

A coupling loss of about 2.0 dB was measured using a lensed fiber with 3.0  $\mu\text{m}$  mode field diameter. The coupling efficiency was flat over large wavelength range, indicating absence of multi-mode effects which prevented some of previously fabricated couplers from functioning properly (see an example in Fig. 66). During packaging of the photonic ADC chip the facet was damaged, increasing the coupling loss to approximately 5 dB.

### Silicon modulator

Electrooptic modulator used in the integrated photonic ADC was based on a reversely-biased silicon diode [46]. The applied RF voltage modulates the distribution of free carriers at the boundaries of the depletion zone; this modulates the refractive index of silicon via the plasma dispersion effect, and therefore the phase of optical radiation propagating through the diodes. An MZ interferometer is used to convert the phase modulation into an amplitude modulation.

In this work, two identical 500  $\mu\text{m}$ -long diodes were used in the arms of the MZ structure, operated in push-pull mode [47, 48]. The diodes were 500 nm wide and 210 nm thick, doped p-type to  $5 \cdot 10^{17} \text{ cm}^{-3}$  everywhere except 50 nm layers at the top and the right sidewall, where it was doped n-type to  $1.5 \cdot 10^{18} \text{ cm}^{-3}$ , and a 50 nm layer at the left sidewall, where it was doped p-type to  $1 \cdot 10^{18} \text{ cm}^{-3}$  (see Fig. 24). This design was selected to achieve improved sensitivity in reverse bias, at the expense of some bandwidth compared to previous designs [48]. DC measurements indicated single-arm  $V_{\pi}L = 1.2 \text{ V} \cdot \text{cm}$  (or  $0.6 \text{ V} \cdot \text{cm}$  in push-pull configuration), and a 3 dB RF bandwidth was found to be 12 GHz. The insertion loss was approximately 3 dB.

A microheater fabricated on top of one of the arms was used to thermally adjust the phase difference between the two arms to bias the modulator at quadrature.  $V_{\pi}L$  of each of the two

diodes was measured to be 1.2 V·cm, and the 3-dB bandwidth of the modulator, determining the analog bandwidth of the ADC, was approximately 12 GHz.

### Microring resonator filter banks

Two matched banks of dual-ring resonator filters, each bank demultiplexing one of the two complimentary modulator output, were implemented. The design parameters of the filters were the following. The silicon waveguides were 210 nm tall and 360 nm wide. The width of the ring waveguides was larger, 450 nm. The center radius of the rings was 2.32  $\mu\text{m}$ , corresponding to the free spectral range of about 41 nm. The coupling gap between the bus and the ring was 225 nm, designed to provide 3.9% power coupling, and the gap between the two rings was 505 nm, designed to provide 0.043% coupling. Titanium microheaters were fabricated 1.1  $\mu\text{m}$  above the waveguides, separated from them by an oxinitride overcladding layer; the titanium wires were 500 nm wide and 100 nm thick. Each microring resonator had its own independently-controlled microheater, used to compensate for fabrication variations and fine-tune all resonances to the desired wavelengths.

### Silicon photodetectors

Silicon photodetectors were used to detect the modulated pulse train. Silicon is normally transparent at the 1.55  $\mu\text{m}$  wavelength used in the experiments; absorption at 1.55  $\mu\text{m}$  was induced by ion implanting Si to damage the silicon lattice and create light-absorbing mid-gap states [50]. The implantation (dose =  $10^{14} \text{ cm}^{-2}$ ), followed by anneal (1 min. at 600°C), takes place after activation of all other implants and leaves mid-gap states, which absorb light at around 1550 nm. The efficiency of the 500  $\mu\text{m}$  photodetectors used in the integrated ADC system was about 0.1 A/W. Longer lengths diodes with different implant and anneal conditions have been shown to be more efficient [50], but the exact conditions necessary for this efficiency have been difficult to reproduce. The bandwidth was measured to be about 3 GHz, enough for detecting 1 GHz pulse trains. Differential detection was not implemented in the present chip, and signals from just one of the two complimentary outputs have been used in the experiments.

## Packaging

The packaging was designed with the chip placed at one edge of the package. Light was edge-coupled into the chip from a fiber lens. A standard printed circuit board contained DC leads for heater and bias control, and also RF waveguides. The RF waveguides were in a Ground-Signal-Ground (G-S-G) co-planer configuration and were used to connect to the modulator and the photodetectors. The RF waveguides met up with K-type connectors at the edge of the package for connecting cables to the package.

## 9. Performance of the integrated photonic ADC

The testbed used to test the integrated photonic ADC was similar to the one used in the discrete-component ADC experiments, except now the heart of the ADC – the modulator, filters, and photodetectors – are on a single silicon chip. Two out of the available three wavelength channels were used. Similar to the discrete-component ADC case, the repetition rate of the laser was approximately 1.05 GSa/a; the aggregate sampling rate of the photonic ADC was therefore 2.1 GSa/s.

A problem encountered in integrated photonic ADC experiments was that the wavelength of the mode-locked laser turned out to be far from the resonant wavelengths of the filters of the filter bank. Although the microheaters fabricated on top of the filters were able to fine-tune the resonant wavelengths, they could not tune the resonance far enough (several tens of nanometers) to match the laser wavelength (an attempt to tune the filters that far would almost certainly destroy the microheaters). Moreover, some of the microheaters were not functional, so the corresponding microring filters could not be used at all. In these circumstances, the laser cavity was adjusted to shift the center wavelength close to 1572 nm in order to match the resonances of the microring filters; the 3-dB bandwidth of the laser at this wavelength was about 13 nm. To avoid the problem of frequency mismatch between the laser and the filters in the future, it would be beneficial to reduce the free spectral range of the filters (which was about 41 nm for the present chip), so that they would need to be tuned over smaller wavelength range; the reliability and maximum tuning range of the heaters need to be improved as well.



The photonic ADC chip was used to sample a 10.555 GHz RF signal. Fig. 18(a) shows spectra of the data captured in each channel, and Fig. 18(b) shows the spectrum of the interleaved data, with 3.5 ENOB and 39 dBc SFDR. It is expected that the ENOB, limited by low signal level at the input of the electronic ADCs, can be significantly improved by optimizing the energy efficiency of the chip components, especially the efficiency of silicon photodetectors. Alternatively, highly efficient germanium photodetectors [49] can be used.

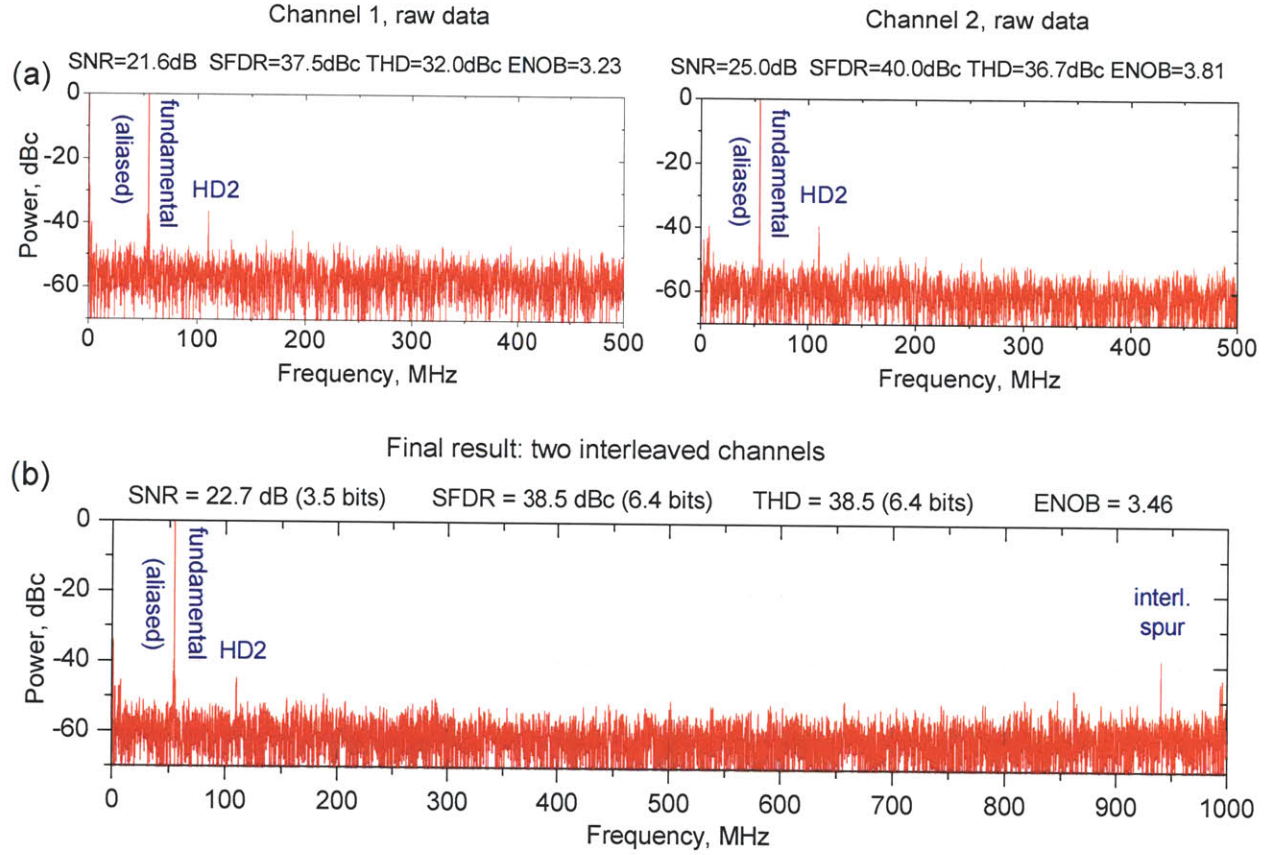


Figure 18. (a) Fourier transform of data points recorded in individual channels, and (b) Fourier transform of interleaved data for a 10 GHz signal digitized using the photonic ADC chip. The 10.555 GHz input signal was aliased to  $|10.555 - 1.05 \cdot 10|$  GHz = 55 MHz. 4096 data points were captured in each channel; Blackman windowing was used to improve the dynamic range.

Harmonic distortions visible in the spectra of Fig. 18 can be attributed to the silicon modulator nonlinearity and are expected to limit the ENOB once the SNR is improved. For the present integrated photonic ADC experiments, taking arcsine of the data did not produce any SFDR improvement, indicating that the nonlinearity of the system comes not from the sinusoidal

nonlinearity of the MZ interferometer, but from other sources (presumably, from the nonlinearity of the silicon modulator). Modulator linearization [53-55] or nonlinearity post-compensation [56] is expected to reduce these distortions.

## 10. Data analysis for ADC experiments

The data captured with photonic ADCs was post-processed offline on a computer. This post-processing was carried out to interleave the channels and compensate for the sinusoidal transfer function of the MZ modulator to improve the SFDR to achieve the results reported in Chapters 7 and 9. This chapter describes the details of the applied post-processing algorithm and discusses its significance.

The data points measured in two differential wavelength channels of the ADC can be expressed as

$$A_1 = c_1 + \alpha_1 \cdot \sin(v_1), \quad (10.1)$$

$$A_2 = c_2 + \alpha_2 \cdot \sin(v_2). \quad (10.2)$$

In these expressions

- $v = v(t)$  is the signal applied to the modulator. It is assumed that  $v$  includes not only RF test signal(s), but the constant bias voltage as well. For simplicity, the modulator responsivity is also included into  $v$ .

- $v_1$  and  $v_2$  are the values of the applied signal  $v(t)$  corresponding to two wavelength channels,

$$v_{1,i} = v(t_i), \quad (10.3)$$

$$v_{2,i} = v(t_i + \Delta t/2 + \delta t). \quad (10.4)$$

In these expressions,  $i$  is the integer index of the data point and  $\Delta t$  is the repetition period (equal to the sampling interval of one ADC channel). The timing points  $t_i$  can be expressed as  $t_i = t_0 + \Delta t \cdot i$ . The value of  $\Delta t/2$  appears in the last equation because the system is assumed to have two channels, which sample the applied signal at uniform intervals. The value of  $\delta t$  is the

timing offset error, which should be zero in an ideal system. It is assumed that  $\delta t$  is not varying in time.

- constants  $\alpha_1$  and  $\alpha_2$  describe gains in the two channels. The values of these constants depend on many parameters of the photonic ADC system, such as input optical power, modulator responsivity, all kind of losses along the wavelength channels, and photoreceiver responsivities. Ideally, the channels are precisely matched and  $\alpha_1$  and  $\alpha_2$  are equal. However, in a practical system it is very difficult to match the channels with accuracy required for high ENOB (besides, matching the channels with high accuracy is not worth the effort because compensation of channel gain mismatch is relatively straightforward). Therefore, it was assumed that  $\alpha_1$  and  $\alpha_2$  are different.

- constants  $c_1$  and  $c_2$  describe offsets in the two channels. Ideally, both of them should be zero; note that in case of a photonic ADC, the DC offsets in each of the complimentary channels are significant, but the differential signal should ideally have no offset. However, it was found that for successful channel interleaving  $c_1 \neq c_2 \neq 0$  needs to be assumed. Note that the offsets depend on the response of given wavelength channel around DC, and the DC values measured in an AC-coupled system can be distorted.

Note that constants  $c_1$ ,  $c_2$  and  $\alpha_1$ ,  $\alpha_2$  describe classic offset and gain mismatch effects, and  $\delta t$  describes clock skew effect, all of which are typical for interleaved ADCs. To recover the original signal applied to the modulator, one needs to know the values of these constants. In a practical ADC, these constants are defined from independent calibration measurements, which are performed off-line prior to ADC operation, or on-line while ADC is running; the latter is preferable because these constants might be slowly varying with time. In this work, a simplistic approach to determine the unknown constant was used, when the values of these constants were selected to minimize distortions for a given test signal. The details of this approach are described below.

To recover the original signal  $v$  from the samples  $A_1$  and  $A_2$  measured in the two channels, the following two steps need to be performed. First, linearization is performed according to (10.1), (10.2):



$$v_1 = \sin^{-1} \left[ \frac{A_1 - c_1}{\alpha_1} \right], \quad (10.5)$$

$$v_2 = \sin^{-1} \left[ \frac{A_2 - c_2}{\alpha_2} \right]. \quad (10.6)$$

Next, the obtained values need to be interleaved in time. In the absence of timing skew ( $\delta t = 0$ ), this corresponds simply to

$$v = (v_{1,1} \quad v_{2,1} \quad v_{1,2} \quad v_{2,2} \quad v_{1,3} \quad v_{2,3} \quad \dots \quad \dots \quad v_{1,N} \quad v_{2,N}). \quad (10.7)$$

In presence of timing skew  $\delta t$ , one of the sequences need to be shifted by  $\delta t$  with respect to the other before applying (10.7).

The idea of the selected approach is to optimize the values of unknown constants  $c_1$ ,  $c_2$ ,  $\alpha_1$ ,  $\alpha_2$ , and  $\delta t$  in such a way that harmonic distortions in the signal recovered using (10.5)-(10.7) are minimized. In case of a single-tone test signal applied to the system, the constants are selected in such a way that all frequency tones which are different from the applied one are minimized. In other words, simultaneous optimization of coefficients  $\{c_1, c_2, \alpha_1, \alpha_2, \delta t\}$  is performed, with objective to minimize the total harmonic distortion of the reconstructed signal. The approach used to perform this optimization is described below, and illustrated using the data from the single-tone 10 GHz experiment described in Chapter 7 (Fig. 12) as an example.

A "naive" approach to find the unknown coefficients  $\{c_1, c_2, \alpha_1, \alpha_2, \delta t\}$  is to divide the problem into two steps. The first step is to find coefficients  $\{c_1, \alpha_1\}$  for the first channel from the requirement that harmonic distortions in the signal obtained with (10.5) are minimized, and independently do the same to find coefficients  $\{c_2, \alpha_2\}$  for the second channel. The second step is to perform interleaving (10.7) while optimizing  $\delta t$  to minimize the total harmonic distortion in the interleaved signal.

The performance of this approach is illustrated in Fig. 19. The data recorded in two wavelength channels show a significant 3rd harmonic due to nonlinear transfer function of the MZ modulator (Fig. 19(a)), which limits SFDR to about 37 dBc. At the first step, the values of  $\{c_1, \alpha_1\}$  and  $\{c_2, \alpha_2\}$  are determined. Fig. 20 shows contour plots of the total harmonic distortion as a function of  $c_1$  and  $\alpha_1$  in the left plot, and  $c_2$  and  $\alpha_2$  in the right. The plots show

clear minima, corresponding to  $\{c_1 = 0.0265, \alpha_1 = 1.750\}$  and  $\{c_2 = -0.00759, \alpha_2 = 1.685\}$ . The spectra of the corresponding signals  $v_1$  and  $v_2$  are shown Fig. 19(b), with SFDR of about 53 dB, indicating about 17 dBc SFDR improvement due to linearization. However, the second step of "naive" algorithm fails – no value  $\delta t$  can suppress the interleaving spurs. Fig. 19(d) shows the best result which can be achieved by  $\delta t$  optimization, with SFDR of only 31 dBc. It is apparent that the "naive" approach has failed.

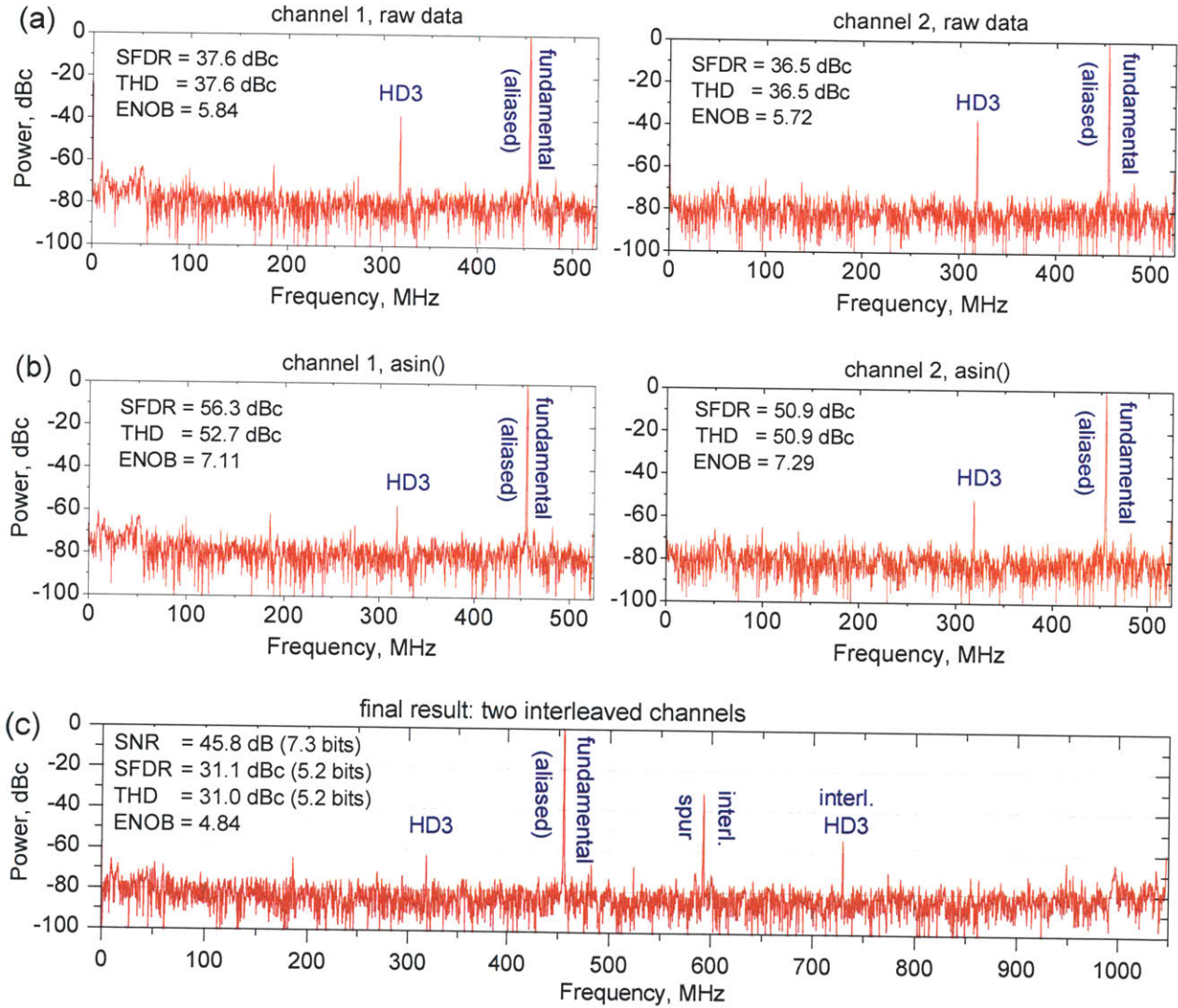


Figure 19. Linearization and interleaving with the "naive" approach, illustrated for the test case with a single tone at 10.025 GHz. (a) Spectra of the unprocessed data measured in channel 1 (left) and channel 2 (right) running at 1.048 GSa/s; (b) spectra of the data after linearization with asin() function; (c) spectrum of the signal obtained by interleaving the two linearized channels, showing large interleaving spur corresponding to the fundamental harmonic, which limits SFDR to only 31 dBc and ENOB to only 4.8 bits.

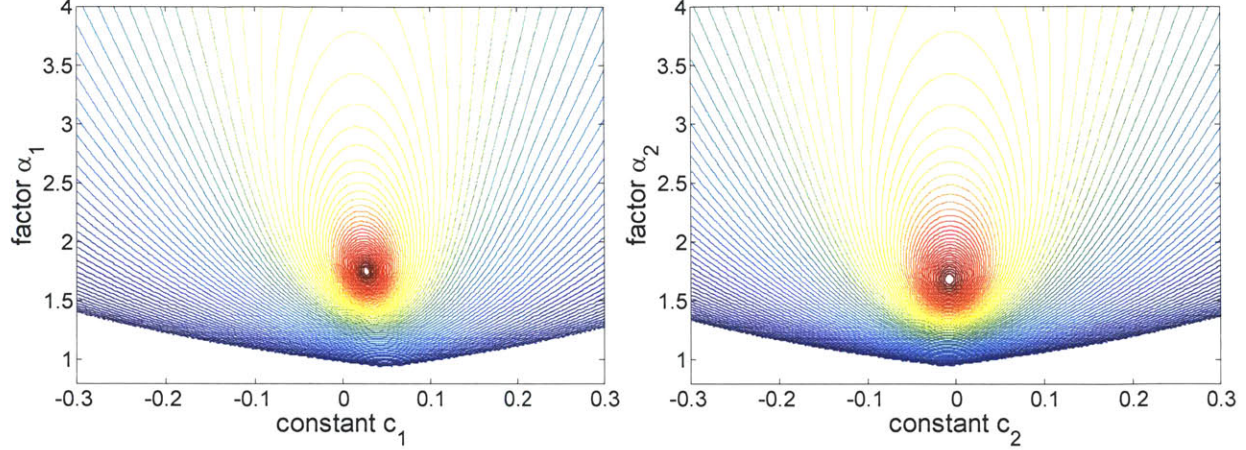


Figure 20. Contour plots of total harmonic distortion after linearization with  $\text{asin}()$  function according to (10.5), (10.6), as a function of  $c_1, \alpha_1$  for channel 1 (left) and  $c_2, \alpha_2$  for channel 2 (right). Blue color correspond to larger values of total harmonic distortion, and red color to smaller values. The optimum values of coefficients  $c$  and  $\alpha$  for the two channels are  $\{c_1 = 0.02646, \alpha_1 = 1.75003\}$  and  $\{c_2 = -0.007588, \alpha_2 = 1.68487\}$ ; these values were used to obtain signals of Fig. 19(b) from the signals of Fig. 19(a).

The reason why the "naive" approach fails is that optimization of coefficients  $\{c_1, \alpha_1\}$  independently from optimization of coefficients  $\{c_2, \alpha_2\}$  for the other channel is not physically valid. Specifically, the values of  $v_1$  and  $v_2$  found according to (10.5), (10.6) are the samples of the same signal, only taken at different time moments. This imposes constraints on possible values of  $\{c_1, \alpha_1, c_2, \alpha_2\}$ , i.e. these constants cannot be independent. The approach used in this work was the following. Because  $v_1$  and  $v_2$  represent the same signal, it must be the case that the amplitude of  $v_1$  equals the amplitude of  $v_2$ , i.e.

$$\max(v_1) - \min(v_1) = \max(v_2) - \min(v_2).$$

Therefore, for physically consistent data, it must be the case that

$$\frac{\max(A_2) - \min(A_2)}{\max(A_1) - \min(A_1)} = \frac{\alpha_2}{\alpha_1} \equiv \gamma. \quad (10.8)$$

The optimization algorithm used in this work optimizes the values of the three coefficients,  $\{c_1, c_2, \alpha_1\}$ , while assuming that  $\alpha_2 = \alpha_1 \cdot \gamma$  according to (10.8). These coefficients are determined to minimize the sum of total harmonic distortion in  $v_1$  found with (10.5) and the total

harmonic distortion in  $v_2$  found with (10.6). At the second step, the timing error  $\delta t$  is found which minimizes the total harmonic distortion in the interleaved signal (10.7).

The results obtained with this algorithm are shown in Fig. 21. The spectra of the unprocessed data measured in the two channels is shown in Fig. 21(a). To perform linearization according to the new algorithm, total harmonic distortion is calculated as a function of  $\{c_1, \alpha_1\}$  and  $\{c_2, \alpha_2 = \alpha_1 \cdot \gamma\}$ , as shown in Fig. 22(a). Note that in this figure  $\alpha_1$  is the variable of the y-axis not only for channel 1, but also for channel 2. For each value of  $\alpha_1$ , constants  $c_1$  and  $c_2$  were selected which correspond to minimum harmonic distortion. Fig. 22(b) shows the corresponding total harmonic distortion as a function of  $\alpha_1$  for both channels. The minima of the curves happen at different positions along the  $\alpha_1$  axis, which means that total harmonic distortion cannot be minimized in two channels simultaneously. In this approach, the value of  $\alpha_1$  which minimizes the average distortion in two channels is selected; this value is not optimum for either channel but it is quite close to the optimum. This leads to coefficient values of  $\{c_1 = 0.0268, \alpha_1 = 1.729\}$  and  $\{c_2 = -0.00741, \alpha_2 = 1.746\}$ . Fig. 21(b) shows the spectra of the linearized signals obtained using these coefficients. Note that the distortions in the linearized signals are just slightly higher than distortions obtained in the "naive" approach, but now the data is self-consistent, i.e. Eq. (10.8) is satisfied. Fig. 21(c) shows the spectrum of the signal obtained after interleaving with  $\delta t$  optimization (optimum  $\delta t = 18.6$  ps), with low interleaving spurs and SFDR of about 54 dBc.



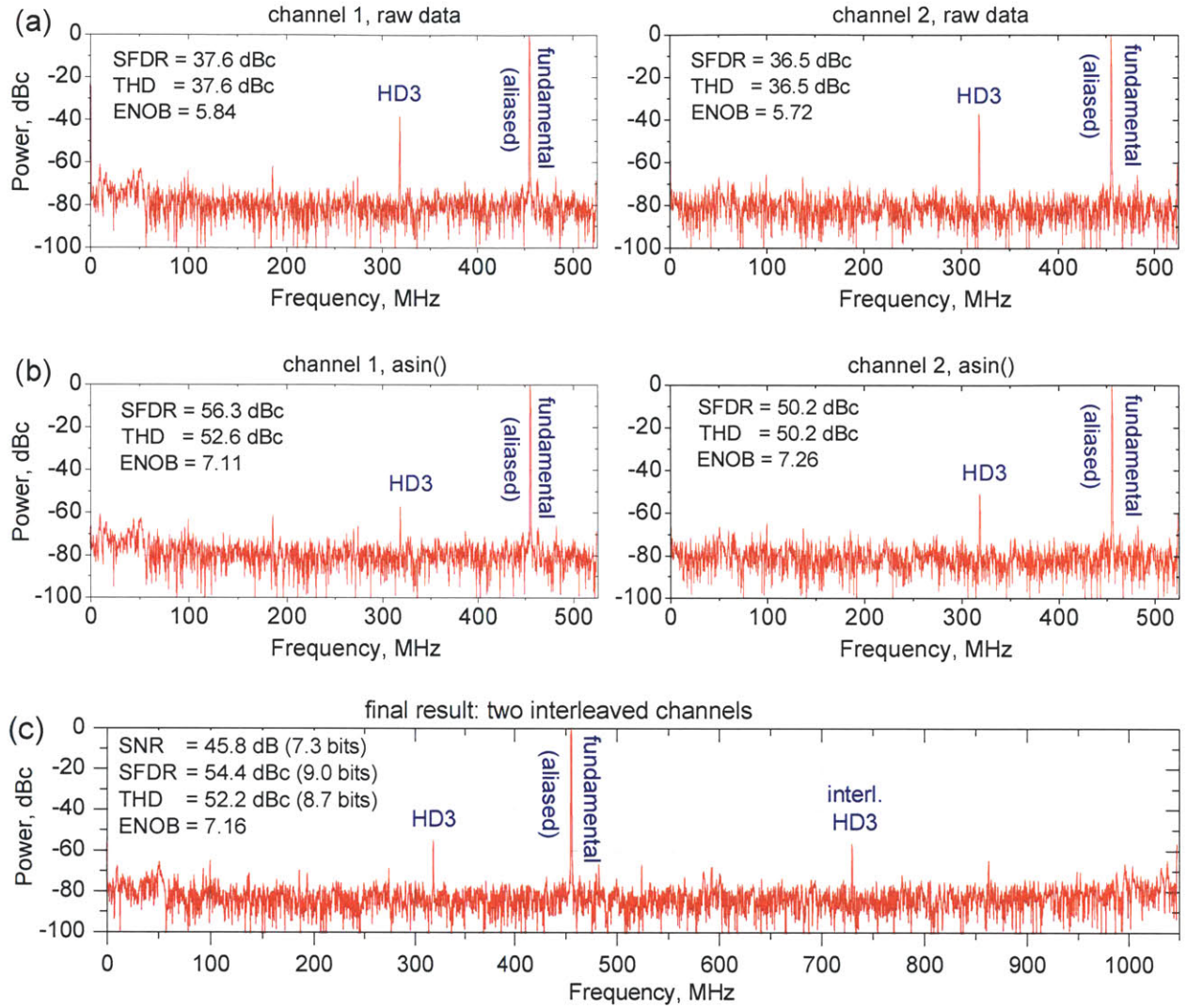


Figure 21. (a) Linearization and interleaving with the approach used in this work, illustrated for the test case with single tone at 10.025 GHz. (a) Spectra of the unprocessed data measured in channel 1 (left) and channel 2 (right) running at 1.048 GSa/s; (b) spectra of the data after linearization with `asin()` function; (c) spectrum of the signal obtained by interleaving the two linearized channels, showing high suppression of interleaving spurs with SFDR of about 54 dBc and ENOB of 7.16 bits. Plots in part (a) are identical to Fig. 12(a), and the plot in part (c) is identical to Fig. 12(b).

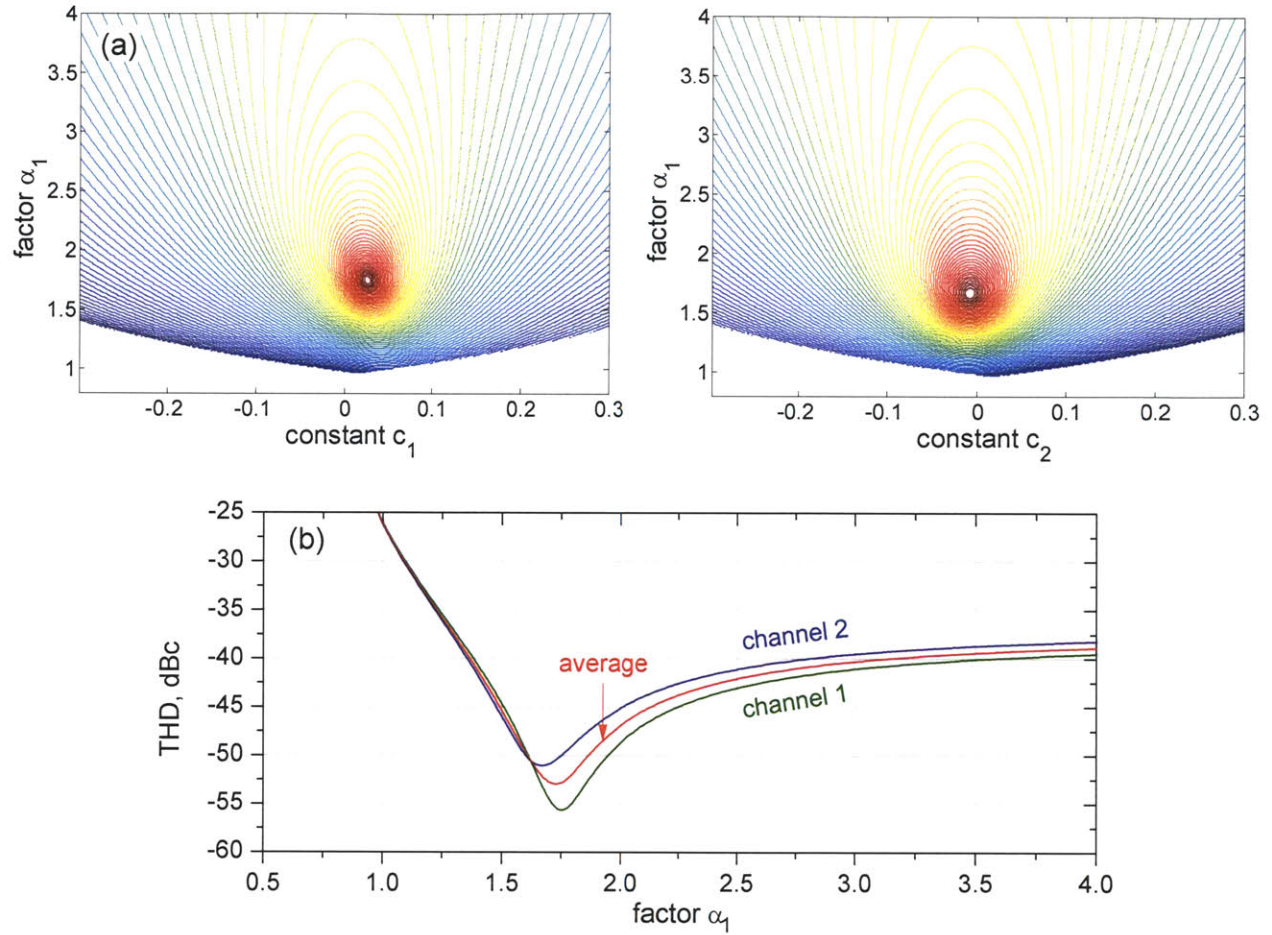


Figure 22. (a) Contour plots of total harmonic distortion after linearization with  $\text{asin}()$  function according to (10.5), (10.6), as a function of  $c_1$ ,  $\alpha_1$  for channel 1 (left) and  $c_2$ ,  $\alpha_1$  for channel 2 (right). Blue color correspond to larger values of total harmonic distortion, and red color to smaller values. (b) Total harmonic distortion as a function of  $\alpha_1$ , with  $c_1$  and  $c_2$  optimized for each value of  $\alpha_1$ . The three lines correspond to channel 1, channel 2, and the average of the two channels. The optimum  $\alpha_1$  is selected at the minimum of the average value curve. The optimum coefficients are  $\{c_1 = 0.02677, \alpha_1 = 1.72936\}$  and  $\{c_2 = -0.007409, \alpha_2 = 1.74568\}$ .

The approach described above has been used to obtain all the results reported in Chapter 7 on discrete ADC performance. The results reported in Chapter 9 on integrated ADC performance has been obtained with a simplified approach. For an integrated ADC with silicon modulator nonlinearity could not be compensated with  $\text{asin}()$  linearization because silicon modulator transfer function is different from the sinusoidal transfer function of the Mach-Zehnder modulator. Therefore, no nonlinearity compensation has been performed, and only the gain and offset mismatch errors were compensated for to ensure successful interleaving.

As explained above, the error compensation approach adopted in this work to recover the applied signal derives the unknown calibration coefficients from the measurements of the applied signal itself. This approach is not useful for practical ADCs, where the applied signal is arbitrary and unknown, and therefore the unknown coefficients need to be determined from independent testing and calibration. What is then the value of the approach used in this work? Although this approach is not rigorous, it still shows that all imperfections observed in the photonic systems can be explained by simple models. In other words, the fact that the measured data points could be successfully linearized and interleaved with the approach described above means that a properly constructed photonic ADC does not contain any unexpected imperfections (this applies to the discrete-component ADC but not to the integrated ADC). This was not always the case at different stages of the experiments, when non-optimum combinations of ADC components resulted in a signal which could not be linearized and interleaved. The fact that linearization and interleaving was successful even with constraint (10.8) means that the measured data is self-consistent. Finally, note that the timing and gain errors observed for the photonic ADC are also common to multi-channel electronic ADCs. To compensate for these errors as well as for the nonlinearity of the modulator, a practical photonic ADC can use one of the multiple calibration and compensation algorithms successfully applied in modern electronic ADCs. Compensation algorithms developed for photonics ADCs can be used as well [29, 33, 34].

We would also like to emphasize that the objective of this work was not to build a fully operational ADC product, but rather to demonstrate that photonic ADC can eliminate the problem of timing jitter and can be the future of high-performance ADCs. The jitter manifests itself as the noise floor, which was unaffected by the data processing applied, which changed only harmonic distortions. The values of ENOB achieved in this work were dominated almost completely by noise rather than distortions. Therefore, the main conclusion of this work – the conclusion that the photonic approach can overcome the problem of electronic timing jitter – holds regardless of the data processing applied.

## **11. Summary and discussion**

This part of the thesis describes demonstrations of a discrete-component and an integrated photonic ADC. The discrete-component photonic ADC was shown to sample a 41 GHz RF

signal with record 7.0 effective bits and 52 dBc SFDR. The results for the integrated ADC, featuring the modulator, filter banks, and photodetectors on a single chip, are 3.5 effective bits and 39 dBc SFDR for a 10 GHz signal. In both experiments, a sample rate of 2.1 GSa/s was obtained by interleaving two 1.05 GSa/s channels; higher sample rates can be achieved by adding more channels similar to the ones which has already been demonstrated.

The discrete-component photonic ADC results demonstrates the potential of the photonic approach to successfully overcome the problem of electronic jitter and overcome the limitations due to comparator ambiguity. The integrated photonic ADC results show that a practical integrated photonic ADC is feasible. For this reason, photonic ADCs can indeed be the path forward in high-speed ADC technology. For this to happen, investments into developing this technology are required and steps need to be taken to solve practical issues associated with building a commercial photonic ADC. Some of these steps are listed below.

- Fabrication technology should be available which enables reliable fabrication of low-loss silicon photonic devices and efficient photodetectors (e.g. Ge photodetectors) with fast turn-around. Energy efficiency of the photonic ADC is a key factor which determines its accuracy and therefore each component of the ADC need to be as energy-efficient as possible. Such fabrication capabilities are already available to few institutions in the world, and are expected to become much more widely available in the nearest future.

- Integration of electronics and photonics on the same chip is a key step towards a practical photonic ADC. Electronic-photonic integration eliminates the need to interconnect different chips and can enhance power efficiency. One of the promising approaches is to use a recently proposed monolithic electronic-photonic integration platform [57].

- Practical calibration and error compensation techniques need to be implemented. Presumably, results of decades of research on electronic interleaved ADC technologies can be applied with very little change to the interleaved photonic ADCs because of similarity of the errors occurring in both ADCs. It is important that the calibration of photonic ADC needs to be performed at run-time, because many components of the photonic ADC can experience slow drifts: the resonant frequencies of the filters can fluctuate in time together with local temperature, the modulator bias phase may fluctuate as well, the bias point of the modulator and photodetector can change in time due to low-frequency noise in the bias voltage, etc.



- Development of practical linearized modulator (e.g. according to the theory developed in Part III) can bring a very positive impact on photonic ADC performance, because improved linearity of the modulator means that higher modulation depth can be used for given level of distortion. This improves the power efficiency of the system, because the required optical power is inversely proportional to the modulation index squared, as well as reduces the reliance on the linearization algorithms for improvement of SFDR.

- There are certain challenges in implementing delay lines for preparing the wavelength-interleaved pulse train which samples the signal in the modulator. Namely, to introduce differential delays on the order of 1 ps, the lengths of the delay lines need to be on the order of 10 cm. This requires the propagation loss in the delay lines to be very low. If the delay lines are implemented with conventional single-mode silicon waveguides with their approximately 3 dB/cm loss, the total loss over 10 cm of waveguide will be too high for practical purposes. Silicon nitride waveguides, which can have very low loss ( $\sim 0.1$  dB/cm), is a much better option for implementation of the delay lines. Another possible difficulty is that the significant length of the delay lines means that they occupy large chip area. In this respect, low-loss slow-light delay lines would be beneficial.

Note that although challenges in commercial implementation of photonic ADCs do exist, these challenges are not fundamental but technical in nature and it is expected that they will be overcome with sufficient effort. The fundamental problems facing modern ADC technology at high frequencies – the aperture jitter and comparator ambiguity – are solved by the photonic approach, as demonstrated in this work.

### III. Linearized Silicon Modulator

This important part of the thesis describes a novel scheme to create a wideband linearized silicon Mach-Zehnder (MZ) modulator. The modulator consists of a single MZ interferometer with identical reverse-biased silicon diode phase shifters in both arms, driven in a push-pull configuration. It is shown that the 3rd order nonlinearity of the modulator can be eliminated by canceling the nonlinearities from the silicon phase shifters and the MZ transfer function against each other. The 2nd order nonlinearity is simultaneously eliminated by differential detection or operation away from the quadrature point. As a result, the linearity of the proposed silicon modulator greatly exceeds the linearity of a conventional MZ modulator with ideal, linear (e.g.  $\text{LiNbO}_3$ ) phase shifters. The simplicity and large optical and RF bandwidth of the proposed modulator make it attractive for analog photonic systems, such as the photonic ADC system studied in this thesis<sup>1</sup>.

#### 12. Introduction to silicon modulators and modulator linearization

Microwave photonics is an active research area with many applications, including antenna remoting, high-definition cable TV, radio over fiber, as well as photonic analog-to-digital conversion studied in this thesis [53, 58-62, 2]. In microwave photonics, an analog radio-frequency (RF) signal is converted into the optical domain with a modulator, processed in the optical domain using photonic devices, and then converted back to the electrical domain. Silicon photonics is an attractive platform for microwave signal processing because of potential low-cost manufacturing and direct integration with CMOS electronics, and because many high-performance devices, such as low-loss waveguides, filters, switches, modulators, and photodetectors have already been demonstrated in the silicon platform [63-67].

In microwave photonics, the RF signal is converted into the optical domain with an electro-optic modulator. This modulator needs to be high-speed, to accommodate the RF bandwidth, and sensitive, to allow low driving voltages. The modulator also needs to be linear because

---

<sup>1</sup> This part of the thesis mostly follows our article [54], with small modifications and additions.

nonlinearities in the modulator create distortions, which is often the factor which limits the performance of a microwave photonic system. In a photonic ADC system, deep modulation is beneficial for SNR and is required for high power efficiency (see Chapter 5); however, deep modulation also leads to increased nonlinear distortions which can negate the improvements in SNR. A modulator with improved linearity is therefore expected to have a significant impact on the performance of photonic ADCs, as well as other microwave photonic systems.

Many techniques to enhance the modulator linearity have been proposed [53, 58, 55-84]. Most techniques can be characterized as either pre-distortion linearization, feedback linearization, or optical transfer function linearization [53, 58]. Pre-distortion linearization methods [68-75] use a nonlinear circuit preceding the modulator to distort the RF signal in such a way that the overall transfer function of the pre-distorter plus the modulator is more linear than that of the modulator alone. Pre-distortion linearization is a widely used approach, and has been successfully applied to linearize MZ modulators [68, 69, 71-75], directional coupler modulators [69], and multiple quantum well electroabsorption modulators [70]. However, to use pre-distortion successfully, the modulator needs to be fast enough to respond to the harmonics of the fundamental signal created by the pre-distorter. This constraint effectively reduces the RF bandwidth of the system by the order of the nonlinearity that needs to be cancelled [53]. In the feedback linearization approach, some fraction of the modulator output signal is detected and compared to the original RF signal; a feedback loop then acts to bring the difference between them to zero, ensuring linear operation. The challenges with this approach are the speed of the feedback loop (which must be fast enough to track the RF signal), and the availability of broadband RF amplifiers with sufficient gain [53]. In optical linearization approaches, two or more modulators are combined to provide a transfer function which is more linear than that of the individual modulators [55, 76-81]. The modulators can be connected in parallel [77, 78] or in series [79-81]. A conceptually similar approach is to modulate signals of different wavelengths [82] or polarizations [83-84] in a single modulator and combine them afterwards to improve the system linearity. The parameters which need to be controlled to achieve linear operation can be the optical power splitting ratio between the modulators, optical power splitting ratio between the arms of an individual MZ modulator, RF voltage splitting ratio between the modulators, and the bias points of the modulators. The number of parameters to be controlled is typically higher for wideband linearization (suppression of 2nd and 3rd harmonics) and lower for sub-octave

linearization (suppression of 3rd harmonic only). It is common for optical linearization approaches to result in an optical power penalty because combining modulator outputs to cancel the nonlinear harmonics usually cancels some part of the fundamental as well.

Silicon modulators are a very active area of research [65, 66], with multiple groups demonstrating high-performance silicon modulators based on reverse-biased diodes [85-94], forward-biased diodes [95-99], and MOS capacitors [100, 101]. Additionally, recent work on silicon-germanium structures using the quantum-confined Stark effect looks very promising [102-104]. Forward biased, ring modulators  $2.5\mu\text{m}$  in radius have achieved a peak-to-peak driving voltage as small as  $0.15\text{V}$  operating at  $1\text{ Gb/s}$  [99]. In reverse-biased silicon diode modulators, the RF bandwidth can extend up to about  $30\text{-}35\text{ GHz}$  [88, 89, 94], and  $V_{\pi}L$ s as small as  $1\text{ V}\cdot\text{cm}$  have been achieved at speeds up to  $10\text{ Gb/s}$  [91]. To date, most studies of silicon modulators have been performed in the context of digital transmission systems, with the modulation quality evaluated using an eye diagram and metrics such as extinction ratio. To our knowledge, no study of the linearity of silicon modulation devices for analog applications has been performed. In this section, we analyze the linearity of Mach-Zehnder (MZ) silicon modulators and predict that, despite the highly nonlinear response intrinsic to silicon, it is possible to make a modulator with linearity greatly exceeding that of a conventional MZ  $\text{LiNbO}_3$  modulator. The proposed modulator configuration is very simple and does not compromise the responsivity, optical bandwidth, or RF bandwidth of the link. The concept is applicable not only to reverse-biased silicon modulators, but also to other modulators with sufficiently high nonlinearity in their phase shifters' response.

The linearized silicon modulator proposed in this work is a push-pull MZ modulator with identical, nonlinear silicon phase shifters in its two arms. Linearization is achieved by canceling the nonlinearity of the silicon phase shifter response against the nonlinearity of the sine-squared MZ transfer function [105]. In some respects, this modulator resembles the optically linearized modulators mentioned above: the modulator is linear by itself, without the help of external electrical circuits. However, this modulator is simpler than optically linearized modulators, because it is just a single MZ structure and the only two parameters to be controlled are the MZ bias phase and the diode bias voltage. In other respects, the proposed modulator resembles pre-distortion linearized modulators: the nonlinearity of a silicon phase shifter can be viewed as analogous to the nonlinearity of a pre-distorter circuit. However, in our case, the pre-distortion

function is internal to the phase shifters, which not only simplifies the implementation, but also means that the modulator RF bandwidth is not compromised by linearization. More specifically, in pre-distortion linearization, the modulator must be able to respond at the harmonics of the applied RF signal, while in our case the optical signal traveling through the silicon diodes automatically captures these harmonics and the increased bandwidth requirement does not apply.

In this work, we first describe the proposed linearization concept, which is applicable to any MZ modulator with sufficiently nonlinear phase shifters, mathematically (Chapter 13). We then apply this concept to a silicon carrier-depletion modulator and show that its linearization is possible (Chapter 14). We study the linearity of this modulator numerically and show that it significantly outperforms a conventional MZ modulator with ideal linear phase shifters. Finally, we examine the optical bandwidth over which the linear operation can be achieved (Chapter 15).

### 13. Concept of linearization of a modulator with nonlinear phase shifters

This chapter presents a mathematical analysis of the linearity of an MZ modulator with nonlinear phase shifters. The modulator transfer function is derived, its Taylor series expansion is analyzed, and it is shown that the 2nd and the 3rd expansion terms can be eliminated with the proper choice of modulator parameters.

A schematic of the MZ modulator considered in this work is shown in Fig. 23. The two arms of the MZ structure have phase shifters which are identical and described by nonlinear voltage-dependent phase  $\varphi(v)$  and loss  $\alpha(v)$ . The same DC bias voltage  $v_{DC}$  is applied to the two arms. The RF signal  $v = v(t)$  is applied in a push-pull configuration, so that the total voltage at the top and bottom phase shifters is  $v_{DC} + v$  and  $v_{DC} - v$ , respectively. The optical power at the top and the bottom outputs of the modulator can be shown to be:

$$P_A = P_{in} \exp\left[-\frac{\alpha_A + \alpha_B}{2}\right] \sin^2\left(\frac{\pi}{4} + \frac{\varphi_A - \varphi_B}{2}\right) + \frac{P_{in}}{4} \left[ \exp\left(-\frac{\alpha_A}{2}\right) - \exp\left(-\frac{\alpha_B}{2}\right) \right]^2, \quad (13.1)$$

$$P_B = P_{in} \exp\left[-\frac{\alpha_A + \alpha_B}{2}\right] \cos^2\left(\frac{\pi}{4} + \frac{\varphi_A - \varphi_B}{2}\right) + \frac{P_{in}}{4} \left[ \exp\left(-\frac{\alpha_A}{2}\right) - \exp\left(-\frac{\alpha_B}{2}\right) \right]^2, \quad (13.2)$$

where  $\varphi_A = \varphi(v_{DC} + v)$  and  $\alpha_A = \alpha(v_{DC} + v)$  are the phase shift and loss in the top phase shifter,  $\varphi_B = \varphi(v_{DC} - v)$  and  $\alpha_B = \alpha(v_{DC} - v)$  are the phase shift and loss in bottom phase shifter, and  $P_{in}$  is the input power. The MZ modulator is assumed to be biased at quadrature, so that the phase shift between the two arms at  $v = 0$  is  $\pi/2$ .

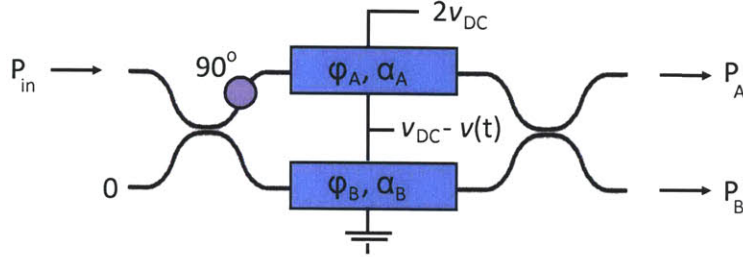


Figure 23. The configuration of the MZ modulator studied in this work. The two arms have identical nonlinear phase shifters biased with DC bias voltage  $v_{DC}$ , driven in a push-pull mode with the RF signal  $v(t)$ . The  $90^\circ$  phase shifter biases the MZ modulator at quadrature; it will be shown that biasing the modulator slightly away from the quadrature point is one of the ways to improve the linearity.

To analyze the linearity of the MZ transfer function, the phase  $\varphi$  and loss  $\alpha$  can be expanded into a Taylor series around the DC voltage  $v_{DC}$ :

$$\varphi(v_{DC} + v) = (\varphi_{DC} + \varphi_1 v + \varphi_2 v^2 + \varphi_3 v^3 + \dots)L, \quad (13.3)$$

$$\alpha(v_{DC} + v) = (\alpha_{DC} + \alpha_1 v + \alpha_2 v^2 + \alpha_3 v^3 + \dots)L, \quad (13.4)$$

where  $L$  is the length of the phase shifters. Note that according to Eqs. (13.1-13.2), the output powers depend not on individual phases  $\varphi_A$  and  $\varphi_B$ , but rather on the phase difference  $\varphi_A - \varphi_B$ .

Using expansion (13.3), this phase difference is

$$\varphi_A - \varphi_B = \varphi(v_{DC} + v) - \varphi(v_{DC} - v) = 2(\varphi_1 v + \varphi_3 v^3 + \dots)L. \quad (13.5)$$

The second and higher-order even terms of the phase response expansion are automatically cancelled in Eq. (13.5) thanks to the symmetry of the push-pull configuration. In the case of a reverse-biased silicon diode, the second-order phase nonlinearity is the dominant nonlinear term, and its cancellation due to the push-pull symmetry is critical for wideband linearization.

Plugging Eqs. (13.3-13.5) into (13.1-13.2) and performing a Taylor expansion, the expressions that describe modulator linearity are finally obtained:

$$P_A = P_{in} e^{-\alpha_{DC} L} \left[ \frac{1}{2} + (\varphi_1 L) v + (\alpha_1^2 L^2 - \alpha_2 L) v^2 + \left( -\frac{2}{3} \varphi_1^3 L^3 + \varphi_3 L - 2\varphi_1 \alpha_2 L^2 \right) v^3 + \dots \right], \quad (13.6)$$

$$P_B = P_{in} e^{-\alpha_{DC} L} \left[ \frac{1}{2} - (\varphi_1 L) v + (\alpha_1^2 L^2 - \alpha_2 L) v^2 - \left( -\frac{2}{3} \varphi_1^3 L^3 + \varphi_3 L - 2\varphi_1 \alpha_2 L^2 \right) v^3 + \dots \right]. \quad (13.7)$$

The above equations can be analyzed as follows. The third-order nonlinear coefficient is the sum of three terms: (i) the term due to the cubic nonlinearity of the sine-squared MZ transfer function, which is present even in the case of ideal linear phase shifters; (ii) the term due to the cubic nonlinearity of the phase shifters; and (iii) the term due to the quadratic nonlinearity of the loss in the phase shifters. If these terms can be made to cancel each other, the third order nonlinear coefficient can be set to zero. Demanding such cancellation yields a quadratic equation in  $L$ :

$$\frac{2}{3} \varphi_1^3 L^2 + 2\varphi_1 \alpha_2 L - \varphi_3 = 0. \quad (13.8)$$

Linearization is possible only if this equation has real, positive solutions for the phase shifter length,  $L$ . Additionally,  $L$  must be long enough for high modulation depth to be possible, but short enough that the modulator does not take up too much chip area. Whether an acceptable length is possible depends on the above coefficients, which are determined by the shapes of the phase shifter response curves  $\varphi(v)$  and  $\alpha(v)$ , as well as by the selected bias voltage  $v_{DC}$ . In the next chapter, it will be shown that a reverse-biased silicon diode phase shifter has nonlinearity suitable for the cancellation of the cubic nonlinear term in the transfer function at practical diode lengths.

The modulator transfer function also has second-order nonlinearity, see Eqs. (13.6-13.7), from the voltage-dependent loss. The quadratic nonlinearity is not a problem in systems with sub-octave bandwidth. However, wideband systems, such as photonic analog-to-digital converters, are affected by quadratic nonlinearity, and suppression of the second-order nonlinear term is highly desirable. The two terms of the second-order nonlinear coefficient can, in principle, cancel each other. However, this cancellation is of limited usefulness because it occurs at a different phase-shifter length than the cancellation of the cubic nonlinearity. There are two



approaches to eliminating the quadratic nonlinearity without compromising the cancellation of the cubic nonlinear term. The first approach is to use differential detection: according to Eqs. (13.6-13.7), the second order nonlinear terms in the complimentary outputs are identical, so subtracting these outputs will eliminate the second order nonlinearity (as well as all other even-order nonlinearities). Because the odd nonlinearities have opposite signs in the two outputs, such subtraction will not eliminate the desired, linear term. The second approach is to shift the operating point of the MZ modulator away from quadrature to introduce a quadratic term in the sine-square MZ transfer function. At the proper operating point, this quadratic term will cancel the quadratic term of Eq. (13.6) or (13.7) and result in MZ modulator operation free of quadratic nonlinearity. A similar analysis to the one above, where the operating point was allowed to change, shows that cancellation of the 3rd order nonlinearity occurs at the same length regardless of operating point. Therefore, the cancellation of the 3rd order nonlinearity is not affected when the operating point is changed to cancel the 2nd order nonlinearity, and simultaneous cancellation of 2nd and 3rd order nonlinearities is straightforward. Note that this approach can eliminate quadratic nonlinearity only in one of the two modulator outputs, which is often sufficient because many applications use only a single output.

Once the 3rd-order and all even order nonlinear terms of the modulator transfer function are eliminated, as described above, the modulator linearity will be limited by the 5th and higher-order odd nonlinear terms. Table 3 summarizes the results of this chapter.

Table 3. Different nonlinear terms and the ways to cancel them as described in Chapter 13.

Nonlinear term	Source of nonlinearity	Method of cancellation
2nd and other even-order terms	quadratic and other even-order nonlinearity of $\varphi(v)$	Cancelled due to push-pull symmetry.
2nd and other even-order terms	linear, quadratic, and other nonlinear terms of $\alpha(v)$	Cancelled by using differential detection.
2nd-order term	linear and quadratic terms of $\alpha(v)$	Cancelled (in one of the two outputs) by shifting the operating point away from quadrature.
3rd order term	cubic term of $\varphi(v)$ + cubic term of MZ transfer function + quadratic term of $\alpha(v)$	Eliminated with proper choice of phase shifter length. At this length, different contributions to the cubic nonlinearity cancel each other.
5th order term		In general, cannot be cancelled simultaneously with the 3rd order term. Limits the linearity of the linearized modulator.

## 14. Linearization of a reverse-biased silicon modulator

The theoretical analysis presented above shows that the transfer function of an MZ modulator with nonlinear phase shifters can be linearized with the proper choice of modulator parameters, provided that the phase shifters have a suitable nonlinear phase  $\varphi(v)$  and loss  $\alpha(v)$  response. While the linearization is not necessarily achievable for arbitrary phase shifter nonlinearity, this chapter shows that a reverse-biased silicon diode phase shifter has the right amount of nonlinearity to enable linearization. The performance of such a linearized silicon modulator is analyzed and compared to a conventional MZ modulator.

A reverse-biased silicon modulator uses the free carrier plasma dispersion effect to modulate the optical signal. The RF voltage applied to a reverse-biased diode changes the width of the depletion region and, thus, the free carrier concentration profile within the diode. The optical mode traveling through the diode experiences a phase shift induced by these free carriers. The MZ structure serves to turn this phase modulation into an amplitude modulation. Free

carriers induce not only a phase shift, but also undesired absorption, which needs to be included in the linearity analysis.

Before proceeding to a rigorous treatment of silicon modulators, rough estimates can be used to illustrate the possibility of canceling the cubic nonlinear term. The quadratic equation (13.8) derived in the previous chapter can be simplified by neglecting the term related to the voltage-induced loss. Eq. (13.8) becomes  $\frac{2}{3}\varphi_1^3 L^2 - \varphi_3 = 0$ . A positive solution for  $L$  is possible only if the phase nonlinear coefficients,  $\varphi_1$  and  $\varphi_3$ , have the same sign. To verify that this is the case for a reverse-biased silicon diode, we can use the Shockley diode model. In this mode, the width of the depletion region is proportional to the square root of the applied voltage,  $\sqrt{v_{DC} + v}$ . The induced change in the effective index of the optical mode is approximately proportional to the width of the depletion zone, therefore  $\varphi(v) \sim \sqrt{v_{DC} + v}$ . Taylor series expansion gives

$$\varphi(v) \sim \sqrt{v_{DC}} \left( 1 + \frac{1}{2} \frac{v}{v_{DC}} - \frac{1}{8} \left( \frac{v}{v_{DC}} \right)^2 + \frac{1}{16} \left( \frac{v}{v_{DC}} \right)^3 + \dots \right). \quad (14.1)$$

The nonlinear coefficients,  $\varphi_1$  and  $\varphi_3$ , indeed have the same sign. Therefore, this modulator can be linearized, i.e. it is always possible to find a positive length  $L$  at which the cubic nonlinearity of the MZ transfer function  $\varphi_1^3 L^3$  cancels the cubic nonlinearity of the phase shifters  $\varphi_3 L$ .

Though a description based on Shockley's diode model gives a qualitative picture of modulator linearization, it is not accurate enough for quantitative analysis. In this work, rigorous numerical simulations were used to find the shapes of the  $\varphi(v)$  and  $\alpha(v)$  curves for a reverse-biased silicon diode. Electrical simulations were performed in Synopsys's Sentaurus<sup>®</sup> software suite [106] and determined the spatial carrier concentration distribution as a function of applied voltage. The electrical model used to find the carrier distributions included mobility, recombination, bandgap and breakdown effects. The carrier concentrations were then converted into refractive index and absorption coefficient distributions [107]. Finally, the obtained index and absorption distributions were substituted into a vectorial mode solver [108] to determine the effective index and attenuation coefficient of the optical mode.

The designs of a reverse-biased silicon diode can be different in terms of waveguide cross-sections and doping profiles. To be specific, we selected the diode design shown in Fig. 24 [109] and used it in the rest of this work. This design was optimized solely to maximize the diode responsivity, without consideration to the diode nonlinear characteristics. The calculated phase and loss response,  $\phi(v)$  and  $\alpha(v)$ , per unit length of the diode phase shifter are shown in Fig. 25. Note that in Fig. 25 and throughout this work, positive voltages are voltages applied in the reverse-bias direction. The wavelength of light is assumed to be fixed at  $1.55\text{ }\mu\text{m}$ ; wavelength dependence of modulator linearity will be studied in Chapter 15.

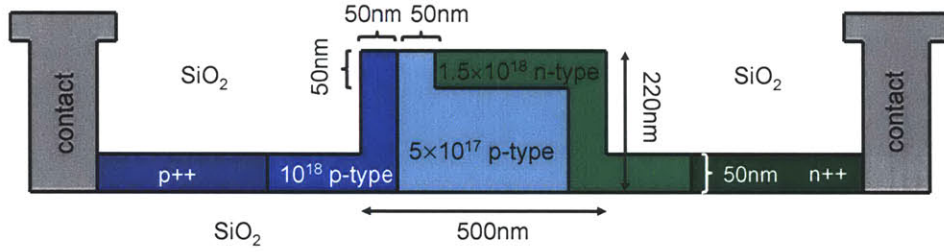


Figure 24. Cross-section of the reverse-biased silicon diode phase shifter studied in this work. This diode was designed to maximize the modulator sensitivity without regards to its linearity.

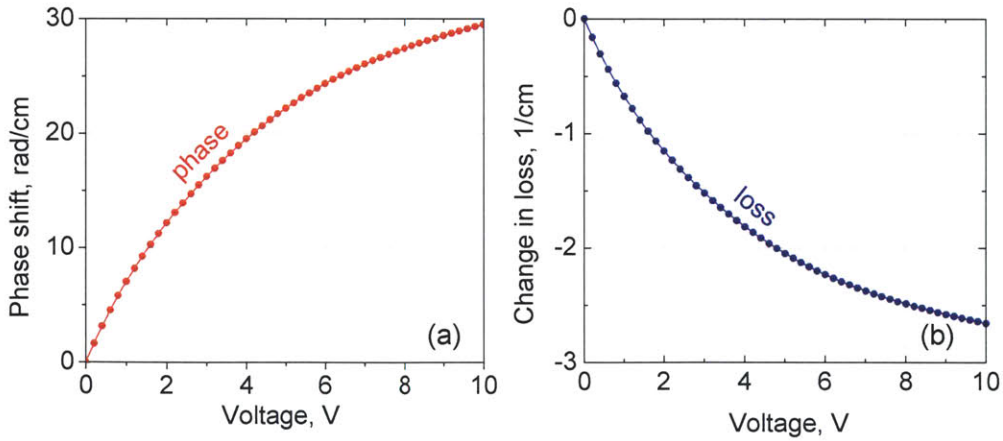


Figure 25. (a) Phase shift and (b) change in the modal loss per centimeter of a silicon diode phase shifter length versus applied voltage. The diode cross-section is shown in Fig. 24. The circles represent simulation data points, and the curves an 8th-order polynomial fit to these points.  $1.55\text{ }\mu\text{m}$  light is assumed.

To study the nonlinear characteristics of the modulator, the modulator transfer functions (13.1-13.2) were generalized to allow for MZ bias values different from quadrature. The phase  $\varphi(v)$  and loss  $\alpha(v)$  were determined by an 8-th order polynomial fit to the simulation data points (shown in Fig. 25). The polynomial fitting provided a way to calculate the phase and loss for arbitrary voltage values. As one has to expect, it was observed that suppression of the harmonics to a level of 60dBc and below is very sensitive to noise in the numerical data, as well as the exact fitting function used, and the exact implementation of the algorithm. Fortunately, while choice of fit creates some shift in the output graphs, all qualitative results remain the same. Moreover, despite the obvious differences in curve values with fitting choice, the quantitative differences were not so great as to exclude using bias-point tuning to achieve the desired linearity, as discussed below. To study the modulator linearity, we generated a single-tone sinusoidal input signal,  $v(t)$ , applied to it the MZ transfer function with  $\varphi(v)$  and  $\alpha(v)$  given by the polynomial fits, and analyzed the harmonic distortions of the obtained output signal.

The extent to which the silicon modulator can be linearized, and the phase shifter length at which linear operation is achieved, can now be found. The nonlinearity of the silicon diode phase shifters depends on the bias voltage. To start, the bias voltage is chosen to be 4V; arbitrary values of the bias voltage will be considered later. Numerical simulations show that the cubic nonlinearity is completely eliminated for  $L=263\mu\text{m}$ . The harmonic distortions as a function of modulation depth for this phase shifter length are shown in Fig. 26(a). The modulation depth is defined as  $\Delta I / \Delta I_{\text{max}}$ , where  $\Delta I$  is the intensity swing at the output of the modulator for given RF amplitude, and  $\Delta I_{\text{max}}$  is the maximum possible intensity swing corresponding to full modulation. The powers of the harmonic distortions are specified relative to the power of the fundamental. The 3rd harmonic distortion in the linearized modulator (“HD3 lin. MZM” curve) is significantly reduced compared to a conventional MZ modulator with ideal linear phase shifters (“HD3, conv. MZM” curve), especially at small modulation depths. Note that in the absence of cubic nonlinearity, HD3 originates from the 5th order nonlinearity, as confirmed by the slope of the curve. The second harmonic (“loss-induced HD2” curve) will not be present in the proposed modulator. This curve corresponds to the second harmonic originating from the voltage-dependent loss  $\alpha(v)$  if the modulator were biased at quadrature. As explained in the

previous chapter, HD2 can be completely eliminated by biasing the modulator away from the quadrature point or by using differential detection.

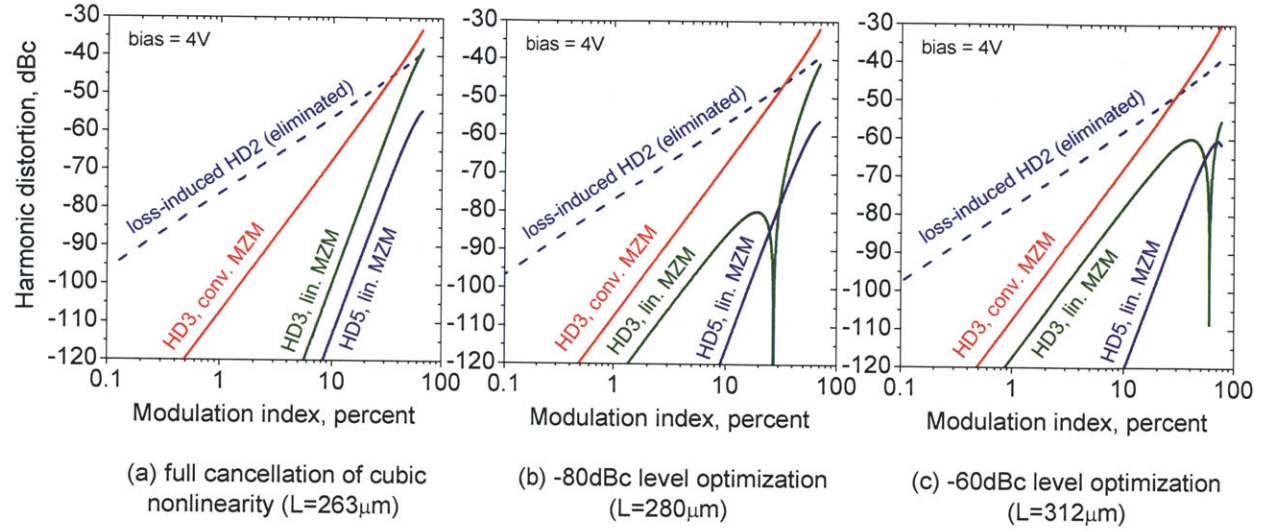


Figure 26. Harmonic distortions in the linearized silicon modulator and a conventional MZ modulator as a function of modulation depth. The curves “HD3, lin MZM” and “HD5, lin MZM” represent the 3rd and 5th harmonic distortions in the linearized silicon modulator, and the curve “HD3, conv. MZM” is the 3rd harmonic distortion in a conventional MZ modulator with ideal, linear phase shifters. The curve “loss-induced HD2” illustrates the amount of the 2nd harmonic distortion due to voltage-dependent loss, which can be completely eliminated by shifting the MZ bias away from quadrature or by using differential detection. The length is selected (a) to completely eliminate the cubic nonlinearity, (b) to achieve the largest modulation depth while keeping HD3 below the -80 dBc level; (c) to achieve the largest modulation depth while keeping HD3 below the -60 dBc level (see Table 2). The silicon diode reverse bias voltage was 4 V; see Fig. 28 for the performance at arbitrary reverse bias voltages.

The performance of the modulator with no cubic nonlinearity (Fig. 26(a)) is limited by the 5th order nonlinearity, which quickly increases with modulation depth and limits the benefit of linearization at high modulation depths. To achieve better linearity at high modulation depths, some amount of cubic nonlinearity can be allowed. The idea is to let the contributions of the cubic and the 5th order nonlinearity to the HD3 cancel at some signal power, thus, yielding a more linear performance at this power. Fig. 4(b) illustrates this concept. Here, the phase shifter length ( $L = 280 \mu\text{m}$ ) is optimized in order to keep the HD3 below the -80 dBc level up to highest possible modulation depth. The modulation depth at which the HD3 first crosses the -80 dBc level is increased from 18% (Fig. 26(a)) to 30%, i.e. the HD3 stays below -80 dBc for all modulation depths lower than 30%. This increase comes at the expense of higher distortion at



lower modulations depths. However, since distortions are small at low modulations depths, generally, their increase is not problematic. In Fig. 26(c), the length,  $L = 312 \mu\text{m}$ , was optimized to achieve the highest possible modulation depth where the HD3 was suppressed below -60 dBc. Compared to the fully cancelled cubic nonlinearity (Fig. 26(a)), the acceptable modulation depth increased from 32% to 68%. A conventional MZ modulator allows only 15% modulation with HD3 below -60 dBc. We will continue to consider these three linearization criteria; for convenience, they are summarized in Table 2.

Table 4. Three criteria for modulator linearization considered in Chapter 14.

No.	Criterion	Explanation
1	Fully cancelled cubic nonlinearity	The cubic nonlinear term of the modulator transfer function is completely eliminated. (Fig. 26(a))
2	-80 dBc level optimization	The modulator is optimized to maximize the modulation depth up to which the third harmonic distortion, HD3, stays below the -80 dBc level. (Fig. 26(b))
3	-60 dBc level optimization	Same as above but with the HD3 below the -60 dBc level. (Fig. 26(c))

The above discussion assumed a diode bias of 4 V; the analysis will now be extended to arbitrary bias voltages. The three linearization criteria listed in Table 2 are again considered. The lengths of the phase shifters which yield the most linear performance as a function of bias voltage are shown in Fig. 27. The length values needed for linearization are in the range of hundreds of microns, and correspond to values that are typically used in MZ silicon modulators.

An important consequence of the relationship between bias voltage and optimum length (Fig. 27) is that, for a modulator of a given length, linear operation can be achieved by adjusting the bias voltage. This is important because the phase shifter length in a fabricated modulator can differ from the design value due to fabrication variations. An equivalent argument applies to other types of fabrication variations (e.g. in diode dimensions, doping profiles, etc.); these variations will change the bias vs. length curve, which means that for a given length, linearization is achieved at a different bias value.

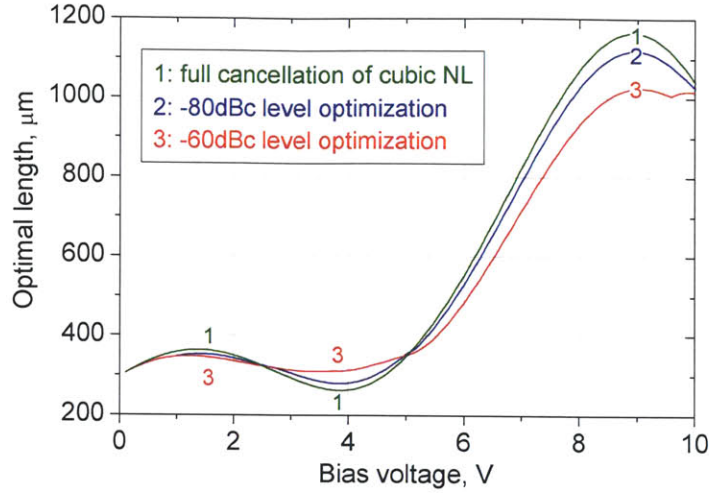
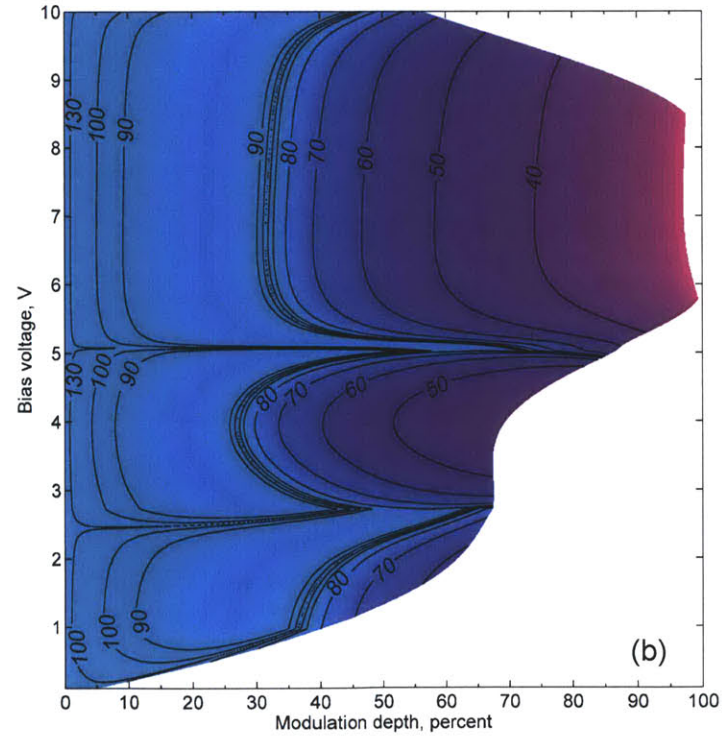
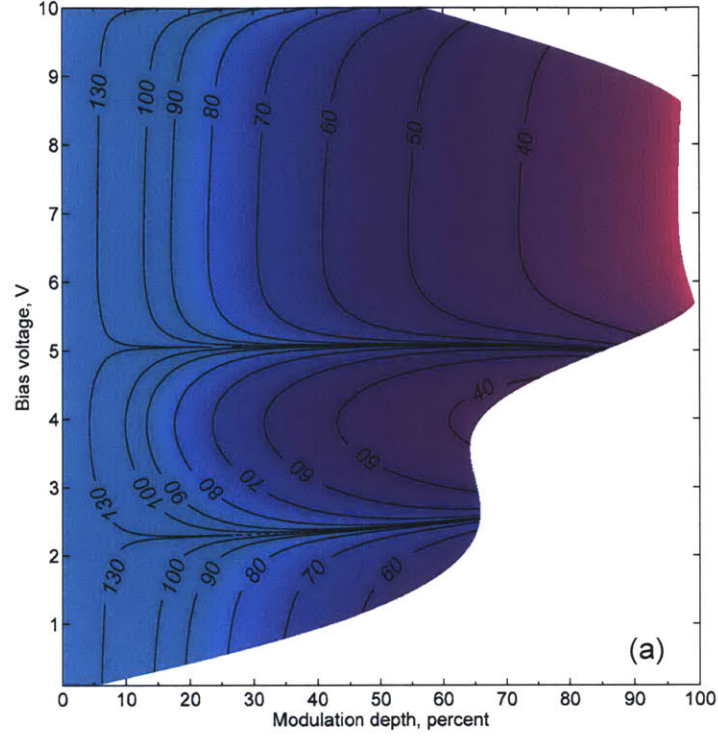


Figure 27. The length of the silicon diodes optimized for the three cases of Table 4: (1) full cancellation of cubic nonlinearity, (2) -80 dBc level optimization, and (3) -60 dBc level optimization.

Contour plots of the HD3 as a function of bias voltage and modulation depth for the three cases of Table 4 are shown in Fig. 28. In these plots, the phase shifter length was optimized at each bias voltage (see Fig. 27). As in Fig. 26, the HD3 grows monotonically with modulation depth when the cubic nonlinearity is canceled (Fig. 28(a)), and has an oscillation when the third harmonic is instead held below the -80 or -60 dBc levels (Fig. 28(b), (c) respectively). The white areas in Fig. 28 represent modulation depths not achievable at the given bias voltage and diode length. The modulation depth is limited because, at every time, the voltage applied must not turn on the diode and because breakdown effects need to be avoided. In this work, voltage values were limited to the  $[0, 13]$  V range. This meant that the RF amplitude could not exceed both  $v_{DC}$  and  $(13 - v_{DC})$ , giving rise to the white areas in Fig. 28.

For comparison, Fig. 29 shows the HD3 of a conventional MZ modulator with ideal, linear phase shifters. It is clear that the proposed linearization scheme significantly extends the range of modulation depths which can be achieved with low harmonic distortion. At two values of the bias voltage, approximately 2.5 V and 5 V, the linearity is especially good: 70% modulation depth can be reached with the third harmonic distortion staying below the -80 dBc level (Fig. 29(b)). The reason for this enhanced linearity is that at certain bias voltages not only the cubic but also the 5-th order nonlinearity of the modulator is minimized. In practice, however, it might be difficult to achieve such high linearity because of fabrication variations. For cubic nonlinearity cancellation, there is one degree of freedom – the bias voltage – which can be used

to compensate for fabrication variations. However, if both the cubic and the 5th order nonlinearities need to be cancelled simultaneously, there is no such freedom, and fabrication variations cannot be compensated by adjusting the bias voltage.



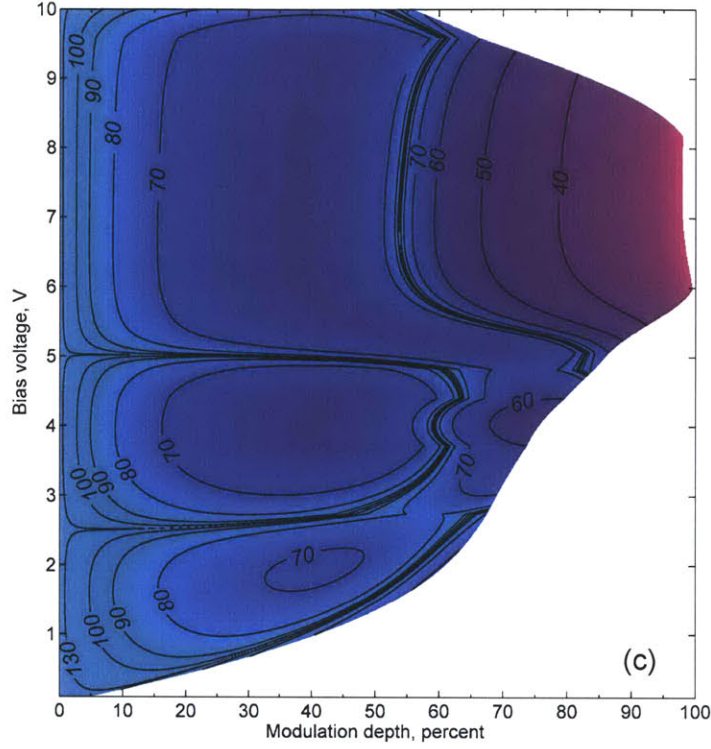


Figure 28. Third harmonic distortion, HD3, in dBc, as a function of the silicon diode bias voltage and modulation depth. At each bias voltage, the length of the silicon diode was optimized (shown in Fig. 27). Three criteria of length optimization have been used (see Table 4): (a) full cancellation of the cubic nonlinearity, (b) maximization of the modulation depth with HD3 below the -80 dBc level, (c) maximization of the modulation depth with HD3 below the -60 dBc level. The white areas in the plots correspond to modulation depths not achievable at given phase shifter length and bias voltage. For comparison, a plot of the HD3 in a conventional MZ modulator with ideal, linear phase shifters is shown in Fig. 29 (see also the curved labeled “HD3, conv. MZM” in Fig. 26). Note that the minus sign in front of the HD3 values has been omitted; in reality, the HD3 is, of course, negative.

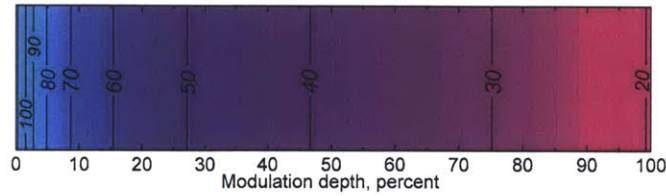


Figure 29. Third harmonic distortion, HD3, in dBc, present in a conventional MZ modulator with ideal linear (e.g. LiNbO<sub>3</sub>) phase shifters. The minus sign in front of the HD3 values has been omitted.

## 15. Optical bandwidth of the linearized silicon modulator

Until now, the optimization and analysis of the modulator linearity was performed for a single optical wavelength. However, in many applications, modulators must be able to operate over a wide wavelength range. For example, in an optical ADC, the optical bandwidth of the pulse train input to the modulator can be 20 nm or more. This chapter addresses the wavelength dependence of the modulator linearity.

In Chapter 13, it was established that the cubic nonlinearity of the modulator is fully cancelled when the length of its phase shifter sections satisfies Eq. (13.8). However, the optical phase shift depends on wavelength, which means that the optimum length also depends on wavelength. The cubic nonlinearity in a given modulator can be zero only at a single wavelength; it will increase as the wavelength differs from this wavelength. This is illustrated in Fig. 30, which shows the third harmonic distortion, HD3, as a function of wavelength for a modulator optimized at 1.55  $\mu\text{m}$ . The HD3 shown is the maximum HD3 over modulation depths ranging from 0 to 20% (rather just the HD3 at 20% depth). The bias voltage was 2 V and the length was 348  $\mu\text{m}$ . One can see that HD3 grows rather quickly with distance from 1.55  $\mu\text{m}$ : HD3 increases by about 10 dB just 3 nm away from 1.55  $\mu\text{m}$ . However, there is still bandwidth over which HD3 remains low. For example, HD3 remains below -100 dBc within a 9 nm bandwidth, and below -90 dB within a 29 nm bandwidth around 1.55  $\mu\text{m}$ , as indicated in Fig. 30. The bandwidth can therefore be plotted as a function of the HD3 level, as it is done in Fig. 31.



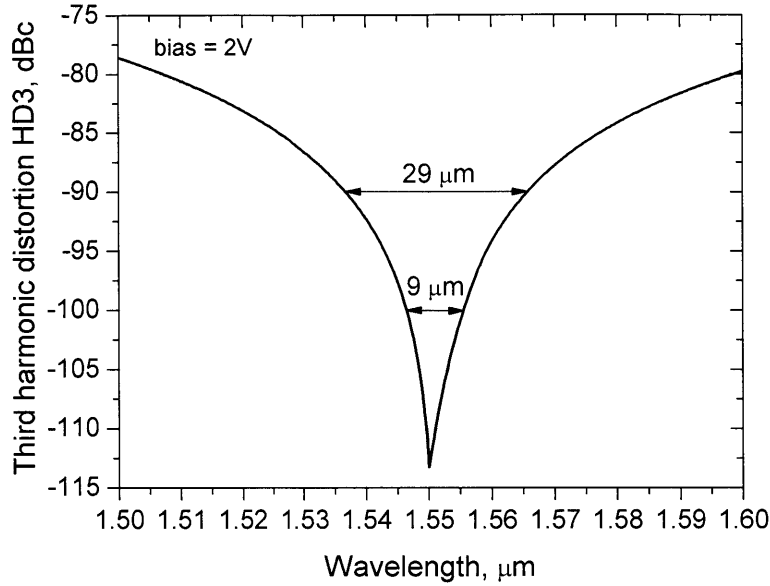


Figure 30. Maximum third harmonic distortion, HD3, with up to 20% modulation depth as a function of optical wavelength. The length was  $L = 348 \mu\text{m}$ , selected to minimize HD3 at  $1.55 \mu\text{m}$ . The bias voltage was 2 V. For comparison, HD3 in a modulator with ideally linear phase shifters at 20% modulation depth is -55 dBc.

Fig. 31 shows how much suppression of nonlinear distortions can be achieved over a given bandwidth. The Y-axis is the bandwidth over which the HD3 stays below the level shown along the X-axis. The curves correspond to different modulation depths. As in Fig. 30, the HD3 values here are the maximum HD3 seen over modulation depths ranging from zero to the given modulation depth. Plots (a)-(d) correspond to reverse biases of 2 V, 3 V, 4 V, and 5 V. The length was optimized independently at each bias voltage and modulation depth. Each curve was extracted from a plot similar to the one shown in Fig. 30; the 20% curve in Fig. 31(a) corresponds to the plot of Fig. 30. As expected, for wide optical bandwidth, the modulator cannot sustain the same high level of linearity it can for narrowband signals. Another observation is that the better the linearity is, the faster it deteriorates as the optical bandwidth increases. For example, among the four biases considered in Figs. 31(a)-(d), the 5 V bias enables the lowest HD3 at low optical bandwidths; however, the HD3 quickly increases with bandwidth and, at high bandwidth values, the HD3 levels are roughly the same for all four biases. Importantly, in all cases, the performance of the linearized modulator is superior to that of a conventional MZ modulator with ideal linear phase shifters (Fig. 31(e)), even for optical bandwidths as high as 100 nm.



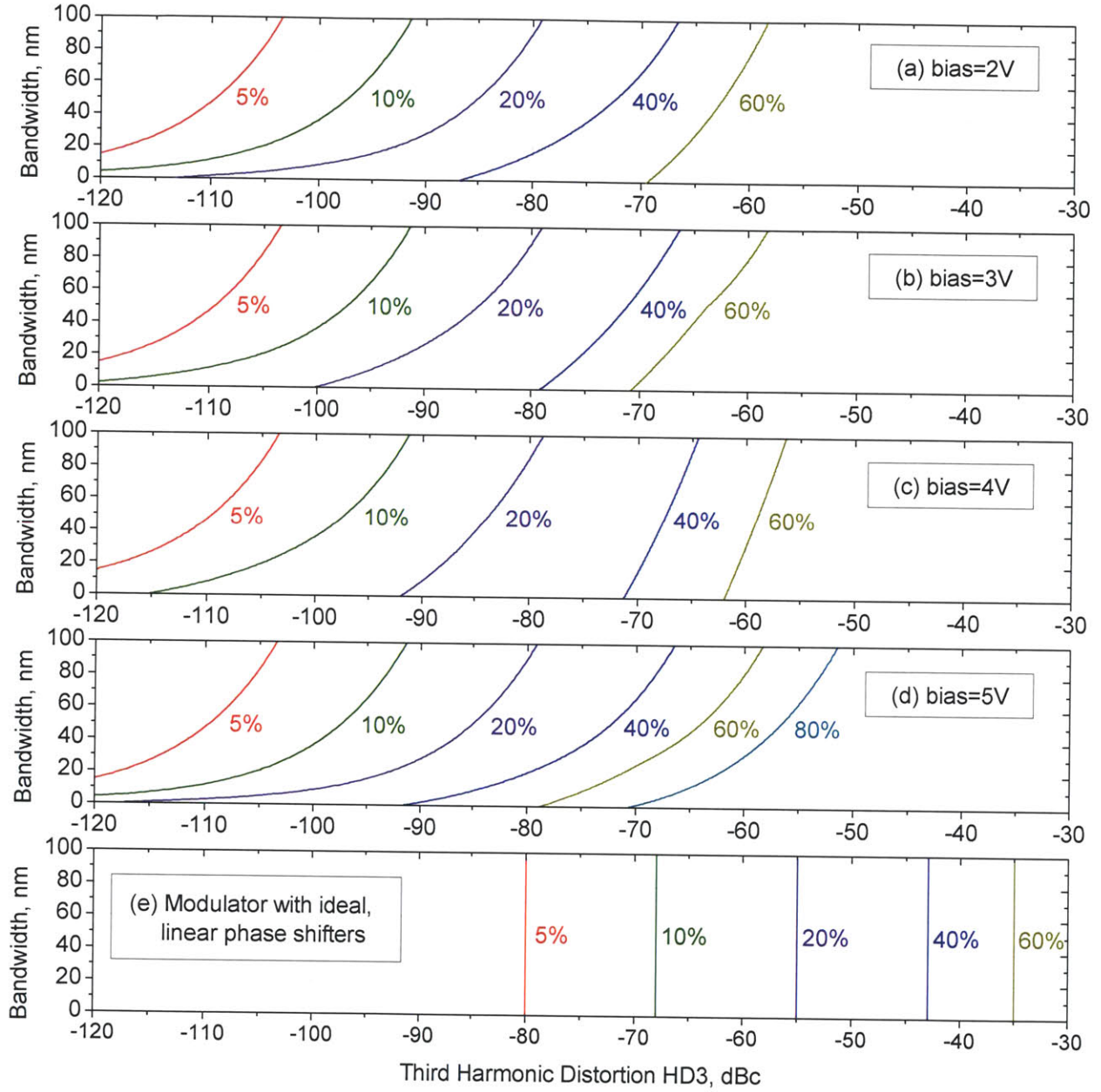


Figure 31. The optical bandwidth over which the third harmonic distortion, HD3, is below the level shown along the x-axis. For each curve, the modulation depth is fixed and is indicated next to the curve. The silicon diode is reverse biased at (a) 2 V, (b) 3 V, (c) 4 V, (d) 5 V. The length was optimized for each bias voltage and modulation depth to achieve the smallest HD3 at 1.55  $\mu\text{m}$  wavelength light. The length values, from the smallest to the largest modulation depths, were (a) 349, 349, 348, 344, 336, (b) 293, 294, 297, 305, 312, (c) 263, 265, 272, 291, 308, (d) 348, 348, 349, 351, 354, and 353 microns. For comparison, the HD3 in a modulator with ideal, linear phase shifters is plotted in (e).

Note that the analysis in this chapter assumes that the only source of wavelength dependence in a silicon MZ modulator is the wavelength dependence of the phase and loss in the silicon diode phase shifters. However, other parameters of the MZ structure can also be wavelength-dependent and, thus, can affect modulator linearity for wideband optical inputs. In particular, the coupling ratio of the directional couplers and the bias phase of the modulator can vary with wavelength. The impact of these variations was not considered because they are not fundamental to the proposed linearization method and will affect the performance of any MZ-based modulator.

## **16. Summary and discussion**

This part of the thesis describes a modulator linearization scheme based on cancellation between the phase shifter and the MZ transfer function nonlinearities. This concept is applicable to any modulator with nonlinear phase shifters, including the reverse-biased silicon diode phase shifters studied in this work. The silicon phase shifters are intrinsically nonlinear, with both phase and loss dependent on the applied voltage in a nonlinear way. That nonlinearity allows overall linear operation to be achieved in the MZ structure at reasonable device operating voltages and lengths. The linearized modulator yields superior linearity to a conventional MZ modulator with ideal linear phase shifters, as illustrated by Figs. 26, 28, 29, and 31. For example, if the third harmonic distortion HD3 needs to be below -80 dBc, a conventional MZ modulator is limited to 5% modulation depth, while the linearized silicon modulator considered in this work enables 30% modulation at a 4 V bias voltage and 57% modulation at a 5 V bias voltage. The linearity of the modulator depends on the optical wavelength, i.e. a modulator optimized for one wavelength will not perform equally well at other wavelengths. In the above example, if the HD3 is additionally required to be below -80 dBc over 100 nm of optical bandwidth, the modulation depth in the linearized modulator is reduced to about 20% at both bias voltages, which is still higher than in the conventional MZ case.

As mentioned in the Introduction, the proposed linearization method resembles the pre-distortion linearization in the sense that the nonlinearity of the phase shifters is conceptually similar to the nonlinearity introduced with a pre-distorter circuit. Unlike pre-distortion linearization methods, the proposed scheme does not require the modulator to work at harmonics

of the applied RF signal, and, therefore, does not compromise the RF bandwidth of the modulator. However, operation at high RF frequencies may still be degraded by possible dynamic nonlinearity, i.e. the dependence of nonlinearity of the silicon phase shifter on the RF frequency. This work does not address the question about the presence and impact of this dynamic nonlinearity on the linearity of the modulator.

As with any linearization approach which relies on nonlinearity cancellation, an important question is the tolerance of the proposed approach to device parameter variations. Specifically, the diode parameters such as layer thicknesses, doping levels, and spatial doping profiles can vary from one fabrication run to another and from diode to diode in the same fabrication run, leading to variations in the nonlinearity in the phase shifters. Because the phase shifter nonlinearity also depends on an adjustable parameter – the diode bias voltage – some variations in phase shifter linearity can be compensated by simply adjusting this voltage. This is particularly true if both arms are still balanced. Fabrication variations can also lead to unbalanced arms, and while it is expected that the proximity of the two diodes on the chip will keep these variations low, the question about their impact on the modulator linearization remains open. Note that fabrication variations might be problematic if one's goal is to achieve the very high linearity associated with simultaneous suppression of the 3rd and 5th order nonlinear terms, which only happens at specific combinations of modulator parameters and bias voltage.

Note that the modulator linearity was studied by analyzing the harmonic distortions created when a single-frequency RF tone is applied to the modulator. A single-tone test was selected for simplicity; a two-tone test could be used instead and intermodulation distortions could be analyzed. The intermodulation distortion analysis would produce different absolute values of distortions, but it would not change the relationship between the distortions in a linearized and a conventional modulator. Therefore, all conclusions of this work would stay the same.

In this work, the modulator linearity is analyzed theoretically, using models and numerical simulations. However, the theory might be different from the experiment for a number of reasons. First, the parameters of a fabricated device might be different from the intended values. Second, some of the diode parameters used in the models might not be very well known; for example, the exact doping profiles. Third, although the authors used rigorous models to find the carrier distributions at given voltages, these models are still approximate: they assume there are no defects in the silicon, that the contacts are perfectly ohmic, use standard, empirical models for

physical parameters like temperature and carrier concentration effects on the bandgap and on index of refraction and loss, etc. For these reasons, differences between the real nonlinearity of the fabricated device and the nonlinearity predicted by the model are unavoidable. Therefore, to make a linearized modulator in a given fabrication process, one needs to establish the nonlinearity of the silicon phase shifters experimentally. The simulation results, such as the results presented in this work, should be viewed as a guide to the performance expected of a properly linearized silicon modulator and an estimation of the parameters necessary for linearization.

An important application of the proposed linearized modulator is photonic analog-to-digital conversion studied in this thesis. In a photonic ADC, modulator nonlinearity directly translates into spurious harmonics and performance degradation; for given distortion level, the linearized modulator makes it possible to use higher modulation depths. High modulation depth is very important for improving energy efficiency of the system, because, for the given energy, SNR is proportional to the modulation depth squared (see Chapter 5). High modulation depth is also important for reducing the impact of nonlinearity, in the sense that higher number of SFDR bits can be achieved in a system with stronger modulation (see Chapter 19). In a system with a conventional MZ modulator large modulation depths result in increased nonlinearity. It is true that this nonlinearity can be inverted at post-processing step, but this is not an ideal solution because this nonlinearity can be significant and its post-compensation might be imperfect. Moreover, noise enhancement and SNR reduction occurs when the sinusoidal transfer function of the modulator is inverted. As shown by Juodawlkis et al. [24], this establishes the optimum modulation depth at about 60%. Stronger modulation an ADC with nonlinearity post-compensation decreases SNR instead of improving it. The proposed linearized modulator does not suffer from either of these problems (or, at least, these problems onset at much higher modulation depths), and therefore is expected to be very important for photonic ADC applications.

## IV. Silicon nonlinearities in photonic ADCs

Optical radiation at telecom wavelengths ( $\sim 1550\text{nm}$ ) and below, propagating in silicon waveguides, experiences two-photon absorption (TPA), when two photons combine to overcome the bandgap of silicon. An instance of TPA generates an electron-hole pair. The free electrons and holes generated by TPA act as absorption centers, the phenomenon called free carrier absorption (FCA). Free electrons and holes also change the refractive index of the material, the phenomenon called free carrier dispersion (FCD) effect. In an integrated photonic ADC built using silicon technology, all nonlinear phenomena mentioned above occur, leading to nonlinear distortions and possibly deterioration of SFDR. The impact of nonlinearities becomes very important when high values of ENOB are to be achieved, which requires high optical power for high SNR and increases the nonlinearities. This section analyzes the magnitude of these nonlinear effects, studies their impact on ADC performance, as proposes some ways to mitigate their impact.

### 17. Two-photon and free-carrier effects in strongly confining waveguides

Modeling of nonlinear phenomena of two-photon absorption and accompanying free-carrier absorption for plane waves propagating in bulk silicon is relatively straightforward. However, in silicon photonic, optical fields are strongly confined inside waveguides and are very different from plane waves, their vectorial structure is essential, and all three field components contribute to nonlinearity. This necessitates changes to the plane-wave-based equations, which can be accomplished by introducing the effective areas of TPA and FCA phenomena, as described in this chapter.

#### 1. Plane-wave equations

For a plane wave of intensity  $I$  propagating in bulk silicon, the nonlinear effect of two-photon absorption is described by

$$\frac{dI}{dz} = -\beta_{TPA} I^2 = -\alpha_{TPA} I, \quad (17.1)$$

where the two-photon-induced loss coefficient  $\alpha_{TPA}$  is

$$\alpha_{TPA} = \beta_{TPA} \cdot I, \quad (17.2)$$

and  $\beta_{TPA}$  is the two-photon absorption coefficient. There is certain discrepancy in the values of  $\beta_{TPA}$  of silicon reported in the literature, as summarized in Table 4-1 of [110]. In different experiments, the measured values were within the range from 0.44 to 0.9 cm/GW. In this work,  $\beta_{TPA} = 0.68$  cm/GW was used, as reported in [110, 111] on the basis of heterodyne pump-probe measurements.

Two-photon absorption generates free carriers according to

$$\frac{dN}{dt} = -\frac{N}{\tau} + \frac{\alpha_{TPA} I}{2hf}, \quad (17.3)$$

where  $N$  is the concentration of electron-hole pairs (units of  $m^{-3}$ ),  $f$  is the optical frequency,  $h$  is Planck constant, and  $\tau$  is free carrier relaxation time. The relaxation time depends on processing conditions and can vary within significant range. Typical values are on the order of 1 ns;  $\tau = 500$  ps [110, 111] was used in this work. Typical relaxation times are much longer than the pulse durations typical for photonic ADCs. Therefore, the exact value of relaxation time is not important for the case of photonic ADC, as long as the carriers mostly relax by the arrival of the next optical pulse arrives. Note that this situation is very different for data communication applications, when the amount of nonlinear loss is directly proportional to the carrier lifetime.

Free-carrier absorption (FCA) and free-carrier dispersion (FCD) due to free electrons and holes are usually described by fitting the data reported by Soref in [107]. In the simplest case, the dependencies of FCA and FCD on carrier concentration are assumed to be linear; however, better matching to Soref's data around 1550 nm wavelength can be obtained with nonlinear equations, such as [48, 112]:

$$\Delta n = -8.8 \cdot 10^{-22} (\Delta N_e) - 8.5 \cdot 10^{-18} (\Delta N_h)^{0.8}, \quad (17.4)$$

$$\Delta \alpha = 9.1 \cdot 10^{-22} (\Delta N_e)^{1.22} + 2.5 \cdot 10^{-20} (\Delta N_h)^{1.13}. \quad (17.5)$$



In these equations,  $\Delta n$  is the change of the refractive index due to FCD,  $\Delta\alpha$  is the change of the absorption coefficient (units of 1/m) due to FCA, and  $\Delta N_e$  and  $\Delta N_h$  are the concentration of free electrons and holes (units of  $m^{-3}$ ). For free electrons and holes generated by TPA,  $\Delta N_e = \Delta N_h \equiv N$ , where  $N$  is given by (17.3). Note that the above equations is just one variant of the dependencies used in the literature, which gives a better fit to the Soref's plots (see the relevant discussion in [112]). Usually the exact functional dependence of (17.4)-(17.5) is not very important as long as they produce  $\Delta n$  and  $\Delta\alpha$  which are roughly accurate (within 10% or so). However, the exact functional dependence of (17.4)-(17.5) becomes critical for analysis of nonlinear distortions in an analog system, such as the photonic ADC system. Unfortunately, no direct measurements have been performed to confirm that the exponents of these formulas are correct and the nonlinearity they predict is accurate. However, (17.4)-(17.5) are the best formulas available at the moment, and therefore they have been used in the present work.

## 2. Strongly-confining waveguides: effective TPA area

While the equations (17.1)-(17.5) given above fully describe TPA and free-carrier effects for a plane wave in bulk silicon, they cannot be used for strongly-confining silicon waveguides. For example, Eq. (17.2) can no longer be used, because for a non-plane-wave field, the TPA is proportional not to the intensity, but to the magnitude of electric field squared,  $|E(x,y)|^2$ , which includes all transversal and longitudinal field components. Another difference from the plane-wave case is that the electric field vector varies across the cross-section of the mode. To describe this phenomena, an effective TPA area  $A_{TPA}$  can be introduced by transforming the plane-wave TPA loss coefficient (17.2) into

$$\alpha_{TPA} = \beta_{TPA} \cdot \frac{P}{A_{TPA}}, \quad (17.6)$$

where  $P$  is the optical power in the waveguide.

A number of different expressions has been used for  $A_{TPA}$  in recent journal articles, five of which are compared in Table 5 [110]. The first two formulas are applicable to weakly confining waveguides only; the last two has been derived specifically for strongly-confining waveguides. The results given by formulas of Table 5 has been compared for two test cases: (i) a  $475 \times 106$  nm

silicon waveguide, which is an example of strongly-confining single-mode waveguide, and (ii) a  $1000 \times 800$  nm waveguide, which has a large mode area and is close to a weakly confining waveguide. The results, shown in Table 5, indicate that while different formula converge to the same result for a weakly-confining waveguide case, as expected. However, the results for strongly-confining waveguides are very different.

To establish which of the formulas of Table 5 gives the best result, a vectorial mode solver [108] has been used to calculate the effective TPA area by solving the mode equation numerically with no physical approximations. To accomplish this, the mode field was first found for a silicon waveguide without nonlinearities. Then, an imaginary part has been introduced to the electrical permittivity, calculated as the electrical susceptibility (found from the plane-wave  $\beta_{TPA}$ ) multiplied by  $|\vec{E}(x, y)|^2$ , where  $\vec{E}(x, y)$  is the electric field vector of the waveguide mode. The cross-section distribution of the electrical permittivity, together with the real and imaginary part introduced to it, was substituted into the mode solver, which calculated the loss coefficient  $\alpha_{TPA}$  by solving the eigenmode equation numerically. The effective area  $A_{TPA}$  was then found from equation (17.6). The obtained values of  $A_{TPA}$  are listed in the last row of Table 5.

From Table 5, one can see that the formula which gives the best agreement with the numerical result is the one given by Koos et al. [113] (a small disagreement which exists can be attributed to the numerical error due to finite step size of the finite difference mode solver),

$$A_{TPA} = \frac{Z_0^2}{n_{inter}^2} \frac{\left[ \int_{-\infty}^{\infty} (\vec{E} \times \vec{H}) \cdot \vec{e}_z dx dy \right]^2}{\int_{core} |\vec{E}|^4 dx dy}. \quad (17.7)$$

In this formula,  $\vec{E}$  and  $\vec{H}$  are the electric and magnetic fields,  $\vec{e}_z$  is the unit vector along the propagation direction,  $x$  and  $y$  are the coordinates in the waveguide cross-section,  $Z_0$  is the characteristic impedance of vacuum, and  $n_{inter}$  is the refractive index of the waveguide core where the nonlinear interactions occur; for silicon waveguides,  $n_{inter}$  this is the refractive index of silicon. The integration in the denominator is limited to the waveguide core. This formula has been used to calculate  $A_{TPA}$  in this work.

**Table 5.** Different methods of calculation of the effective TPA area  $A_{TPA}$  and the results they produce for two test cases [110]. For strong confinement (test case 1, 475×106 nm core), different methods give quite different results; the methods converge to the same result only when the mode is weakly confined (test case 2, 1000×800 nm core). The formula by Koos et al. was found to be most accurate and was used in this work. The refractive indices were 3.476 for silicon, 1.385 for the overcladding, and 1.455 for SiO<sub>2</sub> undercladding; the optical wavelength was 1550 nm. The fundamental TE-polarized mode was considered.

Description of method and of its source	Formula	Test case 1: 475×106 nm core	Test case 2: 1000×800 nm core
Formula for weakly confining waveguides [114]	$\frac{\left[ \int_{-\infty}^{\infty}  E ^2 dx dy \right]^2}{\int_{-\infty}^{\infty}  E ^4 dx dy}$	0.275 $\mu\text{m}^2$	0.474 $\mu\text{m}^2$
Formula for weakly confining waveguides, integration over nonlinear core only [115]	$\frac{\left[ \int_{-\infty}^{\infty}  E ^2 dx dy \right]^2}{\int_{\text{core}}  E ^4 dx dy}$	0.530 $\mu\text{m}^2$	0.475 $\mu\text{m}^2$
Formula used in [116]	$\frac{\left[ \int_{-\infty}^{\infty} (E \times H) \cdot e_z dx dy \right]^2}{\int_{\text{core}} [(E \times H) \cdot e_z]^2 dx dy}$	0.228 $\mu\text{m}^2$	0.437 $\mu\text{m}^2$
Formula for strongly confining waveguides by Afshar et al. [117]	$\frac{Z_0^2}{n_{\text{inter}}^2} \frac{3 \left[ \int_{-\infty}^{\infty} (E \times H) \cdot e_z dx dy \right]^2}{\int_{\text{core}} [2 E ^4 +  E^2 ^2] dx dy}$	0.113 $\mu\text{m}^2$	0.429 $\mu\text{m}^2$
Formula for strongly confining waveguides by Koos et al. [113]	$\frac{Z_0^2}{n_{\text{inter}}^2} \frac{\left[ \int_{-\infty}^{\infty} (E \times H) \cdot e_z dx dy \right]^2}{\int_{\text{core}}  E ^4 dx dy}$	0.096 $\mu\text{m}^2$	0.420 $\mu\text{m}^2$
Numerical computation with a vectorial mode solver		0.097 $\mu\text{m}^2$	0.420 $\mu\text{m}^2$

Note that the choice of the right formula for  $A_{TPA}$  is quite important, since using a wrong formula can lead to significant errors. For example, the first two formulas of Table 5 lead to underestimation of TPA effect by a factor of 3 or more. This happens not because there is some problem with these formulas, but because these formulas were derived for weakly confining structures and were never intended to be used for strongly confined modes. Table 5 illustrates that the hope that the formulas for weakly confined modes would produce acceptable results even for strongly confined modes is unreasonable, and special formulas for strongly confined waveguides must be used.

### 3. Strongly-confining waveguides: effective FCA area

The formulas (17.3)-(17.5) describing free carrier effects also need to be reformulated for the case of strongly confined modes, which can be done by introducing the effective FCA area  $A_{FCA}$ . Calculation of  $A_{FCA}$  proceeds in several steps.

The *first step* is to assume that the free-carrier induced absorption across the core is proportional to the free carrier concentration. This is an approximation because in reality equations (17.4)-(17.5) are nonlinear and the nonlinearities are different for the electrons and holes. This means that, strictly speaking, the efficiency of free carrier effects (as described by effective FCA area later) must be a function of carrier concentration and must be different for electrons and holes. However, the nonlinearity of equations (17.4)-(17.5) is relatively weak, so it is reasonable to assume that the dependencies are linear within the nonlinear waveguide core,

$$\Delta n(x, y) = -\sigma_n N(x, y), \quad (17.8)$$

$$\Delta \alpha(x, y) = \sigma N(x, y). \quad (17.9)$$

In these equations,  $\sigma$  is the absorption cross-section which defines the absorption change,  $\sigma_n$  is its counterpart describing the refractive index change, and  $N(x, y)$  is the concentration of electron-hole pairs. Note that although  $\sigma$  and  $\sigma_n$  are assumed to be constants within the waveguide core, it is not acceptable to assume that they are independent on carrier concentration, because this would ignore the nonlinearity of the original equations (17.4)-(17.5), which is not acceptable for analysis of harmonic distortions in the ADC system. To account for nonlinearity

of (17.4)-(17.5), it was assumed that the coefficients  $\sigma$  and  $\sigma_n$  change with the carrier concentration  $N$  averaged over the core,  $\bar{N}$ . From (17.4)-(17.5) and (17.8)-(17.9),

$$\sigma_n = -8.8 \cdot 10^{-22} - 8.5 \cdot 10^{-18} \bar{N}^{-0.2}, \quad (17.10)$$

$$\sigma = 9.1 \cdot 10^{-22} \bar{N}^{0.22} + 2.5 \cdot 10^{-20} \bar{N}^{0.13}. \quad (17.11)$$

The *second step* describes how to find the carrier concentration averaged over the core. In case of the waveguide propagation, the differential equation (17.3) can be rewritten as

$$\frac{dN_L}{dt} = -\frac{N_L}{\tau} + \frac{\alpha_{TPA} P}{2hf}, \quad (17.12)$$

where  $N_L$  is the density of electron-hole pairs per unit length of the waveguide. The average carrier density in the core is

$$\bar{N} = N_L / A_{geom}, \quad (17.13)$$

where  $A_{geom}$  is the geometrical area of the waveguide core.

The *third step* is to introduce the effective FCA area as follows. For the plane-wave case, the absorption coefficient and refractive index change due to free carriers, with linear approximation (17.8)-(17.9), can be written as

$$\Delta n = -\sigma_n \frac{\alpha_{TPA}}{2hf} I \Delta t, \quad (17.14)$$

$$\alpha_{FCA} = \sigma \frac{\alpha_{TPA}}{2hf} I \Delta t, \quad (17.15)$$

where, for the moment, it has been assumed that constant intensity  $I$  is turned on for some short time  $\Delta t$ , so that the density of TPA-generated carriers, according to (17.3), is  $\frac{\alpha_{TPA} I \Delta t}{2hf}$ . For a

non-constant intensity, the carrier density must be found by integrating the differential equation (17.3) over time. For a waveguide mode, equations (17.14) and (17.15) can be rewritten by replacing the plane-wave intensity  $I$  with the “effective intensity”  $P / A_{FCA}$ ,

$$\Delta n = -\sigma_n \frac{\alpha_{TPA}}{2hf} \frac{P}{A_{FCA}} \Delta t, \quad (17.16)$$

$$\alpha_{FCA} = \sigma \frac{\alpha_{TPA}}{2hf} \frac{P}{A_{FCA}} \Delta t. \quad (17.17)$$

These equations define the effective FCA area  $A_{FCA}$ . The factor  $\frac{\alpha_{TPA} P \Delta t}{2hf}$  can be recognized as  $N_L$ , the carrier density per unit length (as already mentioned, in case of time-dependent power, it needs to be found by integrating (17.12)).

Finally, the *fourth step* is to find the effective FCA area using the vectorial mode solver. The mode solver can be used to find  $\Delta n$  and  $\alpha_{FCA}$  numerically, given the distribution of refractive index change or FCA absorption coefficient across the nonlinear core of the waveguide for given  $P\Delta t$ . The effective area  $A_{FCA}$  can then be found from (17.16) or (17.17). To accomplish this, it is necessary to establish the distribution of free carriers across the nonlinear core. The carriers are initially generated according to the profile of electric field in the core. The generated carriers can then redistribute across the core by means of thermal diffusion. One can distinguish two limiting cases: (i) the case when the carriers had sufficient time to distribute so that their concentration is uniform across the waveguide core, and (ii) the case when the time scale of interest is too short for carriers to redistribute across the core so that their initial distribution is preserved. In the first case, the free-carrier-induced index and absorption change are uniform across the core, and expressions for  $A_{FCA}$  can be readily found in the literature (see, for example, ref. [118]). However, the time scales of interest for photonic ADCs are closer to case (ii). For example, within a typical pulse duration of 20 ps, the electrons diffuse by about  $\sqrt{36 \text{ cm}^2/\text{s} \cdot 20 \cdot 10^{-12} \text{ s}} \approx 270 \text{ nm}$ , and holes by about  $\sqrt{12 \text{ cm}^2/\text{s} \cdot 20 \cdot 10^{-12} \text{ s}} \approx 156 \text{ nm}$  [119]. Although these lengths are not negligible compared to the core dimensions, they indicate that the case (ii) is closer to the photonic ADC situation than the case (iii). Therefore, this work makes an approximation that case (ii) takes place, i.e. no redistribution of carriers occurs within the pulse duration.

With no carrier redistribution across the core, the carrier profile follows the  $|\vec{E}(x, y)|^4$  function, where  $\vec{E}(x, y)$  is the electric field of the waveguide mode. The reason for this is that the TPA absorption coefficient is proportional to  $|\vec{E}(x, y)|^2$ , and the number of photon absorbed



is proportional to the absorption coefficient times  $|\vec{E}(x,y)|^2$ , which gives the  $|\vec{E}(x,y)|^4$  dependence. With such a carrier profile, no expressions for effective FCA area could be found in the literature, and therefore  $A_{FCA}$  was calculated numerically.

With the above in mind, the distributions of refractive index change  $\Delta n(x,y)$  and absorption  $\alpha_{FCA}(x,y)$  due to TPA-generated free carriers are given by

$$\Delta n(x,y) = -\sigma_n \frac{\alpha_{TPA} P \Delta t}{2hf} \cdot e(x,y), \quad (17.18)$$

$$\alpha_{FCA}(x,y) = \sigma \frac{\alpha_{TPA} P \Delta t}{2hf} \cdot e(x,y), \quad (17.19)$$

where  $\frac{\alpha_{TPA} P \Delta t}{2hf}$  is  $N_L$ , the density of carriers generated by TPA per unit length, and

$$e(x,y) \equiv \frac{|\vec{E}(x,y)|^4}{\int_{core} |\vec{E}(x,y)|^4 dx dy}$$

is the normalized free carrier cross-sectional distribution, with  $\int_{core} e(x,y) dx dy = 1$ . The refractive index change and absorption given by (17.18), (17.19) can be substituted into the mode solver, the  $\Delta n$  and  $\alpha_{FCA}$  of the mode can be calculated, and  $A_{FCA}$  can then be expressed from (17.16) or (17.17) (either of them can be used – the result should be the same). For example, for the test case 1 of Table 5 (475×106 nm core),  $A_{FCA}$  was found to be 0.074  $\mu\text{m}^2$ .

To sum up this chapter, the TPA and FCA phenomena in strongly-confined waveguides for optical pulses are described in the following way. The TPA absorption coefficient  $\alpha_{TPA}(t)$  is calculated with (17.6) where  $A_{TPA}$  is found with (17.7). The carrier density per unit length  $N_L(t)$  is determined by integrating the differential equation (17.12). The change in the refractive index  $\Delta n(t)$  and absorption coefficient  $\alpha_{FCA}(t)$  due to TPA-generated free carriers are given by (17.16) and (17.17). The unknown coefficients in these equations are  $\sigma(t)$ ,  $\sigma_n(t)$ , and  $A_{FCA}$ . The values of  $\sigma(t)$  and  $\sigma_n(t)$  are found from (17.10), (17.11), where the carrier density

averaged over core area  $\bar{N}(t)$  is (17.13). The effective FCA area  $A_{FCA}$  is found by substituting  $\Delta n(x, y)$  or  $\alpha_{FCA}(x, y)$  into the mode solver to determine the mode's  $\Delta n$  or  $\alpha_{FCA}$ , which are compared to (17.16) or (17.17) to determine  $A_{FCA}$ . Note that in the latest operation the values of  $P\Delta t$ ,  $\sigma$ , and  $\sigma_n$  should cancel out so that  $A_{FCA}$  is independent on them. This method of  $A_{FCA}$  calculation implies the approximation that the free-carrier induced absorption and index change are linearly proportional to the free carrier concentration within the mode cross-section. This is a good approximation because the carrier concentration is not changing dramatically across the core. The nonlinearity of index change and absorption coefficients are taken into account by adjusting  $\sigma(t)$  and  $\sigma_n(t)$  according to (17.10), (17.11), where the carrier density averaged over core area  $\bar{N}(t)$  is given by (17.13); note that this makes  $\sigma(t)$  and  $\sigma_n(t)$  functions of time.

Using the method of modeling the effects of TPA, FCA, and FCD in strongly confining waveguides, it is now possible to evaluate the impact of these effects on ADC performance.

## 18. Nonlinearity of microring filters in photonic ADCs

This chapter considers pulse propagation in a photonic ADC system and calculated how much of the pulse energy is lost due to nonlinear effects. These results will be used in the next chapter to evaluate the impact of nonlinearities on performance of the photonic ADC system.

### 1. Silicon nonlinearities in different parts of the photonic ADC

In terms of nonlinear effects, the bottleneck of the photonic ADC system under consideration lies in the microring resonator filters due to their internal power enhancement. This can be explained by comparing nonlinearities in the following parts of the path of optical pulses: (i) the path from the output of the pulse interleaver (or the output of the chirp element, in case of a system with continuous time-to-wavelength mapping) to the output of the modulator, (ii) the path from the output of the modulator to the input of the microring filters, and (iii) the path from the input to the output of the microring resonator filters.

In part (i), optical energy of all ADC channels is carried along a single waveguide, and nonlinearities in this part can definitely be non-negligible. However, it is necessary to note that

the pulses in part (i) are already much longer than the pulses at the output of the mode-locked laser, which is true both in case of continuous and discrete time-to-wavelength mapping; this means that peak powers in part (i) are already reduced. Moreover, the pulses in part (i) are unmodulated, and their energies are independent on the signal to be digitized. Therefore, nonlinearities in part (i) cannot introduce nonlinear distortions and decrease the SFDR, which is the reason why they are not considered in this work.

In part (ii), the energies of the pulses are reduced due to losses in the modulator, as well as due to the fact that the energy is now split between the two modulator outputs. However, the pulses are now modulated, which means that nonlinearities in part (ii) can distort the ADC output. Two-photon absorption in part (ii) is significantly smaller than in the microrings because the peak power in the microrings is significantly enhanced. Accumulation of free carriers can present a problem, however. In part (iii), the microrings, the pulses are separated in time by laser's repetition period, so that free carriers have sufficient time to relax before arrival of the next pulse. This is not so for part (ii), where pulses are separated by intervals smaller by the number of channels (or with no interval at all in case of continuous time-to-wavelength mapping). This means that free carriers do not relax by the arrival of the next pulse, and the carrier concentration can build up to significant levels, leading to optical losses due to free carrier absorption (FCA). Still, this effect is not expected to be as significant as nonlinear power loss in the rings, for two reasons. First, the FCA effect is normally smaller than TPA and FCD-induced resonant frequency shifts of the rings, as shown later. Second, it can be estimated that the carrier densities generated in part (ii) are still smaller than those generated in the rings. Indeed, assume that a single, isolated optical pulse in part (ii) generated peak carrier density  $N$ . For an ADC with  $m$  channels, the peak density will be proportional to  $N \cdot m$ , because pulses from all channels will contribute to the carrier density. Inside the rings, the pulse power will be enhanced by approximately a factor of  $m$ , which means that the TPA loss coefficient will increase by a factor of  $m$  and the power lost due to TPA will increase by a factor of  $m^2$ , so that the carrier density will be proportional to  $N \cdot m^2$ . The peak carrier density inside the rings is therefore expected to be  $m$  times larger than the density in the waveguides in part (ii), and therefore FCA inside the rings is expected to be larger (unless long waveguide lengths are used in part (ii), something which needs to be avoided in a properly designed photonic ADC).

In part (iii) – the microring resonators – internal power enhancement leads to power levels larger than in parts (i) and (ii), which means that TPA effect is stronger inside the rings. As explained above, the free carrier absorption is also stronger. An additional effect which can be very important is the resonant frequency shift of the microring resonators. This frequency shift is dependent on the applied RF signal, leading to nonlinear distortions in the ADC. For these reasons, the microring resonators are the area of most concern with regards to nonlinear behavior. The nonlinear effects in the microrings are the subject of the analysis below.

## 2. Modeling nonlinear behavior of a microring resonators

The previous chapter described modeling of nonlinear effects in strongly confining waveguides for optical pulses, which will now be applied to study nonlinear behavior of microring filters made of strongly-confining waveguides.

To model the nonlinear effects inside a ring resonator, one needs to know time-dependent optical power inside the resonator,  $P_{\text{internal}}(t)$ , excited by a short optical pulse. This power can be expressed as

$$P_{\text{internal}}(t) = \frac{h(t) \cdot E_{\text{out}}}{C}. \quad (18.1)$$

In this equation,  $h(t)$  is the impulse response of the filter and  $E_{\text{out}}$  is the energy of the output optical pulse, so that

$$P_{\text{output}}(t) = h(t) \cdot E_{\text{out}}$$

is the output power. The impulse response, which can be found as the inverse Fourier transform of the transfer function of the filter, is normalized so that  $\int h(t) dt = 1$ . The coefficient  $C$  is the ring-bus power coupling coefficient of the microring resonator, and  $1/C$  is the power enhancement factor inside the resonator.

Strictly speaking, the assumption that the temporal profile of the pulse at the output of the ring resonator is given its impulse response is valid only when the filter is the only element which shapes the amplitude and phase of the otherwise flat optical spectrum. In reality, the optical spectrum is also shaped when the time-to-wavelength mapping is introduced. In case of discrete time-to-wavelength mapping, the optical spectrum is shaped by the demultiplexer and

the multiplexer, which leads to a temporal profile different from (18.1). However, the bandwidth of the filters in the demultiplexer and the multiplexer should be commensurate with the bandwidth of the ring filter, and although the temporal duration of the output pulse might be different from (18.1), this difference should be by a constant factor, and qualitative results of the analysis below will be preserved. For example, if the filters in the demultiplexer and the multiplexer have transfer functions identical to the transfer function of the microring filter under consideration, the output pulses will be about 60% longer. This will slightly reduce the nonlinearities in comparison to the predictions below, but the scaling of nonlinearities will remain the same (for example, it will still be true that reducing the filter bandwidth by 2 will increase the pulse duration by 2). Therefore, in order to be as general as possible and avoid assumptions about the transfer functions of the demultiplexer and the multiplexer in the pulse interleaver (which can be implemented in a way which is different from microring resonators), it is assumed that the transfer function of the microring resonators is the only thing which shapes the optical spectrum, and therefore (18.1) is valid. Note that in ADCs with continuous time-to-wavelength mapping, the pulse shape at the output also depends on the amount of dispersion broadening introduced to the signal. The analysis below is not always applicable to dispersion-broadened pulses because of different scaling of the pulse duration with filter bandwidth: the duration of dispersion-broadened pulses increases with filter bandwidth, the opposite to what happens for discrete time-to-wavelength mapping, when the pulses are shorter for wider filters. However, for narrow filters the amount of dispersion broadening is small, so that the pulse duration is defined mostly by the bandwidth of the filter and the following analysis is also applicable to the case of continuous time-to-wavelength scaling.

With the time-dependent power inside the rings given by (18.1), the nonlinearity calculations proceed as follows. The TPA loss per unit length  $\alpha_{TPA}(t)$  can be found from (17.6). This extra propagation loss inside the resonator results can be translated into the corresponding extra drop loss, also time-dependent,

$$drop_{TPA}(t) \approx \frac{2\pi R \alpha_{TPA}(t)}{2C}, \quad (18.2)$$

where  $R$  is the radius of the ring, and  $C$  is the ring-bus power coupling coefficient. This is an approximate equation valid for low losses, low coupling coefficients, and a single-ring filter. In

simulations described below, the drop loss was found not from (18.2), but from directly calculating the filter transmission function with the transfer matrix method. The pulse energy lost due to TPA can be found by integration over the pulse shape,

$$\Delta E_{TPA} = \int P_{output}(t) \cdot drop_{TPA}(t) dt . \quad (18.3)$$

The free carrier concentration inside the rings was found by integrating the differential equation (17.12) over time, with the power  $P(t)$  being the power inside the resonator, as defined by (18.1). The free carriers lead to refractive index change  $\Delta n(t)$  given by (17.16) and FCA propagation loss  $\alpha_{FCA}(t)$  given by (17.17). The energy loss due to free carrier-induced  $\alpha_{FCA}(t)$  is then calculated in the same way as the loss due to  $\alpha_{TPA}(t)$ ,

$$\Delta E_{FCA} = \int P_{output}(t) \cdot drop_{FCA}(t) dt . \quad (18.4)$$

The refractive index change induced by free carriers leads to the change of the resonant frequency of the microring filters. This causes misalignment of the filter passband with respect to the optical channel band, i.e. the frequency band occupied by the input optical signal, as illustrated in Fig. 32. This mismatch leads to optical power loss, which is something to be concerned about because this loss is signal-dependent and therefore cause nonlinear distortions in the ADC output. To study this effect qualitatively, the situation is considered when the optical channel frequency band is formed by a filter with transmission function identical to the transmission function of the ring filter under consideration, i.e. the shapes of the optical spectrum and the transmission function of the filter are identical, as shown in Fig. 32. The output power is maximized when the center frequencies of the two filters are aligned (Fig. 32(a)); the misalignment of center frequencies by  $\Delta f$  results in reduction of the output power (Fig. 32(b)).

The shift of the resonant frequency of a microring filter is related to the refractive index change  $\Delta n$  by

$$\Delta f = \frac{\Delta n}{n_g} f , \quad (18.5)$$

where  $n_g$  is the group index of the waveguide's mode and  $f$  is the resonant frequency [120]. It turns out that the corresponding loss coefficient  $\Delta drop_{FCD}$ , defined as the fraction of the power lost due to frequency mismatch, can be well approximated by a quadratic function



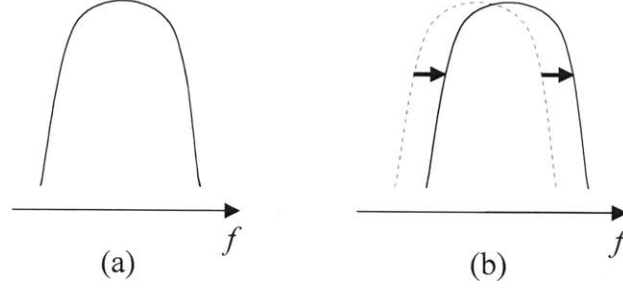


Figure 32. Illustration of misalignment of filter passband with respect to the optical channel band. Grey regions represent spectrum of the input optical channel, as formed by the pulse interleaver, and lines represent filter transmission spectrum before and after the misalignment. (a) the filter is perfectly aligned with the optical channel, (b) the filter is misaligned with respect to the optical channel, which results in increased power loss.

$$\Delta drop_{FCD} = \gamma \cdot \Delta f^2, \quad (18.6)$$

where  $\gamma$  is some constant defined by specifics of the filter transfer function. To find the energy lost due to this effect,  $\Delta n(t)$  is found as described above,  $\Delta f(t)$  is calculated according to (18.5), loss coefficient  $\Delta drop(t)$  is found from (18.6), and finally the energy loss is calculated similar to (18.3) and (18.4),

$$\Delta E_{FCD} = \int P_{output}(t) \cdot drop_{FCD}(t) dt. \quad (18.7)$$

It is necessary to note that strictly speaking, the description of the nonlinear behavior of microring resonators presented above is accurate only for slowly-varying fields. In the case of photonic ADC, the fields are not slowly varying, therefore the approach used in this work is an approximation. This approximation is useful because it provides an easy-to-use tool to estimate the magnitude of nonlinearities, understand their dependence on system parameters, analyze their impact, and to develop ways to reduce this impact.

### 3. Results: nonlinear loss in ring filters and its scaling with filter parameters

The nonlinear losses in microring resonator filters of a photonic ADC system can now be analyzed using the approach described above. To obtain quantitative results, it is necessary to

assume some values for the parameters of the filter bank, such as free-spectral range and filter bandwidth, as well as geometry of the silicon waveguide.

The geometry of the silicon waveguide selected for nonlinearity simulations of this work is shown in Fig. 33. The silicon core was 600 nm wide and 110 nm tall; a waveguide with such a wide core is good in terms of reduced sensitivity to width variations [121]. The group index of the mode was 3.3549. The linear propagation loss in the waveguide was assumed to be 3 dB/cm, a typical value for strongly-confining Si waveguides. The effective TPA and FCA areas for the fundamental TE mode of this waveguide at 1550 nm were found to be  $A_{TPA} = 0.0973 \mu m^2$  and  $A_{FCA} = 0.0711 \mu m^2$ . The effective areas will of course depend on the waveguide geometry, however, to limit the space of parameters being varied, the geometry had to be fixed. Besides, for practical waveguide geometries, the effective areas are not expected to be dramatically different from the ones used in this work. For example, for a waveguide with 450×250 nm core, the effective cross-section would be change to  $A_{TPA} = 0.0776 \mu m^2$  and  $A_{FCA} = 0.0784 \mu m^2$ .

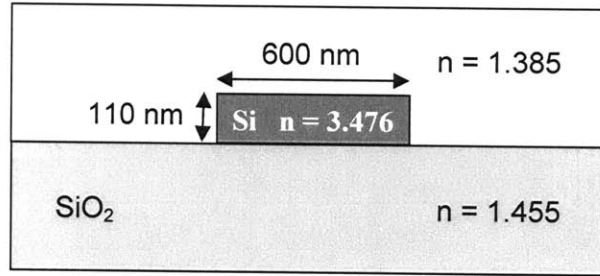


Figure 33. Cross-section of the silicon waveguide used in microring resonators considered in nonlinearity simulations of this chapter as well as Chapter 19. This wide and thin design is useful for improving tolerance to width variations [121]. The effective cross-sections at 1550 nm were found to be  $0.0973 \mu m^2$  for TPA and  $0.0711 \mu m^2$  for FCA.

The microring resonator filters in the nonlinearity analysis were assumed to be two-ring filters. The two ring design is optimum in the sense that it provides fast enough roll-off, as necessary for high extinction of the next channel, which is something a single-ring design can achieve only if the channel frequency spacing is large. At the same time, two-ring filters are more tolerant to errors and are easier to align than filters with more than two rings. This was the reason two-ring filter design was selected. The design of the filter was carried out according to ref. [122]. In all cases considered below, the passband shape was Chebyshev, with parameter  $\varepsilon$

controlling the passband ripple set to 0.1. The resulting ripple, suppressed due to 3 dB/cm loss in the rings, was less than 0.1 dB.

The plots of energy losses due to nonlinearities in microring resonators as a function of pulse energy are shown in Fig. 34. The filter was assumed to have FSR of 2 THz and 3 dB bandwidth of 25 GHz. The two-photon absorption coefficient of  $\beta_{TPA} = 0.68 \text{ cm/GW}$  [111] was used in these and all the following simulations. To produce the plot of nonlinear losses due to free carrier dispersion (FCD), the shift of resonant frequency was calculated as described in the previous chapter. The frequency shift was time dependent; to give an idea about its magnitude, its peak value is shown in Fig. 35 as a function of pulse energy.

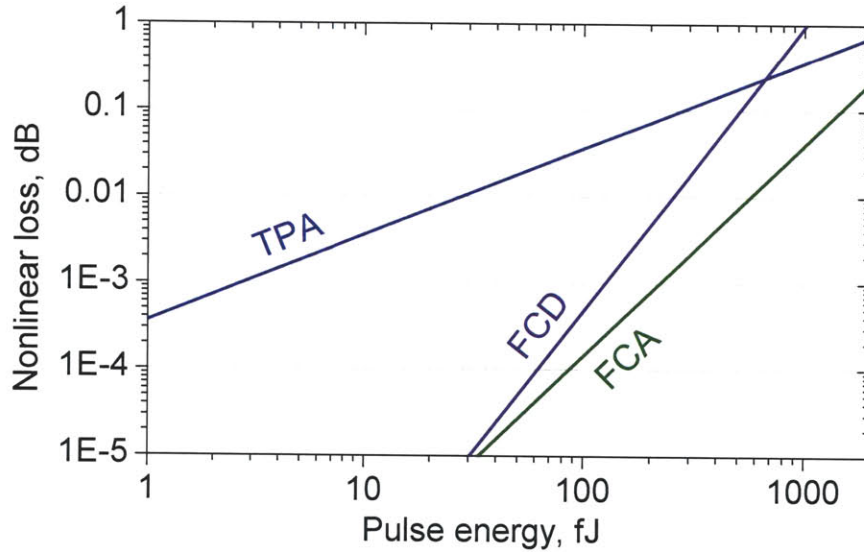


Figure 34. Nonlinear loss due to two-photon absorption (TPA), free-carrier absorption (FCA), and free-carrier dispersion (FCD) in a two-ring resonator. In case of FCD, the loss occurs because the passband of the filter shifts away from the frequency band of the channel, which was assumed to be formed by a filter with the transmission function which is identical to the one being studied. The peak value of the time-dependent frequency shift corresponding to the “FCD” line of this plot is presented in Fig. 35. The filter under consideration has 25 GHz bandwidth and 2 THz FSR, sufficient for implementing an ADC with about 25 wavelength channels.

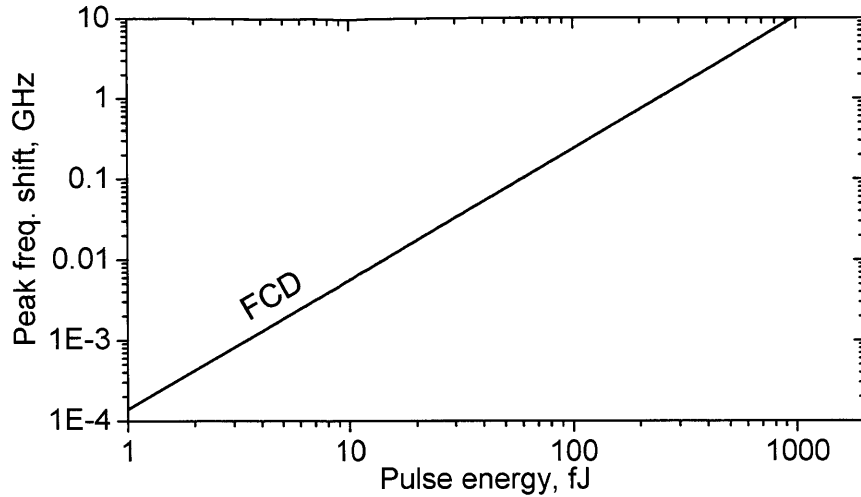


Figure 35. Peak value of the time-dependent frequency shift of the resonant frequency of a microring filter as a function of pulse energy. The filter design is the same as in Fig. 34, with 25 GHz bandwidth and 2 THz FSR.

The nonlinear losses plotted in Fig. 34 indicate that main source of nonlinearity at low pulse energies is TPA. As pulse energies increase, FCA and FCD rapidly go up and overtake TPA for energies above 0.7 pJ. The slope of the TPA loss curve is 1, as expected from Eq. (17.6). The number of free carriers generated by TPA is proportional to the power squared (see (17.12)), which means that the slope of the FCA loss curve would be 2 if the FCA absorption coefficient were linearly proportional to the number of carriers. However, in reality the dependence is nonlinear (see (17.5)), which makes the slope of the FCA loss curve higher than 2. The slope of the FCD loss curve would be 4 if the refractive index change were linearly related to the carrier concentration: the slope of 2 comes from the dependence of the number of carriers on optical power, plus the slope of 2 comes from the dependence of power loss on frequency misalignment (see (18.6)). In reality, the slope of FCD loss is lower than 4 because of nonlinearity of (17.4).

An important question is how the nonlinear losses scale with the ring filter parameters. The plots of nonlinear loss versus pulse energy are shown in Fig. 36 for several values of filter bandwidth. As explained below, the nonlinear losses in a ring filter depend not on the FSR or the bandwidth individually, but on the ratio of the two. The FSR-to-bandwidth ratio is usually called the “finesse” of the resonator. The finesse is shown as the curve parameter in Fig. 36; for example, the case considered above with 25 GHz bandwidth and 2 THz FSR corresponds to the

line labeled “80”. Note that the plots are separated into two parts, (a) TPA and FCA, and (b) TPA and FCD; the sole purpose of this separation was to avoid confusing intersections of multiple lines on a single plot. An important conclusion from the results of Fig. 36 is that nonlinearities increase with resonator finesse, i.e. a system with more wavelength channels is

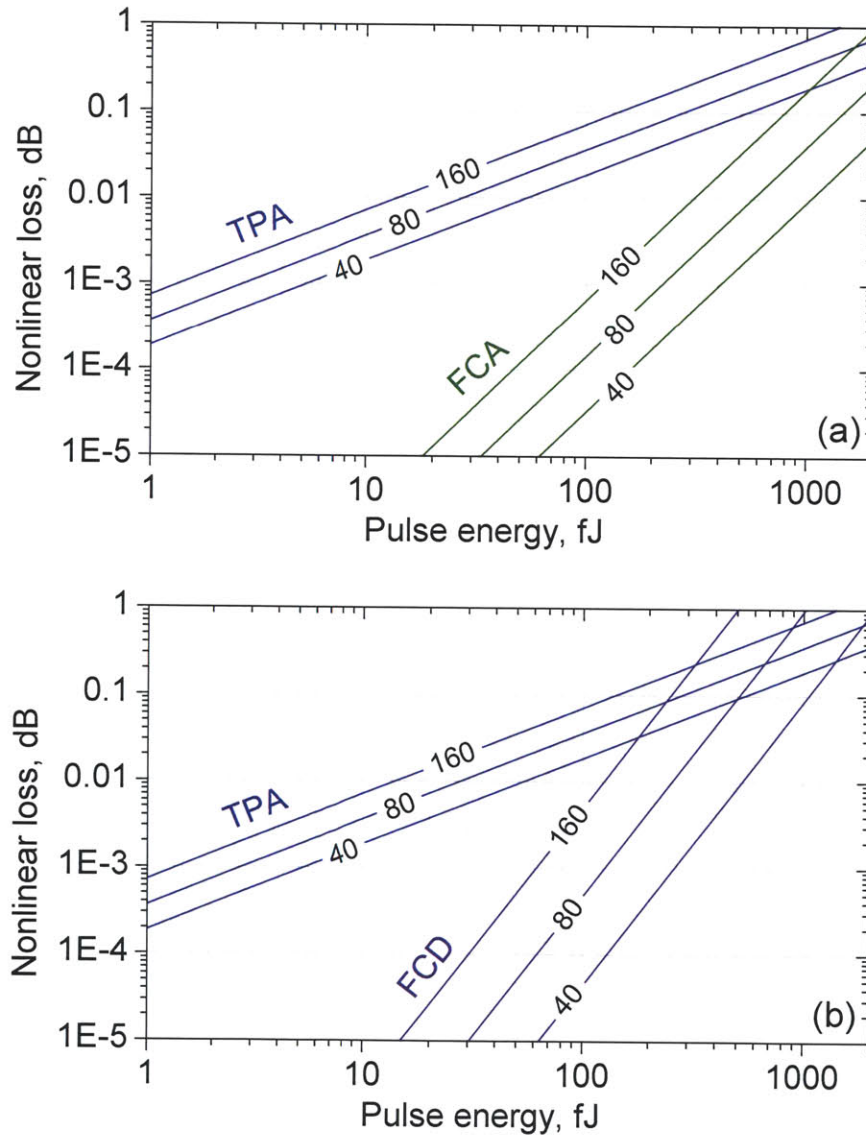


Figure 36. Nonlinear loss due to two-photon absorption (TPA), free-carrier absorption (FCA), and free-carrier dispersion (FCD) in a microring resonator, for three values of the finesse of the ring resonator filter, shown on top of each line. The case with 25 GHz bandwidth and 2 THz FSR shown in Fig. 34 corresponds to the lines labeled “80” in the present figure. To avoid multiple overlapping lines on a single plot, the lines were split into two parts: (a) TPA and FCA, and (b) TPA and FCD.

expected to have stronger nonlinear effects. TPA loss is proportional to the first power of the finesse, FCA loss – to the finesse with the exponent slightly above 2, and FCD loss – to the finesse ratio with the exponent slightly below 4.

The scaling of nonlinearities with filter parameters can be explained with the following qualitative argument. Consider first the case of TPA. Rewriting (18.2), the nonlinear loss coefficient due to TPA can be approximated by

$$drop_{TPA} \approx \frac{2\pi R \alpha_{TPA}}{2C},$$

where  $R$  is the ring radius,  $C$  is the ring-bus coupling coefficient, and  $\alpha_{TPA}$  is the linear propagation loss due to TPA,  $\alpha_{TPA} = \beta_{TPA} \cdot P_{\text{internal}} / A_{TPA}$  (Eq. (17.6)). The internal power in the resonator  $P_{\text{internal}} \sim \frac{E_{\text{out}}}{C\Delta t}$ , where  $E_{\text{out}}$  is the output energy and  $\Delta t$  is the duration of the pulse. The pulse duration is inversely proportional to the resonator bandwidth,  $\Delta t \sim 1/\Delta f$ . Substitution of these proportionalities into the above formula gives

$$drop_{TPA} \sim \frac{2\pi R}{2C} \beta_{TPA} \cdot \frac{P_{\text{internal}}}{A_{TPA}} \sim \frac{R}{C} \cdot P_{\text{internal}} \sim \frac{R}{C} \frac{E_{\text{out}}}{C\Delta t} \sim \frac{R}{C^2} E_{\text{out}} \Delta f.$$

Finally, because  $FSR \sim 1/R$  and  $\Delta f \sim FSR \cdot C$ , the drop loss due to TPA is proportional to

$$drop_{TPA} \sim \frac{FSR^{-1}}{(\Delta f / FSR)^2} E_{\text{out}} \Delta f = \frac{FSR}{\Delta f} E_{\text{out}}. \quad (18.8)$$

This confirms the TPA loss is proportional to  $FSR / \Delta f$ , which is the finesse of the resonator.

In case of FCA, assuming for a moment that FCA loss is linearly proportional to the carrier concentration,

$$drop_{FCA} \sim \frac{2\pi R}{2C} \alpha_{TPA} P_{\text{internal}} \Delta t,$$

where  $\alpha_{TPA} P_{\text{internal}} \Delta t$  describes the carrier density generated by TPA. The factor preceding  $P_{\text{internal}} \Delta t$  can be replaced with (18.8),

$$drop_{FCA} \sim \frac{FSR}{\Delta f} E_{\text{out}} P_{\text{internal}} \Delta t.$$



The factor  $P_{\text{intenal}}\Delta t$  can be expressed as  $P_{\text{intenal}}\Delta t = P_{\text{out}}\Delta t / C = E_{\text{out}} / C \sim E_{\text{out}} \cdot FSR / \Delta f$ , so

$$drop_{FCA} \sim \left( \frac{FSR}{\Delta f} \right)^2 E_{\text{out}}^2,$$

which again depends only on the finesse. Similar argument can be developed for  $drop_{FCD}$ .

## 19. Impact of silicon nonlinearities on photonic ADC performance

The previous chapters described a way to determine the nonlinear power loss due to nonlinearities in microring resonator filters – the element of the ADC most sensitive to nonlinear effects in silicon. However, the question of interest is not how large these losses are, but how big impact they have on the accuracy of the photonic ADC. This chapter examines ENOB degradation due to these nonlinear losses and its dependence on ADC parameters for the case when one of the two complimentary modulator outputs is used. Possible ways to mitigate the impact of nonlinearities, including the use of differential detection, are discussed in the next chapter.

Once the nonlinear loss as a function of pulse energy is determined as described in the previous chapters, calculation of nonlinearity-limited ENOB is straightforward. If a sinusoidal signal is applied to the photonic ADC, the pulse energies in the complimentary outputs can be expressed as

$$E_A(t) = E_0 \frac{1 + m \cdot \sin(\omega t)}{2}, \quad (19.1)$$

$$E_B(t) = E_0 \frac{1 - m \cdot \sin(\omega t)}{2}, \quad (19.2)$$

where  $m$  is the modulation depth and  $\omega$  is the signal frequency. The constant  $E_0$  can be interpreted as the maximum possible energy for full modulation ( $m = 1$ ), or as the total energy in the complimentary channels. Note that the above equations assume a modulator with an ideal transfer function. A realistic modulator, such as a Mach-Zehnder modulator, has a nonlinear transfer function; however, this nonlinearity is not relevant for the analysis of this chapter, and, if

included, would only complicate interpretation of the results. For this reason an idealized modulator was assumed.

With pulse energies given by (19.1), (19.2), nonlinear losses are found as described in the previous chapters; typical dependencies of the nonlinear loss on pulse energy are shown in Figs. 34 and 36. The nonlinear energy loss is then subtracted from (19.1), (19.2), producing distorted signals  $E_A^{(NL)}(t)$  and  $E_B^{(NL)}(t)$ . These distorted signals are analyzed in frequency domain to calculate SFDR and the number of SFDR bits. To evaluate the impact of FCD, it was taken into account that the average frequency shift between the optical channel band and the filter is non-zero because the pulses (19.1), (19.2) have non-zero average energy. This average shift can always be compensated by fine-tuning the filter (e.g. with a microheater); the simulations therefore assume that the average frequency shift is zero.

Figure 37 shows spectra of the distorted signals at the output of microring resonators calculated with the above method. The input was a single-tone sinusoidal signal. The frequencies in the plots are normalized by the input frequency, and the powers are normalized by the output power at fundamental frequency. The finesse of the filter is 80, the modulation index is  $m = 0.6$ , and the average pulse energy (which is  $E_0/2$  in the notation of Eq. (19.1), (19.2)) was 500 fJ. As expected, the TPA effect leads to purely quadratic nonlinearity, while FCA and FCD effects result in the second, third, and other higher-order harmonic distortions. An important result is that in all the cases, the second harmonic distortion is the leading distortion term which determines the SFDR.

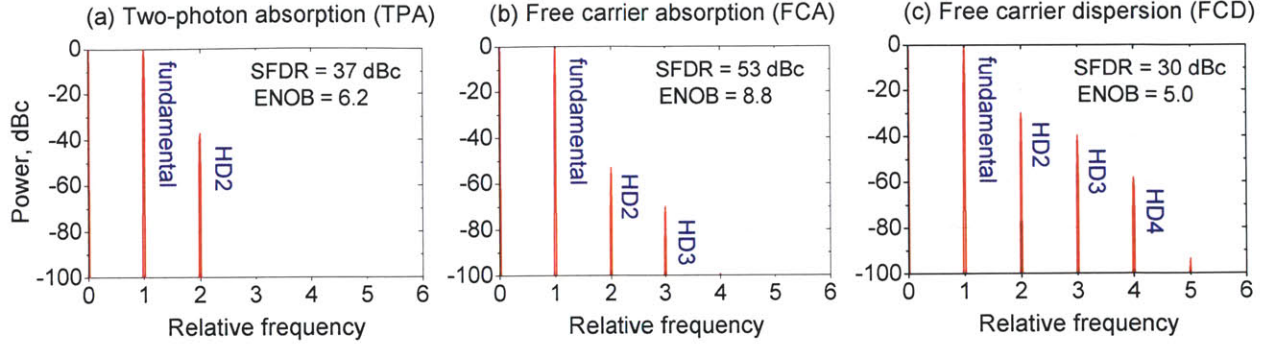


Figure 37. Spectra of the photonic ADC output for a single-tone input, showing harmonic distortions due to nonlinear behavior of microring resonator filters. The frequencies are shown relative to the frequency of the applied tone, and the powers – relative to the measured power of the fundamental. The nonlinear effects considered are (a) TPA, (b) FCA, and (c) FCD. The finesse of the filter is 80, the modulation index  $m$  is 0.6, and the average energy is 500 fJ. The case considered in this figure corresponds to the 500 fJ point of Fig. 39(d) below. The labels “HD2”, “HD3”, and “HD4” indicate the 2<sup>nd</sup>, 3<sup>rd</sup>, and 4<sup>th</sup> harmonic distortions.

The plots of effective number of bits as a function of pulse energy are shown in Figs. 38-40 below. The pulse energies along the x-axes are the average energies at the ring filter output in one of the two complimentary channels, which is  $E_0/2$  in notation of Eqs. (19.1) and (19.2). Also shown is the number of SNR bits as limited by the shot noise, calculated as described in Chapter 5. The plots within each figure correspond to different modulation depths  $m$  (0.1, 0.2, 0.4, 0.6, 0.8, and 1.0), and different figures correspond to different values of the finesse of the resonator (40, 80, and 160, sufficient for an ADC with approximately 12, 25, and 50 channels, respectively).

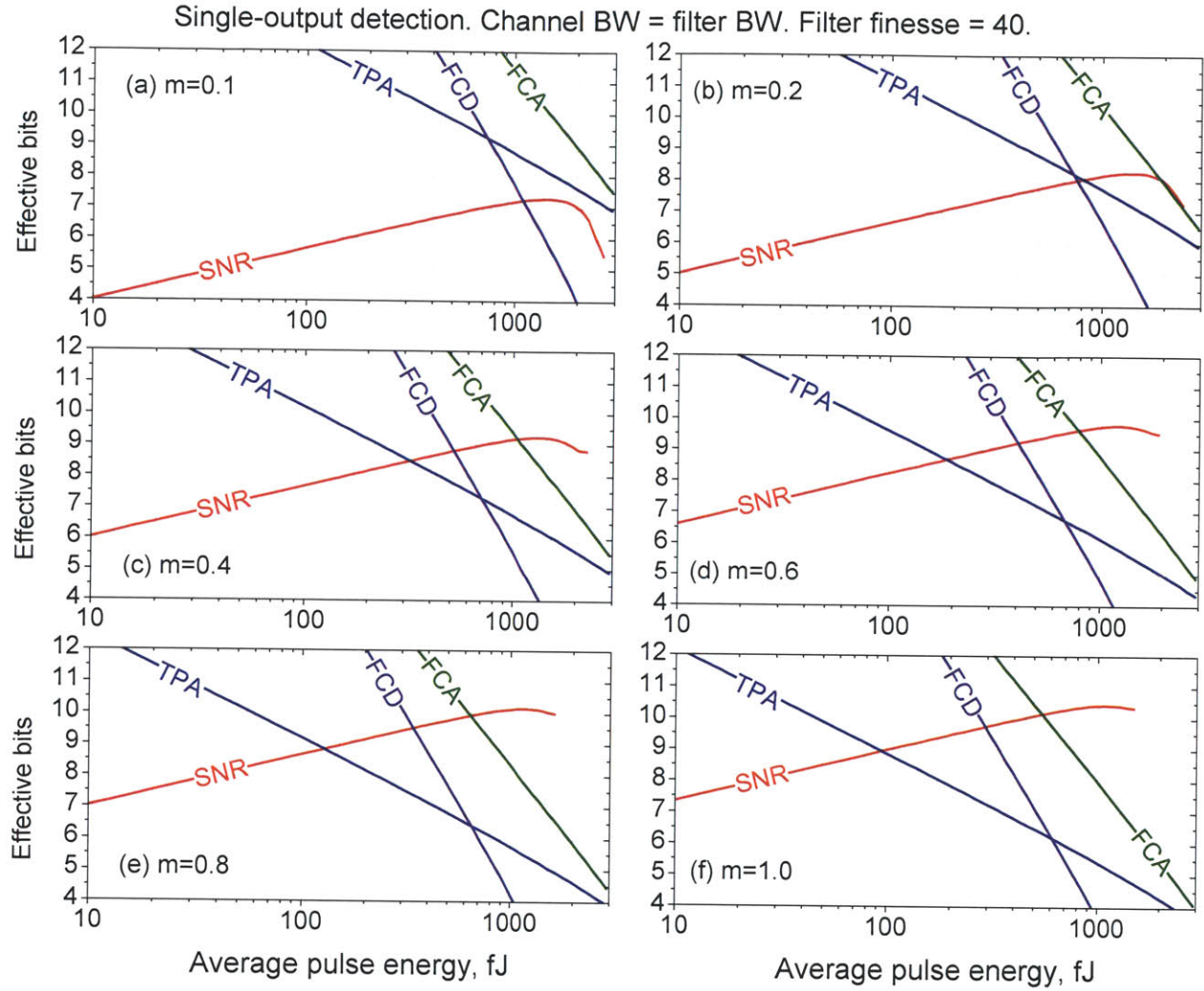


Figure 38. Effective number of bits in a photonic ADC system versus average optical pulse energy at the output of the ring filter. The curves correspond to SFDR bits as limited by TPA, FCA, and FCD in the filter, as well as SNR bits as limited by shot noise. The finesse of the filter is 40, sufficient for an ADC with about 12 channels. The modulation depth  $m$  is (a) 0.1 (b) 0.2 (c) 0.4 (d) 0.6 (e) 0.8 (f) 1.0.

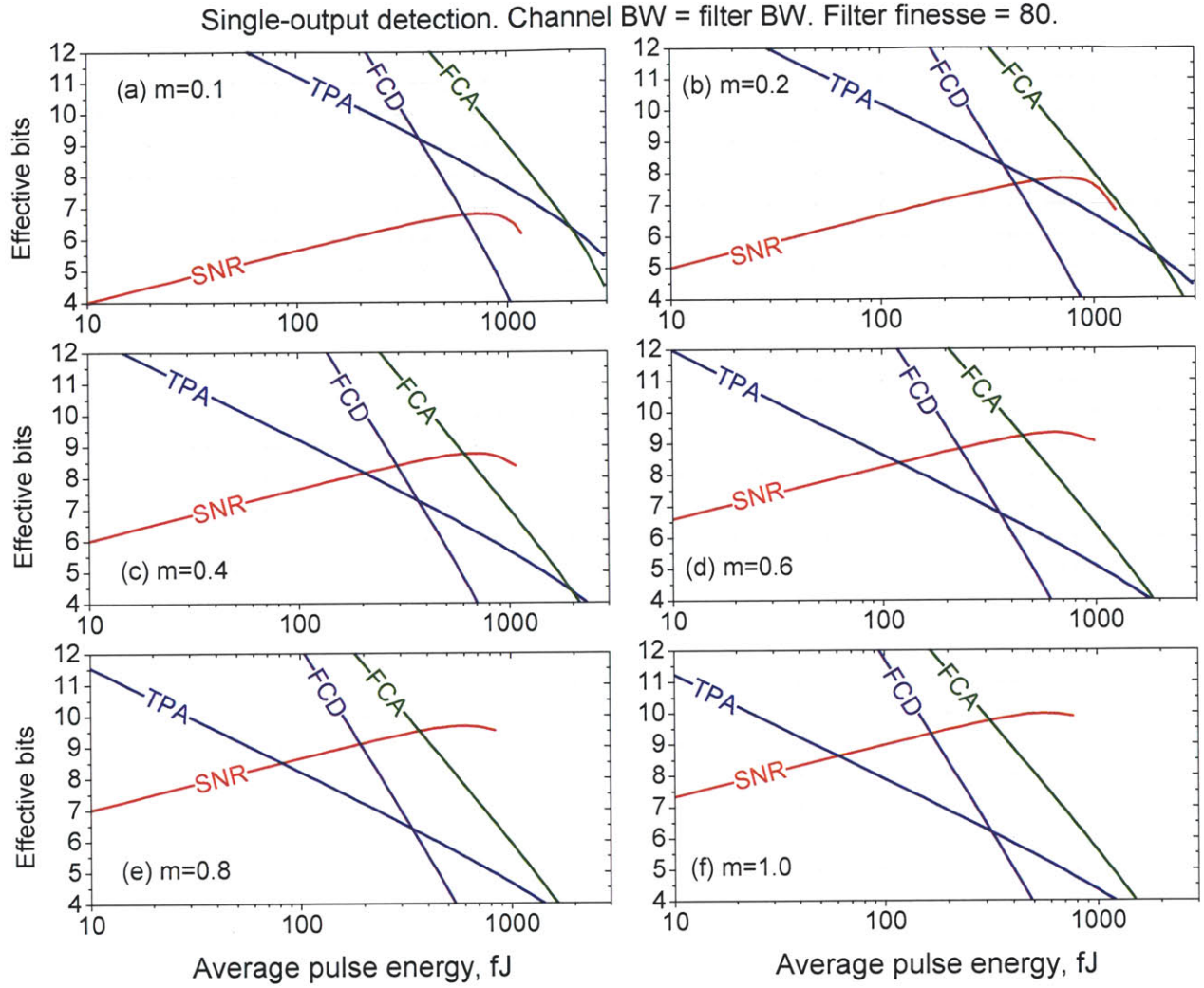


Figure 39. Effective number of bits in a photonic ADC system versus average optical pulse energy at the output of the ring filter. The curves correspond to SFDR bits as limited by TPA, FCA, and FCD in the filter, as well as SNR bits as limited by shot noise. The finesse of the filter is 80, sufficient for an ADC with about 25 channels. The modulation depth  $m$  is (a) 0.1 (b) 0.2 (c) 0.4 (d) 0.6 (e) 0.8 (f) 1.0.



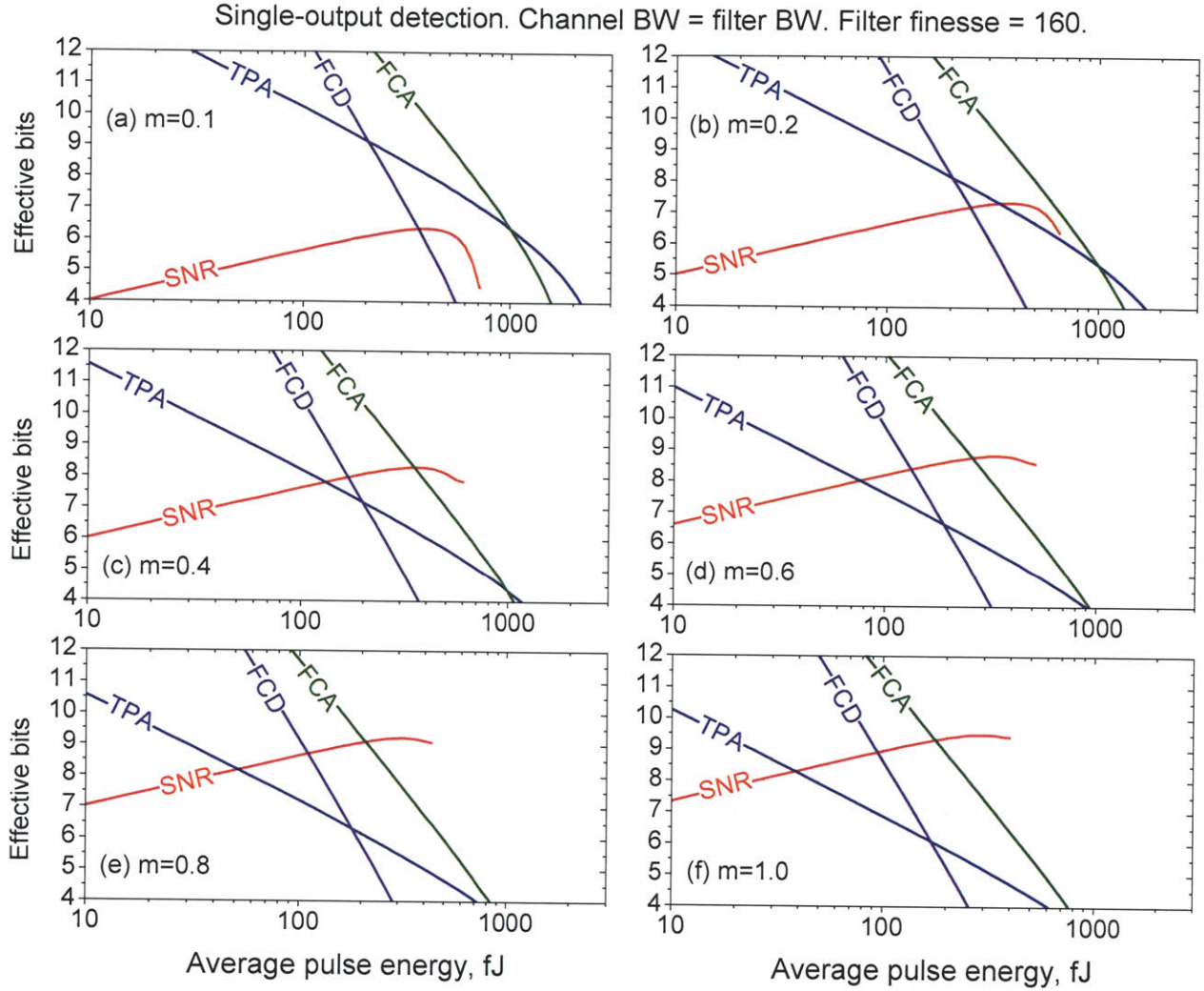


Figure 40. Effective number of bits in a photonic ADC system versus average optical pulse energy at the output of the ring filter. The curves correspond to SFDR bits as limited by TPA, FCA, and FCD in the filter, as well as SNR bits as limited by shot noise. The finesse of the filter is 160, sufficient for an ADC with about 50 channels. The modulation depth  $m$  is (a) 0.1 (b) 0.2 (c) 0.4 (d) 0.6 (e) 0.8 (f) 1.0.

The plots show that for low pulse energies the nonlinearities are very low and their impact on the ADC accuracy is much smaller than the impact of the shot noise and can be ignored. To achieve more SNR-limited effective bits, the pulse energy needs to be increased; for each additional SNR bit, the energy needs to be increased by a factor of 4. As the pulse energy increases, the nonlinearities increase as well. For each factor of 2 in pulse energy, the number of SFDR bits goes down by 1 in case of TPA, by 2.5 in case of FCA, and by about 3.3 in case of FCD. As the number of SFDR bits becomes equal to the number of SNR bits, further increase in pulse energy

brings limited returns because of quick raise of nonlinear distortions. Speaking figuratively, the ADC hits the “nonlinear wall”, the point after which ENOB improvement becomes increasingly difficult. This “wall” is especially pronounced in case of FCD nonlinearity: once the number of SNR bits becomes equal to the number of FCD-limited SFDR bits, the gain of one additional SNR bit results in the loss of about 6.6 SFDR bits, the loss which is hardly possible to recover with error compensation algorithms. As a rule of thumb, once the “nonlinearity wall” is reached, i.e. the number of SNR bits becomes equal to the number of SFDR bits, further increase in pulse energy can improve ENOB by at most 0.5-1 bits, and even this improvement relies heavily on error compensation algorithms to eliminate nonlinear distortions. Note that this is an approximate rule which is not always valid; Figs. 38-40 should be consulted whenever more accurate results are needed. For example, once the “nonlinear wall” is reached in case of low modulation indices – see plots (a) in Figs. 38-40 – further ENOB improvement is hardly possible at all.

The onset of the “nonlinear wall” depends on the system parameters, namely, on the modulation depth and the finesse of the filter. Higher modulation depth is beneficial for offsetting the “nonlinear wall” to higher ENOB values. In other words, strong modulation is good not only in terms of power efficiency, but also in terms of nonlinear behavior of the system. For example, in the systems of Figs. 38-40, the accuracy is limited to at most 6-7 bits when  $m = 0.1$ , while 9-10 bits are possible in the same systems when  $m = 1.0$ . Of course, it is necessary to keep in mind that higher modulation index can lead to higher nonlinearities in the modulator, possibly eliminating the advantage of reduced silicon nonlinearities. Modulator nonlinearities are not considered in this chapter; it is expected that these nonlinearities will make high modulation depths such as  $m = 0.8$  and especially  $m = 1.0$  unpractical in a real system.

The number of SNR bits in Figs. 38-40 starts to decrease beyond certain pulse energies. This happens because the nonlinear losses become so high that they start to deplete the pulse energy. For a given system, this represents the ultimate limit on the ENOB which can be achieved, the limit which cannot be overcome with any nonlinearity compensation. Note that the x-axis in Figs. 38-40 corresponds to the energy at the output of the ring filter found in the linear case, with no nonlinearities present. At the same time, the shot noise-limited SNR was calculated for the output energies found in the nonlinear case, i.e. with nonlinear energy loss taken into account.



The finesse of the filters is another parameter which determines the onset of the “nonlinear wall”. A system with more channels needs to have filters with higher finesse, which increases the nonlinearities and reduces the ENOB which is possible to achieve. For each factor of 2 in finesse increase, the “nonlinear wall” reduces the achievable ENOB by roughly 0.4-0.5 bits.

## 20. Mitigation of silicon nonlinearities in a photonic ADC

The results of the previous chapter suggest the presence of “nonlinear wall”, which makes increasingly difficult to improve ENOB beyond a certain level. For a typical set of ADC parameters, this corresponds to ENOBs of about 8-9 bits. This chapter suggests two methods for moving the “nonlinear wall” to higher ENOB values.

The first method which mitigates the impact of silicon nonlinearities is the use of differential detection. The previous chapter discussed exclusively the case when a single modulator output is used. With differential detection, the output signal is equal to the difference of the signals measured in the two complimentary outputs of the modulator. If the energies in the complimentary outputs are the same, all nonlinear terms must also be the same. The odd-order nonlinear terms must have opposite signs, while the even-order terms must have the same sign. This means that subtraction of the two complimentary outputs must eliminate all even-order nonlinear terms; the same technique was studied in Chapter 13 as a way to eliminate even-order nonlinear terms of the silicon MZ modulator transfer function. It was shown in the previous chapter that the leading nonlinear term for all three nonlinear effects (TPA, FCA, and FCD) is the quadratic term (see Fig. 37). It is expected that, ideally, differential detection will completely eliminate this term, significantly reducing nonlinear distortions.

The second method to reduce the impact of nonlinearities is to adjust the relationship between the filter passband and the optical channel band to make the nonlinear loss less sensitive to the FCD-induced misalignments between them.

This method can be illustrated with the following example. Consider the case when the optical channel bandwidth is 20 GHz and the filter is an ideal flat-top filter with 30 GHz bandwidth, see Fig. 41(a). In this case, the filter will pass the full channel bandwidth even when the filter frequency is varied within  $[-5...5]$  GHz range, so that the output energy will be completely insensitive to filter frequency variations within this range. The same will be true if

the optical band is wider than the filter bandwidth, see Fig. 41(b). In reality, ideal flat-top filters cannot be implemented, so the energy cannot be completely insensitive to frequency variations, although this sensitivity can be reduced by proper filter design. All previous simulations of the impact of FCD assumed that the spectrum of the channel exactly corresponds to the transmission function of the filter (Fig. 32). If the filter bandwidth is increased, one should expect the magnitude of the power loss due to FCD to go down, see Fig. 41(c). The same effect can be achieved if the optical band is wider than the filter, see Fig. 41(d). In simulations below, the situation of Fig. 41(d) was assumed, with the optical channel band 4 wider than the bandwidth of the ring filter.

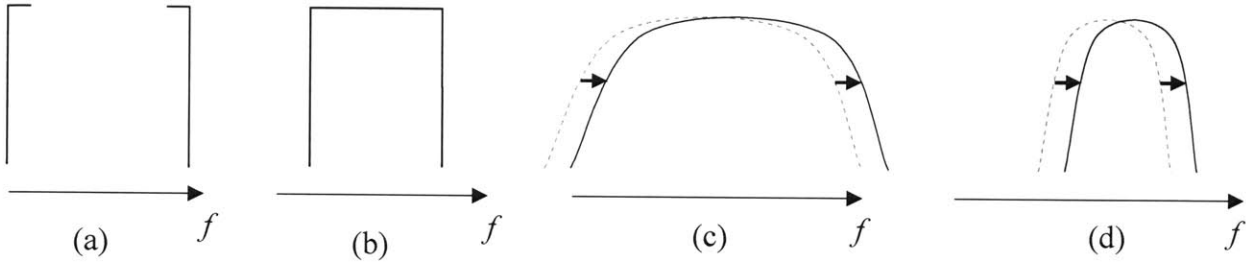


Figure 41. Misalignment of filter passband with respect to the optical channel band for several relationships between the two, designed to reduce nonlinear loss for given amount of misalignment. Gray regions represent spectrum of the input optical channel, as formed by the pulse interleaver, and lines represent filter transmission function before and after the misalignment. Ideal flat-band spectra and filters are considered in (a) and (b) and realistic shapes are considered in (c) and (d). The filter is wider than the optical channel for (a) and (c); the opposite is the case for (b) and (d).

The plots of effective number of bits presented in Figures 42-44 correspond to performance of the ADC utilizing the two nonlinearity mitigation methods described above, using differential detection and making the optical channel band wider than the filter passband – in this particular case, 4 times wider. Apart from differential detection and wider optical channels, all parameters of the system, including all filter parameters, are identical to the ones of Figs. 38-40. Comparison of Figs. 42-44 to Figs. 38-40 indicates significant reduction of nonlinear distortions thanks to differential detection even without wide optical channels (see dashed lines in Figs. 42-44). The distortion due to TPA is completely eliminated, and distortions due to FCA and FCD are significantly reduced, improving the accuracy by 1-2 effective bits. Part of this improvement comes from 3 dB gain in SNR due to differential detection (note that for consistency with 38-40, the x-axis shows the average energy in one of the two complimentary outputs, although

differential detection implies that the energies of both complimentary outputs are used). Distortions due to FCD, which are dominant source of distortions left after differential detection eliminated distortions due TPA, can be greatly reduced by adjusting the relationship between the optical channel band and the filter bandwidth. Using optical channels with 4 times the filter bandwidth (solid lines in Figs. 42-44) offsets the “FCD wall” by roughly 0.5-1 bits. At this point, the accuracy of the photonic ADC is limited or is very close to being limited by SNR. The shot noise-limited SNR flattens out as the pulse energies increase because of energy depletion by nonlinear losses. This sets the ultimate limit on the accuracy which can be achieved. Note that compared to the situation of the previous chapter, this limit has been increased by nonlinearity mitigation techniques: differential detection improves SNR by 3 dB, and filter passband adjustment significantly reduces the energy depletion due to FCD. With FCD losses reduced, the SNR limit is determined by TPA and FCA losses, and cannot be further improved without changing the system design.

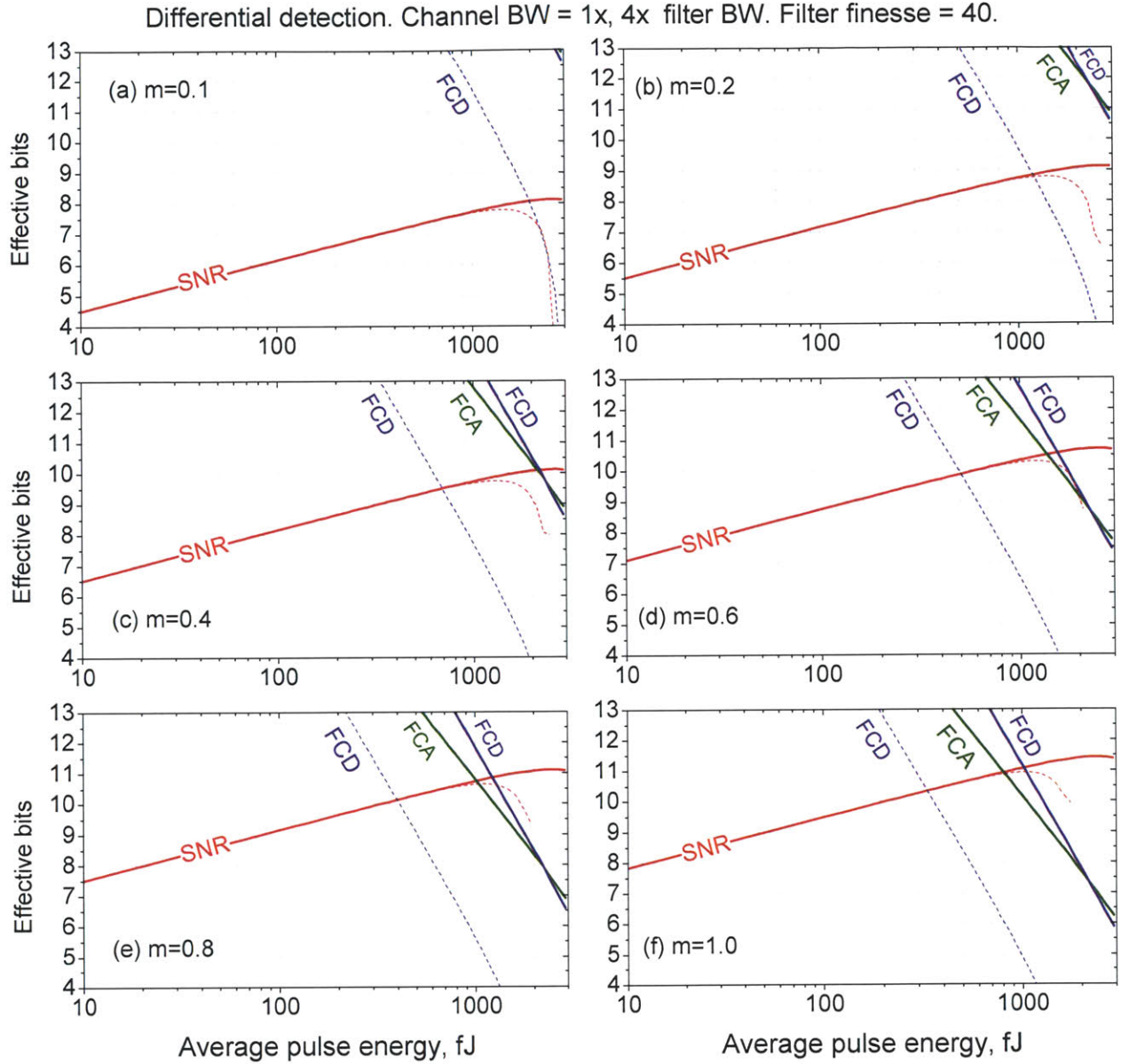


Figure 42. Effective number of bits in a photonic ADC system versus average optical power at the output of a ring filter. Differential detection is assumed. The curves correspond to SFDR bits as limited by FCA and FCD in the filter, as well as the number of SNR bits due to shot noise limitations. The dashed lines corresponds to the case when the optical channel band exactly matches the filter passband, and solid lines correspond to the case when the optical channel is 4 times wider than the filter passband. The finesse of the filter is 40, and the modulation depth  $m$  is (a) 0.1, (b) 0.2, (c) 0.4, (d) 0.6, (e) 0.8, and (f) 1.0.

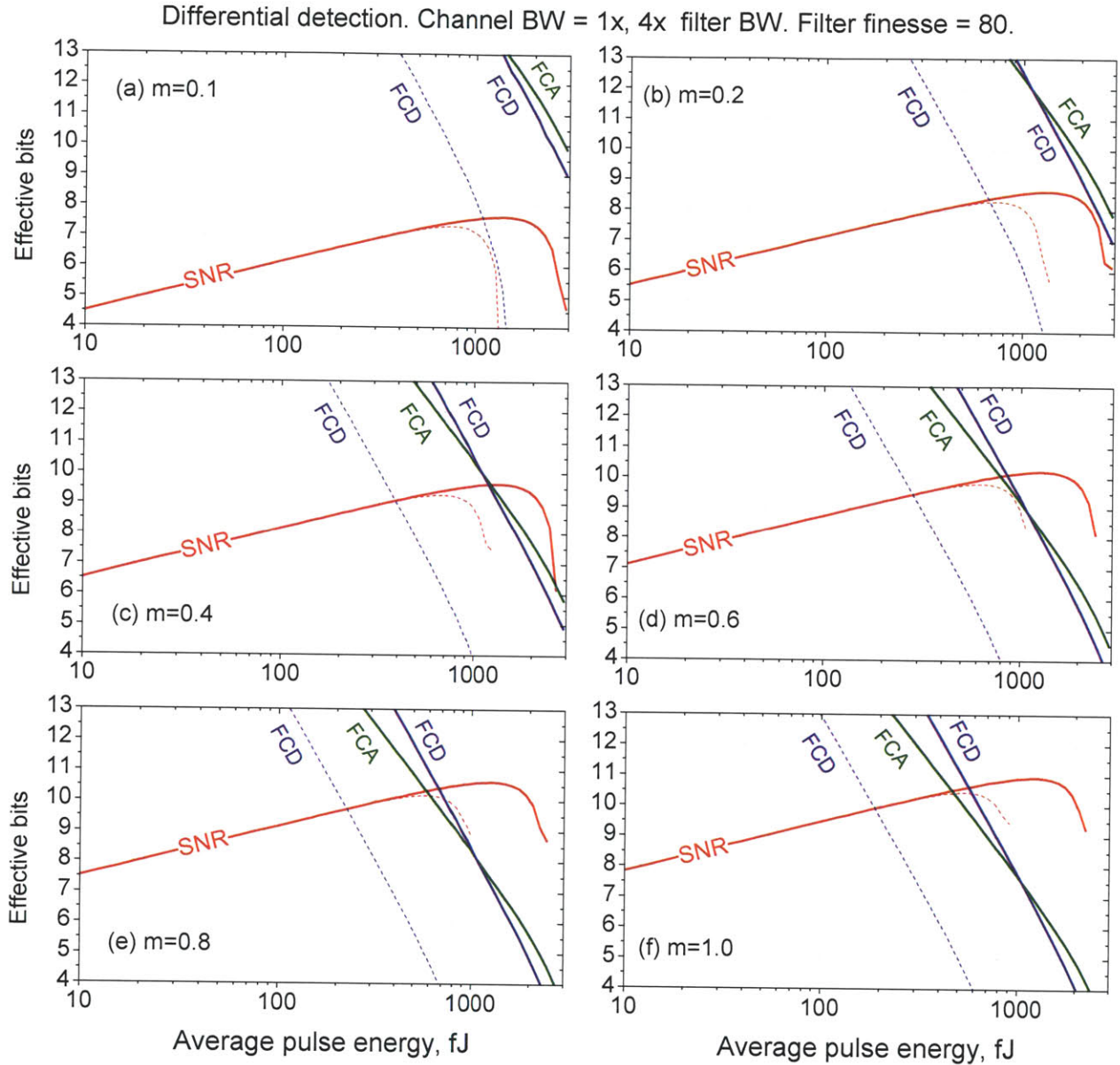


Figure 43. Effective number of bits in a photonic ADC system versus average optical power at the output of a ring filter. Differential detection is assumed. The curves correspond to SFDR bits as limited by FCA and FCD in the filter, as well as the number of SNR bits due to shot noise limitations. The dashed lines corresponds to the case when optical channel band exactly matches the filter passband, and solid lines correspond to the case when the optical channel is 4 times wider than the filter passband. The finesse of the filter is 80, and the modulation depth  $m$  is (a) 0.1, (b) 0.2, (c) 0.4, (d) 0.6, (e) 0.8, and (f) 1.0.



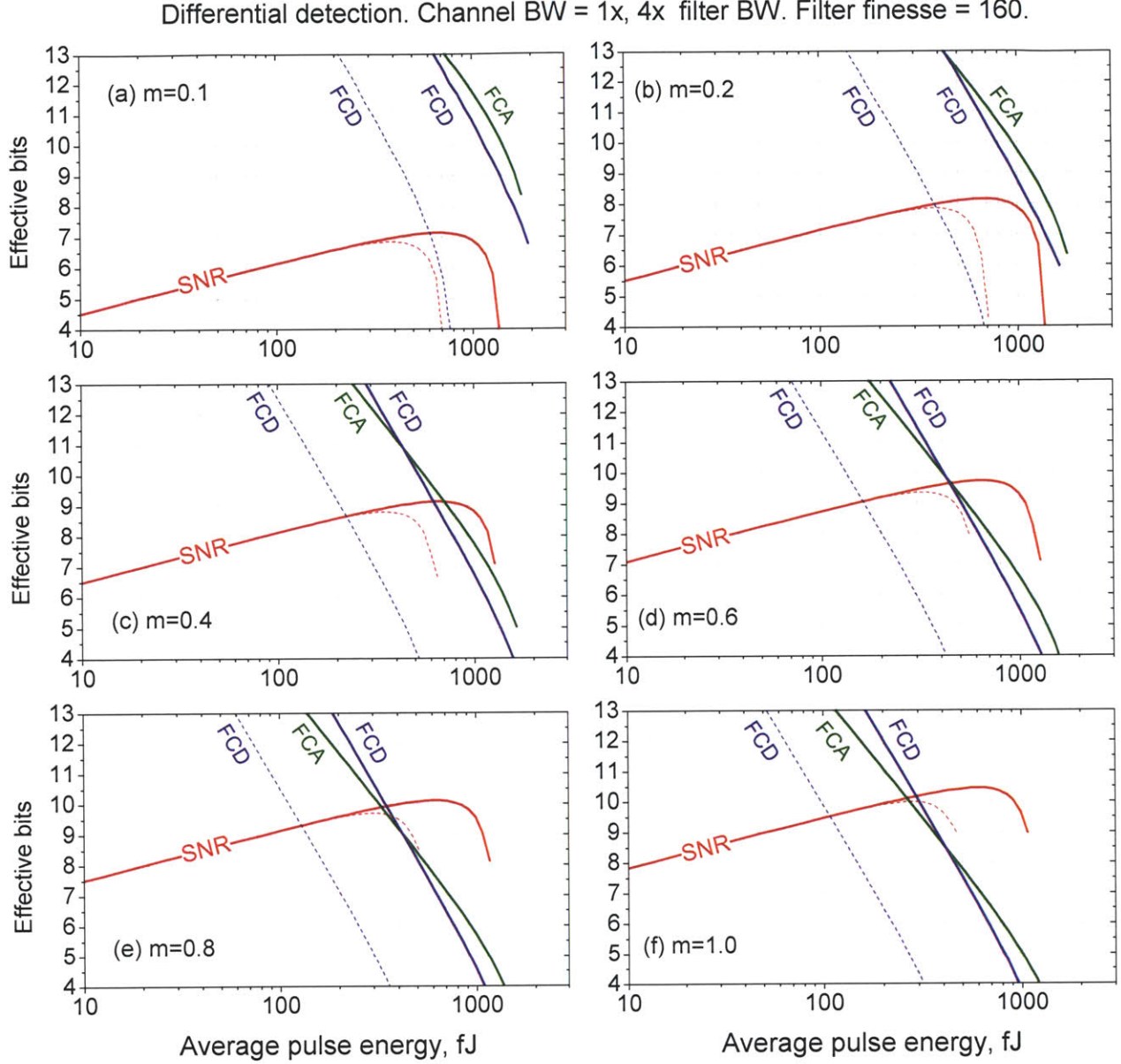


Figure 44. Effective number of bits in a photonic ADC system versus average optical power at the output of a ring filter. Differential detection is assumed. The curves correspond to SFDR bits as limited by FCA and FCD in the filter, as well as the number of SNR bits due to shot noise limitations. The dashed lines corresponds to the case when optical channel band exactly matches the filter passband, and solid lines correspond to the case when the optical channel is 4 times wider than the filter passband. The finesse of the filter is 160, and the modulation depth  $m$  is (a) 0.1, (b) 0.2, (c) 0.4, (d) 0.6, (e) 0.8, and (f) 1.0.



## 21. Summary and discussion

To sum up the nonlinearity analysis performed in the preceding chapters, it has been shown that the microring resonators are the most critical part of a photonic ADC system with respect to nonlinear effects in silicon. The nonlinear effects are the energy loss due to two-photon absorption (TPA), free-carrier absorption (FCA), and resonant frequency shift caused by free-carrier dispersion (FCD), the latter leading to energy loss due to mismatch between the optical channel band and the passband of the filters. When optical power is increased, shot-noise limited SNR improves relatively slowly, while the raise of nonlinearities is quite fast. Specifically, the optical power needs to be increased by 4 to bring one additional SNR bit, which reduces the SFDR by 2 bits in case of TPA, by about 5 bits in case of FCA, and by about 6.5 bits in case of FCD. This steep increase of nonlinear distortions means that improving the ADC accuracy beyond a certain level becomes increasingly difficult and is only possible with distortion compensation. At some point, the accuracy can no longer be improved by increasing the power even with distortion compensation because pulse energy becomes depleted by nonlinear loss and shot noise-limited SNR starts to decrease. The maximum ENOB which can be achieved depends on the modulation index  $m$  and the finesse (FSR/bandwidth ratio) of the microring resonator filter. For the case when single output of the modulator is used, the achievable number of bits ranges roughly from 6-7 bits for  $m = 0.1$  to 9-10 bits for  $m = 1.0$ . Differential detection had been shown to eliminate all even-order nonlinear terms, including the second order nonlinear term which otherwise dominates the nonlinearity, and improve the achievable ENOB by roughly 1-2 bits. Using different bandwidth of the optical channels and the filters was shown reduce sensitivity to resonant frequency variations and reduce FCD loss, further improving the accuracy by 0.5-1 bit. Note that these bit numbers are approximate and Figs. 38-44 should be consulted for more accurate performance data.

Note that according to Figs. 42-44, quite high number of effective bits can be reached without high nonlinear distortions. However, in practice this can be challenging because it relies on differential detection to accurately quite significant distortions, something which is possible only if the complimentary channels are precisely balanced. For example, in case of filter finesse of 80 and modulation index  $m = 0.6$ , the SNR limit is about 10.2 bits, reached for 1-2 pJ average output pulse energies (see Fig. 43(d)). From Fig. 39(d), for these pulse energies, the TPA

distortions in each complimentary output are at the 4-5 bit level, and FCA distortions are at the 4-6 bit levels. Differential detection needs to bring these distortions from the 4-6 bit level to better than 10 bit level – a challenging task requiring careful matching of the complimentary signal paths.

The results presented above assume that all photons at the output of the rings are converted into current in the photodetector with 100% efficiency. If the efficiency is lower, optical power needs to be larger to reach the same SNR, which increases nonlinear distortions beyond the levels predicted with the analysis above. As a result, for each factor of 2 of energy reduction due to losses after the filters, the maximum achievable accuracy is reduced by up to 0.5 bits.

The analysis of FCA and FCD nonlinearities relied on data fits (17.4)-(17.5) for relating the carrier concentrations with the change in refractive index and absorption coefficient it induces. These equations are one of the best fits to the data available in the literature and usually their accuracy is sufficient for device design and analysis. However, for analog applications, with photonic ADC being one of them, the exact functional form of these equations is of important. Unfortunately, it is unknown how accurate is the nonlinearity of Eqs. (17.4)-(17.5). Therefore, there is some uncertainty about the magnitude of FCA and FCD effects obtained in this work. If, for example, instead of nonlinear dependence (17.4), the loss due to free carriers is actually proportional to the first power of the concentration, as it is frequently assumed in the literature [123, 124], the relationship between the second and the third harmonics of FCD-distorted signal would be different, and the SFDR after elimination of the 2<sup>nd</sup> harmonic by differential detection would be different as well.

The method proposed for mitigation of nonlinearity caused by variations of resonant frequency of the filter is to adjust the bandwidth of the optical channel and the passband of the filter. For example, if the optical channel bandwidth is 30 GHz and the filter bandwidth is 20 GHz, and both have perfect flat-top profiles, the output power will stay constant for variations of filter frequency within [-5..5] GHz range (the situation of Fig. 41(b)). A realistic filter is not flat-top, therefore the benefit of the proposed approach is smaller. In the example considered above, the optical channel was assumed to be 4 times wider than the filter bandwidth (the situation of Fig. 41(d)), which significantly reduced FCD-induced power loss. However, the 4 times bandwidth difference is far from an ideal solution, because it means that the number of ADC channels must be reduced (otherwise the filters of the demultiplexer and the multiplexer

would have to have an unrealistically steep roll-off). However, if the number of channels is reduced, an alternative of having 4 times difference between the optical band and filter bandwidth, is simply increase the filter bandwidth by 4 to match the optical band. This alternative would mean lower filter finesse and therefore all nonlinearities would be reduced. As a result, the example with 4 times bandwidth mismatch is something which makes little sense in practice. The value of this example is to illustrate that the FCD-induced nonlinearity is not fundamental and can be reduced by optimizing the filter passband. A solution which would not require a large mismatch between the optical band and the filter bandwidth is to have filter shapes closer to an ideal flat-top profile. If the filters of the pulse interleaver are implemented as ring resonator filters, using a design with more than 2 rings to achieve a flatter passband should be beneficial.

Note that this work considers nonlinearities for the case of discrete time-to-wavelength mapping, when the channels are formed with a wavelength demultiplexer, differential delay lines, and a wavelength multiplexer. An alternative approach is the continuous time-to-wavelength mapping introduced by a dispersive element with linear chirp. In this case, the nonlinearities can be lower because chirping increases the duration of the pulses so that for the given energy, the peak powers are reduced. This difference is more pronounced when number of ADC channels is low and the filters are wide; as the number of channels is increased and each channel becomes narrower, the impact of dispersion broadening is also reduced and the duration of the output pulse is determined mostly by the filter. Therefore, the results of this work are applicable also to the ADCs with continuous time-to-wavelength mapping, provided that the number of channels is high. The exception is the impact of FCD, which is completely different for the case of discrete and continuous time-to wavelength mapping: in the first case, FCD changes the loss, while in the second case FCD shifts the temporal location of the sampling point. The effect of the resulting modulation of the sampling time needs to be studied in future work.

The present analysis of nonlinear behavior of microring resonator is based on a model which is strictly valid only slowly-varying fields. However, the pulses in a photonic ADC are not slowly-varying, which means that the presented results are approximate, and more accurate model of field behavior inside a resonator with time-varying properties is needed for exact description of nonlinearities. However, the approximate analysis of this work is still valuable for

gaining insight into nonlinear behavior, its dependence on ADC parameters, and obtaining quantitative estimates of achievable ENOB levels.

The impact of free carriers generated by the preceding pulses has been neglected. In reality, this effect might play a role if the carrier lifetime is long, leading to inter-pulse crosstalk. If this is the case, measures need to be taken to reduce the carrier lifetime at fabrication stage, or creating a diode which extracts free carriers during the interval between the pulses.

This work assumed two-ring filters for nonlinearity analysis. Although ring filters are a good option for a photonic ADC, they are not the only option, and filter designs with lower nonlinearities might be considered. For example, AWG filters have no internal field enhancement so their nonlinearity is very low; they can be a viable option if they can provide low inter-channel crosstalk and can be reasonably compact. Alternatively, designing a microring filter with lower internal power enhancement factor might be possible. Using filters with faster roll-off away from the passband might be beneficial because faster roll-off means that, for given extinction of the next channel, the filter bandwidth can be increased, i.e. the filter finesse can be reduced, which decreases the power enhancement and nonlinear penalty. Examples of the filters with faster roll-off might be series-coupled rings with more than two rings [125], or loop-coupled rings which can provide the fastest possible roll-off for the given number of rings [126].

The ultimate solution of nonlinearity problem is to replace silicon with a material without two-photon absorption at the laser wavelength. In this respect, silicon nitride is a good candidate because it is TPA-free at telecom wavelengths, CMOS-compatible, and can provide a relatively high FSR (although the FSR is lower than possible in Si). It depends on fabrication constraints whether SiN rings are a possibility; if they are, this would completely eliminate any concern about nonlinearities. According to the results presented in this work, implementing filters in a TPA-free material might be the only way to scale photonic ADCs to very high speeds and accuracy exceeding 10 bits.

## V. Microring resonator filter banks

Microring resonator filters are widely considered for silicon photonics applications such as WDM interconnects, resonant modulators, and sensors. The interest in microring resonators for filter applications is explained by the fact that a microring is a relatively simple and compact structure, yet it provides a lot of flexibility in filter design, making low-loss high-quality filters possible. Microring resonators can also be very sensitive to refractive index change, which can be used to create very sensitive modulators and sensors.

One of the key components of a photonic ADC is the wavelength demultiplexer which splits a modulated wavelength-interleaved or chirped pulse train into individual wavelength channels. The filters of this demultiplexer should have low loss, flat passband, and fast roll-off to ensure high spectral efficiency, i.e. high ratio of the channel bandwidth to channel spacing. These requirements can be satisfied with microring resonator filters, which were used in this work to create a multi-channel wavelength demultiplexer for the photonic ADC. This part of the thesis describes the design parameters and results of implementation of multi-channel microring resonator filter banks.

### 22. Introduction to microring resonator filters

This chapter briefly describes some principles of operation and design of microring resonator filters. More detailed descriptions of microring resonator filters can be found in multiple publications on the topic [127, 128, 120].

The layouts of a single-ring and dual-ring resonator filters are shown in Fig. 45(a)-(b). The single-ring filter functions similarly to a Fabry-Perot resonator: the light on resonance and at nearby frequencies is transmitted to the other side of the structure (the “drop port”), and the light off-resonance passes through unaffected (the “through port”). The resonance is defined by the condition that the ring round-trip phase shift is an integer number of  $2\pi$ ,

$$2\pi R k_0 n_{eff} = 2\pi m,$$

where  $R$  is the radius of the ring,  $k_0 = 2\pi/\lambda$  is the vacuum wave number,  $n_{eff}$  is the effective index of the mode, and  $m$  is an integer. Different values of  $m$  correspond to different resonances; the resonances are spaced apart by the free spectral range (FSR):

$$FSR = \frac{c}{2\pi R} n_{gr},$$

where  $n_{gr}$  is the group index of the mode and  $c$  is the speed of light in vacuum.

The transmission function of a single-ring filter is a Lorentzian; a typical transmission function is shown in Fig. 45(c). To improve the rate at which the transmission rolls off away from the passband, a filter with more than one ring resonator can be used. Fig. 45(b) shows the layout of a two-ring filter, and Fig. 45(d) shows its transmission function. The single-ring and the two-ring filters in Fig. 45(c) and (d) are designed to have the same 3-dB bandwidth. It is apparent that the dual-ring design provides a much faster roll-off than the single-ring design. The roll-off rate can be further increased by concatenating more than two rings with properly selected coupling coefficients.

Different shapes of the passband can be designed by controlling the coupling coefficients between the input and output waveguides (“bus waveguides”) and the rings, as well as the between the rings themselves. The formulas which provide coupling coefficients required to achieve different passband shapes, such as Chebyshev, Butterworth, and others, can be found in refs. [122], [127].

The filter banks of the photonic ADCs described in this work were implemented as two-ring filters. A single ring filter is not a very good solution because of its slow roll-off, which means that the channels need to be spaced far apart in frequency in order to have high enough next-channel extinction. This has negative impact on ADC performance because a low ratio of channel bandwidth to channel spacing, i.e. the spectral fill ratio (see Chapter 5), means that only a small fraction of the power generated by the laser is used. For given FSR, reduced bandwidth-to-spacing ratio also means increased finesse of the ring resonator, which increases the impact of silicon nonlinearities (see Chapter 18). Finally, for small bandwidth-to-spacing ratio, implementing a large number of channels might not be possible because a large number of channels would require a large FSR, but there is a limit to how large FSR can be achieved for a



given index contrast. Two-ring filters increase the bandwidth-to-spacing ratio, which improves power efficiency, reduces the finesse, and increases the maximum possible number of channels.

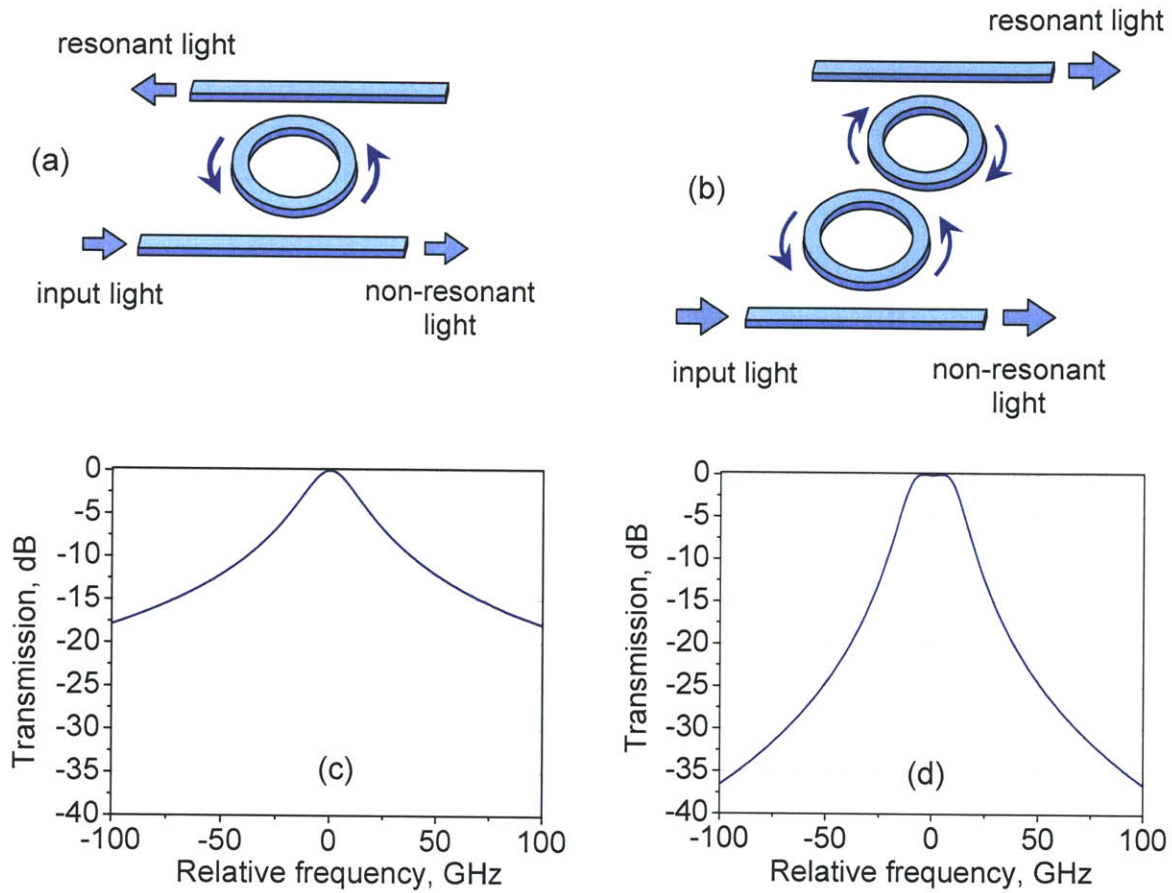


Figure 45. Layout of (a) a single-ring and (b) a two-ring resonator filter. The light at resonant frequencies is transmitted to the “drop port” by the filter, i.e. to the waveguide on the opposite side of the ring(s). The light at non-resonant frequencies is transmitted to the “through port”, i.e. continues to propagate in the same waveguide after passing by the rings unaffected. Example of the power transmission function of a single-ring and a dual-ring filter are compared in (c) and (d). The filters have the same 3dB bandwidth and free spectral range. The dual-ring design permits much faster roll-off than the single-ring design.

## 23. Eleven-channel filter bank

This chapter presents results of the design, fabrication, and characterization of an 11-channel filter bank for application in a photonic ADC [129, 130].

The filter bank was implemented with two-ring resonator filters. The waveguide design with a wide and thin silicon core was selected because it provides reduced sensitivity to width

errors [121]. The waveguide width was 600 nm for the bus waveguide and 495 nm for the ring waveguide; different widths were selected to reduce scattering losses in the coupling region [131]. The height of the waveguides was 105 nm. The overcladding was 1.0  $\mu\text{m}$ -thick with the refractive index of 1.385, and the  $\text{SiO}_2$  undercladding had the refractive index of 1.455. The cross-section of the waveguide is shown in Fig. 46(a). The radius of the ring (as measured from the center of the ring to the center of the bent waveguide) was 6.735  $\mu\text{m}$  [120], which provided FSR of 2.14 THz.

The target 3-dB filter bandwidth was 20 GHz, and the target channel spacing was 124 GHz (1 nm). The power coupling coefficients needed to implement a Chebyshev passband with such characteristics were  $3.8 \cdot 10^{-2}$  for coupling between the bus and the ring waveguide, and  $4.4 \cdot 10^{-4}$  for coupling between the ring waveguides. In order to select the corresponding coupling gap widths, three-dimensional finite-difference time domain (FDTD) simulations have been performed<sup>1</sup> [132]. The calculated coupling coefficients are plotted in Fig. 47 as a function of the gap width. From this plot, the required bus-ring gap is found to be 344 nm, and the required ring-ring gap is found to be 703 nm. The obtained filter design parameters are illustrated in Fig. 46(b).

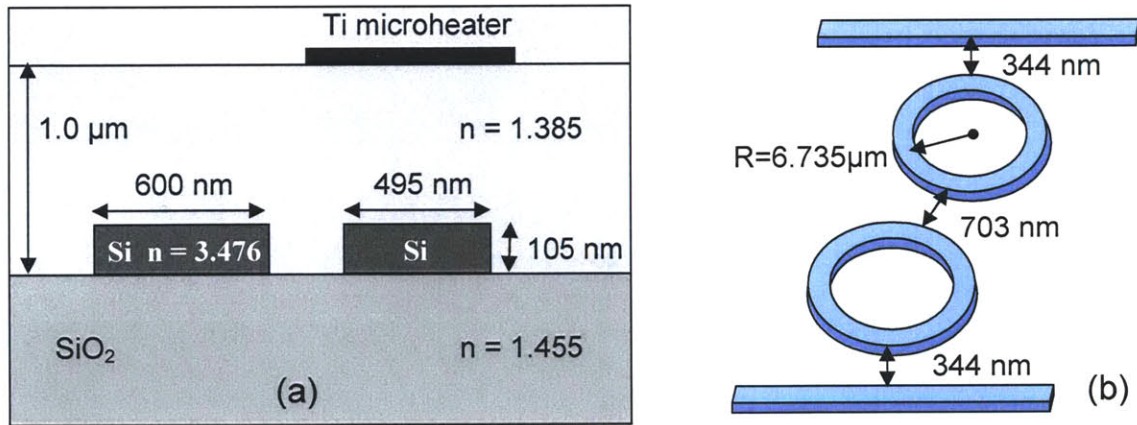


Figure 46. (a) Cross-section of the silicon waveguide structure used to implement the 11-channel filter bank described in this chapter. The wider waveguide on the left is the ring waveguide, and the narrower waveguide on the right is the straight (bus) waveguide. (b) The ring radius and the width of the coupling gaps of the two-ring filters used to create the filter bank. The filter had FSR = 2.14 THz and the 3-dB bandwidth of the filters = 20 GHz.

<sup>1</sup> The FDTD code was developed by Christina Manolatu, Mike Watts, and Milos Popovic.



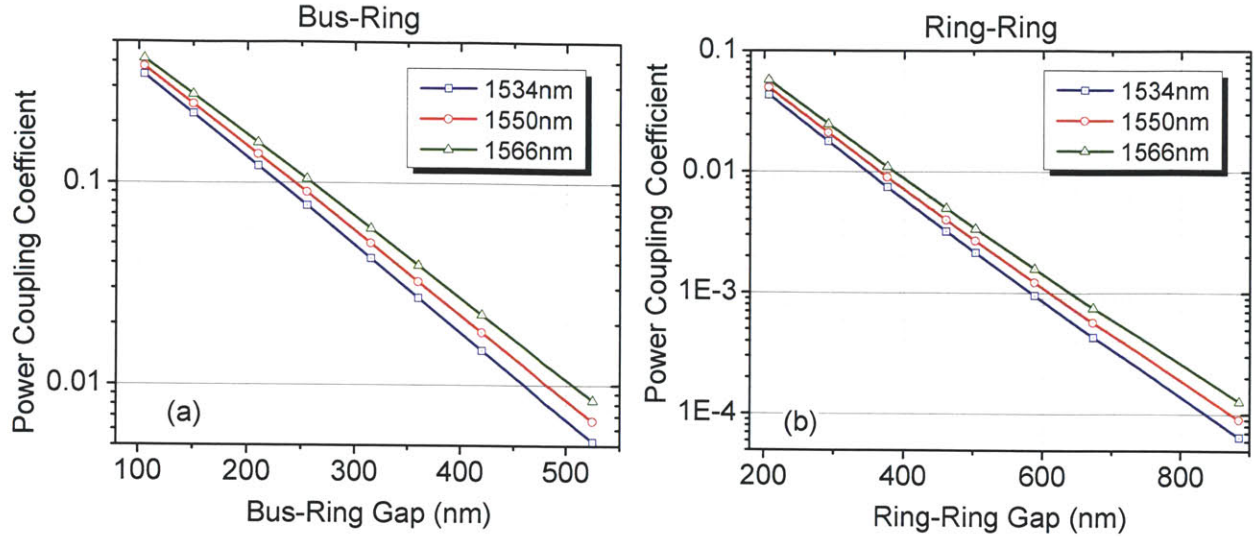


Figure 47. Power coupling coefficient between (a) the bus (straight) waveguide and the ring waveguide, and (b) between two ring waveguides, as a function of gap width. The three curves correspond to optical wavelengths of 1534, 1550, and 1566 nm. The symbols represent the coupling coefficient values obtained with 3d FDTD simulations, and solid curves represent the fits to these values. The waveguide cross-section was the one shown in Fig. 46(a), the ring radius was  $6.735 \mu\text{m}$ . The above plots were used to calculate the gaps corresponding to the required values of the coupling coefficient; these gap values are shown in Fig. 46(b).

The designed filter bank has been fabricated<sup>1</sup> on a SOI wafer using e-beam lithography [129, 133-135]. The top-view photographs of the chip are shown in Fig. 48. Part (a) of this figure shows the filter bank photographed before the metallization step, and part (b) shows two filters of the bank after metallization step, when the microheaters and the microheater contacts have been created. Note that the number of channels in Fig. 48(a) is 20, while this chapter is titled “an 11-channel filter bank”. This is not a contradiction: the number of channels in the fabricated bank was indeed 20, but it turned out that only 11 of these channels work properly. The other 9 channels could not be used because some of the microheaters were damaged, which prevented proper filter alignment. Additionally, several the channels had excessive losses, presumably from waveguide damage. As a result, only 11 out of 20 channels of the filter bank could be used. Note that while the requirement of uniform channel spacing was imposed for this filter bank, the uniformity is a strict requirement only in case of continuous time-to-wavelength mapping. For discrete time-to-wavelength mapping, the channel spacing does not have to be uniform; the only

<sup>1</sup> Filter bank was fabricated by C. W. Holzwarth of Prof. H. Smith’s group at MIT Microsystems Laboratory.

requirement is that the filter frequency must match the optical channel frequency, as formed by the demultiplexer and the multiplexer of the pulse interleaver.

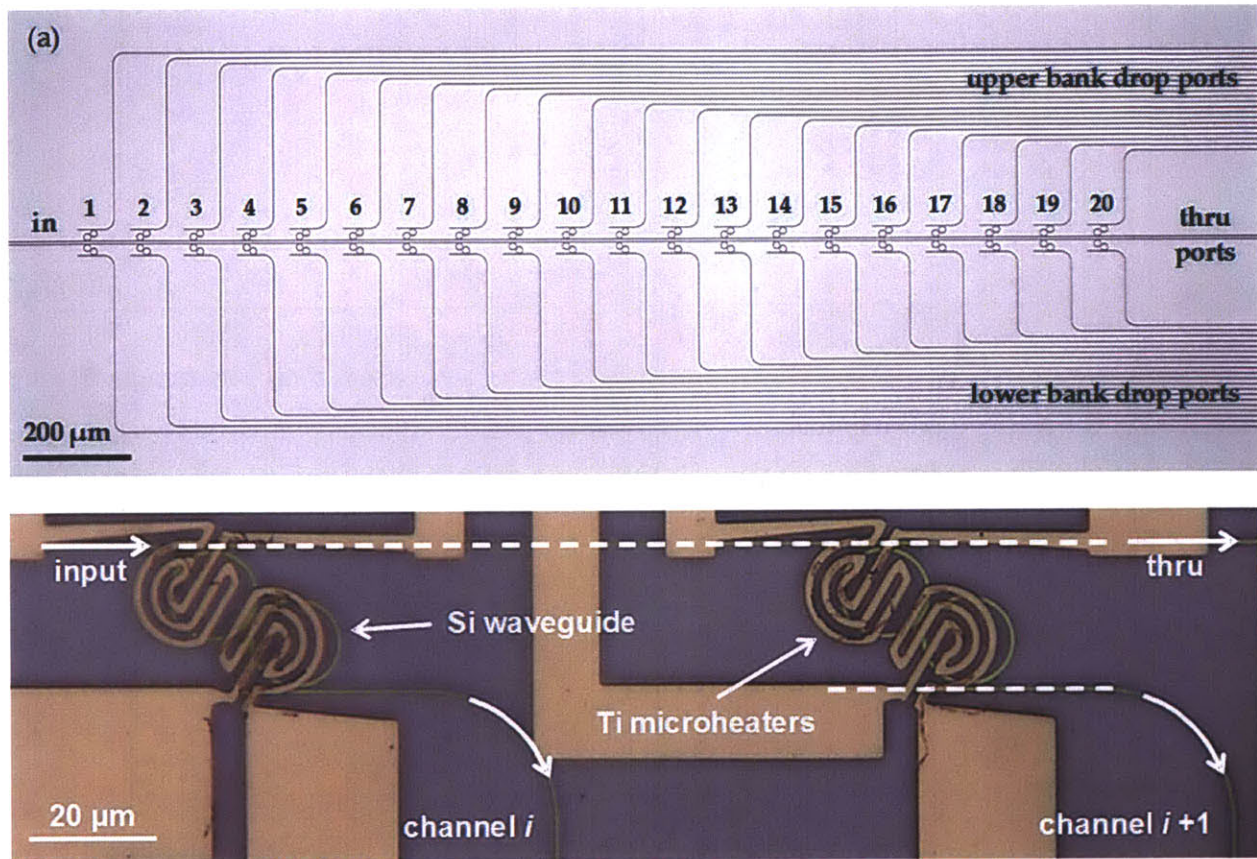


Figure 48. (a) Photographs of a dual 20-channel filter bank, taken prior to metallization step; (b) photograph of two filters of this filter bank after deposition of Ti microheaters above the silicon waveguide layer.

The measured transmission spectra<sup>1</sup> of 11 channels of one of the two filter banks are shown in Fig. 49. Part (a) of this figure corresponds to the channels without any tuning, indicating significant misalignment of the filters from a regular grid as well as misalignment between the two rings of a single filter. Part (b) shows the channels after thermal tuning was used to compensate for the misalignments. Note that only one channel at a time was tuned in the measurements of Fig. 49(b), while a photonic ADC requires simultaneous tuning of all channels.

<sup>1</sup> The measurements were done by M. Dahlem of Prof. E. Ippen's group at MIT.



Automatic misalignment monitoring and compensation needs to be implemented to accomplish this task.

The aligned channels of Fig. 49(b) show regular passbands with about 20 GHz bandwidth, 124 GHz (1 nm) channel spacing, and 0.5 dB loss. The extinction of the adjacent channels was at least 35 dB, sufficient for implementing a photonic ADC with more than 10 effective bits. In fact, the extinction was almost certainly higher than 35 dB, but the measurement noise floor was not low enough to measure it.

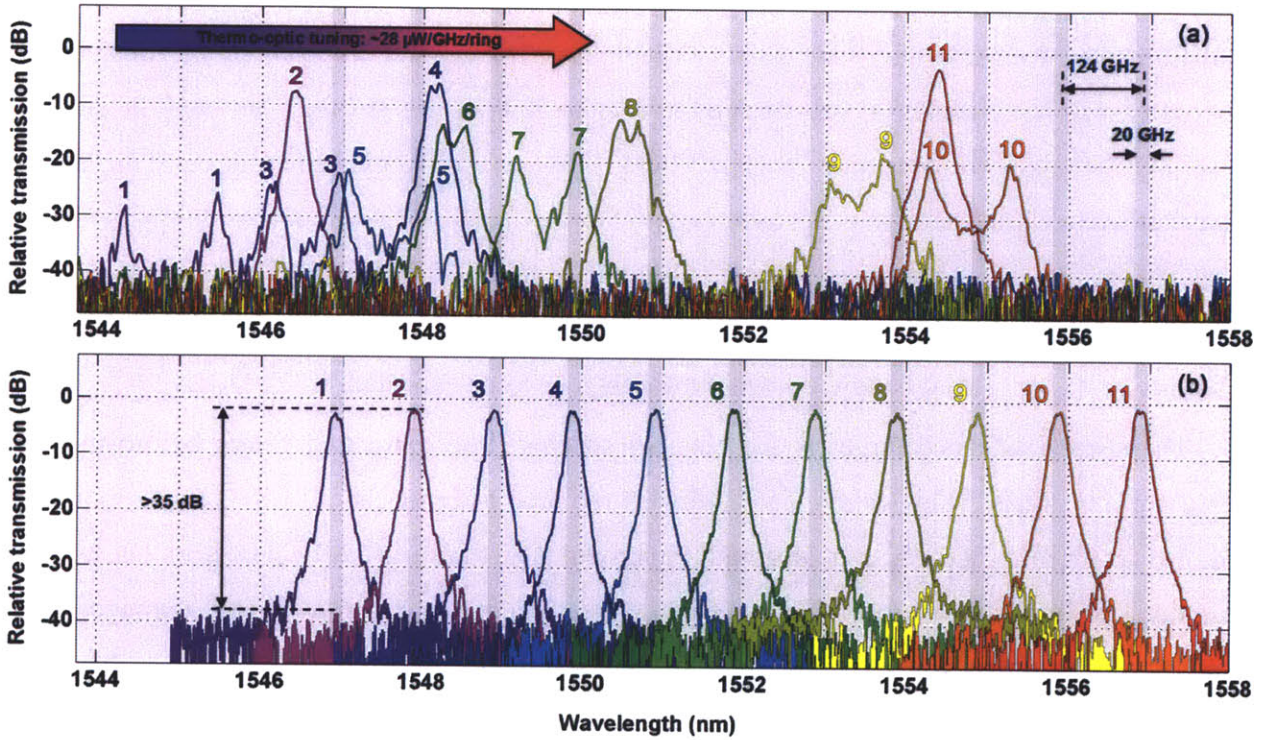


Figure 49. Transmission of 11 channels of the fabricated 20-channel filter bank (a) before and (b) after thermal tuning. The thermal tuning of resonant frequency is performed using the microheaters fabricated above the rings. Because of damage in some of the microheaters, only 11 of the 20 channels could be aligned to the required frequency grid. The filter bank has the bandwidth of 20 GHz, channel spacing of 124 GHz (1 nm), and next-channel extinction of about 45 dB.

The amount of next-channel extinction achieved in this filter bank is sufficient for implementing a photonic ADC with at least 10 effective bits. One point which is might be confusing is how can the 35 dB extinction, i.e. the 35 dB crosstalk, be sufficient for an ADC with 10 bits? Isn't it a well-known fact that ENOB scales as 6 dB per bit, as per Eq. (1.2), so that 60 dB extinction is needed for 10 effective bits? The answer is no, because the extinction value

applies to the optical power, while 6 dB per bit applies to the electrical power, which is proportional the square of the optical power. This means that each 3 dB of reduction of optical cross-talk gives 6 dB reduction of electrical crosstalk, i.e. one addition effective bit.

It is mentioned in this chapter that the filter bank had the target bandwidth of 20 GHz and the target channel spacing of 124 GHz. However, it is necessary to mention that these were the “adjusted” targets, while initial targets were 25 GHz bandwidth and 80 GHz channel spacing. The story behind the bandwidth adjustments is the following. In a previous fabrication of filters with the same parameters and varying bandwidths, it was established that a design with 20 GHz bandwidth produced 25 GHz wide filters. The reason for difference between the design and experiment was not clear and it was decided to use the 20 GHz designs for filter bank fabrication as well, with the goal of obtaining 25 GHz filters. However, the fabricated filter bank turned out to have 20 GHz wide filters, in exact agreement with the design. This is the reason why the target bandwidth of 20 GHz is mentioned above. Although in this particular fabrication, the design and the experiment displayed exactly the same bandwidth, this is probably a coincidence and some difference of experimental bandwidth from the design is to be expected.

The second adjusted target is the channel spacing. The fabricated filters before thermal tuning are misaligned (Fig. 49(a)), and tuning is required to bring them to the target frequency grid. However, only few channels could be brought to the target 80 GHz grid because of limitations of how much power can be applied to a microheater before it gets damaged, and because the rings can only be tuned one way, towards longer wavelength. However, if a 1 nm (124 GHz) frequency grid is selected, as many as 11 channels could be put onto this grid. Therefore, the target channel spacing was adjusted to 124 GHz. Although this increased channel spacing-to-bandwidth ratio means somewhat reduced power efficiency, increased silicon nonlinearities, and reduced maximum channel count, the ADC will still be fully functional with performance somewhat below the optimum level.



## 24. Dual twenty-channel filter bank

Another variant of a dual filter bank has been fabricated using optical lithography<sup>1</sup> [136]. The target bandwidth was 25 GHz, the target channel spacing was 80 GHz. The waveguide cross-section was close to the one used in the first filter bank, except now the thickness of the silicon core was 114 nm and the overlcladding refractive index was 1.56 (the index in the fabricated structure turned out to be a bit smaller, 1.55). The cross-section of the corresponding waveguide is shown in Fig. 50(a). The ring radius was  $6.735\text{ }\mu\text{m}$ . The plots of coupling coefficients calculated with FDTD method as a function of coupling gap width are shown in Fig. 51. The coupling coefficients needed for 25 GHz bandwidth were selected to be  $3.8 \cdot 10^{-2}$  for bus-ring waveguide coupling and  $4.4 \cdot 10^{-4}$  for coupling between the rings. According to Fig. 51, to obtain such coupling coefficients, the bus-ring coupling gap needs to be 297 nm and the ring-ring coupling gap needs to be 620 nm. The obtained filter design parameters are shown in Fig. 50(b).

The photographs of the filter bank fabricated on a silicon chip using 248 nm optical lithography are shown in Fig. 52(a). The photographs were taken after completion of all fabrication steps, including the metallization step to create microheaters on top of each of the 80 rings to thermally fine-tune their resonant frequencies.

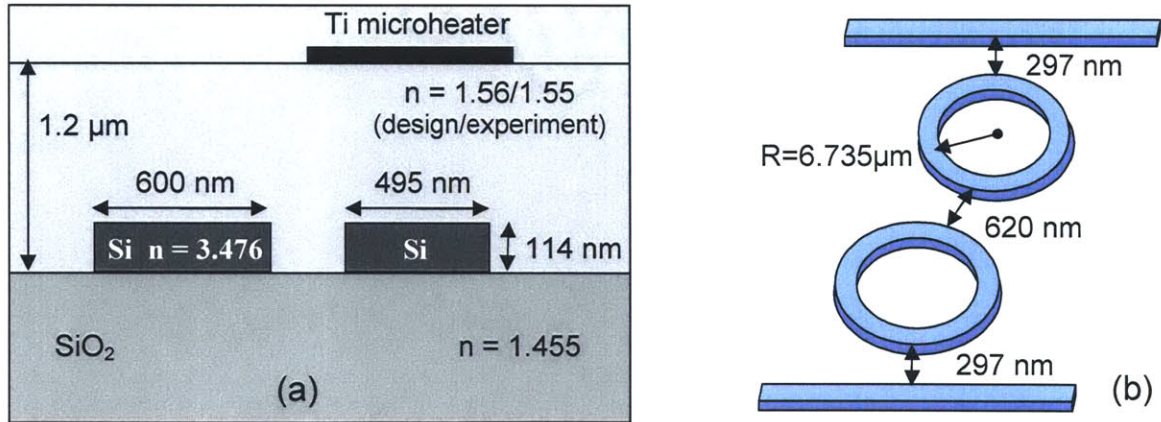


Figure 50. (a) Cross-section of the silicon waveguide structure used to implement the 20-channel filter bank described in this chapter. The wider waveguide on the left is the ring waveguide, and the narrower waveguide on the right is the straight (bus) waveguide. (b) The ring radius and the width of the coupling gaps of the two-ring filters used to create the filter bank. The design FSR was 2.13 THz and the 3-dB bandwidth of the filters was 25 GHz.

<sup>1</sup> The filter bank was fabricated by Steven J. Spector of MIT Lincoln Laboratory.



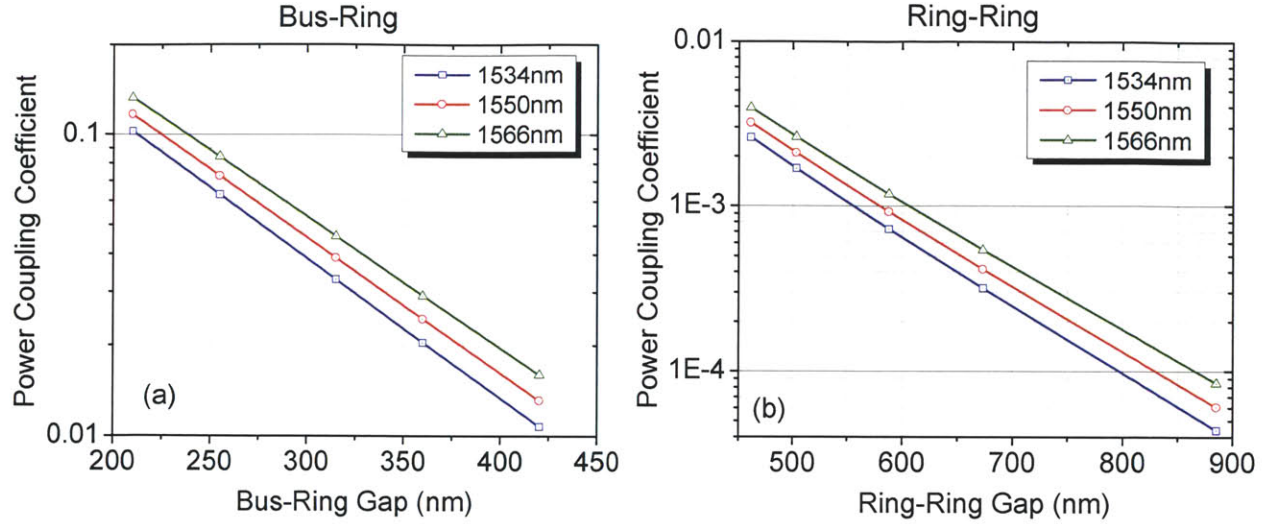


Figure 51. Power coupling coefficient between (a) the bus and the ring waveguide, and (b) between the two ring waveguides, as a function of gap width. The three curves correspond to optical wavelengths of 1534, 1550, and 1566 nm. The symbols represent the coupling coefficient values obtained with 3d FDTD simulations, and solid curves represent the fits to these values. The waveguide cross-section was the one shown in Fig. 50(a), the ring radius was  $6.735 \mu\text{m}$ . The above plots were used to calculate the gaps corresponding to the required values of the coupling coefficient; these gap values are shown in Fig. 50(b).

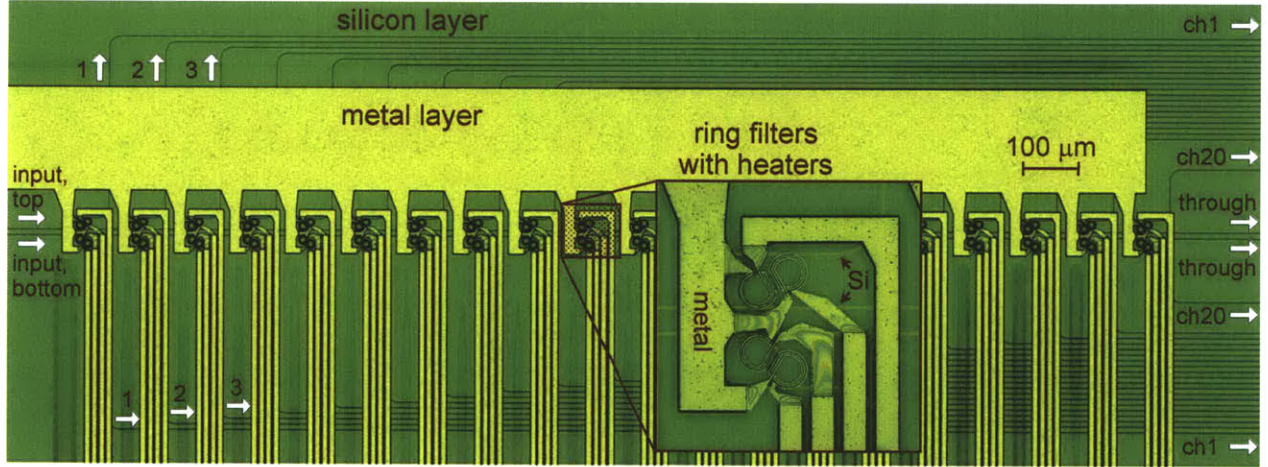


Figure 52. Photograph of two matched 20-channel filter banks fabricated on a silicon chip. Each bank is intended to demultiplex one of the two complementary outputs of the MZ modulator. The filters are second-order microring-resonator filters. Microheaters fabricated on top of each ring are used to thermally tune resonant frequencies in order to compensate for fabrication errors and put the resonances on a desired grid.

The measured transmission of the filters is shown in Fig. 53. The two lines for each of the 20 filters correspond to the two complimentary modulator outputs. Thermal tuning has been used to obtain the result of Fig. 53. All channel passbands are clearly defined, with 21-26 GHz 3-dB bandwidth, and are located on the target 80 GHz grid. The frequencies of the complimentary channels are well matched to each other. The next-channel extinction was 32-36 dB. The performance of this filter bank is sufficient for implementing a 20-channel ADC with more than 10 effective bits. Note that similar to the experiments described in the previous chapter, only one channel at a time was tuned and characterized. The tuning efficiency was 50 GHz/mW, and the total power to tune all channels was about 400 mW.

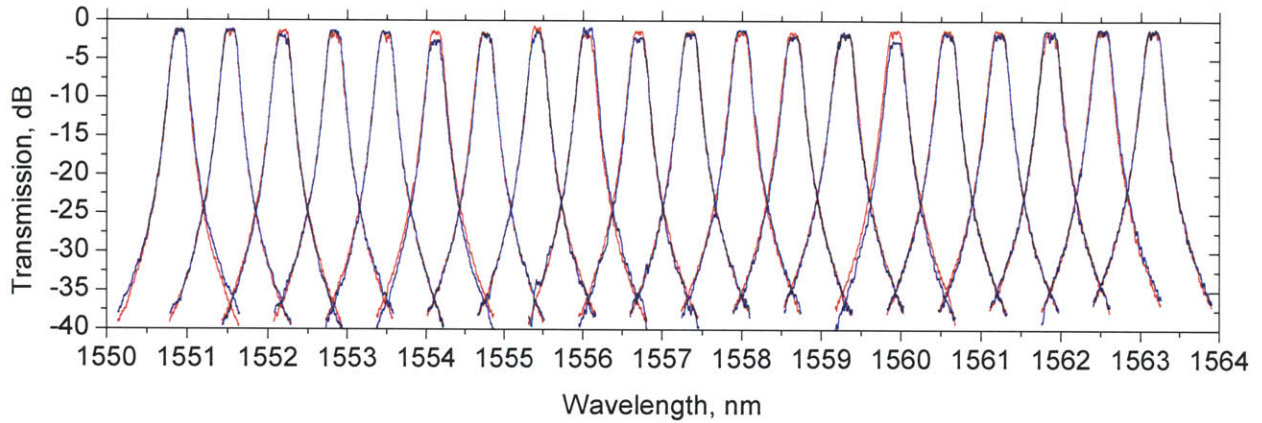


Figure 53. Measured transmission of the dual 20 channel filter bank. The overlapping red and the blue lines correspond to the two matched banks. The channels exhibit 21-26 GHz bandwidth, 80 GHz channel spacing, and 32-36 dB extinction at center wavelength of an adjacent channel. The transmission is normalized to the transmission of off-resonance light through the system. The average insertion loss is 1.7 dB; values for individual channels range from 1.1 to 2.8 dB likely due to fiber-to-chip coupling loss variations.

## 25. Summary and discussion

This part of the thesis presented the results of design, fabrication, and characterization of two multi-channel filter banks, an 11-channel and a 20-channel banks. The demonstrated filter banks have flat passbands, regular channel spacing, and more than 30 dB extinction of the next channel. Both filter banks are the high-quality filter banks with the most channels created to date.

Although these particular banks were not used in the ADC demonstrations described in Part II of the thesis, they prove that one of the key components of a multi-channel ADC – the

high-quality multi-channel filter bank – can be implemented with the technology available today. While the photonic ADCs described in part II used just two channels and were operated in undersampling mode, using the filter banks presented above, the sampling rate can be raised by simply utilizing more wavelength channels similar to the ones which have already been demonstrated. For example, the 20-channel filter bank described in Chapter 24 can be used to create a 20 GSa/s photonic ADC (assuming a 1 GHz mode-locked laser); the total optical bandwidth required to run such a system is about 13 nm, which is easily within the bandwidth of mode-locked lasers at 1550 nm.

The filter bank fabricated using optical lithography (Chapter 24) had lower frequency variations and more reliable microheaters than the filter bank fabricated using e-beam lithography (Chapter 23). Although the e-beam lithography has much better resolution than the optical lithography, it might be the case that optical lithography has better local uniformity, which results in lower resonant frequency variations and requires less power for their compensation; similar results were observed in [57]. In the particular fabrication efforts described in this work, larger than expected frequency variations in the filter bank fabricated with e-beam lithography partially contributed to reducing the number of useful channels from 20 to 11. Microheater yield, longevity, and damage threshold were other important factors, which, if improved, would increase the number of useful channels.

Finally, note that in order to record the filter shapes reported in this work (Figs. 49, 53), microring frequencies were fine-tuned thermally using dedicated microheaters. One filter at a time was tuned; it was hard to tune all filters simultaneously because microheater voltages were adjusted manually. In a practical ADC, all microheaters need to be controlled simultaneously and automatically. A reliable method of monitoring of resonance frequencies (or temperatures) of microring resonators is therefore required. In a multi-ring filters, which are the filters of most practical interest, the frequency of each individual ring need to be monitored independently.

## VI. TWO-STAGE FIBER-TO-CHIP COUPLERS

This part of the thesis proposes a new, efficient adiabatic in-plane fiber-to-chip coupler design<sup>1</sup>. In this design, the light from the fiber is coupled into a low-index waveguide with matching mode size. The mode is first adiabatically reduced in size with a rib taper, and then transferred into a high-index (e.g. silicon) waveguide with an inverse taper. The two-stage design allows to reduce the coupler length multiple times in comparison with pure inverse taper-based couplers of similar efficiency. The magnitude of length reduction increases with the refractive index of the low-index waveguide and the fiber mode size.

### 26. Introduction to fiber-to-chip couplers

In silicon photonics, the light source is usually located outside the chip, because generation of light directly on a silicon chip is problematic due to significant two photon absorption and indirect bandgap of silicon. Active work is going on to circumvent these problems [137]. Perhaps the most promising approach is to use compound semiconductors, such as GaAs or InP, for light generation; these materials can be grown on silicon epitaxially [138] or introduced by wafer bonding [139]. The main issue with this approach is its incompatibility with standard CMOS fabrication process. Another proposed approach is to generate light in epitaxially grown strained germanium [140], which has improved probability of radiative recombination as compared to silicon. Despite these exciting developments, it is still unclear whether practical on-chip lasers will become a reality. This is particularly true for lasers with special properties, such as low-jitter femtosecond lasers used in photonic ADCs; in the photonic ADC experiments described in Chapter 8, all lasers were implemented off-chip. In some applications, such as communications between different cores of a processor, having the laser on-chip can even be detrimental, because the laser, depending on its efficiency, can generate a lot of heat and may be a significant contributor to the thermal budget of the chip. For these reasons, off-chip laser sources are likely to stay very important in the near future. The light from an off-chip source is usually delivered to

---

<sup>1</sup> This part closely follows our article [141], with appropriate modifications and extensions.

the silicon photonic chip with an optical fiber, and coupled from the fiber into the chip by means of a fiber-to-chip coupler.

Coupling of light between the fiber and a sub-micron strong-confinement waveguide is not a trivial task because of the enormous mode mismatch between them. The mode area needs to be reduced several hundred times for coupling light from a standard single-mode fiber into a sub-micron silicon waveguide, as illustrated in Fig. 54. This part of the thesis describes a new, two-section planar coupler design that transforms the mode from a fiber to a sub-micron strong-confinement waveguide with high efficiency and a reduced footprint on the chip [141-143]. In addition to the detailed analysis of the proposed two-stage couplers, this section also presents some fundamental results on plain inverse taper-based couplers, such as the dependence of mode conversion loss on the cross-section and refractive index of the low-index waveguide. Although the plain inverse-taper based couplers have by now been used by many groups, this is the first time a detailed analysis of their performance is carried out.

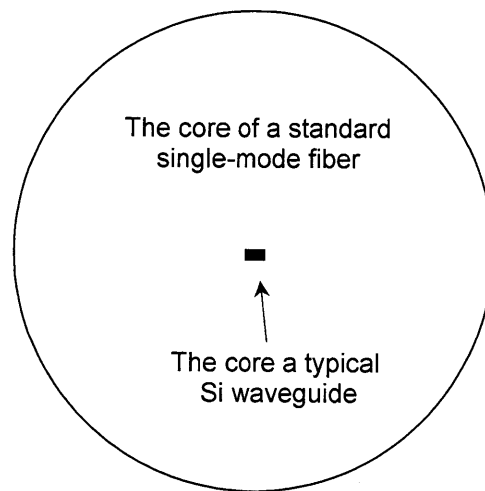


Figure 54. The core of a standard single-mode fiber (circle) and a silicon waveguide (rectangle), drawn to scale, to illustrate the large difference in the mode area which needs to be overcome by a fiber-to-chip coupler.

A number of solutions for coupling light between optical fibers and submicron strong-confinement waveguides have been developed [144]. These solutions can be categorized into in-plane and out-of-plane, depending on whether or not the optical fiber is located in the same plane with the optical chip. The benefit of in-plane approach is that a chip with the input/output fibers is easier to package, as compared to the case of out-of-plane couplers, where fibers are usually



oriented at an angle to the chip surface. The out-of-plane approach is advantageous when coupling light into an arbitrary location on a chip (not just into the end facet of the chip) is required; the total number of input/output connections can also be larger than for the in-plane approach. The most prominent in-plane and out-of-plane couplers are probably the inverse taper-based and grating-based couplers, respectively.

In couplers based on inverse tapers, the light from the fiber is first coupled into an intermediate waveguide with a mode size matching that of the fiber (see Fig. 55(a)). This waveguide is sometimes called the low index waveguide, because the index contrast between its core and undercladding is typically much lower than the index contrast of a strong-confinement (e.g. silicon) waveguide. An inverse high-index taper is then introduced inside the low-index waveguide. In the inverse taper, the high-index waveguide is very narrow in the beginning so that the fundamental mode is not confined to its core and virtually matches the mode of the low-index guide. The high-index waveguide is then adiabatically widened until the fundamental

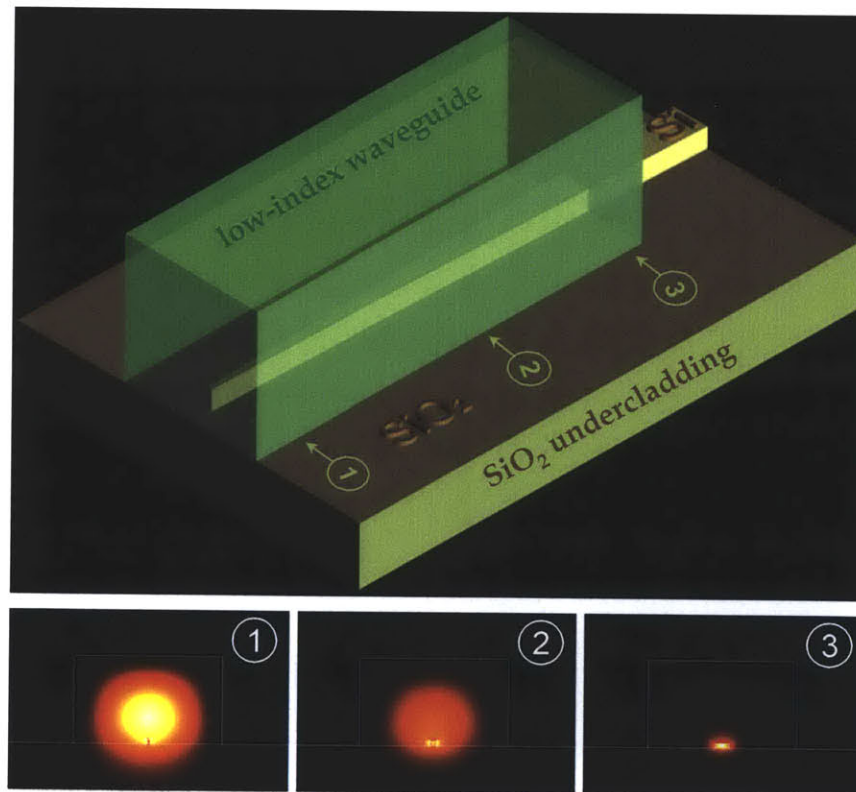


Figure 55. (a) Layout of the inverse taper-based adiabatic coupler (not drawn to scale). The light from the fiber is coupled into the fiber-matched low-index waveguide and transferred into a sub-micron Si waveguide with an inverse Si taper; (b) example of intensity distributions of the fundamental TE mode at positions labeled with numbers in Fig. 55(a).



mode of the structure becomes well-confined in the high-index core (see an example of mode evolution in Fig. 55(b)).

Inverse tapers have previously been used for coupling light between fibers and semiconductor lasers [145], and later the same concept was applied to Si waveguides [146-151]. Shoji and colleagues achieved 0.8 dB coupling loss between a fiber with 4.3  $\mu\text{m}$  mode size and a  $0.3 \times 0.3 \mu\text{m}$  Si waveguide [146]. They later reduced the loss to 0.5 dB by perfecting the fabrication and using a better material for the low-index waveguide [147]; the coupler length was more than 200  $\mu\text{m}$ . A coupling loss of 2.5 dB was measured for a standard fiber with 9  $\mu\text{m}$  mode. In the work of McNab and colleagues [148], 0.5 dB coupling loss has been reported between a microlensed fiber with 2.1  $\mu\text{m}$  beam diameter and a  $0.45 \times 0.22 \mu\text{m}$  Si waveguide with 150  $\mu\text{m}$  inverse taper length; the measurement uncertainty was 0.4 dB. In the work of Almeida and colleagues [149], a compact 40  $\mu\text{m}$ -long inverse taper with parabolic width profile has been proposed, with theoretical coupling loss of about 0.5 dB for the TE mode. Because the inverse taper did not have a fiber-matched low-index waveguide on top of it, high efficiency could not be achieved for TE and TM modes simultaneously; in addition, the coupling efficiency was sensitive to errors in Si tip width, because the diameter of the deconfined mode at the tip is strongly dependent on small changes in its width. The experimental coupling loss for a fiber with  $\sim 5 \mu\text{m}$  mode field diameter was 3.3 dB for TE and 6.0 dB for TM modes. While the other works mentioned above relied on e-beam lithography for coupler fabrication, in [150] and [151] the coupler was made with CMOS fabrication tools using 248 nm deep UV lithography. In [150], 1 dB mode conversion loss and 1.9 dB total loss have been demonstrated between a lensed fiber and a sub-micron silicon waveguide with  $3 \times 3 \mu\text{m}$  overlaying low-index waveguide. In [151], a coupling loss of less than 1 dB has been reported between a  $4.5 \times 4.5 \mu\text{m}$  low-index waveguide and a  $0.4 \times 0.7 \mu\text{m}$  high-index waveguide with 2.05 refractive index, and 350  $\mu\text{m}$  inverse taper.

The second important class of fiber-to-chip couplers is out-of-plane grating-based couplers, in which the light propagating in a waveguide is scattered by a grating; the scattered light is collected by a fiber which is placed in the vertical plane, usually at an angle to the chip normal. An important benefit of vertical couplers is that the light can be coupled in and out at an arbitrary location on the chip, and not only at the chip facet. A number of vertical coupler designs has been proposed and demonstrated [152-157]. To achieve high coupling efficiency, it is necessary to break the top-bottom symmetry of the structure, otherwise the light from the waveguide will

be scattered both upwards and downwards. To break the symmetry, a reflector at the bottom of the waveguide can be introduced; 0.4 dB coupling loss was predicted for a coupler with a dual-layer Bragg reflector [153], and a coupler with about 1.5 dB loss utilizing a gold reflecting layer has been demonstrated [155]. Another way to break the symmetry is to use a two-level grating teeth design [157].

There exists another class of in-plane fiber-to-chip coupler structures where the light from the fiber is coupled into a fiber-matched waveguide with a rib which is adiabatically reduced in width along the coupler in order to shrink the mode size vertically by "squeezing" the mode out from the rib [158-163]. Such structures are usually used for coupling light into rib waveguides, which is an easier problem than coupling into wire waveguides because the mode size in the former is much larger. In [158, 159], the light from a fiber is first coupled into a rib waveguide with matching mode, and then transferred into a rib waveguide with smaller mode size. In [158], the measured coupling loss was less than 0.5 dB, the input waveguide rib width was 12  $\mu\text{m}$ , and the taper length was 1 mm. In [159], a coupling loss of less than 1 dB was reported. The fiber mode diameter was 10.4  $\mu\text{m}$ , the input fiber-matched rib waveguide was 12.5 $\times$ 12.5  $\mu\text{m}$  (width  $\times$  height) with 10  $\mu\text{m}$  etch depth, the output rib waveguide was 3 $\times$ 4  $\mu\text{m}$  with 2  $\mu\text{m}$  etch depth, and the taper length was about 3 mm. In [160], the mode conversion between a 6.8 $\times$ 9.4  $\mu\text{m}$  rib waveguide and a 2.8 $\times$ 3.8  $\mu\text{m}$  rib waveguide has been demonstrated with the loss of 0.7 $\pm$ 0.2 dB; this number did not include the loss due to mode mismatch between the fiber and the rib waveguide. In [161], the upper-layer silicon rib was separated from the lower silicon layer by a thin oxide layer. The effective indices in the upper and the lower layers were matched and light was transferred into the lower layer according to coupled mode theory. This concept eliminates the need to create a very narrow and tall tip at the point where the upper layer is terminated. Simulations predicted less than 0.5 dB coupling loss into a sub-micron silicon rib waveguide for a 810  $\mu\text{m}$ -long coupler with a 5 $\times$ 5  $\mu\text{m}$  input Si facet. In [162], a coupler with two ribs with adiabatically decreasing widths has been proposed and fabricated. The introduction of two ribs allowed coupling of light from a standard single-mode fiber rather than from a small-core fiber with reasonable device length. The measured coupling loss from SMF-28 fiber into a 1.5  $\mu\text{m}$ -thick silicon rib waveguide was about 1.5 dB with a coupler length of 1mm. In [163], it was proposed to use a tapered-rib coupler to couple light directly into a silicon wire waveguide. The simulations predicted 0.5-1 dB coupling loss, depending on the height of the output wire

waveguide, for a 700  $\mu\text{m}$ -long coupler with optimized shape. At the input, the silicon thickness was 4.1  $\mu\text{m}$  and the rib width was 2.4  $\mu\text{m}$ .

Many other coupler designs have been proposed and demonstrated [164-169]. Many of them rely on complex fabrication techniques to shrink the mode size vertically along the coupler. For example, two cascaded tapers, a horizontal one with varying width and a vertical one with varying thickness, were used in [164] to demonstrate 0.5 dB conversion loss from a Si wire waveguide into a  $5.1 \times 9.2 \mu\text{m}$  mode. The coupler length was about 2 mm. Other fabrication efforts of vertical tapers with varying thickness include [165] and [166], with measured coupling losses of 2.2-3.5 dB and 16-17 dB, respectively. Another approach is to use a graded index layered structure in vertical direction which acts as a lens, combined with a short non-adiabatic taper in horizontal direction [167]. The coupling loss of about 2 dB [168] and 0.45 dB [169] has been demonstrated for a 20  $\mu\text{m}$ -long coupler.

In this section, we introduce a novel two-stage in-plane coupler design, which combines a rib taper and inverse taper to achieve high mode conversion efficiency [141-143]. It is shown that the two-stage design allows to reduce coupler length at least 2-3 times compared to the pure inverse taper-based coupler of equal efficiency. This allows to couple light from fibers with larger mode size than is possible with inverse taper-based couplers.

In a recent work, a coupler which, similarly to our design, has both a rib taper and an inverse taper has been proposed and demonstrated [170]. The low-index material was  $\text{SiO}_2$  itself, with the silicon substrate below it locally removed to form a suspended  $\text{SiO}_2$  waveguide. The input  $6 \times 6 \mu\text{m}$  cross-section of the suspended  $\text{SiO}_2$  waveguide was reduced to  $2 \mu\text{m}$  horizontally and  $5 \mu\text{m}$  vertically using a lateral and a rib taper. After this, a two-layer inverse Si taper was used to convert the mode into Si waveguide. The theoretical loss for a 150  $\mu\text{m}$ -long coupler was 0.9 dB for TE mode, and the measured loss was 1.7-2.0 dB for TE mode and 2.0-2.4 dB for TM mode for a lensed fiber with 5  $\mu\text{m}$  mode diameter. For a fiber with 9.2  $\mu\text{m}$  mode diameter, the loss was 3.8 dB for TE mode and 4.0 dB for TM mode. Note that although the concept used in [170] is close to the one proposed in our work because it uses both a rib and an inverse taper, there are several important differences. First, our design does not require fabrication of suspended structures and underetching of Si substrate. Second, the rib taper plays a much more prominent role in our design, reducing the vertical extent of the mode by a factor of two or more,

while in [170] the vertical size was reduced only from 6 to 5  $\mu\text{m}$ . Third, the focus of our work is on understanding the benefits of the two-stage coupler and studying how its performance depends on multiple parameters, while in [170] only one coupler design with fixed parameters has been considered.

The principles of operation of the proposed two-stage coupler are explained in Chapter 27 and optimization of its parameters is described in Chapter 28. The performance of the two-stage coupler is analyzed in Chapter 29. Chapters 30 and 31 discuss the choice of the refractive index of the low-index waveguide and the polarization dependence of the coupler, and the concluding Chapter 32 summarizes the results. Throughout this section, the proposed two-stage design is compared to the design based on pure inverse tapers.

## **27. Concept of the two-stage coupler**

The layout of the proposed two-stage coupler is shown in Fig. 56(a). The mode evolution along both stages of the coupler is illustrated in Fig. 56(b). In stage I, the light from the fiber is coupled into a rectangular low-index waveguide with matching mode size. A rib is then introduced in this waveguide. The rib is gradually tapered down along the coupler so that the light is adiabatically transferred into the wider bottom section of the waveguide. When the rib becomes narrow enough, the mode is confined mostly in the wider bottom section of the waveguide, therefore the rib can be terminated at a finite (non-zero) width with very low optical loss. In this way stage I of the coupler, which is referred to as a “rib taper,” adiabatically transfers the optical field from a large fiber-matched rectangular waveguide into a rectangular waveguide of smaller size.

In stage II of the coupler, a high-index inverse taper is introduced inside the low-index waveguide. In this work we consider silicon as the high-index waveguide material, however, the proposed two-stage coupler concept is expected to be useful also for coupling into other strong-confinement waveguides, such as silicon nitride waveguides. The inverse silicon taper starts from a very narrow tip, so that the mode of the structure is poorly confined in the tip and virtually matches the mode of the lower-index waveguide. The width of the silicon waveguide is then gradually increased so that the mode becomes more and more confined in the Si core, until most of the light is adiabatically transferred from the lower-index into the Si waveguide. At this

point the low-index waveguide can be terminated. Stage II of the coupler, which we will also refer to as an “inverse taper,” thus adiabatically converts the fundamental optical mode of the low-index waveguide into the mode of the sub-micron high-index waveguide.

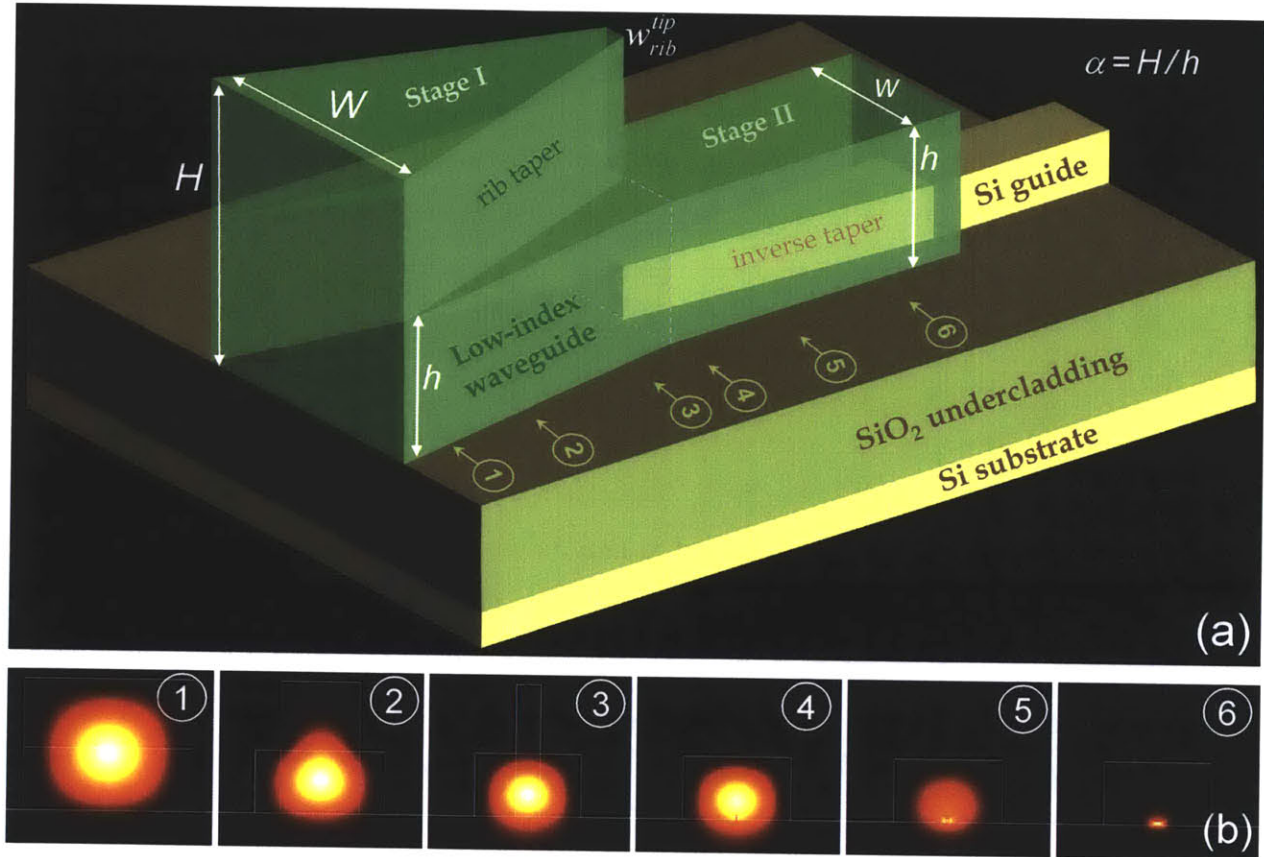


Figure 56. (a) Layout of the two-stage adiabatic coupler (not drawn to scale). The light from the fiber is coupled into the fiber-matched low-index waveguide, transferred into a smaller waveguide in stage I using a rib taper, and coupled into sub-micron Si waveguide in stage II using an inverse Si taper; (b) intensity distribution of the fundamental TE mode at positions labeled with numbers in Fig. 56(a). Positions 1-3 correspond to the rib taper and 4-6 to the inverse taper.

As described in Chapter 26, other groups have already used mode converters based on inverse tapers [145-151] as well as rib tapers [158-163]. The inverse taper has been demonstrated to work well for small-core fibers [145-151]. However, as shown in the following chapter, as the fiber core size increases, the length of the inverse taper required for efficient mode conversion increases rapidly, making the inverse taper-based design impractical for fibers with large cores.

Rib tapers easily match to large cores and were demonstrated to be efficient in reducing the mode size several times [158-163], but they cannot reduce the mode size dramatically with realistically short taper lengths. In the proposed two-stage design [143], the rib taper and inverse taper are sharing the mode reduction so that each of them is used efficiently: the rib taper matches to a fiber and reduces the mode size by a moderate amount, and the inverse taper couples the resultant mode into a sub-micron silicon waveguide. As a result, the combination of the two tapers couples light between a fiber and a sub-micron waveguide, overcoming the hundred-fold mode area mismatch with high efficiency and small footprint. Note that a coupler using both a rib and an inverse taper has been a topic of a recent work [170] discussed in Chapter 26.

The coupler proposed here can be fabricated as a post-processing step to silicon photonic circuit fabrication, by the deposition of low index layers and a two-step lithography. It should be noted that the two-step lithography can be performed on a single material deposition using dual masks, as previously demonstrated [171, 172]. Therefore, we expect that the fabrication complexity of this device is low in comparison to various designs requiring multi-layer fabrication or grayscale lithography, especially relative to the prospective gains in performance.

## 28. Optimization of two-stage couplers

This chapter explains the principles of finding the optimal parameters of the two-stage coupler. These principles will be used in the next chapter to evaluate the performance of the two-stage couplers in general and compare them to the pure inverse taper-based couplers.

Let  $H$  and  $h$  be the heights of the low-index waveguide at stages I and II, respectively (see Fig. 56(a)). Let  $\alpha$  be the ratio of heights of the two stages,  $\alpha = H/h$ , determining the amount by which the vertical extent of the mode is reduced by the rib taper. The low-index waveguide has width  $W$  at the beginning of stage I and is narrowed down to  $w$  in the base and  $w_{rib}^{tp}$  in the rib part. It is assumed that the low-index waveguide surrounding the inverse taper has width  $w$  which is constant along the taper. The refractive index of the low-index waveguide is  $n$ .

The values of some coupler parameters have not been subject to optimization and had been fixed in all simulations of this work. The silicon waveguide (refractive index 3.48) at the output of the coupler is assumed to be 600 nm wide and 105 nm tall. Such a design, having high aspect



ratio, offers low sensitivity to width variations and sidewall roughness [121]. A different silicon waveguide cross-section is only considered in Chapter 31 when discussing polarization dependence. The silicon oxide undercladding (refractive index 1.45) is assumed to be 3.0  $\mu\text{m}$ -thick, minimizing the optical leakage into the underlying silicon substrate. The optical wavelength of 1550 nm is used everywhere except the finite difference time domain simulations of Chapters 29 and 31.

The optimal choice of some coupler parameters is relatively straightforward. The cross-section  $W \times H$  of the low-index waveguide at the coupler's input facet is found from the requirement that the mode mismatch with the optical fiber is minimized. An optimal choice of the input cross-section leads to the mode mismatch loss of about 0.2-0.3 dB, assuming that there is no air gap between the fiber and the coupler input facet. In the two-stage coupler, optical losses are possible at locations where the optical structure is discontinuous, i.e. at the points where the rib is terminated, where the inverse Si taper is introduced, and where the low-index structure is terminated and only the Si waveguide remains. To avoid losses at the point where the low-index rib is terminated, the rib tip width  $w_{rib}^{tip}$  must be small enough so that the optical mode is confined mostly in the wider bottom section of the waveguide and is not affected by the termination of the rib. To minimize scattering at the tip of the inverse Si taper, the tip must be narrow enough so that the distortion it introduces to the low-index waveguide is very low and therefore the scattering loss is very low too. In this work, we assumed that the Si tip width is 50 nm and the rib tip width  $w_{rib}^{tip} = 0.5 \mu\text{m}$ . Finally, some optical loss can occur at the end of the coupler where the Si waveguide exits the low-index waveguide. For the Si waveguide cross-section of 600×105 nm, the loss is around 0.09 dB. If this loss needs to be reduced, the Si waveguide outside the coupler can be overlapped with a thin layer ( $\sim 1 \mu\text{m}$ ) of another material such as  $\text{SiO}_2$  (not shown in Fig. 56), so that the refractive index discontinuity experienced by the light traveling in the overlapping is minimized. Another solution is to widen the Si waveguide exiting the coupler in order to improve light confinement in the Si core and thus reduce the impact of the overlapping index discontinuity. For example, if the Si waveguide exiting the coupler is not 600 nm-wide but 1  $\mu\text{m}$ -wide, the loss is reduced from approximately 0.09 dB to 0.04 dB. We assumed that the losses at the tip of the inverse taper, at the tip of the rib taper, and

at the exit from the coupler can be reduced to negligible values, and therefore did not include any of them into consideration in the rest of this work.

There are also some important coupler parameters the optimization of which needs to be described in more detail. These parameters are the lengths of the two tapers and the height ratio  $\alpha=H/h$ . The coupler design and performance also depends on the refractive index of the low-index waveguide; this dependence will be investigated in the next chapters.

We first assume that the cross-sections of the two stages of the coupler are fixed and describe a way to find the optimal lengths of these stages. As an example, consider a coupler with  $W=H=10\text{ }\mu\text{m}$ ,  $w=h=4.5\text{ }\mu\text{m}$ , and low-index material refractive index  $n=1.50$ . The mode conversion losses of the fundamental TE mode in the rib and inverse tapers as a function of length of these tapers are shown in Figs. 57(a) and (b). Throughout this work, we consider TE-polarized light only, except in Chapter 31, where the polarization dependence in two-stage couplers is discussed. Unless stated otherwise, the light propagation in the tapered structures was simulated using the eigenmode expansion method, as implemented in the FIMMWAVE/FIMMPROP software package [173].

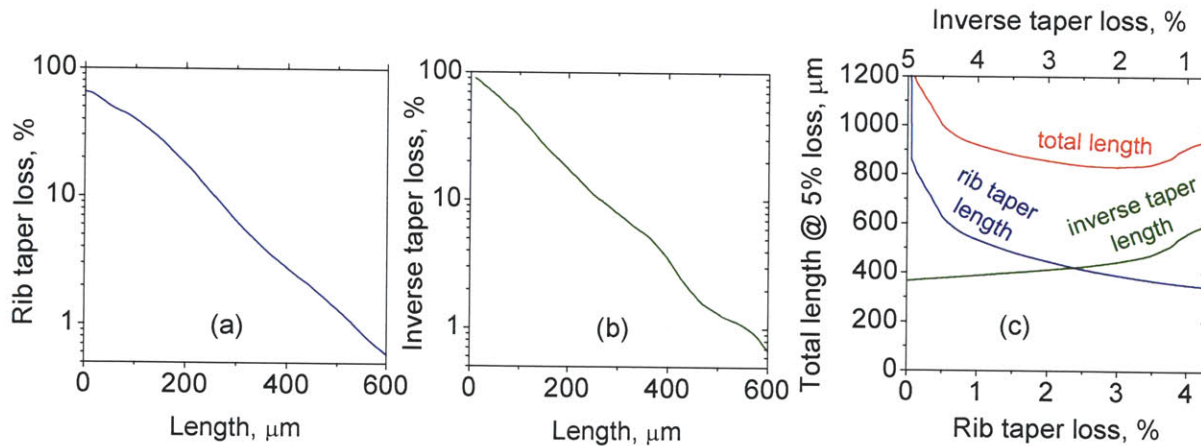


Figure 57. Optimization of rib and inverse taper lengths for a coupler with  $W = H = 10\text{ }\mu\text{m}$ ,  $w = h = 4.5\text{ }\mu\text{m}$ , and  $n = 1.50$ . Plots (a) and (b) show loss vs. length in the rib and inverse tapers. Plot (c) shows rib taper length, inverse taper length, and total length as a function of loss in the rib taper (bottom axis) and inverse taper (top axis), assuming 5% total loss in both tapers.

To minimize the mode conversion loss, the tapers should be made as long as possible. However, making the tapers very long is impractical not only because of chip area restrictions,

but also because of other sources of loss that are present in addition to the mode conversion loss. For example, the optical mode experiences scattering due to sidewall roughness of the inverse Si taper. The longer the taper, the higher the scattering loss, therefore increasing the taper length to improve its efficiency does become counterproductive at some point. Somewhat arbitrarily, we selected 5% mode conversion loss as the criterion for designing a coupler which is quite efficient yet reasonably short.

To make a two-stage coupler with 5% mode conversion loss as short as possible, the total loss of 5% should be split between the rib and inverse tapers in a way which minimizes the overall length. Fig. 57(c) shows the lengths of the rib taper, inverse taper, and the sum of the two (i.e. the total coupler length) as a function of loss in the rib taper (bottom axis) for our example. The loss in the inverse taper (top axis) is simply 5% minus the loss in the rib taper. We can see that the plot of the total length has a minimum at about 3% loss in the rib taper and 2% loss in the inverse taper. In a similar way, we can find the optimal lengths of the two stages for any given cross-sections of the two stages.

The next step is to choose the optimal value of the height ratio  $\alpha=H/h$ . This parameter controls how much of the total mode area reduction occurs in the rib, and how much in the inverse taper. Larger  $\alpha$  means the mode area is reduced more in the rib taper and less in the inverse taper, therefore the rib taper needs to be longer and the inverse taper can be shortened. This is illustrated in Fig. 58, which shows the lengths required for 5% mode conversion loss in the rib taper (Fig. 58(a)) and inverse taper (Fig. 58(b)) as a function of stage II height  $h$ . In this example, it is assumed that  $W=H=10\text{ }\mu\text{m}$ ,  $w=h$ , and refractive index  $n=1.50$ . The total length of the coupler is the sum of the rib taper length and the inverse taper length, the former increasing and the latter decreasing with  $\alpha$ . One might expect that there exists an optimal height ratio  $\alpha$  which minimizes the total length of the two stages. Fig. 59 plots the total length as a function of  $\alpha$ . For each  $\alpha$ , the algorithm described in the previous paragraph has been used to optimize the lengths of the rib and inverse tapers; these optimized values are also plotted in Fig. 59. We can see that the plot of total length versus  $\alpha$  indeed has a minimum, in this example reached for  $\alpha$  around 2.2-3.0. Using this approach we can find the optimum value of  $\alpha$  for any coupler with given input width  $W$ , height  $H$ , and refractive index  $n$ .

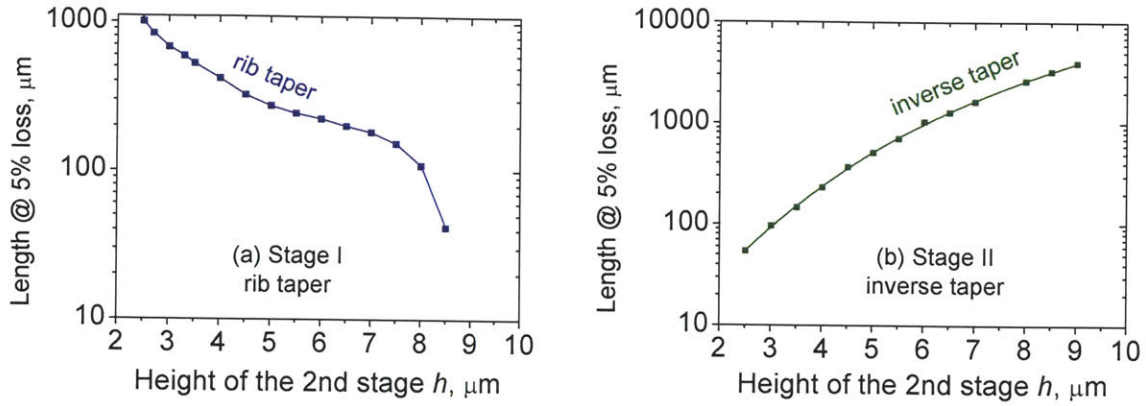


Figure 58. (a) Length of stage I (rib taper) and (b) length of stage II (inverse taper) as a function of stage II height  $h$ . It is assumed that  $W=H=10\text{ }\mu\text{m}$ ,  $w=h$ , and  $n=1.50$ . The lengths correspond to 5% mode conversion loss.

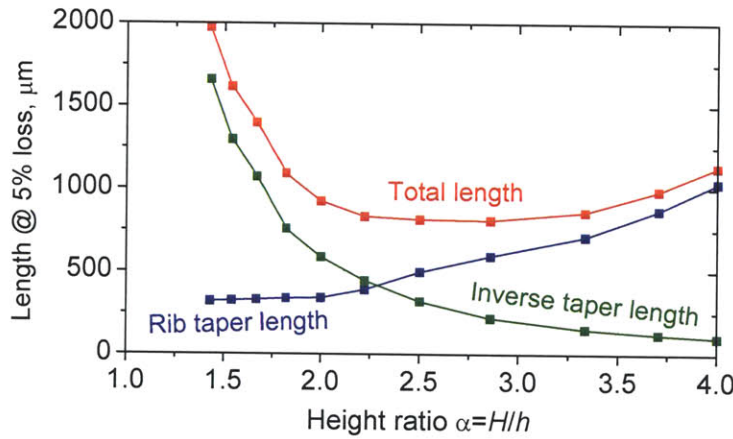


Figure 59. The total coupler length corresponding to 5% mode conversion loss as a function of height ratio  $\alpha$  for  $H=W=10\text{ }\mu\text{m}$ ,  $w=h$ ,  $n=1.50$ . For each  $\alpha$ , the lengths of the rib and inverse tapers were optimized (the optimal values are also plotted) to minimize the total length.

One important observation in Fig. 58(b) is how fast the length of the inverse taper increases with the height  $h$  of the low-index waveguide. This fast increase is presumably the reason why inverse taper-based couplers developed so far were limited to matching small-core fibers only [146-151]. In our example with low-index waveguide with  $W=H=10\text{ }\mu\text{m}$  and  $n=1.50$ , if an inverse taper only is used to transfer the light into the Si waveguide (i.e.  $w=h=10\text{ }\mu\text{m}$ ), the inverse taper length needs to be about 6 mm for 5% mode conversion loss. This is too much for most applications. By using the optimized two-stage design, the length can be reduced to about

800  $\mu\text{m}$  (Fig. 59), which is already practical for many applications. The proposed two-stage concept therefore allows one to create couplers for fibers with core sizes larger than is possible with pure inverse taper-based couplers.

Also note the fact that there exists a wide range of values of  $\alpha$ , roughly from 2 to 3, over which the coupler design is close to the optimum. Because tall and narrow ribs can be challenging to fabricate, one might prefer to choose a smaller rather than larger  $\alpha$  at the expense of a modest increase in coupler length.

## 29. Performance of optimized two-stage couplers

This chapter studies the performance of the optimized two-stage fiber-to-chip couplers as a function of the fiber mode size and the refractive index of the low-index waveguide. The performance of the two-stage couplers is also quantitatively compared to the current state-of-the-art in in-plane couplers, i.e. the couplers based on inverse tapers.

The performance of the inverse and rib tapers depends on the refractive index of the low-index waveguide. To illustrate this, we calculated the length required for 5% mode conversion loss in a rib taper with  $W = H = 4.0 \mu\text{m}$ ,  $w = h = 2.0 \mu\text{m}$  (see Fig. 56(a) for the notation) and an inverse taper with  $w = h = 4.0 \mu\text{m}$  as a function of refractive index  $n$  (see Fig. 60). We can see that the length of the inverse taper changes considerably with  $n$ , while the length of the rib taper changes only slightly. Therefore, one can expect the dependence of the coupler length on the refractive index to be different for the inverse taper-based coupler and the two-stage coupler, which incorporates both the rib and the inverse taper. To make a valid comparison between the two designs, one needs to make the refractive index a parameter of this comparison.



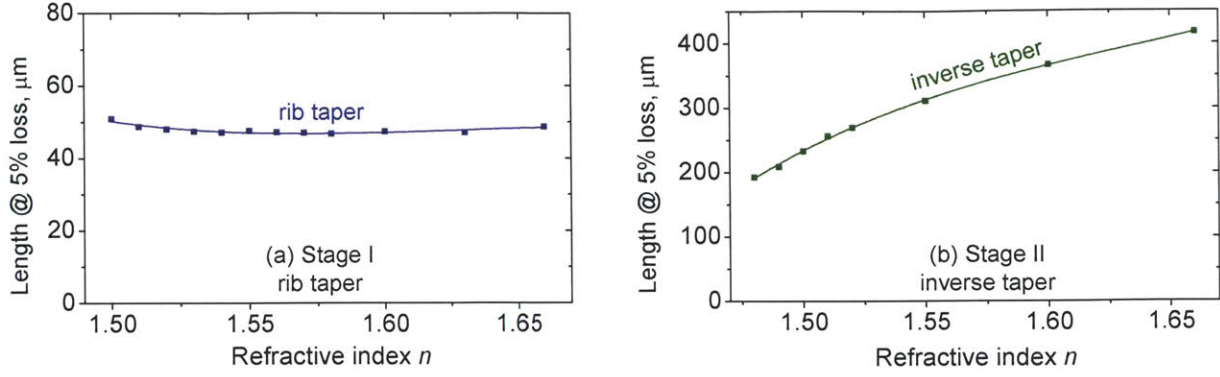


Figure 60. Dependence of length on refractive index for (a) rib taper with  $H = W = 4 \mu\text{m}$ ,  $h = w = 2 \mu\text{m}$ , (b) inverse taper with  $w = h = 4 \mu\text{m}$ . The refractive index of the  $\text{SiO}_2$  undercladding is 1.45.

To evaluate and compare the performance of the two-stage and the inverse taper-based couplers, we optimized the coupler design for two values of fiber mode field diameter (MFD) and multiple values of low-index waveguide refractive index  $n$ . The values of MFD were  $4.0 \mu\text{m}$  and  $8.0 \mu\text{m}$ , as defined by the  $1/e^2$  intensity diameter.  $4.0 \mu\text{m}$  is the MFD of a small-core fiber, while  $8.0 \mu\text{m}$  is a MFD close to the  $10 \mu\text{m}$  MFD of a standard single-mode fiber. The optimization results are presented in Figs. 61 and 62. In these figures, the plots on the left correspond to  $\text{MFD} = 4.0 \mu\text{m}$ , plots on the right to  $\text{MFD} = 8.0 \mu\text{m}$ , and the refractive index  $n$  is the x-axis parameter in all the plots. Fig. 61(a) shows the lengths of the two-stage and inverse taper-based couplers matched to the same fiber and having the same mode conversion loss. Fig. 61(b) shows the ratio of these two lengths, indicating how much the coupler length can be reduced by switching from the inverse taper-based design to the proposed two-stage design.

For each data point of Fig. 61, the two-stage coupler parameters were optimized as described in the previous chapter. The optimized parameter values are presented in Fig. 62. The lengths of each section as well as the total length of the two-stage coupler are plotted in Fig. 62(a). The height ratio  $\alpha$  of the optimized designs is shown in Fig. 62(b). One can see that as  $n$  increases, the optimal  $\alpha$  becomes larger, i.e. the role of the rib taper, which has almost index-independent efficiency, becomes more important. This allows the length of the optimized two-stage coupler to be a weaker function of  $n$  than the length of the inverse taper-based coupler.

To minimize the loss at the fiber–low index waveguide interface, the width  $W$  and height  $H$  of the low-index waveguide must be selected to maximize the overlap with the fiber mode.



Because the waveguide mode profile depends on its refractive index  $n$ , the values of  $W$  and  $H$  must be adjusted for each value of  $n$  to ensure matching to the fiber. Fig. 62(c) shows  $W$  and  $H$  which were used for our two-stage and inverse taper-based designs. According to Fig. 62(c), the waveguide height varies more with refractive index than the width, which happens because the index contrast between the low-index waveguide and SiO<sub>2</sub> undercladding is relatively low and the mode extends more and more into the undercladding as the refractive index decreases.

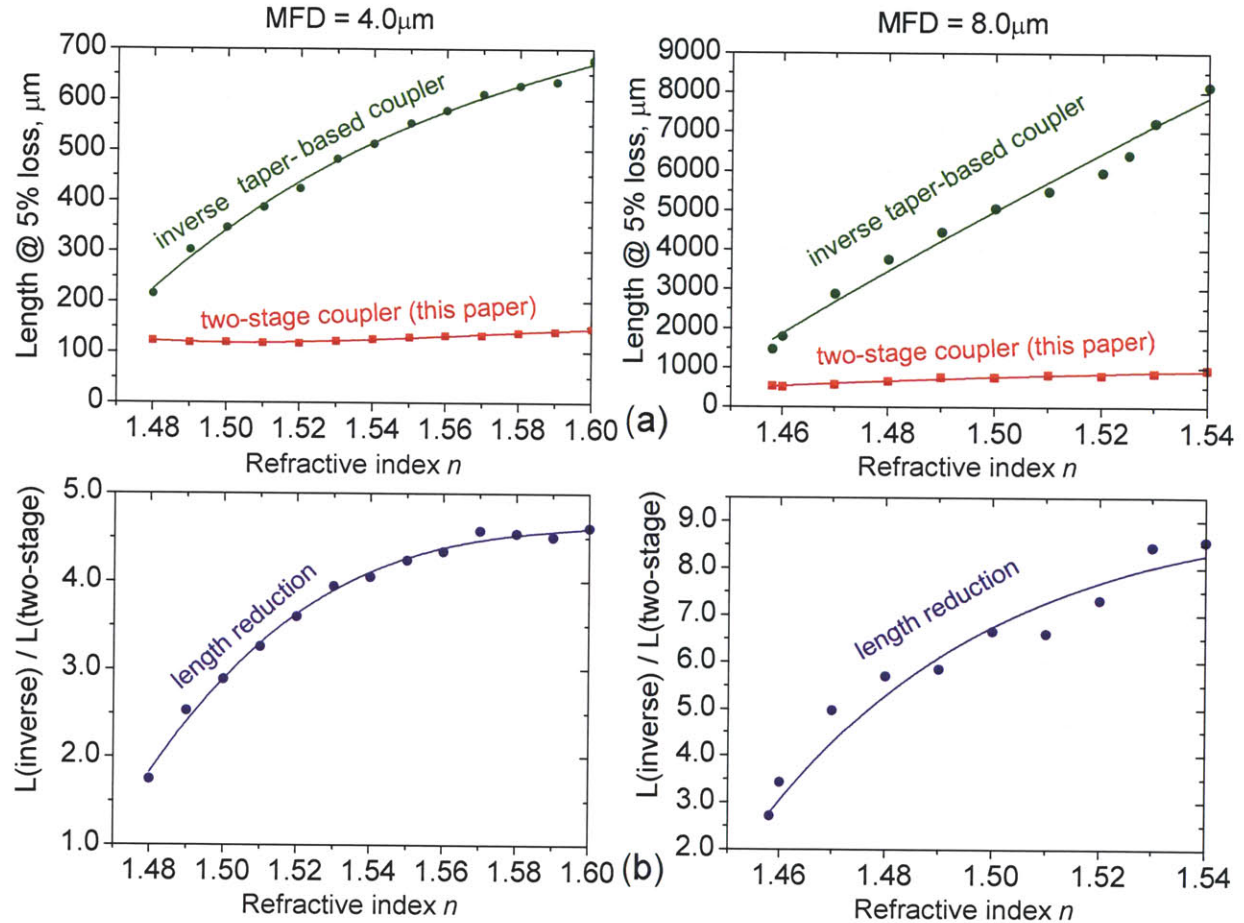


Figure 61. Performance of the two-stage and inverse taper-based couplers designed for fibers with MFD=4.0  $\mu\text{m}$  (plots on the left) and 8.0 $\mu\text{m}$  (plots on the right) as a function of the refractive index  $n$ . (a) Lengths of the optimized two-stage and inverse taper-based couplers with the same input cross-sections and 5% mode conversion loss, and (b) the ratio of these two lengths. The data points represent simulation results, and the curves are the fits to these points. The details of the designs can be found in Fig. 62.

There is one parameter of the two-stage coupler – the width  $w$  of the low-index waveguide in the inverse taper section – which has not been discussed yet. It turns out that the inverse taper

length is a much weaker function of width  $w$  than of height  $h$ , as illustrated in Fig. 63. For this reason, instead of performing rigorous optimization of  $w$ , we assumed that the rib taper reduces both the height and the width by the same geometry shrink factor  $\alpha$ , i.e.  $w = W / \alpha$ . There is a concern, however, that for low refractive indices the fundamental mode of the waveguide with  $w = W / \alpha$  and  $h = H / \alpha$  might experience loss due to leakage through the SiO<sub>2</sub> undercladding. Having a thick enough undercladding is therefore important for efficient operation of low-index two-stage couplers; 3.0  $\mu\text{m}$  thickness is assumed in this work. Still, for large  $\alpha$  and low  $n$  the leakage loss can be non-negligible. To resolve this problem, we adopted the following approach: if the leakage loss for  $w = W / \alpha$  exceeded 10 dB/cm, we increased the width  $w$  until the loss was reduced below 10 dB/cm. This increase in width  $w$  for large  $\alpha$  means that the inverse taper needs to be longer and therefore the length of the two-stage coupler will increase. This shifts the optimal geometry shrink factor  $\alpha$  to smaller values for low refractive indices. This approach has been used to obtain the results of Fig. 61; the corresponding widths  $w$  are shown in Fig. 62(c) together with heights  $h$  which are always equal to  $H/\alpha$ . Note, that the local substrate removal [174, 170] can eliminate the leakage loss altogether and therefore result in better performance of low-index two-stage couplers.

One observation with respect to the simulation results that is worth addressing is that the plots of some of the data are not entirely smooth (see Figs. 61, 62 as well as Figs. 58-60). This is because the underlying dependence of mode conversion loss on taper length is typically not a perfectly smooth function but exhibits some oscillations due to phase-dependent energy exchange between the fundamental and multiple higher-order modes. This energy exchange occurs because pushing these designs to shorter lengths means a departure from entirely adiabatic behavior, and a need to deal with some degree of mode coupling. For example, consider the last three points ( $n=1.58, 1.59, 1.60$ ) of the inverse taper length plot for MFD = 4.0  $\mu\text{m}$  (left plot in Fig. 61(a)), which are irregularly spaced along the y-axis. Fig. 64 shows how the mode conversion loss depends on taper length for these three refractive indices. We can observe that the loss decays with length in somewhat irregular way (see also Figs. 57(a), (b)), and sometimes the curves in Fig. 64 even intersect. As a result, the length shown in Fig. 61(a) is not a perfectly smooth function of the refractive index. The oscillations are especially visible in Fig. 62(b) showing the optimal height ratio  $\alpha$ . However, these oscillations

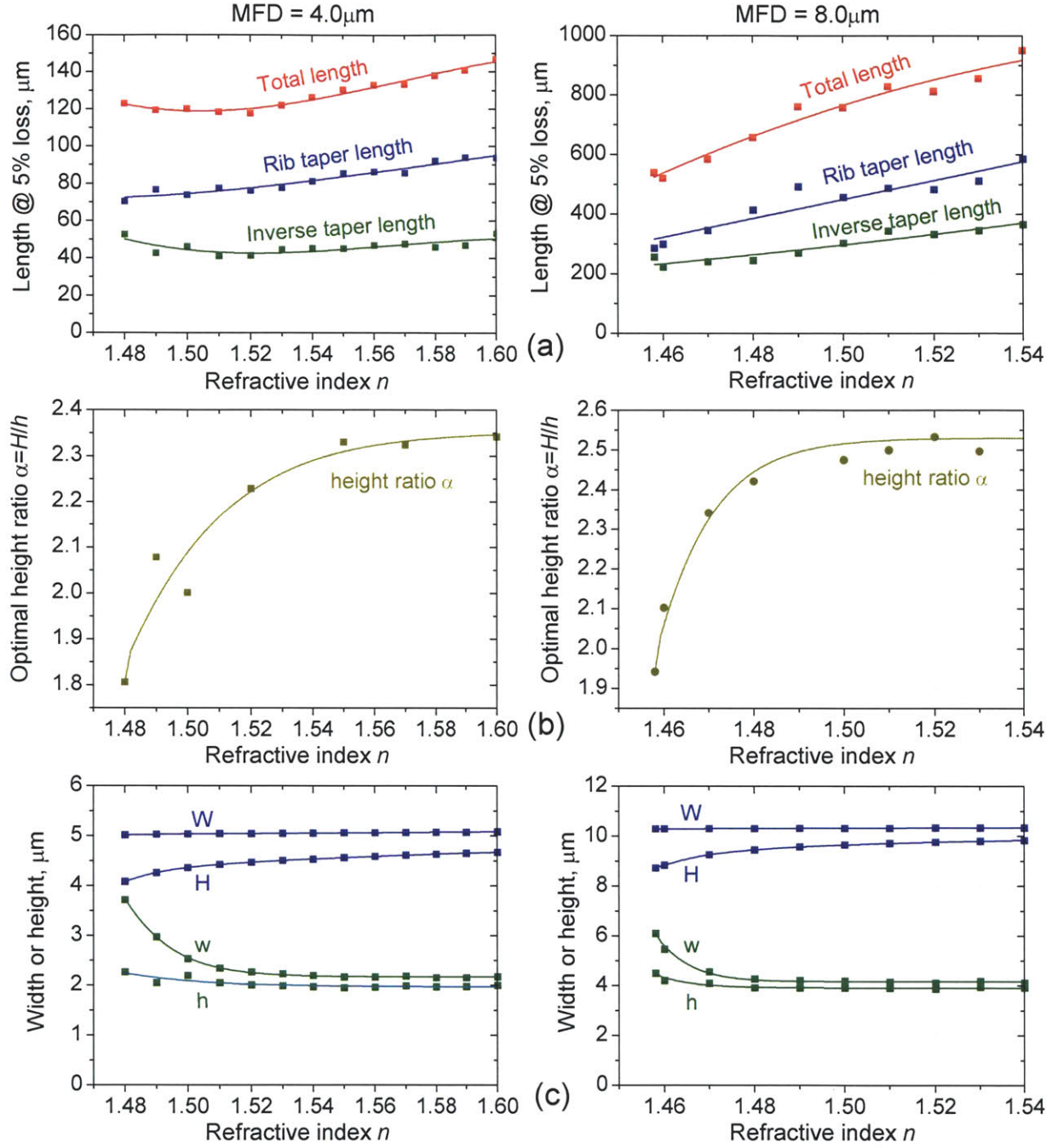


Figure 62. Parameters of the optimized two-stage couplers whose lengths are plotted in Fig. 61. The fiber MFD is  $4.0\mu\text{m}$  and  $8.0\mu\text{m}$  for the left- and the right-hand plots, respectively, and the coupler parameters are plotted as a function of refractive index  $n$ . (a) Lengths of the inverse taper section, rib taper section, and the total length of the optimized two-stage coupler with 5% mode conversion loss; (b) the height ratio  $\alpha$  of the optimized two-stage coupler; (c) width  $W$  and height  $H$  of the low-index waveguide at the input where it matches the fiber, as well as width  $w$  and height  $h$  of the low-index waveguide in the inverse taper section. The data points represent simulation results, and the curves are the fits to these points.

are not a problem because the range of  $\alpha$  for which the coupler performance is very close to the optimum is quite wide (see Fig. 59). Despite some oscillations, the general trend of all plots in Figs. 58-62 is stable.

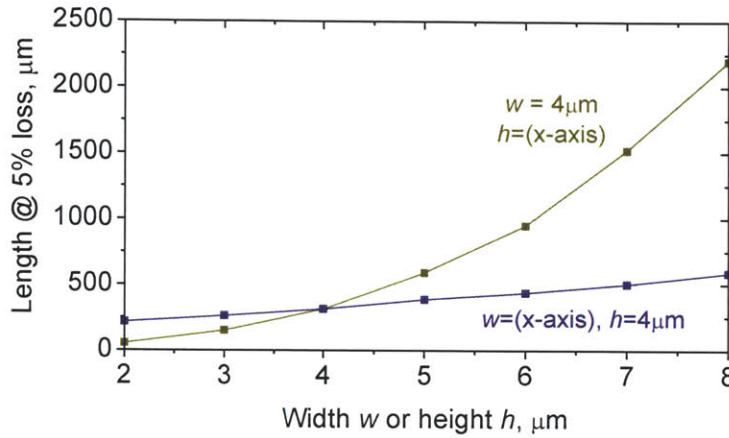


Figure 63. Dependence of inverse taper length on width  $w$  and height  $h$  of the low-index waveguide with  $n=1.55$ . For one curve, the width is  $4 \mu\text{m}$  and the height is the x-axis parameter, and for the other curve, the height is  $4 \mu\text{m}$  and the width is the x-axis parameter.

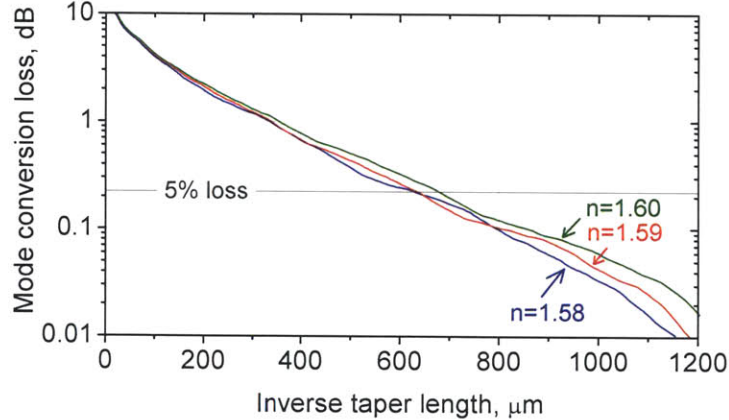


Figure 64. Mode conversion loss as a function of length of an inverse taper-based coupler matched to a fiber with  $\text{MFD}=4.0 \mu\text{m}$  for  $n=1.58, 1.59$ , and  $1.60$ . The last three points in the upper line in the left plot of Fig. 61(a) are given by intersection of the three curves of Fig. 64 with the 5% loss line.

All coupler simulations described in this and the previous chapters were carried out with the eigenmode expansion method [173], which allows relatively quick simulation of the light propagation in tapers. Once the output for one taper length is evaluated using this method, the

output for any other length can be obtained almost instantaneously, which has been very valuable for the taper optimizations performed in this work. However, the accuracy of the eigenmode expansion method depends on the number of modes included in the simulation, and in practice this number is limited. To verify that the accuracy of our eigenmode expansion simulations was sufficient, we performed a rigorous finite-difference time-domain (FDTD) simulation for one of the coupler designs.

Fig. 65(a) shows the mode conversion loss calculated with FDTD method for one of the two-stage coupler designs from Figs. 61, 62. The design selected for these simulations was for the coupler matched to a fiber with  $MFD = 4.0 \mu\text{m}$  with the refractive index of the low-index waveguide  $n = 1.55$ . The lengths of the rib taper section, inverse taper section, and the total length were  $85.5 \mu\text{m}$ ,  $45.1 \mu\text{m}$ , and  $130.6 \mu\text{m}$ , respectively. The low-index waveguide dimensions were  $W = 5.05 \mu\text{m}$ ,  $H = 4.56 \mu\text{m}$ ,  $w = 2.15 \mu\text{m}$ ,  $h = 1.95 \mu\text{m}$ , and  $w_{rib}^{up} = 0.5 \mu\text{m}$  (see Fig. 56 for notation), the silicon waveguide cross-section was  $50 \times 105 \text{ nm}$  at the beginning and  $600 \times 105 \text{ nm}$  at the end of the inverse taper. Similar to all coupler designs presented in Figs. 61, 62, this design was optimized for 5% (0.22 dB) mode conversion loss for TE-polarized light. FDTD simulation predicts 0.17-0.18 dB loss (Fig. 65(a)), confirming the validity of using the eigenmode expansion method for coupler optimization.

For comparison, the mode conversion loss in a pure inverse taper-based coupler of the same length and input cross-section was also calculated with FDTD method. The results are shown in Fig. 65(b). As expected, the pure inverse taper-based coupler of this length does not perform well, having about 10 times larger loss than the optimized two-stage coupler.

Notice that the two-stage coupler is very broadband, with very little efficiency variation over the simulated wavelength range of 100 nm (Fig. 65(a)). This was to be expected from a device based on the principle of adiabatic mode evolution.



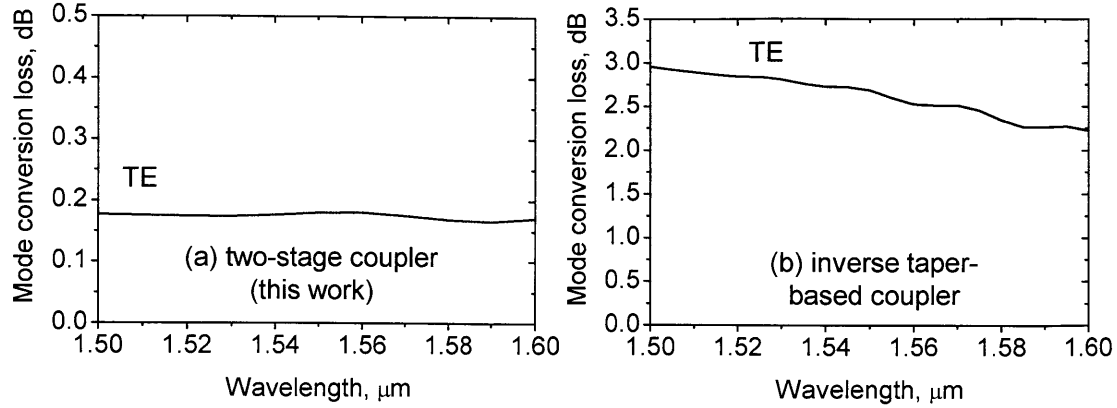


Figure 65. The loss in (a) an optimized two-stage coupler and (b) an inverse taper-based coupler of the same length, obtained with 3D FDTD simulations. The couplers were matched to a fiber with MFD = 4.0  $\mu\text{m}$ , the total length was 130.6  $\mu\text{m}$ , and the low-index waveguide had  $n = 1.55$ . The two-stage coupler was optimized for 5% (0.22dB) mode conversion loss at 1550 nm with the eigenmode expansion method [173].

### 30. Choice of refractive index of the low-index waveguide

As mentioned in the previous chapters, the performance of both the proposed two-stage couplers and inverse taper-based couplers depends on the refractive index of the low-index waveguide. Now, we would like to discuss the choice of refractive index in more detail.

In general, it is better to choose a lower value of refractive index  $n$  for both the two-stage and the inverse taper-based designs. This is true for two reasons, one being that the coupler length decreases as  $n$  becomes lower, especially in the case of pure inverse taper-based couplers. The second reason is that as  $n$  increases, the low-index waveguide at the coupler input turns from a single- into a multi-mode regime. In the two examples with MFD = 4.0  $\mu\text{m}$  and 8.0  $\mu\text{m}$  discussed in the previous chapters (see Figs. 61 and 62), the transition into multi-mode regime happens at  $n = 1.485$  and  $n = 1.459$ , respectively. It is often desirable to stay away from the multi-mode regime because of the possibility of multi-mode effects in the coupler. However, while a lower refractive index  $n$  is preferred, it should not be too low for three reasons: (1) if  $n$  is too low, the fundamental mode leaks through the  $\text{SiO}_2$  undercladding into the Si substrate; (2) the length of the two-stage coupler might actually increase when it becomes necessary to widen up the inverse taper stage for low values of  $n$ , as discussed in the previous chapter; (3) as  $n$  becomes lower, the index contrast with the undercladding is reduced, the fundamental mode becomes asymmetric, and the mode mismatch with the fiber increases. We did not perform



rigorous optimization of coupler performance which considers the impact of leakage loss of the fundamental mode and the increased mismatch with the fiber in case of low refractive indices. However, if the refractive index is chosen at the 2nd mode cutoff, i.e. if the refractive index is not too low while the coupler is still single-mode, the factors (1)-(3) mentioned above should not be significant and the coupler performance should be close to optimal. In our examples with  $MFD = 4.0 \mu\text{m}$  and  $8.0 \mu\text{m}$ , the refractive indices  $n = 1.485$  and  $n = 1.459$  should therefore give close-to-optimal performance. For these refractive indices, the two-stage design allows a reduction of the coupler length compared to the inverse taper-based design approximately by a factor of 2 and 3 for  $MFD = 4.0 \mu\text{m}$  and  $MFD = 8.0 \mu\text{m}$ , respectively.

However, it is not always possible to operate the low-index waveguide in the single-mode regime. This may happen because it might be difficult to select a material which has the specific value of refractive index necessary for optimum coupler performance and at the same time is compatible with existing fabrication processes and has the desired physical properties. Even if such a material is available, it might happen that the exact value of its refractive index cannot be controlled precisely enough, i.e. it is difficult to make sure that the refractive index of the fabricated waveguide is equal to the given pre-defined value in a reproducible way. Especially sensitive to refractive index variations are couplers designed for large mode field diameter fibers. In our example of the single-mode coupler with  $MFD = 8 \mu\text{m}$  and  $n = 1.459$ , an error in refractive index of 0.01 will cause the fundamental mode to be cut-off. To be on the safer side and make sure the coupler will function even if the refractive index turns out to be lower than expected, one may choose to use a material with a higher nominal refractive index value, in which case the coupler will operate in a multi-mode regime. For multi-mode couplers, the advantage of the two-stage design over inverse taper-based designs is especially high, as shown in Fig. 61(b).

If the low-index waveguide of the coupler is multi-mode, this does not necessarily leads to problems associated with multi-mode behavior. If the quality of fabrication is high enough, i.e. the imperfections such as sidewall roughness are low, there will be no energy exchange between the modes as they travel along the coupler because the effective mode coupling will be insufficient to overcome their propagation constant mismatch. If some of the higher-order modes happen to be excited due to misalignment of the input fiber, they will just radiate away at the end of the coupler and only the fundamental mode will be adiabatically coupled into the single-mode

Si waveguide. However, if the fabrication quality is not high enough, the coupling coefficients between the fundamental and the higher-order modes may be non-zero so that the modes will exchange energy as they propagate along the taper and the transmission spectrum of the coupler will exhibit oscillations, as observed in our previous work [175]. Depending on the magnitude of fabrication errors, these oscillations might be severe enough to render the coupler unusable. An example of such oscillations, measured for one of the multi-mode couplers, can be found in Fig. 66. Nevertheless, if the fabrication quality is high, as can be expected from today's photonic fabrication processes [176, 177], the coupling between the modes will be negligible and a multi-mode coupler will be fully functional, as demonstrated in [150] for an inverse taper-based coupler. If fabrication quality is high and multi-mode structures are acceptable, the two-stage design gives much more freedom in the choice of refractive index because its performance is not nearly as index-dependent as that of the inverse taper-based design (see Fig. 61(a)). This significantly broadens the range of materials that can be used for fabrication of the low-index waveguide.

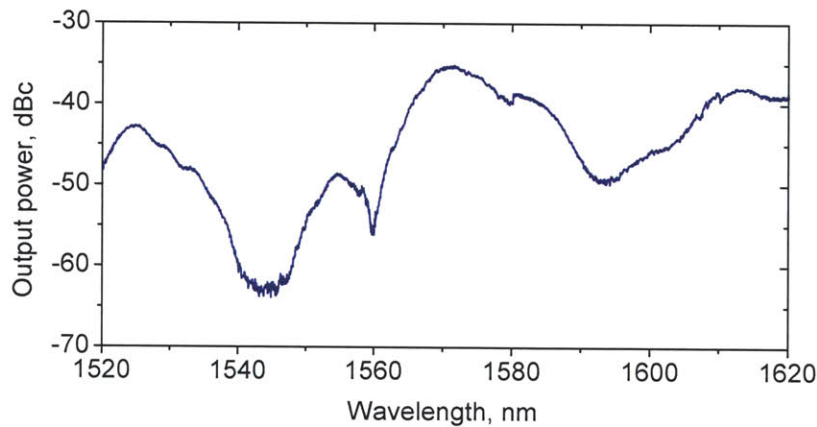


Figure 66. Spectral oscillations observed in a multi-mode coupler structure, with 8 concatenated inverse taper-based couplers [175]. The oscillations are attributed to multi-mode effects induced by fabrication imperfections. This example illustrates that single-mode structures might be required in some situations. However, if the fabrication quality is high, multi-mode effects are expected to disappear and multi-mode coupler structures are expected to be fully functional, as demonstrated in [150].

### 31. Polarization dependence in two-stage couplers

The designs presented in the previous chapters were optimized for TE-polarized light; the TM polarization was not considered. Couplers working only with TE polarization are useful for many applications, such as intra- and inter-chip communications and on-chip photonic analog-to-digital conversion, when the optical integrated circuits work with TE polarization only and the TM-polarized light is not used. However, in other applications, such as in fiber optics, polarization-independent coupler performance is essential [172]. Although we did not perform a rigorous study of the two-stage couplers for TM-polarized light, we predict that the two-stage design will be efficient in this case as well.

To confirm that the two-stage concept is efficient also for TM light, we selected one coupler design and performed FDTD simulations for both polarizations. In previous chapters, we considered silicon waveguides with  $600 \times 105$  nm cross-section which was optimized for TE light and had poor confinement of the TM mode. To make sure the TM mode is well-confined in the Si core, we increased the waveguide thickness to 220 nm. Assuming that the input fiber has  $MFD = 4.0$   $\mu\text{m}$  and the low-index waveguide has  $n = 1.55$ , we optimized the two-stage coupler design for TE light using the algorithm described in the pervious chapters. The lengths of the rib taper section, inverse taper section, and the total length were 85.2  $\mu\text{m}$ , 43.2  $\mu\text{m}$ , and 128.4  $\mu\text{m}$ , respectively. The low-index waveguide dimensions were  $W = 5.06$   $\mu\text{m}$ ,  $H = 4.56$   $\mu\text{m}$ ,  $w = 2.16$   $\mu\text{m}$ ,  $h = 1.96$   $\mu\text{m}$ ,  $w_{rib}^{tip} = 0.5$   $\mu\text{m}$ , and the Si waveguide was 50 nm wide at the beginning and 440 nm wide at the end of the inverse taper. According to the eigenmode expansion method, this TE-optimized design gives 5% (0.22 dB) mode conversion loss at 1550 nm.

The results of FDTD simulations are shown in Fig. 67(a). One can see that although the coupler was optimized for TE-polarized light, it performs quite well also for the TM polarization. For comparison, the loss in the pure inverse taper-based coupler of similar length and input cross-section was calculated, see Fig. 67(b). This loss is several times higher than for the two-stage design.

One detail to keep in mind when designing a polarization-independent two-stage coupler is that for low refractive indices the leakage through the  $\text{SiO}_2$  undercladding is higher for TM- than for TE-polarized light. Therefore, for small refractive indices, the height ratio  $\alpha$  might need to be reduced to make the coupler work efficiently for both polarizations.

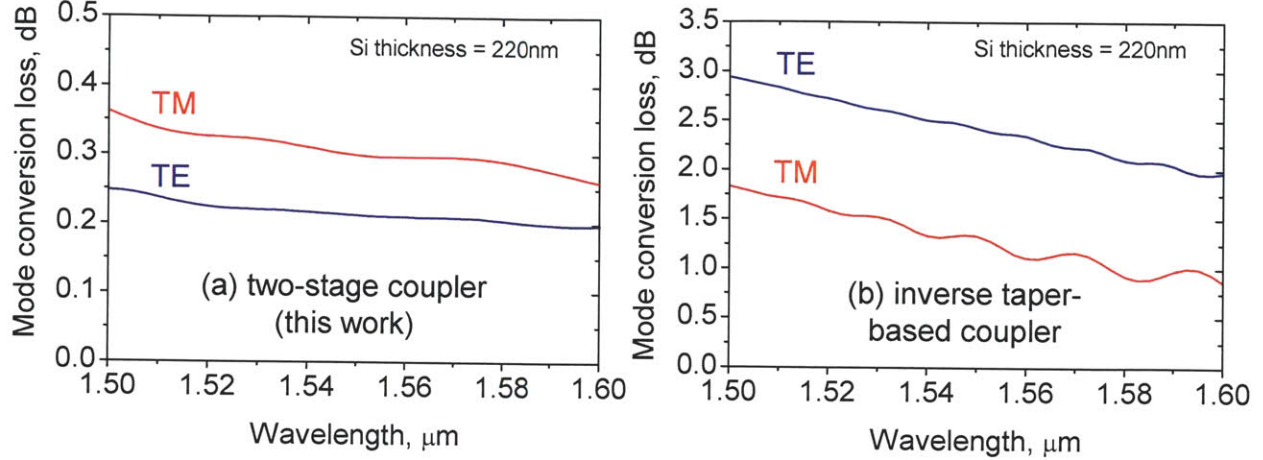


Figure 67. The loss in (a) an optimized two-stage coupler and (b) an inverse taper-based coupler obtained with three-dimensional FDTD simulations. The input fiber had MFD=4.0  $\mu\text{m}$ , the total length was 128.4  $\mu\text{m}$ , and the low-index waveguide had  $n=1.55$  for both cases. Compared to the other simulations of this work, the silicon waveguide thickness was increased from 105 nm to 220 nm to improve the confinement of the TM mode.

## 32. Summary and discussion

In this work, we described a new design of an adiabatic in-plane fiber-to-chip coupler which consists of two stages, a rib taper and an inverse taper. This design is compatible with planar fabrication technology and does not require to use such fabrication techniques as gray-scale lithography. Because the coupler operation is based on the principle of adiabatic mode evolution, its performance is broadband and is expected to be tolerant to fabrication errors.

The proposed two-stage design allows to reduce coupler length as compared to the state-of-the-art couplers based on inverse tapers with the same mode conversion efficiency. The magnitude of length reduction depends on the refractive index of the low-index material of the coupler and mode size of the fiber for which the coupler is designed. If the low-index waveguide is single-mode, the length of the couplers matched to fibers with MFD = 4.0  $\mu\text{m}$  and 8.0  $\mu\text{m}$  is reduced 2- and 3-fold, respectively. If the refractive index is higher, e.g. because no material with the required low index is available in the given fabrication process, the advantage of the two-stage design is even larger, enabling length reduction of up to about 4.5-fold for MFD = 4.0  $\mu\text{m}$  and even more for MFD = 8.0  $\mu\text{m}$ , depending on the exact value of the refractive index. However, the use of higher refractive index implies that the fiber-matched waveguide is

multi-mode, in which case the fabrication quality must be high enough to avoid power exchange between the modes propagating along the coupler.

To achieve high efficiency in a two-stage coupler, one needs to optimize the cross-section of the fiber-matched waveguide, the lengths of the rib and inverse tapers, the height ratio  $\alpha$ , as well as some other parameters. The optimization procedure is described in Chapter 28. For our two examples with  $\text{MFD} = 4.0 \text{ } \mu\text{m}$  and  $8.0 \text{ } \mu\text{m}$ , the optimal values of  $\alpha$  were between 2 and 3. It was found that the performance of the coupler is close to optimal within a quite wide range of  $\alpha$  so that the precise value of  $\alpha$  is not very important. For low refractive indices, care must be taken to avoid optical loss due to leakage of the fundamental mode through the oxide undercladding. The leakage loss can be reduced by limiting  $\alpha$  and widening the low-index waveguide in the inverse taper section.

The increased conversion efficiency offered by the two-stage coupler means that the footprint of the coupler on a chip can be reduced. Importantly, this also means that for a given footprint, the two-stage design can work with fibers with increased mode size. The increased fiber mode size leads to improved misalignment tolerances and simplified chip packaging. In addition, if a lensed fiber is used to bring light to the chip, a larger focal spot size usually means lower insertion loss because the lensed fiber losses are strongly spot size-dependent.

It is necessary to note that while in this work we were mostly discussing the mode conversion loss, there may be also other sources of loss in the coupler, such as the loss due to mode mismatch with the fiber (0.2-0.3 dB). Therefore, whenever it is mentioned that a coupler has a mode conversion loss of 5% (0.22 dB), it is necessary to keep in mind that the total loss of such a coupler is approximately 0.5 dB. Additional losses at locations where the rib taper ends, inverse taper starts, and the low-index waveguide overlaying the inverse taper is terminated can be avoided with proper design.

Another source of loss is the scattering loss induced by the sidewall roughness of the inverse Si taper. For given roughness, scattering losses increase as the waveguide becomes narrower [178], therefore the roughness-induced loss in the inverse taper will be higher than in a full-width Si waveguide of the same length. We did not consider the scattering-induced loss because it is determined by the fabrication quality and can in principle be reduced to a very low value as fabrication techniques are being improved. Even if this loss is high, e.g. 20 dB/cm, the

total loss in the inverse taper of the two-stage coupler is only around 0.1 dB for MFD=4.0  $\mu\text{m}$  and 0.5 dB for MFD = 8.0  $\mu\text{m}$  for the designs of Fig. 62. Note that compared to pure inverse taper-based couplers, the scattering loss in two-stage couplers is lower because their length is shorter and because the inverse taper occupies only a part of this length.

Although all optimizations in this work were carried out for TE-polarized light, we predict that the two-stage coupler concept is efficient for TE and TM polarizations simultaneously. This was confirmed with FDTD simulations for one example of a coupler design. In this example a Si waveguide with thicker core – 220 nm rather than 105 nm as in the rest of this work – has been assumed. Efficient operation of the two-stage coupler in this case illustrates that the two-stage design can be efficient for different Si waveguide geometries.

The couplers were designed assuming linear taper shapes in the two stages. Initial results on optimized taper shapes show that switching from a linear to an optimized taper shape [179] allows to gain a factor of 2-3 in length, which is in addition to the gain achieved by switching from the conventional inverse taper-based design to the two-stage design. This additional improvement in coupler efficiency should make it possible to practically couple light directly from standard single-mode fibers with 10  $\mu\text{m}$  mode field diameter. This subject requires further investigation.



## Appendix A. List of acronyms

ENOB	Effective Number of Bits
SNR	Signal-to-Noise Ratio
SFDR	Spur-Free Dynamic range
THD	Total Harmonic Distortion
SINAD	Signal-to-Noise and Distortion Ratio
dBc	dB below carrier
FSR	Free Spectral Range
MZ	Mach-Zehnder
MZM	Mach-Zehnder Modulator
TPA	Two-Photon Absorption
FCA	Free-Carrier Absorption
FCD	Free-Carrier Dispersion
FDTD	Finite Difference Time Domain methos

## Bibliography

1. R. Walden, "Analog-to-Digital Conversion in the Early Twenty-First Century," Wiley Encyclopedia of Computer Science and Engineering, pp. 126–138, 2008.
2. G. Valley, "Photonic analog-to-digital converters," *Opt. Express* **15**, pp. 1955–1982 (2007), <http://www.opticsinfobase.org/oe/abstract.cfm?URI=oe-15-5-1955>.
3. B. L. Shoop, "Photonic Analog-to-Digital Conversion" (Springer, New York, 2000).
4. Fujitsu Europe Press Release. Fujitsu launches second generation ultra-fast 65 GSa/s 8-Bit ADC technology for 100G optical transport. ([http://www.fujitsu.com/emea/news/pr/fseu-en\\_20100913-978.html](http://www.fujitsu.com/emea/news/pr/fseu-en_20100913-978.html)), September 13 (2010).
5. Y. M. Greshishchev, J. Aguirre, M. Besson, R. Gibbins, C. Falt, P. Flemke, N. Ben-Hamida, D. Pollex, P. Schvan, and S. Wang, "A 40 GS/s 6b ADC in 65 nm CMOS", International Solid State Circuits Conference (ISSCC), paper 21.7 (2010).
6. M. Chu, P. Jacob, Jin-Woo Kim, M. R. LeRoy, R. P. Kraft, and J. F. McDonald, "A 40 GS/s time interleaved ADC using SiGe BiCMOS technology," *IEEE J. Solid State Circuits* **45**, pp. 380–390 (2010).
7. J. Kim and F. X. Kärtner, "Attosecond-precision ultrafast photonics," *Laser & Photonics Reviews* **4**, pp. 432–456 (2010).
8. A. J. Benedick, J. G. Fujimoto, and F. X. Kärtner, "Ultrashort laser pulses: Optical flywheels with attosecond jitter," submitted to *Nature Photonics*.
9. H.A. Haus and A. Mecozzi, "Noise of Mode-Locked Lasers," *IEEE J. Quantum Electron.* **29**, pp. 983–996 (1993).
10. D. von der Linde, "Characterization of noise in continuously operating mode-locked lasers," *Appl. Phys. B* **39**, pp. 201–217 (1986).
11. D. E. Spence, J. M. Evans, W. E. Sleat, and W. Sibbett, "Regeneratively initiated self-mode-locked Ti : sapphire laser," *Opt. Lett.* **16**, pp. 1762–1764 (1991).
12. U. Keller, C. E. Socolich, G. Sucha, N. M. Islam, and M. Wegener, "Noise characterization of femtosecond color-center lasers," *Opt. Lett.* **15**, pp. 974–976 (1990).
13. D. R. Walker, D. W. Crust, W. E. Seat, and W. Sibbett, "Reduction of phase noise in passively mode-locked lasers," *IEEE J. Quantum Electron.* **28**, pp. 289–296 (1992).
14. J. Kim, J. Chen, J. Cox, and F. X. Kärtner, "Attosecond-resolution timing jitter characterization of free-running mode-locked lasers using balanced optical cross-correlation," *Opt. Lett.* **32**, pp. 3519–3521 (2007).
15. J. A. Cox, A. H. Nejadmalayeri, J. W. Kim, and F. X. Kärtner, "Complete characterization of Quantum-limited timing jitter in passively mode-locked fiber lasers," *Opt. Lett.* **35**, pp. 3522–3524 (2010).

16. H. Byun, A. Hanjani, S. Frolov, E. P. Ippen, D. Pudo, J. Shmulovich, F. X. Kärtner, "Integrated Low-Jitter 400-MHz Femtosecond Waveguide Laser," *IEEE Photon. Technol. Lett.* **21**, pp.763–765 (2009).
17. G. Gagliardi, M. Salza, S. Avino, P. Ferraro and P. De Natale, "Probing the Ultimate Limit of Fiber-Optic Strain Sensing," *Science* **330**, pp. 1081–1084 (2010).
18. S. A. Diddams, J. C. Bergquist, S. R. Jefferts and C. W. Oates, "Standards of Time and Frequency at the Outset of the 21st Century," *Science* **306**, pp. 1318–1324 (2004).
19. J. Lee, Y.-J. Kim, K. Lee, S. Lee, and S. Kim, "Time-of-flight measurement with femtosecond light pulses," *Nat. Photonics* **4**, pp. 716–720 (2010).
20. U. Keller, "Recent developments in compact ultrafast lasers," *Nature* **424**, pp. 831–838 (2003).
21. E. U. Rafailov, M. A. Cataluna, and W. Sibbett, "Mode-locked quantum-dot lasers," *Nature Photonics* **1**, pp. 395–401 (2007).
22. H. F. Taylor, M. J. Taylor, and P. W. Bauer, "Electro-optic analog-to-digital conversion using channel waveguide modulators," *Applied Physics Letters* **32**, pp. 559–561 (1978).
23. J. A. Bell, M. C. Hamilton, D. A. Leep, T. D. Moran, H. F. Taylor, and Y. H. Lee, "Extension of electronic A/D converters to multi-gigahertz sampling rates using optical sampling and demultiplexing techniques," *Twenty-Third Asilomar Conference on Signals, Systems and Computers*, pp. 289–293 (1989).
24. P. W. Juodawlkis, J. C. Twichell, G. E. Betts, J. J. Hargreaves, R. D. Younger, J. L. Wasserman, F. J. O'Donnell, K. G. Ray, R. C. Williamson, "Optically sampled analog-to-digital converters," *IEEE Transactions on Microwave Theory and Techniques* **49**, pp. 1840–1853 (2001).
25. J. A. Valdmanis, "Real time picosecond optical oscilloscope," *Proc. 5th OSA Top. Meet., Ultrafast Phenomena V*, pp. 82–85 (1986).
26. M. Y. Frankel, J. U. Kang, and R. D. Esman, "High performance photonics analogue digital converter," *Electron. Lett.* **33**, pp. 2096–2097 (1997).
27. A. Yariv and R. Koumans, "Time interleaved optical sampling for ultra-high speed A/D conversion," *Electronics Letters* **34**, pp. 2012–2013 (1998).
28. J. U. Kang and R. D. Esman, "Demonstration of time interweaved photonic four-channel WDM sampler for hybrid analogue-digital converter," *Electronics Letters* **35**, pp. 60–61 (1999).
29. R. C. Williamson, R. D. Younger, P. W. Juodawlkis, J. J. Hargreaves, J. C. Twichell, "Precision calibration of an optically sampled analog-to-digital converter," *2003 Digest of the LEOS Summer Topical Meetings*, pp. MC4.2/22–MC4.2/23, 14–16 July 2003.
30. A. S. Bhushan, F. Coppinger, and B. Jalali, "Time-stretched analogue-to-digital conversion," *Electronics Letters* **34**, pp. 1081–1083 (1998).
31. Y. Han and B. Jalali, "Photonic Time-Stretched Analog-to-Digital Converter: Fundamental Concepts and Practical Considerations," *J. Lightwave Technol.* **21**, pp. 3085–3103 (2003).
32. J. Chou, O. Boyraz, D. Solli, and B. Jalali, "Femtosecond real-time single-shot digitizer," *Applied Physics Letters* **91**, p. 161105 (2007).

33. G. Sefler, J. Chou, J. Conway, and G. Valley, "Distortion Correction in a High-Resolution Time-Stretch ADC Scalable to Continuous Time," *Journal of Lightwave Technology* **28**, pp. 1468–1476 (2010).
34. S. Gupta and B. Jalali, "Time warp correction and calibration in photonic time stretch analog-to-digital converter," *Opt. Lett.* **33**, pp. 2674–2676 (2008).
35. J. Chou, J. A. Conway, G. A. Sefler, G. C. Valley, and B. Jalali, "Photonic Bandwidth Compression Front End for Digital Oscilloscopes," *J. Lightwave Technol.* **27**, pp. 5073–5077 (2009).
36. P. W. Juodawlkis, J. J. Hargreaves, R. D. Younger, G. W. Titi, and J. C. Twichell, "Optical down-sampling of wide-band microwave signals," *Journal of Lightwave Technology* **21**, pp. 3116–3124 (2003).
37. J. Kim, M. J. Park, M. H. Perrott, and F. X. Kärtner, "Photonic subsampling analog-to-digital conversion of microwave signals at 40-GHz with higher than 7-ENOB resolution," *Opt. Express* **16**, pp. 16509–16515 (2008).
38. M. Jarrahi, R. Pease, D. Miller, and T. Lee, "Optical Spatial Quantization for Higher Performance Analog-to-Digital Conversion," *IEEE Transactions on Microwave Theory and Techniques* **56**, pp. 2143–2150 (2008).
39. J. Stigwall and S. Galt, "Demonstration and Analysis of a 40-Gigasample/s Interferometric Analog-to-Digital Converter," *J. Lightwave Technol.* **24**, pp. 1247–1256 (2006).
40. K. Ikeda, J. M. Abdul, H. Tobioka, T. Inoue, S. Namiki, and K. Kitayama, "Design Considerations of All-Optical A/D Conversion: Nonlinear Fiber-Optic Sagnac-Loop Interferometer-Based Optical Quantizing and Coding," *J. Lightwave Technol.* **24**, pp. 2618–2628 (2006).
41. G. C. Valley, "Photonic analog-to-digital converters: fundamental and practical limits," *Proceedings of SPIE* **5618**, pp. 96-106, 2004.
42. A. Nejadmalayeri, M. E. Grein, A. Khilo, J. Wang, M. Sander, M. Peng, C. Sorace, E. P. Ippen, and F. X. Kärtner, "A 16 fs aperture jitter photonic ADC: 7.0 ENOB at 40 GHz," *Conference on Lasers and Electro-Optics (CLEO) 2011*, paper CThI4.
43. H. Byun, M. Y. Sander, A. Motamedi, H. Shen, G. S. Petrich, L. A. Kolodziejski, E. P. Ippen, and F. X. Kärtner, "Compact stable 1 GHz femtosecond Er-doped fiber lasers," *Appl. Opt.* **49**, pp. 5577–5582 (2010).
44. T. R. Clark, M. Currie, and P. J. Matthews, "Digitally Linearized Wide-Band Photonic Link," *J. Lightwave Technol.* **19**, pp. 172-179 (2001).
45. J. C. Twichell, R. Helkey, "Phase-encoded optical sampling for analog-to-digital converters," *IEEE Photonics Technology Letters* **12**, pp. 1237–1239 (2000).
46. G. T. Reed, G. Mashanovich, F. Y. Gardes, and D. J. Thomson, "Silicon optical modulators," *Nature Photonics* **4**, pp. 518–526 (2010).
47. S. Spector, M. Geis, G. Zhou, M. Grein, F. Gan, M. Popovic, J. Yoon, D. Lennon, E. Ippen, F. Kärtner, and T. Lyszczarz, "CMOS-compatible dual-output silicon modulator for analog signal processing," *Opt. Express* **16**, pp. 11027–11031 (2008).

48. S. J. Spector, C. M. Sorace, M. W. Geis, M. E. Grein, J. U. Yoon, T. M. Lyszczarz, E. P. Ippen, F. X. Kärtner, "Operation and Optimization of Silicon-Diode-Based Optical Modulators", *IEEE Journal of Selected Topics in Quantum Electronics* **16**, pp. 165–172 (2010).
49. J. Michel, J. Liu, and L. C. Kimerling, "High-performance Ge-on-Si photodetectors," *Nature Photonics* **4**, 527–534 (2010).
50. M. W. Geis, S. J. Spector, M. E. Grein et al., "All silicon infrared photodiodes: photo response and effects of processing temperature," *Opt. Express* **15**, pp. 16886–16895 (2007).
51. M. E. Grein, S. J. Spector, A. Khilo, A. Najadmalayeri, M. Sander, M. Peng, J. Wang, C. Sorace, M. Geis, M. Willis, D. Lennon, J. U. Yoon, T. M. Lyszczarz, E. P. Ippen, and F. X. Kärtner, "Demonstration of a 10 GHz CMOS-Compatible Integrated Photonic Analog-to-Digital Converter," *Conference on Lasers and Electro-Optics (CLEO) 2011*, paper CThI1 (invited).
52. T. Shoji, T. Tsuchizawa, T. Watanabe, K. Yamada, H. Morita, "Low loss mode size converter from 0.3  $\mu\text{m}$  square Si wire waveguides to singlemode fibres," *Electronics Letters* **38**, pp. 1669–1670 (2002).
53. C.H. Cox, III, "Analog optical link: Theory and practice" (Cambridge University Press, Cambridge, U.K, 2004).
54. A. Khilo, C. M. Sorace, and F. X. Kärtner, "Broadband linearized silicon modulator," *Opt. Express* **19**, pp. 4485–4500 (2011).
55. W. B. Bridges and J. H. Schaffner, "Distortion in linearized electrooptic modulators," *IEEE Trans. Microwave Theory Tech.* **43**, pp. 2184–2197 (1995).
56. E. Balestrieri, P. Daponte, and S. Rapuano, "A State of the Art on ADC Error Compensation Methods," *IEEE Trans. Instr. Meas.* **54**, pp. 1388–1394, 2005.
57. J. S. Orcutt, A. Khilo, C. W. Holzwarth, M. Popović, H. Li, J. Sun, T. Bonifield, R. Hollingsworth, F. X. Kärtner, Henry I. Smith, V. Stojanović, R. J. Ram, "Nanophotonic Integration in State-of-the-Art CMOS Foundries," *Optics Express* **19**, pp. 2335–2346, 2011.
58. C. Chang (Ed.), "RF photonics technology fiber links" (Cambridge University Press, 2002).
59. A. J. Seeds and K. J. Williams, "Microwave photonics," *J. Lightwave Technol.* **24**, pp. 4628–4641 (2006).
60. J. Capmany and D. Novak, "Microwave photonics combines two worlds," *Nat. Photonics* **1**, pp. 319–330 (2007).
61. R. C. Williamson and R. D. Esman, "RF Photonics," *J. Lightw. Technol.* **26**, pp. 1145–1153 (2008).
62. P. Juodawlkis, J. Twitchell, G. Betts, J. Hargreaves, R. Younger, J. Wasserman, F. O'Donnell, K. Ray, and R. C. Williamson, "Optically sampled analog-to-digital converters," *IEEE Trans. Microw. Theory Tech.* **49**, pp. 1840–1853 (2001).
63. R. A. Soref, "The past, present, and future of silicon photonics," *IEEE J. Sel. Top. Quantum Electron.* **12**, pp. 1678–1687 (2006).
64. B. Jalali and S. Fathpour, "Silicon photonics," *J. Lightwave Technol.* **24**, pp. 4600–4615 (2006).

65. G. T. Reed, G. Mashanovich, F. Y. Gardes, and D. J. Thomson, "Silicon optical modulators," *Nat. Photonics* **4**, pp. 518–526 (2010).
66. B. G. Lee, A. Biberman, and J. Chan, K. Bergman, "High-performance modulators and switches for silicon photonic networks-on-chip," *IEEE Journal of Selected Topics in Quantum Electronics* **16**, pp. 6–22 (2010).
67. J. Michel, J. Liu, and L. C. Kimerling, "High-performance Ge-on-Si photodetectors," *Nat. Photonics* **4**, pp. 527–534 (2010).
68. R. B. Childs and V. A. O'Byrne, "Multichannel AM video transmission using a high-power Nd:YAG laser and linearized external modulator," *IEEE J. Select. Areas Commun.* **8**, pp. 1369–1376 (1990).
69. M. Nazarathy, J. Berger, A. Ley, I. Levi, and Y. Kagan, "Progress in externally modulated AM CATV transmission systems," *J. Lightwave Technol.* **11**, pp. 82–105 (1993).
70. G. C. Wilson, T. H. Wood, M. Gans, J. L. Zyskind, J. W. Sulhoff, J. E. Johnson, T. Tanbun-Ek, and P. A. Morton, "Predistortion of electroabsorption modulators for analog CATV systems at 1.55  $\mu\text{m}$ ," *J. Lightwave Technol.* **15**, pp. 1654–1662 (1997).
71. Y. Chiu, B. Jalali, S. Garner, and W. Steier, "Broad-band electronic linearizer for externally modulated analog fiber-optic links," *IEEE Photon. Technol. Lett.* **11**, pp. 48–50 (1999).
72. V. Magoon and B. Jalali, "Electronic linearization and bias control for externally modulated fiber optic link," in *IEEE Int. Microw. Photon. Meeting*, Oxford, U.K., Sep. 2000, pp. 145–147.
73. R. Sadhwani and B. Jalali, "Adaptive CMOS predistortion linearizer for fiber-optic links," *J. Lightw. Technol.* **21**, pp. 3180–3193 (2003).
74. A. Katz, W. Jemison, M. Kubak, and J. Dragone, "Improved radio over fiber performance using predistortion linearization," in *IEEE MTT-S Int. Microw. Symp. Dig.*, Philadelphia, PA, Jun. 2003, pp. 1403–1406.
75. V. J. Urick, M. S. Rogge, P. F. Knapp, L. Swingen, and F. Bucholtz, "Wide-band predistortion linearization for externally modulated long-haul analog fiber-optic links," *IEEE Trans. Microw. Theory Tech.* **54**, pp. 1458–1463 (2006).
76. U. V. Cummings and W. B. Bridges, "Bandwidth of linearized electrooptic modulators," *J. Lightwave Technol.* **16**, pp. 1482–1490 (1998).
77. S. K. Korotky and R. M. DeRidder, "Dual parallel modulation schemes for low-distortion analog optical transmission," *IEEE J. Select. Areas Commun.* **8**, pp. 1377–1380 (1990).
78. J. L. Brooks, G. S. Maurer, and R. A. Becker, "Implementation and evaluation of a dual parallel linearization system for AM-SCM video transmission," *J. Lightwave Technol.* **11**, pp. 34–41 (1993).
79. H. Skeie and R. Johnson, "Linearization of electro-optic modulators by a cascade coupling of phase modulating electrodes," *Proc. SPIE* **1583**, pp. 153–164 (1991).
80. G. Betts, "Linearized modulator for suboctave-bandpass optical analog links," *IEEE Trans. Microwave Theory Tech.* **12**, pp. 2642–2649 (1994).
81. M. L. Farwell, Z. Q. Lin, E. Wooten, and W. S. C. Chang, "An electrooptic intensity modulator with improved linearity," *IEEE Photon. Technol. Lett.* **3**, pp. 792–795 (1991).



82. E. Ackerman, "Broad-band linearization of a Mach-Zehnder electrooptic modulator," *IEEE Trans. Microwave Theory Tech.* **12**, pp. 2271–2279 (1999).
83. L. M. Johnson and H. V. Roussel, "Reduction of intermodulation distortion in interferometric optical modulators," *Opt. Lett.* **13**, pp. 928–930 (1988).
84. L. M. Johnson and H. V. Roussel, "Linearization of an interferometric modulator at microwave frequencies by polarization mixing," *IEEE Photon. Technol. Lett.* **2**, pp. 810–811 (1990).
85. F. Gan and F.X. Kärtner, "High-speed silicon electrooptic modulator design," *IEEE Photonics Technology Letters* **17**, pp. 1007–1009 (2005).
86. F. Y. Gardes, G. T. Reed, N. G. Emerson, and C. E. Png, "A sub-micron depletion-type photonic modulator in silicon on insulator," *Opt. Express* **13**, pp. 8845–8854 (2005), <http://www.opticsinfobase.org/abstract.cfm?URI=oe-13-22-8845>
87. A. Liu, L. Liao, D. Rubin, H. Nguyen, B. Ciftcioglu, Y. Chetrit, N. Izhaky, and M. Paniccia, "High-speed optical modulation based on carrier depletion in a silicon waveguide," *Opt. Express* **15**, pp. 660–668 (2007), <http://www.opticsinfobase.org/oe/abstract.cfm?URI=oe-15-2-660>
88. L. Liao, A. Liu, D. Rubin, J. Basak, Y. Chetrit, H. Nguyen, R. Cohen, N. Izhaky, and M. Paniccia, "40 Gbit/s silicon optical modulator for high-speed applications," *Electron. Lett.* **43**, pp. 1196–1197 (2007).
89. S. Spector, M. Geis, G. Zhou, M. Grein, F. Gan, M. Popovic, J. Yoon, D. Lennon, E. Ippen, F. Kärtner, and T. Lyszczarz, "CMOS-compatible dual-output silicon modulator for analog signal processing," *Opt. Express* **16**, pp. 11027–11031 (2008), <http://www.opticsinfobase.org/oe/abstract.cfm?URI=oe-16-15-11027>
90. M. R. Watts, D. C. Trotter, R. W. Young, and A. L. Lentine, "Ultralow power silicon microdisk modulators and switches," in *5th IEEE International Conference on Group IV Photonics*, 4–6 (2008).
91. M. R. Watts, W. A. Zortman, D. C. Trotter, R. W. Young, and A. L. Lentine, "Low-voltage, compact, depletion-mode, silicon Mach-Zehnder modulator," *IEEE Journal of Selected Topics in Quantum Electronics* **16**, pp. 159–164 (2010).
92. N. Feng, S. Liao, D. Feng, P. Dong, D. Zheng, H. Liang, R. Shafiiha, G. Li, J. Cunningham, A. Krishnamoorthy, and M. Asghari, "High speed carrier-depletion modulators with 1.4V-cm  $V_{\pi}L$  integrated on 0.25 $\mu\text{m}$  silicon-on-insulator waveguides," *Opt. Express* **18**, pp. 7994–7999 (2010), <http://www.opticsinfobase.org/oe/abstract.cfm?URI=oe-18-8-7994>
93. X. Zheng, J. Lexau, Y. Luo, H. Thacker, T. Pinguet, A. Mekis, G. Li, J. Shi, P. Amberg, N. Pinckney, K. Raj, R. Ho, J. E. Cunningham, and A. V. Krishnamoorthy, "Ultra-low-energy all-CMOS modulator integrated with driver," *Opt. Express* **18**, pp. 3059–3070 (2010), <http://www.opticsinfobase.org/oe/abstract.cfm?URI=oe-18-3-3059>
94. D. M. Gill, M. Rasras, K.-Y. Tu, Y.-K. Chen, A. E. White, S. S. Patel, D. Carothers, A. Pomerene, R. Kamocsai, C. Hill, and J. Beattie, "Internal bandwidth equalization in a CMOS compatible Si-ring modulator," *Photon. Technol. Lett.* **21**, pp. 200–202 (2009).

95. Q. Xu, B. Schmidt, S. Pradhan, and M. Lipson, "Micrometre-scale silicon electro-optic modulator," *Nature* **435**, pp. 325–327 (2005).
96. W. M. Green, M. J. Rooks, L. Sekaric, and Y. A. Vlasov, "Ultra-compact, low RF power, 10 Gb/s silicon Mach-Zehnder modulator," *Opt. Express* **25**, pp. 17106–17113 (2007), <http://www.opticsinfobase.org/oe/abstract.cfm?URI=oe-15-25-17106>
97. Q. Xu, S. Manipatrani, B. Schmidt, J. Shakyia, and M. Lipson, "12.5 Gbit/s carrier-injection-based silicon micro-ring silicon modulators," *Opt. Express* **15**, pp. 430–436 (2007), <http://www.opticsinfobase.org/oe/abstract.cfm?URI=oe-15-2-430>
98. S. Manipatrani, X. Qianfan, B. Schmidt, J. Shakyia, and M. Lipson, "High speed carrier injection 18 Gb/s silicon micro-ring electro-optic modulator," *IEEE Proc. Lasers and Electro-Optics Soc.* pp. 537–538 (2007).
99. S. Manipatrani, K. Preston, L. Chen, and M. Lipson, "Ultra-low voltage, ultra-small mode volume silicon microring modulator," *Opt. Express* **18**, pp. 18235–18242 (2010), <http://www.opticsinfobase.org/oe/abstract.cfm?URI=oe-18-17-18235>
100. A. Liu, R. Jones, L. Liao, D. Samara-Rubio, D. Rubin, O. Cohen, R. Nicolaescu, and M. Paniccia, "A high-speed silicon optical modulator based on a metal-oxide-semiconductor capacitor," *Nature* **427**, pp. 615–618 (2004).
101. L. Liao, D. Samara-Rubio, M. Morse, A. Liu, D. Hodge, D. Rubin, U. Keil, and T. Franck, "High speed silicon Mach-Zehnder modulator," *Opt. Express* **13**, pp. 3129–3135 (2005) <http://www.opticsinfobase.org/oe/abstract.cfm?URI=oe-13-8-3129>
102. Y. Kuo, Y. K. Lee, Y. Ge, S. Ren, J. E. Roth, T. I. Kamins, D. A. B. Miller, and J. S. Harris, "Strong quantum-confined Stark effect in germanium quantum-well structures on silicon," *Nature* **437**, pp. 1334–1336 (2005).
103. J. E. Roth, O. Fidaner, R. K. Schaevitz, Y. -H. Kuo, T. I. Kamins, J. S. Harris, and D. A. B. Miller, "Optical modulator on silicon employing germanium quantum wells," *Opt. Express* **15**, pp. 5851–5859 (2007), <http://www.opticsinfobase.org/oe/abstract.cfm?URI=oe-15-9-5851>
104. J. Liu, M. Beals, A. Pomerene, S. Bernardis, R. Sun, J. Cheng, L. C. Kimerling, and J. Michel, "Waveguide-integrated, ultralow-energy GeSi electro-absorption modulators," *Nat. Photonics* **2**, pp. 433–437 (2008).
105. C. C. Sorace, A. Khilo, and F. X. Kärtner, "Broadband linear silicon Mach-Zehnder modulators," in *Integrated Photonics Research (IPR), Silicon and Nanophotonics*, 2010, paper IWA4.
106. Synopsys, *Sentaurus Device User Guide*, Z-2010.03 ed., March 2010.
107. R. Soref and B. Bennett, "Electrooptical effects in silicon," *IEEE J. of Quantum Electron.* **23**, pp. 123–129 (1987).
108. M. Popović, "Complex-frequency leaky mode computations using PML boundary layers for dielectric resonant structures," in *Integrated Photonics Research 2003*, Washington, DC, June 17, 2003, paper ITuD4.
109. S. J. Spector, C. M. Sorace, M. W. Geis, M. E. Grein, J. U. Yoon, T. M. Lyszczarz, E. P. Ippen, and F. X. Kärtner, "Operation and Optimization of Silicon-Diode-Based Optical Modulators," *IEEE J. Sel. Top. Quantum Electron.* **16**, pp. 165–172 (2010).

110. A. Motamedi, "Ultrafast nonlinear optical properties of passive and active semiconductor devices," Ph.D. Thesis, Massachusetts Institute of Technology, Cambridge, MA, 2011.
111. A. R. Motamedi, A. Nejadmalayeri, A. Khilo, F. X. Kärtner, E. P. Ippen, "Ultrafast nonlinear optical processes and free-carrier lifetime in silicon nanowaveguides," Conference on Lasers and Electro-Optics (CLEO) 2011, paper CFO2.
112. Cheryl M. Sorace, "Advanced Silicon Photonic Modulators," M.S. thesis, Massachusetts Institute of Technology, Cambridge, 2010.
113. C. Koos, L. Jacome, C. Poulton, J. Leuthold, and W. Freude, "Nonlinear silicon-on-insulator waveguides for all-optical signal processing," *Opt. Express* **15**, pp. 5976-5990 (2007).
114. G. Agrawal, "Nonlinear Fiber Optics" (Academic Press, 2006).
115. A. Villeneuve, J. S. Aitchison, B. Vogege, R. Tapella, J. U. Kang, C. Trevino, and G. I. Stegeman, "Waveguide design for minimum nonlinear effective area and switching energy in AlGaAs at half the bandgap," *Electron. Letters* **31**, pp. 549-551 (1995).
116. M. Foster, K. Moll, and A. Gaeta, "Optimal waveguide dimensions for nonlinear interactions," *Opt. Express* **12**, pp. 2880-2887 (2004).
117. S. Afshar V and T. M. Monro, "A full vectorial model for pulse propagation in emerging waveguides with subwavelength structures part I: Kerr nonlinearity," *Opt. Express* **17**, pp. 2298-2318 (2009).
118. A. W. Snyder, J. Love, "Optical waveguide theory" (Springer, 1983).
119. Ioffe Institute of Physics database, <http://www.ioffe.ru/SVA/NSM/Semicond/>.
120. M. Popović, "Theory and Design of High-Index-Contrast Microphotonic Circuits," Ph.D. Thesis, Massachusetts Institute of Technology, Cambridge, MA, 2008.
121. M. A. Popović, T. Barwicz, E. P. Ippen and F. X. Kärtner, "Global design rules for silicon microphotonic waveguides: sensitivity, polarization and resonance tunability," in *Conference on Lasers and Electro-Optics/Quantum Electronics and Laser Science*, Technical Digest (CD) (Optical Society of America, 2006), paper CTuCC1.
122. A. Melloni, M. Martinelli, "Synthesis of direct-coupled-resonators bandpass filters for WDM systems," *J. Lightwave Technol.* **20**, pp. 296-303 (2002).
123. L. Pavesi, D. J. Lockwood (Eds.), "Silicon Photonics" (Springer, Heidelberg, Germany, 2004).
124. S. R. Giguere, L. Friedman, R. A. Soref, J. P. Lorenzo, "Simulation studies of silicon electro-optic waveguide devices," *J. Appl. Phys.* **68**, pp. 4964-4970 (1990).
125. M.A. Popović, T. Barwicz, M.S. Dahlem, F. Gan, C.W. Holzwarth, P.T. Rakich, H.I. Smith, E.P. Ippen and F.X. Kärtner, "Tunable, Fourth-Order Silicon Microring-Resonator Add-Drop Filters," European Conference on Optical Communication 2007, paper 1.2.3.
126. M.A. Popović, T. Barwicz, P.T. Rakich, M.S. Dahlem, C.W. Holzwarth, F. Gan, L. Socci, M.R. Watts, H.I. Smith, F.X. Kärtner and E.P. Ippen, "Experimental demonstration of loop-coupled microring resonators for optimally sharp optical filters," Conference on Lasers and Electro-Optics (CLEO) 2008, paper CTuNN3.

127. B. E. Little, S. T. Chu, H. A. Haus, J. Foresi, J.-P. Laine, "Microring resonator channel dropping filters," *J. Lightwave Technol.* **15**, pp. 998-1005 (1997).
128. C. K. Madsen, J.H. Zhao, "Optical Filter Design and Analysis: A Signal Processing Approach," (John Wiley & Sons, New York, 1999).
129. M. S. Dahlem, C. W. Holzwarth, A. Khilo, F. X. Kärtner, H. I. Smith, and E. P. Ippen, "Reconfigurable multi-channel second-order silicon microring-resonator filterbanks for on-chip WDM systems," *Opt. Express* **19**, pp. 306-316 (2011).
130. M. Dahlem, "Studies of advanced integrated nano-photonic devices in silicon," Ph.D. Thesis, MIT, 2011.
131. M. Popovic, M. Watts, T. Barwicz, P. Rakich, L. Socci, E. Ippen, F. Kartner, H. Smith, "High-index-contrast, wide-FSR microring-resonator filter design and realization with frequency-shift compensation", OFC 2005, paper OFKI.
132. A. Taflove, "Computational Electrodynamics: The Finite-Difference Time-Domain Method" (Artech House Publishers, 2005).
133. C. W. Holzwarth, T. Barwicz, M. A. Popović, P.T. Rakich, E.P. Ippen, F.X. Kärtner, H.I. Smith, "Accurate resonant frequency spacing of microring filters without postfabrication trimming," *J. Vac. Sci. Technol. B* **24**, 3244-3247, 2006.
134. C. W. Holzwarth, "Material selection and nanofabrication techniques for electronic photonic integrated circuits," Ph.D. Thesis, MIT, 2009.
135. T. Barwicz, "Accurate Nanofabrication Techniques for High-Index-Contrast Microphotonic Devices," Ph.D. Thesis, MIT, 2005.
136. S. J. Spector, A. Khilo, M. Peng, F. X. Kärtner, and T. M. Lyszczarz, "Thermally Tuned Dual 20-Channel Ring Resonator Filter Bank in SOI (Silicon-on-Insulator)," Conference on Lasers and Electro-Optics (CLEO) 2011, paper CWM2.
137. Di Liang and J. E. Bowers, "Recent progress in lasers on silicon," *Nat. Photonics* **4**, pp. 511–517 (2010).
138. M. E. Groenert, A. J. Pitera, R. J. Ram, and E. A. Fitzgerald, "Improved room temperature continuous wave GaAs/AlGaAs and InGaAs/GaAs/AlGaAs lasers fabricated on Si substrates via relaxed graded  $\text{Ge}_x\text{Si}_{1-x}$  buffer layers," *J. Vac. Sci. Tech. B* **21**, pp. 1064–1069 (2003).
139. J. Van Campenhout, P. Rojo Romeo, P. Regreny, C. Seassal, D. Van Thourhout, S. Verstuyft, L. Di Cioccio, J.-M. Fedeli, C. Lagae, and R. Baets, "Electrically pumped InP-based microdisk lasers integrated with a nanophotonic silicon-on-insulator waveguide circuit," *Opt. Express* **15**, pp. 6744–6749 (2007).
140. J. Liu, X. Sun, R. Camacho-Aguilera, L. C. Kimerling, J. Michel, "Ge-on-Si laser operating at room temperature," *Opt. Lett.* **35**, pp. 679–681 (2010).
141. A. Khilo, M. A. Popović, M. Araghchini, and F. X. Kärtner, "Efficient Planar Fiber-to-Chip Coupler based on Two-Stage Adiabatic Evolution," *Optics Express* **18**, pp. 15790–15806 (2010).

142. A. Khilo and F. X. Kärtner, "Efficient Planar Single-Mode Fiber-to-Chip Coupler based on Two-Stage Adiabatic Evolution," in *Conference on Lasers and Electro-Optics/Quantum Electronics and Laser Science*, Technical Digest (CD) (Optical Society of America, 2010), paper JThE30.
143. A. Khilo, M. Popović, F.X. Kärtner, "Efficient Planar Fiber-to-Chip Coupler based on Two-Stage Adiabatic Evolution," presented at ICONO/LAT Conference, Minsk, Belarus, 2007, paper IO2/VIII-1.
144. R. Orobtcouk, "On Chip Optical Waveguide Interconnect: the Problem of the In/Out Coupling," in *Optical Interconnects: the Silicon Approach*, L. Pavesi, G. Guillot, eds. (Springer, 2006).
145. Y. Shani, C. H. Henry, R. C. Kistler, K. J. Orlowsky, and D. A. Ackerman, "Efficient coupling of a semiconductor laser to an optical fiber by means of a tapered waveguide on silicon," *Appl. Phys. Lett.* **55**, pp. 2389–2391 (1989).
146. T. Shoji, T. Tsuchizawa, T. Watanabe, K. Yamada and H. Morita, "Low loss mode size converter from 0.3 $\mu$ m square Si wire waveguides to singlemode fibres," *Electron. Lett.* **38**, pp. 1669–1670 (2002).
147. T. Tsuchizawa, K. Yamada, H. Fukuda, T. Watanabe, J. Takahashi, M. Takahashi, T. Shoji, E. Tamechika, S. Itabashi, and H. Morita "Microphotonic Devices Based on Silicon Microfabrication Technology," *IEEE J. Sel. Top. Quant. Electron.* **11**, pp. 232–240 (2005).
148. S. McNab, N. Moll, and Y. Vlasov, "Ultra-low loss photonic integrated circuit with membrane-type photonic crystal waveguides," *Opt. Express* **11**, pp. 2927–2939 (2003), <http://www.opticsinfobase.org/abstract.cfm?URI=oe-11-22-2927>
149. V. R. Almeida, R. R. Panepucci, and M. Lipson, "Nanotaper for compact mode conversion," *Opt. Lett.* **28**, pp. 1302–1304 (2003).
150. G. Roelkens, P. Dumon, W. Bogaerts, D. Van Thourhout, R. Baets, "Efficient fiber to SOI photonic wire coupler fabricated using standard CMOS technology," *IEEE Photon. Technol. Lett.* **17**, pp. 2613–2615 (2005).
151. K. K. Lee, D. R. Lim, D. Pan, C. Hoepfner, W.-Y. Oh, K. Wada, L. C. Kimerling, K. P. Yap, and M. T. Doan, "Mode transformer for miniaturized optical circuits," *Opt. Lett.* **30**, pp. 498–500 (2005).
152. D. Taillaert, W. Bogaerts, P. Bienstman, T. F. Krauss, P. Van Daele, I. Moerman, S. Verstuyft, K. De Mesel, and R. Baets, "An out-of-plane grating coupler for efficient butt-coupling between compact planar waveguides and single-mode fibers," *IEEE J. Quantum Electron.* **38**, pp. 949–955 (2002).
153. D. Taillaert, P. Bienstman, and R. Baets, "Compact efficient broadband grating coupler for silicon-on-insulator waveguides," *Opt. Lett.* **29**, pp. 2749–2751 (2004).
154. B. Wang, J. Jiang, D. M. Chambers, J. Cai, and G. P. Nordin, "Stratified waveguide grating coupler for normal fiber incidence," *Opt. Lett.* **30**, pp. 845–847 (2005).
155. F. Van Laere, G. Roelkens, M. Ayre, J. Schrauwen, D. Taillaert, D. Van Thourhout, T. F. Krauss, and R. Baets "Compact and Highly Efficient Grating Couplers Between Optical Fiber and Nanophotonic Waveguides," *J. Lightwave Technol.* **25**, 151-156 (2007).

156. Dirk Taillaert, "Grating couplers as Interface between Optical Fibres and Nanophotonic Waveguides," Ph.D. Thesis, Ghent University, Ghent, Belgium, 2005.
157. M. Fan, M. Popović, and F. X. Kärtner, "High Directivity, Vertical Fiber-to-Chip Coupler with Anisotropically Radiating Grating Teeth," in *Conference on Lasers and Electro-Optics/Quantum Electronics and Laser Science*, Technical Digest (CD) (Optical Society of America, 2007), paper CTuDD3.
158. I. E. Day, I. Evans, A. Knights, F. Hopper, S. Roberts, J. Johnston, S. Day, J. Luff, H. K. Tsang, and M. Asghari, "Tapered Silicon Waveguides for Low Insertion Loss Highly-Efficient High-Speed Electronic Variable Optical Attenuators," in *Optical Fiber Communication Conference*, Technical Digest (CD) (Optical Society of America, 2003), paper TuM5.
159. R. J. Bozeat, S. Day, F. Hopper, F. P. Payne, S. W. Roberts, M. Asghari, "Silicon Based Waveguides," in *Silicon Photonics*, L. Pavesi, D. J. Lockwood, eds. (Springer, 2004).
160. T. Aalto, K. Solehmainen, M. Harjanne, M. Kapulainen, P. Heimala, "Low-loss converters between optical silicon waveguides of different sizes and types," *IEEE Photon. Technol. Lett.* **18**, pp. 709–711 (2006).
161. J. K. Doylend, A. P. Knights, "Design and Simulation of an Integrated Fiber-to-Chip Coupler for Silicon-on-Insulator Waveguides", *IEEE J. Sel. Top. Quant. Electron.* **12**, pp. 1363–1370 (2006).
162. A. Barkai, A. Liu, D. Kim, R. Cohen, N. Elek, H. Chang, B. H. Malik, R. Gabay, R. Jones, M. Paniccia, and N. Izhaky, "Double-Stage Taper for Coupling Between SOI Waveguides and Single-Mode Fiber," *J. Lightwave Technol.* **26**, pp. 3860–3865 (2008).
163. D. Dai, S. He, and H. Tsang, "Bilevel Mode Converter Between a Silicon Nanowire Waveguide and a Larger Waveguide," *J. Lightwave Technol.* **24**, pp. 2428–2433 (2006).
164. K. Shiraishi, H. Yoda, A. Ohshima, H. Ikedo, and C. S. Tsai, "A silicon-based spot-size converter between single-mode fibers and Si-wire waveguides using cascaded tapers," *Appl. Phys. Lett.* **91**, 141120 (2007).
165. A. Sure, T. Dillon, J. Murakowski, C. Lin, D. Pustai, and D. Prather, "Fabrication and characterization of three-dimensional silicon tapers," *Opt. Express* **11**, pp. 3555–3561 (2003), <http://www.opticsinfobase.org/abstract.cfm?URI=oe-11-26-3555>
166. M. Fritze, J. Knecht, C. Bozler, C. Keast, J. Fijol, S. Jacobson, P. Keating, J. LeBlanc, E. Fike, B. Kessler, M. Frish, and C. Manolatou, "Fabrication of three-dimensional mode converters for silicon-based integrated optics," *J. Vac. Sci. Technol. B* **21**, pp. 2897–2902 (2003).
167. C. Manolatou, H. A. Haus, "Passive components for dense optical integration" (Kluwer Academic Publishers, 2001), chap. 6.
168. V. Nguyen, T. Montalbo, C. Manolatou, A. Agarwal, C. Hong, J. Yasaitis, L. C. Kimerling, and J. Michel, "Silicon-based highly-efficient fiber-to-waveguide coupler for high index contrast systems", *Appl. Phys. Lett.* **88**, 081112 (2006).
169. R. Sun, V. Nguyen, A. Agarwal, C. Hong, J. Yasaitis, L. Kimerling, and J. Michel, "High performance asymmetric graded index coupler with integrated lens for high index waveguides," *Appl. Phys. Lett.* **90**, 201116 (2007).



170. Qing Fang, Tsung-Yang Liow, Jun Feng Song, Chee Wei Tan, Ming Bin Yu, Guo Qiang Lo, and Dim-Lee Kwong, "Suspended optical fiber-to-waveguide mode size converter for silicon photonics," *Opt. Express* **18**, pp. 7763–7769 (2010), <http://www.opticsinfobase.org/abstract.cfm?URI=oe-18-8-7763>
171. M. Qi, M. R. Watts, T. Barwicz, L. Socci, P. Rakich, E. P. Ippen, and H. I. Smith, "Fabrication of Two-Layer Microphotonic Structures without Planarization," in *Conference on Lasers and Electro-Optics/Quantum Electronics and Laser Science*, Technical Digest (CD) (Optical Society of America, 2005), paper CWD5.
172. T. Barwicz, M. R. Watts, M. A. Popovic, P. T. Rakich, L. Socci, F. X. Kärtner, E. P. Ippen and H. I. Smith, "Polarization-transparent microphotonic devices in the strong confinement limit," *Nature Photonics* **1**, pp. 57–60 (2007).
173. FIMMWAVE/FIMMPROP by Photon Design, <http://www.photond.com>.
174. C. W. Holzwarth, J. S. Orcutt, H. Li, M. A. Popović, V. Stojanović, J. L. Hoyt, R. J. Ram, and H. I. Smith, "Localized Substrate Removal Technique Enabling Strong-Confinement Microphotronics in Bulk Si CMOS Processes," in *Conference on Lasers and Electro-Optics/Quantum Electronics and Laser Science*, Technical Digest (CD) (Optical Society of America, 2008), paper CThKK5.
175. A. Khilo, "Integrated Optical Analog-to-Digital Converter," M.S. thesis, Massachusetts Institute of Technology, Cambridge, 2008.
176. S. Selvaraja, P. Jaenen, W. Bogaerts, D. VanThourhout, P. Dumon, and R. Baets, "Fabrication of Photonic Wire and Crystal Circuits in Silicon-on-Insulator Using 193-nm Optical Lithography," *J. Lightwave Technol.* **27**, pp. 4076–4083 (2009).
177. T. Barwicz, M. A. Popović, M. R. Watts, P. T. Rakich, E. P. Ippen, H. I. Smith, "Fabrication of Add-Drop Filters Based on Frequency-Matched Microring Resonators," *J. Lightwave Technol.* **24**, pp. 2207–2218 (2006).
178. T. Barwicz and H. A. Haus, "Three-Dimensional Analysis of Scattering Losses Due to Sidewall Roughness," *J. Lightwave Technol.* **23**, pp. 2719–2732 (2006).
179. G. H. Song, W. J. Tomlinson, "Fourier Analysis and Synthesis of Adiabatic Tapers in Integrated Optics," *J. Opt. Soc. Am. A* **9**, pp. 1289–1300 (1992).